

Silica-Based Nanomaterials for Cancer Theranostics

A Dissertation
Presented to the Faculty of the Graduate School
of Cornell University
In Partial Fulfillment of the Requirements for the Degree of
Doctor of Philosophy

by
Kai Ma
February 2016

© 2016 Kai Ma

ALL RIGHTS RESERVED

Silica-Based Nanomaterials for Cancer Theranostics

Kai Ma

Cornell University 2016

Nanomedicine is the medical application of nanomaterials. It is expected to have a revolutionary impact on health care. One of the most exciting concepts in nanomedicine is the development of multifunctional nanoparticles that enable the simultaneous detection and treatment of diseases with unprecedented precision (theranostics). This thesis focuses on the development of an ultras-small silica-based nanomaterials platform for theranostics applications. The synthesis and detailed characterization of a variety of silica-based nanomaterials are discussed with novel structures and tunable dimensions in the sub-10nm regime. Fluorescence correlation spectroscopy is introduced as an appropriate tool for fluorescent nanoparticle characterization. Particular focus is on surface modifications of nanoparticles synthesized in water with biocompatible polyethylene glycol and cancer targeting ligands. Such clinically applicable silica-based nanomaterials (C'dots) have received FDA approval as an investigational new drug (IND). Multiple human clinical trials with C' dots on cancer patients are currently ongoing at Memorial Sloan Kettering Cancer Center (MSKCC). The study of silica nanomaterials further provides insights to fundamental questions regarding the early formation mechanisms of self-assembled nanostructures. To that end investigations of the formation process of quasi-crystalline mesoporous silica nanoparticles is discussed that highlight structural details of building blocks and pathways responsible for the switch between crystalline (cubic symmetry) and quasicrystalline states.

Biographical Sketch

Kai Ma is from Shenzhen, China and received his bachelor's degree in condensed matter physics from University of Science and Technology of China (USTC) in 2009. During his undergraduate study in the Physics department at USTC, he used to work on multiple research projects in grammatically different areas, including string theory, the rotation of the ring of Saturn, zinc oxide superhydrophobic membrane and magmatic nickel nanoparticles, and finally navigated his research interest to nanomaterials. Upon completing his bachelor's degree in 2009, he came to Cornell University together with his wife who was also a graduate student of veterinary school of Cornell. He joined Wiesner Group in 2009 as a master student and had worked on fluorescent correlation spectroscopy and chemiluminescent nanoparticles until 2010. In 2010, he started his PhD program in Wiesner Group working on silica-based nanomaterials for cancer theranostics.

Acknowledgements

Foremost, I would like to express my sincere gratitude to my advisor Prof. Ulrich Wiesner for accepting me into the PhD program at Cornell, for the continuous support of my PhD study, for his patience, motivation and immense knowledge. I feel that I am extremely fortunate to have the chance in my life to become one of students of Prof. Ulrich Wiesner. I will still feel proud of it many years later when I turns old. First of all, I wish to thank Prof. Ulrich Wiesner for transferring me from the master program to the PhD program in 2009, therefore, my wife, who was a graduate student of veterinary school of Cornell, and I were able to stay together for our graduate studies at Cornell and have our small family. I wish to thank Prof. Ulrich Wiesner for offering me the great opportunities to work on this exciting project about clinically applicable silica-based nanomaterials, *e.g.* Cornell dots. It is such a promising area and I am very proud of that I am part of the development of Cornell dots which have already been used in clinic providing real benefits to cancer patients. I wish to thank Prof. Ulrich Wiesner for giving me a lot of freedom in my PhD research and always encouraging me to bravely explore the undiscovered area. I wish to thank Prof. Ulrich Wiesner for giving me many advices as a great mentor not only on research, but also on collaboration, career, language and even interpersonal skills. Prof. Ulrich Wiesner has taught me so much knowledge, well beyond the study and research, which has become a great treasure of my life. Last but not least, I wish to thank for Prof. Ulrich Wiesner for helping me overcome setbacks and stay focused on my graduate study in the hard time of my life. His guidance helped me in all the time and I could not have imagined having a better advisor and mentor for my PhD study.

Besides my advisor, I would like to thank the rest of my thesis committee, Prof. Lara Estroff and Prof. Dan Luo for their insightful comments, but also for the hard questions which incited me to widen my view of research. I also wish to thank them for giving me a lot of advices in career design. Their precious support is so important to me for finalizing my PhD study.

I am also grateful to Prof. Jack Blakely, Prof. Rüdiger Dieckmann and again my advisor Prof. Ulrich Wiesner, who were the lecturers of thermodynamics, kinetics and chemistry in the first year of my study. I wish to thank them for sharing expertise, and sincere and valuable guidance and encouragement extended to me. Even through the classes were difficult, I learned such a lot, especially the logical thinking which plays an important role in the rest of my PhD study.

I also wish to thank Prof. Richard Robinson who was the lecturer of the class for which I was the teaching assistance. He gave me so much freedom so that I had the chance to explore myself for the design of homework problems, prelims and also lab work. I was also given by the chance to give a few lectures myself. It was a great opportunity for me to improve my teaching skills and it was such a pleasure to work as the teaching assistance with Prof. Richard Robinson.

I also would like to thank all the members of Wiesner group for stimulating discussions and for all fun we have had in the past years. I love the atmosphere of the group that everyone communicates with others and offers assistance whenever other people need help. Especially, I wish to thank Dr. Hiroaki Sai, Dr. Teeraporn Suteewong, Dr. Srikant Iyer, Dr. Zihui Li, Jennifer Drewes, Dr. Yao Sun, Dr. Kwan Tan, Teresa Kao, Melik Turker

and Ferdinand Kohle for their help in experiments, experiment arrangements and lab management. To me Wiesner group was always like a family.

In addition, I wish to give special thanks to our collaborators at Memorial Sloan Kettering Cancer Center (MSKCC) for their effort in the clinical applications using the nanoparticles that I synthesized. Especially, I wish to express my sincere thanks to Prof. Michelle Bradbury at MSKCC for the excellent collaborations in the past several years, for the stimulating discussions and for her advices on both research and career. It is impossible for us to reach that far regarding the medical application of the nanomaterials developed in my PhD without the effort of Prof. Michelle Bradbury. In addition, I wish to thank Dr. Barney Yoo and Dr. Sarah Cheal at MSKCC for their input to the research projects and it was a great pleasure to work with them.

Furthermore, I also wish to express my sincere thanks to all the master, undergraduate and exchange students that I have mentored in my PhD including Gordian Horchler, Carlie Mendoza, Duhan Zhang, Ying Cong and Alyssa Travitz for their exceptional work and all the fun we had together in the past. They were so motivated, hard-working, considerable and responsible, and they provided significant input to my PhD research. Without their great effort, it is impossible for me to finalize many of the research projects.

Last but not least, I wish to express my sincere thanks to my parents, my wife and my daughter for supporting me spiritually throughout my PhD study. I feel extremely fortunate for having such a lovely family and there are no words to express my gratitude to my family. Thank you for everything and I love you!

Table of Contents

Abstract.....	I
Biographical Sketch.....	II
Acknowledgements	III
Table of Contents	VI
List of Figures.....	XIII
List of Tables	XVII
Chapter 1. Introduction.....	1
1.1 References.....	4
Chapter 2. Control of Ultrasmall Sub-10 nm Ligand Functionalized Fluorescent Core-Shell Silica Nanoparticle Growth in Water	7
2.1 Abstract.....	7
2.2 Introduction.....	9
2.3 Experimental section	13
2.3.1 Materials.	13
2.3.2 Synthesis of sub-10nm PEGylated silica nanoparticles.....	13
2.3.3 Synthesis of sub-10nm PEGylated fluorescent silica nanoparticles.	15
2.3.4 Synthesis of sub-10nm PEGylated core-shell silica nanoparticles and sub- 10nm PEGylated fluorescent core-shell silica nanoparticles.....	16

2.3.5	Synthesis of sub-10nm PEGylated aluminosilicate nanoparticles and PEGylated aluminosilicate core-silica shell aluminosilicate nanoparticles.....	17
2.3.6	Synthesis of sub-10 nm PEGylated fluorescent aluminosilicate nanoparticles and sub-10 nm PEGylated fluorescent aluminosilicate core-silica shell aluminosilicate nanoparticles covalently encapsulating Cy5 or Cy5.5 fluorophores... ..	18
2.3.7	PEGylated particle surface modification with easily accessible ligands.....	18
2.3.8	Gel permeation chromatography characterization (GPC).....	19
2.3.9	Characterization of particle morphology.....	20
2.3.10	Characterization of fluorophore encapsulating particles.....	20
2.3.11	²⁹ Si and ²⁷ Al solid-state NMR characterization.....	21
2.3.12	Thermogravimetric analysis (TGA).....	22
2.3.13	Molecular model of c(RGDyC) functionalized C' dot.....	22
2.4	Results and discussion	24
2.4.1	Controlled blank silica nanoparticle growth.....	24
2.4.2	Controlled fluorescent silica nanoparticle growth.....	29
2.4.3	Controlled fluorescent core-shell silica nanoparticle growth.....	31
2.4.4	Controlled fluorescent silica nanoparticle growth with different inorganic compositions.....	38
2.4.5	Ligand functionalized fluorescent silica nanoparticles.....	43
2.4.6	Molecular models of ligand functionalized PEGylated fluorescent core-shell silica nanoparticles.....	47
2.5	Conclusions.....	49

2.6	Acknowledgments	50
2.7	References.....	51
	Appendix A: Supplementary information for Chapter 2.....	57
Chapter 3. Ultra-small Sub-10 nm Near Infrared Fluorescent Mesoporous Silica		
	Nanoparticles.....	72
3.1	Abstract.....	72
3.2	Introduction.....	73
3.3	Experimental section	75
3.3.1	Materials	75
3.3.2	Synthesis of sub-10nm ultra-small mesoporous silica nanoparticles.	75
3.3.3	Synthesis of Cy5.5 labeled single-pore silica nanoparticles.	76
3.3.4	Characterization of particle morphology and size.	76
3.3.5	Particle size distribution from TEM image analysis.....	77
3.3.6	TEM characterization of the distribution of the number of pores per particle.	77
3.3.7	Characterization of the fluorescent properties of Cy5.5 doped mC dots.....	78
3.3.8	Liquid ¹ H NMR analysis.....	79
3.3.9	Nitrogen sorption/desorption analysis	80
3.4	Results and discussion	81
3.5	Acknowledgements	89
3.6	References.....	90
	Appendix B: Supplementary information for Chapter 3.....	95

Chapter 4. Controlling Growth of Ultra-Small Sub-10nm Fluorescent Mesoporous Silica Nanoparticles	102
4.1 Abstract.....	102
4.2 Introduction.....	104
4.3 Experimental section	110
4.3.1 Materials.	110
4.3.2 Synthesis of ultrasmall mesoporous silica nanoparticles using L-lysine as catalyst.	110
4.3.3 Synthesis of ultrasmall mesoporous silica nanoparticles using ammonium hydroxide as catalyst.....	111
4.3.4 Synthesis of ultra-small single-pore fluorescent silica nanoparticles (mC dots) with different colors.....	112
4.3.5 Characterization of particle morphology.	112
4.3.6 Analysis of particle size distribution.....	113
4.3.7 Analysis of number of pores per particle distribution.	113
4.3.8 ¹³ C and ²⁹ Si solid state NMR characterization.....	113
4.3.9 Characterization of fluorescent properties of dye encapsulating mC dots.	114
4.3.10 Characterization of PEG contamination, zeta-potential and long-term stability.	115
4.4 Results and discussion	117
4.4.1 Controlling particle growth through optimizing hydrolysis and condensation.	117
4.4.2 Quenching particle growth through addition of PEG-silane.....	120

4.4.3	Synthesis using ammonium hydroxide as catalyst.....	126
4.4.4	Morphology characterization of ultra-small mesoporous silica nanoparticles.	133
4.4.5	Local structure and long-term stability of ultra-small single pore silica nanoparticles.	138
4.4.6	Ultra-small florescent single-pore silica nanoparticles with multiple colors....	143
4.5	Conclusions	146
4.6	Acknowledgements	148
4.7	References	149
Chapter 5. Elucidating the Mechanism of Silica Nanoparticle PEGylation Processes using Fluorescence Correlation Spectroscopies		157
5.1	Abstract	157
5.2	Introduction	158
5.3	Experimental Section	161
5.3.1	Materials.	161
5.3.2	Conjugation of Cy5-silane.	161
5.3.3	Conjugation of ATTO488-PEG.....	162
5.3.4	Conjugation of c(RGDyC)-PEG-silane.	162
5.3.5	Synthesis of ultrasmall silica nanoparticles.	162
5.3.6	Zeta potential measurements.....	163
5.3.7	DLS size measurements.....	163
5.3.8	TEM measurements.	164

5.3.9	TGA measurements.	164
5.3.10	FCS and FCCS measurements.	164
5.3.11	Conductivity measurements.	165
5.3.12	Estimation of PEG-silane and c(RGDyC)-PEG-silane reaction conversion percentage.	165
5.4	Results and discussion	167
5.5	Conclusions	179
5.6	Acknowledgements	180
5.7	References	181
	Appendix C: Supplementary Information for Chapter 5	188
Chapter 6. Formation Pathways of Mesoporous Silica Nanoparticles with		
Dodecagonal Tiling		
		206
6.1	Introduction	206
6.2	Experimental section	208
6.2.1	Materials	208
6.2.2	Synthesis of MSNs with varying [TMB] (TEOS/AEAPTMS system)	208
6.2.3	Synthesis of MSNs with varying [TMB] and pH (TMOS/APTMS system).	209
6.2.4	Characterization	210
6.2.5	Tiling Analysis	210
6.2.6	Growth Simulations	212
6.2.7	Fitting of the relationship between $R_{g\perp}$ and the total number of squares before the first triangle is attached.	215

6.3	Results and discussion.	218
6.4	Conclusions	227
6.5	Acknowledgements	228
6.6	References	229
	Appendix D: Supplementary information for Chapter 6	233
	Chapter 7. Conclusions	242

List of Figures

<i>Figure 2.1. Illustration of synthesis system</i>	24
<i>Figure 2.2. Characterizations of blank and fluorescent SNPs</i>	28
<i>Figure 2.3. Characterizations of core-shell fluorescent SNPs.</i>	34
<i>Figure 2.4. Optical characterizations of C' dots encapsulating different fluorophores...</i>	36
<i>Figure 2.5. Characterizations of aluminosilicate nanoparticles</i>	39
<i>Figure 2.6. SNP surface functionalization with c(RGDyC) peptides</i>	46
<i>Figure 2.7. Molecular rendering of C' dot</i>	47
<i>Figure A1. In-situ FCS measurement results</i>	57
<i>Figure A2. TEM images of SNPs synthesized with/without high temperature treatment.</i>	59
<i>Figure A3. FCS characterization of Cy5 labeled C' dots</i>	60
<i>Figure A4 TEM images of of Cy5-encapsulated SNPs.</i>	62
<i>Figure A5 Characterization of blank PEGylated core-shell SNPs</i>	63
<i>Figure A6. Switching the particle growth mechanism in a single synthesis</i>	64
<i>Figure A7. Characterization of aluminosilicate C' dots</i>	66
<i>Figure A8. GPC characterization of C' dots right after the synthesis</i>	67
<i>Figure A9. FCS characterizations of c(RGDyC) labeled C' dots</i>	68
<i>Figure A10. Thermogravimetric analysis of C' dots</i>	70
<i>Figure 3.1. TEM images of silica particles with different diameters</i>	81
<i>Figure 3.2. Size distribution of mesoporous particles</i>	84
<i>Figure 3.3. Distribution of number of pores per particle</i>	85
<i>Figure 3.4. Characterization of Cy5.5 labeled mC dots</i>	86
<i>Figure B1. Size analysis of particles using TEM images</i>	96

<i>Figure B2. Diameter distribution of 8.2nm sample measured by TEM.....</i>	<i>97</i>
<i>Figure B3. Optical characterization of mC dots</i>	<i>98</i>
<i>Figure B4. TEM images of 9.3nm particles at different magnification.</i>	<i>98</i>
<i>Figure B5. Liquid 1H NMR spectra.....</i>	<i>99</i>
<i>Figure B6. N2 sorption isotherms of 9.3nm single-pore particles</i>	<i>100</i>
<i>Figure B7. Pore size distribution, surface area and pore volume of 9.3nm single-pore particles.....</i>	<i>101</i>
<i>Figure 4.1. Schematics for the synthesis system.</i>	<i>105</i>
<i>Figure 4.2. Relationship between particle size and stability.....</i>	<i>117</i>
<i>Figure 4.3. Particle growth terminated by PEG addition</i>	<i>121</i>
<i>Figure 4.4. Control of particle size of mesoporous silica nanoparticles.....</i>	<i>123</i>
<i>Figure 4.5. TEM images of mesoporous silica particles with different average diameters</i>	<i>124</i>
<i>Figure 4.6. Map of synthesis parameters.....</i>	<i>129</i>
<i>Figure 4.7. TEM images of silica particles with different average diameters</i>	<i>132</i>
<i>Figure 4.8. Analysis of particle size and morphology distributions</i>	<i>134</i>
<i>Figure 4.9. Morphology evolution dependent on particle size</i>	<i>136</i>
<i>Figure 4.10. Solid state NMR spectra of 9.3nm mesoporous silica particles.....</i>	<i>140</i>
<i>Figure 4.11. Long-term stability of PEGylated single-pore silica nanoparticle.....</i>	<i>142</i>
<i>Figure 4.12. Characterization of mC dots with different colors.....</i>	<i>143</i>
<i>Figure 5.1. Illustration of SNP PEGylation mechanism as characterized by FCS and FCCS.....</i>	<i>167</i>
<i>Figure 5.2. Long-term stability test and SNP stability transition.....</i>	<i>169</i>

<i>Figure 5.3. PEGylation process as monitored by FCS and conductivity measurements</i>	171
<i>Figure 5.4. Association of PEGs and SNPs as characterized by FCS and FCCS</i>	174
<i>Figure 5.5. Association of ligands and SNPs under different conditions</i>	177
<i>Figure C1. Characterization of SNPs with varying surface PEG density</i>	191
<i>Figure C2. Optimization of zeta-potential measurements</i>	192
<i>Figure C3. Linear plot of results of long-term SNP stability tests</i>	193
<i>Figure C4. FCS and FCCS experimental setups</i>	194
<i>Figure C5. Particle size changes before and after PEG additions</i>	195
<i>Figure C6. PEGylation reactions as monitored by FCS</i>	197
<i>Figure C7. Comparison of kinetics of SNP formation and PEGylation steps</i>	197
<i>Figure C8. Labeling PEGs with ATTO488 fluorophores</i>	198
<i>Figure C9. Unattached PEG-silane recognized by DLS</i>	203
<i>Figure C10. Release of adsorbed PEGs from SNPs</i>	205
<i>Figure 6.1. Four MSN structures observed as a function of [TMB] and their structural characterization</i>	218
<i>Figure 6.2. Analysis of MSNs with dodecagonal tiling</i>	220
<i>Figure 6.3. Analysis of MSN structures exhibiting transitions from cubic to dodecagonal symmetry</i>	223
<i>Figure 6.4. Analysis of single particle growth trajectories</i>	225
<i>Figure D1. Single-tilt TEM images of a multicompart ment MSN with two branches</i>	233
<i>Figure D2. Single-tilt TEM images of another multicompart ment MSN with one branch</i>	234

<i>Figure D3. FFT analysis of multicompartment MSN derived from TEOS/AEAPTMS system.....</i>	<i>235</i>
<i>Figure D4. Single-tilt TEM study of a MSN with dodecagonal tiling</i>	<i>236</i>
<i>Figure D5. Pore size analyses for particles synthesized with increasing [TMB]</i>	<i>237</i>
<i>Figure D6. TEMs images of structure evolution of MSNs as a function of stirring rate</i>	<i>238</i>
<i>Figure D7. SAXS and nitrogen sorption measurements of structure evolution of MSNs as a function of stirring rate.....</i>	<i>239</i>
<i>Figure D8. Structural comparison of MSNs synthesized with varying [TMB] using two different silane systems as revealed by TEM.....</i>	<i>240</i>
<i>Figure D9. MSNs with varying particle size and quasicrystallinity.....</i>	<i>240</i>
<i>Figure D10. Analysis of quasicrystallinity of MSNs synthesized with the TEOS/AEAPTMS silane system</i>	<i>241</i>

List of Tables

<i>Table 2.1. Optical characterization C' dots wish different fluorophores.</i>	<i>37</i>
<i>Table 2.2. Optical characterization of aluminosilictae C' dots.</i>	<i>42</i>
<i>Table A1. Synthesis condition of particles with different size</i>	<i>57</i>
<i>Table A2. Synthesis condition of particles with different size</i>	<i>58</i>
<i>Table A3. Characterizations of particles obtained at different reaction stages.</i>	<i>66</i>
<i>Table A4. Characterization of c(RGDyC) functionalized C' dots.</i>	<i>69</i>
<i>Table B1. Synthesis condition of particles with different size</i>	<i>95</i>
<i>Table B2. Comparison of the diameters measured by DLS and TEM</i>	<i>95</i>
<i>Table B3. FCS characterizations of mC dots.</i>	<i>95</i>
<i>Table C1. Estimation of number of PEG chains per SNP and surface PEG density</i>	<i>189</i>
<i>Table C2. Summary of FCCS measurement results</i>	<i>202</i>

Chapter 1 . Introduction

Nanomedicine is the medical application of nanotechnologies and is expected to have a revolutionary impact on health care.¹ One of the most exciting concepts in nanomedicine is multifunctional nanoparticles enabling simultaneous detection and treatment of diseases with high precision.² The access to such nanomaterials would not only introduce unprecedented efficacy and accuracy to traditional theranostics, but also provide new investigational methodologies for biology studies, *e.g.* of brain functionality.² Since the 1980s, many organic-based nanomedicines have been successfully developed and translated into the clinic including polymer-drug conjugates,³ liposomes,⁴ polymeric nanoparticles,⁵ immunotoxins⁶ and so on. Compared to these organic nanomaterials, inorganic nanomaterials further provide advantages in nanoparticle structure control, intrinsic physical properties and *in-vivo* stability, and thus are also promising candidates for nanomedicine.⁷ However, since most inorganic materials are not biodegradable, the medical application of inorganic-based nanomaterials is highly challenging and many essential questions regarding their *in-vivo* functionality and safety are yet to be answered.⁸ Therefore, although many inorganic nanomaterials have been proposed for theranostics applications, *e.g.* gold nanoshells,⁹ carbon nanotubes,¹⁰ graphene,¹¹ quantum dots^{12,13} and magnetic metal nanoparticles,¹⁴ few of them have been successfully translated from the laboratory to the clinic.

There are several challenges which need to be overcome for the safe clinical translation of inorganic-based nanomedicine. First, since the size threshold of nanoparticles

for efficient renal clearance is about 10nm, the inorganic particles should be smaller than 10nm for their safe *in-vivo* usage.¹⁵ In addition, since most of the inorganic nanoparticles have highly charged surfaces usually resulting in protein adsorption in physiological environments,¹⁶ additional surface modification is required to endow the particles with improved biocompatibility and favorable biodistribution profiles.¹⁷ Last but not least, in order to further endow these nanoparticles with therapeutic functionality, it is highly desirable to further tune particle structure, *e.g.* by generating additional inner surfaces for drug delivery.¹⁸ Despite many years of studies, the development of an inorganic nanoparticle synthesis platform which simultaneously enables precise control of particle size, morphology and surface properties still remains a challenge. This lack of comprehensive control at the desired level of accuracy in turn hinders the development of clinically applicable inorganic-based nanomedicines.

The goal of my PhD was to overcome this challenge and develop an inorganic-based nanomaterial platform for cancer theranostics that is clinically applicable.

I focused on silica as the inorganic material because silica is one of the most commonly found inorganic compositions in biology¹⁹ and has high bio-compatibility. Since the early 2000s, our group has been working on silica and has developed a series of silica nanomaterials which show potential in nanomedicine applications.²⁰⁻²³ For example, Cornell dots, or in short C dots, which are fluorescent core-shell silica nanoparticles, have already received FDA approval in 2010 as an investigational new drug (IND) for human clinical trials. The first trial results published in 2014 were encouraging as they demonstrated the safe *in-vivo* use of silica-based nanomaterials.²⁴

The work of my PhD can be sectioned into three main parts. The first part includes Chapters 2 to 4. It describes the synthesis and detailed characterization of a variety of silica-based nanomaterials with novel structures and tunable dimensions in the sub-10nm regime with precise size control close to the single atomic level. The second part described in Chapter 5 introduces fluorescence correlation spectroscopy as an appropriate tool for the investigation of the mechanism of nanoparticle surface modification with biocompatible polyethylene glycol (PEG) and cancer targeting ligands. Based on the success on both the nanoparticle synthesis and the control of particle surface properties, I have successfully developed a synthesis platform, which provides access to a series of silica-based nanomaterials that are clinically applicable. Especially Cornell prime dots (C' dots), fluorescent silica nanoparticles synthesized in water, have already been successfully used in the clinic. Multiple human clinical trials with C' dots on cancer patients are currently ongoing at Memorial Sloan Kettering Cancer Center (MSKCC) in New York City. Furthermore, the study of such ultras-small silica nanomaterials provides insights into fundamental questions regarding early formation mechanisms of self-assembled nanostructures. To that end the third part of the thesis, Chapter 6, focuses on the investigation of the formation process of quasi-crystalline mesoporous silica nanoparticles that highlight the structural details of building blocks and pathways responsible for the switch between crystalline (cubic symmetry) and quasicrystalline states.

1.1 References

- (1) Wagner, V.; Dullaart, A.; Bock, A. K.; Zweck, A. The Emerging Nanomedicine Landscape. *Nat. Biotechnol.* **2006**, *24*, 1211–1217.
- (2) Doane, T. L.; Burda, C. The Unique Role of Nanoparticles in Nanomedicine: Imaging, Drug Delivery and Therapy. *Chem. Soc. Rev.* **2012**, *41*, 2885–2991.
- (3) Duncan, R. Polymer Conjugates as Anticancer Nanomedicines. *Nat. Rev. Cancer* **2006**, *6*, 688–701.
- (4) Torchilin, V. P. Recent Advances with Liposomes as Pharmaceutical Carriers. *Nat. Rev. Drug Discov.* **2005**, *4*, 145–160.
- (5) Couvreur, P.; Vauthier, C. Nanotechnology: Intelligent Design to Treat Complex Disease. *Pharm. Res.* **2006**, *23*, 1417–1450.
- (6) Pastan, I.; Hassan, R.; Fitzgerald, D. J.; Kreitman, R. J. Immunotoxin Therapy of Cancer. *Nat. Rev. Cancer.* **2006**, *6*, 559–65.
- (7) Huang, H. C.; Barua, S.; Sharma, G.; Dey, S. K.; Rege, K. Inorganic Nanoparticles for Cancer Imaging and Therapy. *J. Control Release.* **2011**, *155*, 344–57.
- (8) Peer, D.; Karp, J. M.; Hong, S.; Farokhzad, O. C.; Margalit, R.; Langer, R. Nanocarriers as an Emerging Platform for Cancer Therapy. *Nature Nanotech.* **2007**, *751*, 751–760.
- (9) Lal, S.; Clare, S. E.; Halas, N. J. Nanoshell-Enabled Photothermal Cancer Therapy: Impending Clinical Impact. *Acc. Chem. Res.* **2008**, *41*, 1842–1851.
- (10) Liu, Z.; Tabakman, S.; Welsher, K.; Dai, H. Carbon Nanotubes in Biology and Medicine: In Vitro and In Vivo Detection, Imaging and Drug Delivery. *Nano Res.* **2009**, *1*, 85–120.

- (11) Liu, Z.; Robinson, J. T.; Sun, X.; Dai, H. PEGylated Nanographene Oxide for Delivery of Water-Insoluble Cancer Drugs. *J. Am. Chem. Soc.* **2008**, *130*, 10876–10877.
- (12) Michalet, X.; Pinaud, F. F.; Bentolila, L. A.; Tsay, J. M.; Doose, S.; Li J. J.; Sundaresan, G.; Wu, AM.; Gambhir, S. S.; Weiss, S. Quantum Dots for Live Cells, In Vivo Imaging and Diagnostics. *Science*. **2005**, *307*, 538–44.
- (13) Medintz, I. L.; Uyeda, H. T.; Goldman, E. R.; Mattoussi, H. Quantum Dot Bioconjugates for Imaging, Labelling and Sensing. *Nat. Mater.* **2005**, *4*, 435–446.
- (14) Bárcena, C.; Sra, A. K.; Gao, J. Applications Of Magnetic Nanoparticles in Biomedicine. *J. Phys. D Appl. Phys.* **2003**, *36*, 591–626.
- (15) Choi, H. S.; Liu, W.; Misra, P.; Tanaka, E.; Zimmer, J. P.; Ipe, B. I.; Bawendi, M. G.; Frangioni, J. V. Renal Clearance Of Quantum Dots. *Nat. Biotechnol.* **2007**, *25*, 1165–1170.
- (16) Xia, X.-R.; Monteiro-Riviere, N. A.; Riviere, J. E. An Index for Characterization of Nanomaterials in Biological Systems. *Nature Nanotech.* **2010**, *5*, 671–675.
- (17) Jokerst, J. V.; Lobovkina, T.; Zare, R. N.; Gambhir, S. S. Nanoparticle PEGylation for Imaging and Therapy. *Nanomedicine* **2011**, *6*, 715–728.
- (18) Torney, F.; Trewyn, B. G.; Lin, V. S.-Y.; Wang, K. Mesoporous Silica Nanoparticles Deliver DNA and Chemicals into Plants. *Nat. Nanotech* **2007**, *2*, 295–300.

- (19) Aizenberg, J.; Weaver, J. C.; Thanawala, M.S.; Sundar, V. C.; Morse, D. E.; Fratzl, P. Skeleton Of Euplectella Sp.: Structural Hierarchy from the Nanoscale to the Macroscale. *Science* **2005**, *309*, 275–278.
- (20) Ow, H.; Larson, D. R.; Srivastava, M.; Baird, B. A.; Webb, W. W.; Wiesner, U. Bright and Stable Core–Shell Fluorescent Silica Nanoparticles. *Nano Lett.* **2005**, *5*, 113–117.
- (21) Burns, A. A.; Vider, J.; Ow, H.; Herz, E.; Penate-Medina, O.; Baumgart, M.; Larson, S. M.; Wiesner, U.; Bradbury, M. Fluorescent Silica Nanoparticles with Efficient Urinary Excretion for Nanomedicine. *Nano Lett.* **2009**, *9*, 442–448.
- (22) Benezra, M.; Penate-Medina, O.; Zanzonico, P. B.; Schaer, D.; Ow, H.; Burns, A.; Destanchina, E.; Longo, V.; Herz, E.; Iyer, S.; *et al.* Multimodal Silica Nanoparticles Are Effective Cancer-Targeted Probes in a Model of Human Melanoma. *J. Clin. Invest.* **2011**, *121*, 2768–2780.
- (23) Suteewong, T.; Sai, H.; Hovden, R.; Muller, D.; Bradbury, M. S.; Gruner, S. M.; Wiesner, U. Multicompartment Mesoporous Silica Nanoparticles With Branched Shapes: An Epitaxial Growth Mechanism. *Science* **2013**, *340*, 337–341.
- (24) Phillips, E.; Penate-Medina, O.; Zanzonico, P. B.; Carvajal, R. D.; Mohan, P.; Ye, Y.; Humm, J.; Gonen, M.; Kalaigian, H.; Schoder, H.; *et al.* Clinical Translation of an Ultrasmall Inorganic Optical-PET Imaging Nanoparticle Probe. *Science Transl. Med.* **2014**, *6*, 260ra149.

Chapter 2 . Control of Ultrasmall Sub-10 nm Ligand Functionalized Fluorescent Core-Shell Silica Nanoparticle Growth in Water

Reprinted with permission from Ma, K.; Mendoza, C.; Hanson, M.; Werner-Zwanziger, U.; Zwanziger, J.; Wiesner, U. Control Of Ultrasmall Sub-10 Nm Ligand-Functionalized Fluorescent Core–Shell Silica Nanoparticle Growth in Water. *Chem. Mater.* **2015**, *27*, 4119–4133. Copyright (2015) American Chemical Society.

2.1 Abstract

Ultrasmall fluorescent silica nanoparticles (SNPs) and core-shell SNPs surface functionalized with polyethylene glycol (PEG), specific surface ligands, and overall SNP size in the regime below 10 nm are of rapidly increasing interest for clinical applications due to their favorable bio-distribution and safety profiles. Here we present an aqueous synthesis methodology for the preparation of narrowly size-dispersed SNPs and core-shell SNPs with size control below 1 nm, *i.e.* at the level of a single atomic layer. Different types of fluorophores, including near infrared (NIR) emitters, can be covalently encapsulated. Brightness can be enhanced via addition of extra silica shells. This methodology further enables synthesis of <10 nm sized fluorescent core and core-shell SNPs with previously unknown compositions. In particular addition of an aluminum sol gel precursor leads to fluorescent aluminosilicate nanoparticles (ASNPs) and core-shell ASNPs. Encapsulation efficiency and brightness of highly negatively charged NIR fluorophores is enhanced relative to the corresponding SNPs without aluminum. Resulting particles show quantum yields of ~0.8, *i.e.* starting to approach the theoretical brightness limit. All particles can be PEGylated providing steric stability. Finally, heterobifunctional PEGs can be employed to

introduce ligands onto the PEGylated particle surface of fluorescent SNPs, core-shell SNPS, and their aluminum containing analogues, producing ligand functionalized <10 nm NIR fluorescent nanoprobe. In order to distinguish these water based synthesis derived materials from the earlier alcohol-based modified Stöber process derived fluorescent core-shell SNPs referred to as Cornell dots or C dots, the SNPs and ASNPs described here and synthesized in water will be referred to as Cornell prime dots or C' dots and AIC' dots. These organic-inorganic hybrid nanomaterials may find applications in nanomedicine, including cancer diagnostics and therapy (theranostics).

2.2 Introduction

Currently, ultrasmall inorganic nanoparticles are of rapidly increasing interest as nanomedicines for cancer theranostics.^{1,2} Some organic-based nanomedicines^{3,4} are already more competitive than conventional chemotherapy drugs due to multifunctionality and multivalency effects.^{5,6} Inorganic nanoparticles further diversify the building elements of nanomedicines and may provide advantages associated with their intrinsic physical properties and lower manufacturing costs, *vide infra*.^{7,8} Safe translation of nanoparticles from the laboratory to the clinic requires overcoming a number of substantial scientific and regulatory hurdles. The most important criteria are favorable bio-distribution and its time evolution (pharmacokinetics, PK) profiles.⁹ The size threshold for renal clearance is below 10 nm.¹⁰ Until today only a small number of inorganic nanoparticle platforms have been synthesized with sizes below 10nm allowing for efficient renal clearance.^{10,11,12,13} Among those only <10nm sized polyethylene glycol coated (PEGylated) fluorescent core-shell silica nanoparticles (SNPs) referred to as Cornell dots or simply C dots have been approved by the U.S. Food and Drug Administration (FDA) as an investigational new drug (IND) for first in-human clinical trials.¹⁴ Although the first clinical trial results with melanoma patients are encouraging,¹⁵ several synthesis challenges remain for such sub 10 nm sized fluorescent organic-inorganic hybrid SNPs:

First, all previous C dot-type SNP synthesis efforts followed a modified Stöber process^{11,16} in which alcohol was used as solvent.¹⁷ For materials for use in biological or clinical applications, however, water as a reaction medium would be preferred. It would greatly simplify synthesis and cleaning protocols leading to less volatile waste, thereby rendering particle production substantially faster and more cost effective. Furthermore,

although the Stöber process is widely used to produce SNPs with diameters from tens of nm to microns,¹⁸ particle sizes of 10 nm and below are at the limit of size control of this synthesis process due to reaction kinetics limitations in alcohol.^{19,20}

Second, covalently covering silica particle surfaces with PEG can be tricky as the loss of surface charge during PEGylation may result in particle aggregation or at least broadening of the particle size distribution. This effect is more pronounced for ultrasmall particles due to the increase of particle surface energy, and thus limits the particle monodispersity and size control ability.

Third, as a result of the negative surface charge of silica above its isoelectric point at pH 2-3, covalent encapsulation efficiencies for silane-conjugated organic fluorescent dyes with negatively charged groups into SNPs are low as a result of electrostatic repulsion between silica and fluorophore.²¹ This is particularly true for near-infrared (NIR) emitting dyes most desirable for imaging applications in living tissue. NIR dyes have large delocalized π -electron systems and to be soluble in water typically require multiple negatively charged functional groups (*e.g.* sulfates) on their periphery. Low incorporation efficiencies are a problem for these dyes as their typical costs are of order \$200-\$300 per mg and re-use of typically employed silane-dye conjugates after the initial synthesis is problematic.

Finally, to the best of our knowledge, no inorganic elemental compositions other than silica have been reported for < 10 nm sized fluorescent SNPs and core-shell SNPs. In particular, compositions are of interest leading to higher rigidity of the organic dye environments as increases in rigidity have directly been correlated with increases in per dye fluorescence yield as a result of decreases in non-radiative rates.^{22,23} Here silica

compositions derived from aluminum alkoxides as additives are particularly interesting as they are known hardening components in alkoxy silane derived silica and alumina is an approved adjuvant added to high-volume vaccinations injected intramuscularly and subcutaneously.^{24,25}

All these challenges suggest revisiting the original fluorescent core-shell SNP (C dot) synthesis in order to systematically develop a water based approach to <10 nm organic-inorganic hybrid dots with improved size control, previously unknown compositions, and enhanced performance characteristics. Here we present the results of synthesis studies of ultrasmall SNPs using water as the reaction medium. Combining fast hydrolysis, slow condensation and efficient PEG-silane induced termination of particle growth, we demonstrate precise size control of ultrasmall, <10nm diameter, SNPs in steps below 1 nm, with narrow particle size distributions. We show that by co-condensing different silane-conjugated fluorophores into the silica matrix this synthesis process can be used to produce <10 nm diameter fluorescent SNPs with optical characteristics tuned from the visible into the NIR part of the optical spectrum. We further demonstrate that additional silica shells can be added to the synthesis protocol while keeping the overall particle diameter below 10 nm. As in previous studies this core-shell architecture leads to improved fluorescence brightness as compared to the parent cores.^{16,23} In order to distinguish the materials synthesized in water from the past particles synthesized via a modified Stöber process in alcohol, we will refer to the different water based fluorescent SNPs described here as Cornell prime dots, or simply C' dots. The water based synthesis approach is quite versatile. Here we show that it enables previously unknown inorganic compositions of the particles, without loss of particle size control. To that end as an example we move from silica to

mixed compositions derived from the addition of aluminum alkoxides as sol-gel precursors. The resulting growth conditions of these mixed inorganic NPs allow for more efficient incorporation of highly negatively charged NIR emitting fluorophores as compared to the plain silica based particles. At the same time the resulting NPs show enhanced quantum efficiency of encapsulated dye as compared to particles synthesized without the aluminum alkoxide addition. These aluminum containing fluorescent SNPs will be referred to as AIC' dots. Fluorescent SNPs, core-shell SNPs, and their aluminum containing analogues are PEGylated to provide steric stability. Finally, heterobifunctional PEGs are employed to introduce ligands onto the PEGylated particle surface of fluorescent SNPs and core-shell SNPs, as well as their aluminum containing analogues, producing ligand functionalized <10 nm NIR fluorescent nanoprobe for preclinical and clinical use in diagnostic and therapeutic applications. This is demonstrated with $\alpha_v\beta_3$ integrin-targeting cyclo(arginine-glycine-aspartic acid-D-tyrosine-cysteine), c(RGDyC) peptides used in earlier studies to target melanoma tumor in animal models and a first human clinical trial.^{14,15} Besides the ability to synthesize size controlled and highly fluorescent silica-based nanoprobe for biotechnological and clinical applications, comparison of water-based particle growth pathways with those of the conventional Stöber process may contribute to a better fundamental understanding of the exact formation mechanisms of SNPs and other silica-based nanomaterials.²⁶

2.3 Experimental section

2.3.1 Materials.

All chemicals are used as received. Dimethyl sulfoxide (DMSO), isopropanol, (3-mercaptopropyl) trimethoxysilane (MPTMS), (3-Aminopropyl)triethoxysilane (APTES), tetramethyl orthosilicate (TMOS), tetraethyl orthosilicate (TEOS), polyethylene glycol chains (PEG, molar mass around 400), aluminum-tri-sec-butoxide, 2.0 M ammonia in ethanol and 27wt% ammonium hydroxide are purchased from Sigma Aldrich. Methoxy-terminated poly(ethylene glycol) chains (PEG-silane, molar mass around 500 g/mole) are purchased from Gelest. Heterobifunctional PEGs with maleimide and NHS ester groups (mal-PEG-NHS, molar mass around 870g/mole) are purchased from Quanta BioDesign. Acetic acid is purchased from Mallinckrod. Cy5 and Cy5.5 florescent dyes are purchased from GE. Rhodamine green (RhG) and tetramethylrhodamine (TMR) fluorescent dyes are purchased from Life Technologies. DY782 florescent dye is purchased from Dyomics and CW800 florescent dye is purchased from Li-cor. Absolute anhydrous 99.5% ethanol is purchased from Pharmco-Aaper. cyclo (Arg-Gly-Asp-D-Tyr-Cys) peptide, c(RGDyC), is purchased from Peptide International. De-ionized water (DI water) is generated using a Millipore Milli-Q system.

2.3.2 Synthesis of sub-10nm PEGylated silica nanoparticles.

For the synthesis of 4.2nm PEGylated silica nanoparticles (SNPs), 1ml of 0.02M ammonia aqueous solution, which is prepared by mixing 100 μ l of 2.0M ammonia in ethanol and 10ml Di water, is added into 9ml of DI water. The solution is stirred at room

temperature for 10 mins. and 0.43mmol of TMOS is then added under vigorous stirring and the solution is stirred at room temperature overnight. Following that, 0.21mmol of PEG-silane is added and the solution is stirred at room temperature overnight. In the next step, the temperature is increased to 80⁰C and stirring is stopped. The solution is then left static at 80⁰C overnight. Afterwards, the solution is cooled to room temperature and then transferred into a dialysis membrane tube (Pierce, Molecular Weight Cut off 10.000). The solution in the dialysis tube is dialyzed in 2000ml DI-water and the water is changed once per day for six days to wash away any remaining reagents. The particles are then filtered through a 200nm syringe filter (fisher brand) to remove any aggregates or dust present in the particle solution. The resulting particle solution is then subjected to long term storage at room temperature and characterization including TEM, DLS, TGA and NMR (*vide infra*). The molar ratios of the reaction are 1 TMOS: 0.093 ammonia: 0.49 PEG-silane: 1292 H₂O. Particle size was varied by tuning synthesis conditions. Details are summarized in Table A1.

It is necessary to note here that the same particles with the same size dispersity and structure control can also be synthesized using a 27wt% ammonium hydroxide solution instead of the 2.0M ammonia in ethanol as the ammonium hydroxide source as long as the solution pH is tuned to around 8. This indicates that the key to this C' dot particle synthesis is the correct pH plus water environment for optimized silica reaction kinetics. Small contamination of ethanol (around 10 μ l ethanol in a 10ml reaction) does not have any detectable effect on the particle synthesis as it does not greatly disturb the reaction kinetics.

2.3.3 Synthesis of sub-10nm PEGylated fluorescent silica nanoparticles.

Cy5, Cy5.5, RhG, TMR, DY782 and CW800 dyes with maleimido functionality are first conjugated to MPTMS in DMSO with a molar ratio fluorophore: MPTMS = 1: 25. The silane-conjugated fluorophore is then added together with TMOS into the synthesis solution to co-condense into the particles. The molar ratio of silane-conjugated fluorophore to TMOS is around 1: 1000. The remainder of the synthesis protocol is the same as described for the synthesis of the 4.2nm particles under section 2.3.2. (vide supra).

In order to obtain the most precise fluorescence characterization of the fluorescent particles, any fluorophore labeled particles prepared in this study are further purified by GPC after the filtration step to further remove any remaining free dye molecules, which could disturb FCS and emission spectra measurements, and to maximize the fluorescent particle product purity. In detail, the cleaned particle solution is concentrated by about 30 times using spin-filters (GE healthcare Vivaspin with MWCO 30k) and then purified by GPC column (see section 2.3.8 for details). Since the solvent used in the GPC setup is a 0.9wt% NaCl solution, the purified particles are finally transferred back to DI water using spin-filters for further characterizations and long-term storage. In order to transfer the particles back to DI water, the purified particles are first concentrated by 30 times using spin-filters (GE healthcare Vivaspin with MWCO 30k). DI water is then added into the concentrated particle solution to dilute it back to the normal volume. This process is repeated for at least 8 times to decrease the concentration of NaCl to close to zero. The purified particle sample is then subjected to long-term storage at 4⁰C and for further characterizations.

2.3.4 Synthesis of sub-10nm PEGylated core-shell silica nanoparticles and sub-10nm PEGylated fluorescent core-shell silica nanoparticles.

The synthesis protocol for PEGylated core-shell SNPs is the same as that for the synthesis of the 4.2 nm particles except a shell addition step is added after the formation of the particles and before the addition of PEG-silane. One day after the addition of TMOS (and silane-conjugated fluorophore for the synthesis of PEGylated fluorescent core-shell SNPs) the reaction is cooled down to room temperature if a temperature above room temperature was applied for core particle formation (see Table A1). The solution is then diluted 5 times with DI water. After that, a mixture of TEOS and DMSO (volume ratio 1:4) is dosed into the solution under vigorous stirring at room temperature. The volume of each dose is 10 μ l and the time gap between doses is 30 mins. 50 doses are added for the addition of one layer of silica shell resulting in a shell thickness close to 0.5nm (particle size increase by around 1 nm). This process is repeated until the desired layers of shells (typically 1-4, see main text) are added. During the shell addition, the solution pH decreases as a result of the addition of extra TEOS and the formation of silicic acid. To keep the pH at neutral for optimized reaction kinetics, around 2ml of 0.02M ammonium hydroxide solution is further added into the reaction solution after the deposition of every two layers of silica shell. Afterwards, 1.05mmol of PEG-silane (same PEG-silane concentration as for the PEGylation of core particles) is added and 80⁰C heat treatment is applied following the same procedure as described for the 4.2 nm particle synthesis. Purification steps are applied as described above in section 2.3.3.

2.3.5 Synthesis of sub-10nm PEGylated aluminosilicate nanoparticles and PEGylated aluminosilicate core-silica shell aluminosilicate nanoparticles.

For the synthesis of sub-10 nm PEGylated aluminosilicate nanoparticles (ASNPs), 1ml of 0.5N HCl solution is added into 9 ml of DI water and the solution is stirred for 10 mins. Following that, 0.43 mmol of TMOS and 0.043 mmol of aluminum-tri-sec-butoxide (dissolved in isopropanol with volume ratio 1:9) are added under vigorous stirring at room temperature. 10-15 mins. later, 0.21 mmol PEG-silane is added followed by switching back of solution pH to neutral via adding about 140 μ l of 27 wt% ammonium hydroxide. The final pH is double checked with pH paper. Afterward, the solution is kept at 80⁰C overnight without stirring. The remainder of the synthesis protocol follows the same procedures as described for the synthesis of 4.2 nm particles in section 2.3.2 and 1.3.8.

For the synthesis of core-shell ASNPs, 0.21 mmol PEG (molar mass around 400g/mole) is added instead of PEG-silane before the reaction pH is switched back to neutral. After the reaction pH is switched back to neutral, a mixture of TEOS and DMSO (volume ratio 1:8) is dosed into the solution under vigorous stirring at room temperature. The volume of each dose is 10 μ l and the time gap between doses is 30 mins. 50 doses are added for the addition of one layer of silica shell resulting in a shell thickness close to 0.5nm (particle size increase by around 1nm). This process is repeated until the desired layers of shells (typically 2, see main text) are added. Afterwards, 0.21 mmol PEG-silane is added and the 80⁰C heat treatment is applied without stirring. The remainder of the synthesis protocol follows the same procedures as described for the synthesis of 4.2 nm particles in section 2.3.2. The addition of PEG before switching solution pH back to neutral is not absolutely necessary, but we found that in our study this can improve the

monodispersity of synthesized ASNPs and prevent their aggregation during the process of changing pH.

2.3.6 Synthesis of sub-10 nm PEGylated fluorescent aluminosilicate nanoparticles and sub-10 nm PEGylated fluorescent aluminosilicate core-silica shell aluminosilicate nanoparticles covalently encapsulating Cy5 or Cy5.5 fluorophores.

In order to covalently encapsulate fluorophores into ASNPs, silane-conjugated Cy5 or Cy5.5 fluorophore is added right after the addition of TMOS and aluminum-tri-sec-butoxide using the same conjugation conditions and dye concentration as described in section 2.3.3. The remainder of the synthesis protocol is the same as described for the synthesis of blank ASNPs in section 2.3.5 and purification steps are applied as described above in section 2.3.3.

2.3.7 PEGylated particle surface modification with easily accessible ligands.

In order to functionalize the surface of any of the PEGylated particles in this study with *e.g.* c(RGDyC) peptide ligands, the heterobifunctional NHS-PEG-mal is first conjugated with APTES in DMSO to produce mal-PEG-silane. The concentration of NHS-PEG-mal in DMSO is around 0.22M. The reaction mixture is left at room temperature under nitrogen overnight. As the next step c(RGDyC) is then added into the DMSO solution and the solution is left at room temperature under nitrogen overnight. The molar ratio of c(RGDyC) : NHS-PEG-mal : APTES is 1.1: 1.0: 0.9 to ensure every heterobifunctional PEG condensed on the particle surface has c(RGDyC) attached. Afterwards, the produced

c(RGDyC)-PEG-silane is added followed by the addition of PEG-silane in the PEGylation step during nanoparticle synthesis. Different molar ratios of c(RGDyC)-PEG-silane to PEG-silane can be used to vary the amount of ligands on the particle surface. For example, a molar ratio of c(RGDyC)-PEG-silane : PEG-silane of about 1: 40 gives around 22 c(RGDyC) ligands per 7nm diameter particle, while decreasing the ratio to 1: 400 will result in about 5 c(RGDyC) ligands per 7nm particle. The remainder of the synthesis is the same as that described for the conventional PEGylation in section 2.3.4. The same methodology can be applied to all particles described in this study for producing surface functionalized probes, including blank and fluorescent SNPs, core-shell SNPS, and their aluminum containing analogues, all with different types of covalently encapsulated fluorophores. Other ligands that can be used in this way include, but are not limited to, other linear and cyclic peptides, antibody fragments, various DNA and RNA segments (*e.g.* siRNA), therapeutic molecules including drugs and radioisotopes and their respective chelating moieties, as well as combinations thereof.

2.3.8 Gel permeation chromatography characterization (GPC).

GPC characterization is performed using a BioLogic LP system equipped with a 275nm UV detector and with resin Superdex 200 from GE healthcare. While the blank SNPs can hardly be detected by the 275nm UV detector due to the low absorbance of silica, the fluorescent SNPs show strong signals in the GPC setup because the encapsulated fluorophores have absorbance overlapping with the 275nm detecting channel. As a result, GPC can be used to further increase the purity of cleaned C' dot products for characterizations and further clinical applications. Before usage, the GPC system is

calibrated by protein standards from Bio-Rad, which are a mixture of thyroglobulin, bovine γ -globulin, chicken ovalbumin, equine myoglobin, and vitamin B12 with known molar masses. Afterwards, around 400 μ l of particle solution is injected into the GPC setup and fractions are collected by a BioFrac fraction collector. A detailed analysis of different GPC fractions is displayed in Figure A8. By collecting the particle fractions, the particle product purity can be further maximized.

2.3.9 Characterization of particle morphology.

Transmission electron microscopy (TEM) images are taken using a FEI Tecnai T12 Spirit microscope operated at an acceleration voltage of 120kV. Hydrodynamic particle sizes and size distributions are measured by dynamic light scattering (DLS) using a Malvern Zetasizer Nano-SZ operated at 20⁰C. Each DLS sample is measured three times and results are superimposed in the respective figures in this paper. Number percentage curves are used to present the measurement results. The average diameter of each sample is calculated by averaging the mean diameters of number percentage curves from three measurements.

2.3.10 Characterization of fluorophore encapsulating particles.

Absorbance spectra of samples are measured by a Varian Cary 5000 spectrophotometer. By varying sample concentration, the absorbance spectra of different samples are matched and thus the optical density of different samples are adjusted to be the same. Afterwards, the absorbance-matched samples are subjected to emission scans using a Photon Technologies International Quantamaster spectrofluorometer. The peak intensity

of emission spectra of particles is divided by the peak intensity of the absorption-matched solution of free dye for quantum efficiency enhancement calculations.²³

Fluorescence correlation spectroscopy (FCS) measurements are conducted using a home built FCS setup. A 488nm solid-state laser is used as the laser source for RhG fluorophore. A 543nm HeNe laser is used as the laser source for TMR fluorophore. A 633nm solid-state laser is used as the laser source for Cy5 and Cy5.5 fluorophores. A 785nm solid-state laser is used as the laser source for DY782 and CW800 fluorophores. The hydrodynamic size, brightness per particle and particle concentration are obtained from fits of the FCS auto-correlation curves.²³ Dividing particle concentration obtained from FCS by fluorophore concentration obtained from absorbance measurements, the number of fluorophores per particle is calculated as described elsewhere.²³

2.3.11 ²⁹Si and ²⁷Al solid-state NMR characterization.

The ²⁹Si cross-polarization (CP)/ magic angle spinning (MAS) NMR experiments are carried out on a Bruker Avance NMR spectrometer with a 9.4T magnet using a probe head for rotors of 4 mm diameter. During the ²⁹Si CP/MAS NMR experiments the samples are spun at 7.00 kHz rotation frequency at the magic angle. For the final spectra, up to 3200 scans are accumulated using CP with ramped proton powers during the 5 ms CP contact times and detection with TPPM proton decoupling. The ²⁹Si CP/MAS NMR scans are accumulated with repetition time of 3 s due to the probe duty cycle.

The ²⁷Al NMR experiments are performed on a Bruker Avance NMR spectrometer with a 16.45T magnet (182.47 MHz ²⁷Al Larmor frequency) using a probe head for rotors of 2.5 mm diameter. Potassium alum serves as external ²⁷Al NMR chemical shift secondary

reference (at -0.033 ppm) and for calibration of the 90 degree pulse lengths and rf power. The final ^{27}Al NMR MAS spectra are acquired with a nominally 10 degree direct excitation pulse at 95 kHz rf field strength, adding up to 6144 scans with 100 ms repetition times, while spinning the sample at 15.00 kHz at the magic angle. The ^{27}Al background of the probe head and rotor are characterized by acquiring the spectrum of an empty rotor under identical conditions and subtracting it from the sample spectra.

2.3.12 Thermogravimetric analysis (TGA).

The particle solution is first frozen in liquid nitrogen and then left under vacuum at -20°C over three nights to dry. The powder after freeze-drying is further left under vacuum at 60°C overnight. The dried out particle sample is then subjected to TGA. The TGA is conducted using a TA Instruments Q500 thermogravimetric analyzer. During the measurement, the temperature is increased from room temperature to 100°C with a ramp of $10^{\circ}\text{C}/\text{min}$ and then remains at 100°C for 2h to fully exclude any residual water. Afterward, the temperature is further increased to 600°C with a ramp of $10^{\circ}\text{C}/\text{min}$ removing any organic moieties and leaving pure inorganic silica or aluminosilicate behind. The average amount of PEG chains on a particle is then estimated according to these TGA results.

2.3.13 Molecular model of c(RGDyC) functionalized C' dot.

Based on the full analysis of the C' dot structure, *e.g.* core size, shell thickness, PEG surface density, number of surface ligands, and number of fluorophores encapsulated, a schematic molecular model was generated displaying the architecture of a C' dot at the

atomic level with realistic scale. In order to do this, we first constructed a 4nm SiO₂ sphere which is a continuous random network of Si and O atoms. The coordinates of each Si and O atoms inside the network are generated by reverse Monte Carlo simulation of a silica glass.^{27,28} We used a total of about 800 SiO₂ units present inside the silica particle which agrees well with a calculation using the density of amorphous silica. Following this, a volume inside this silica particle is manually created where one encapsulated Cy5 fluorophore is drawn. Afterwards, around 100 PEG-silane chains and 16 c(RGDyC)-functionalized PEG-silane chains covalently bonded to the silica particle surface are added manually. The final drawing represents one C' dot particle with a ~3 nm core, ~0.5 nm shell, one encapsulated Cy5 fluorophore, around 100 PEG chains, and 16 c(RGDyC) ligands on the surface. It is important to note that the model is not the result of a true simulation, but is rather a scaled schematic drawing which provides a realistic visualization of the relative size scale of the different building blocks of one C' dot particle.

2.4 Results and discussion

2.4.1 Controlled blank silica nanoparticle growth.

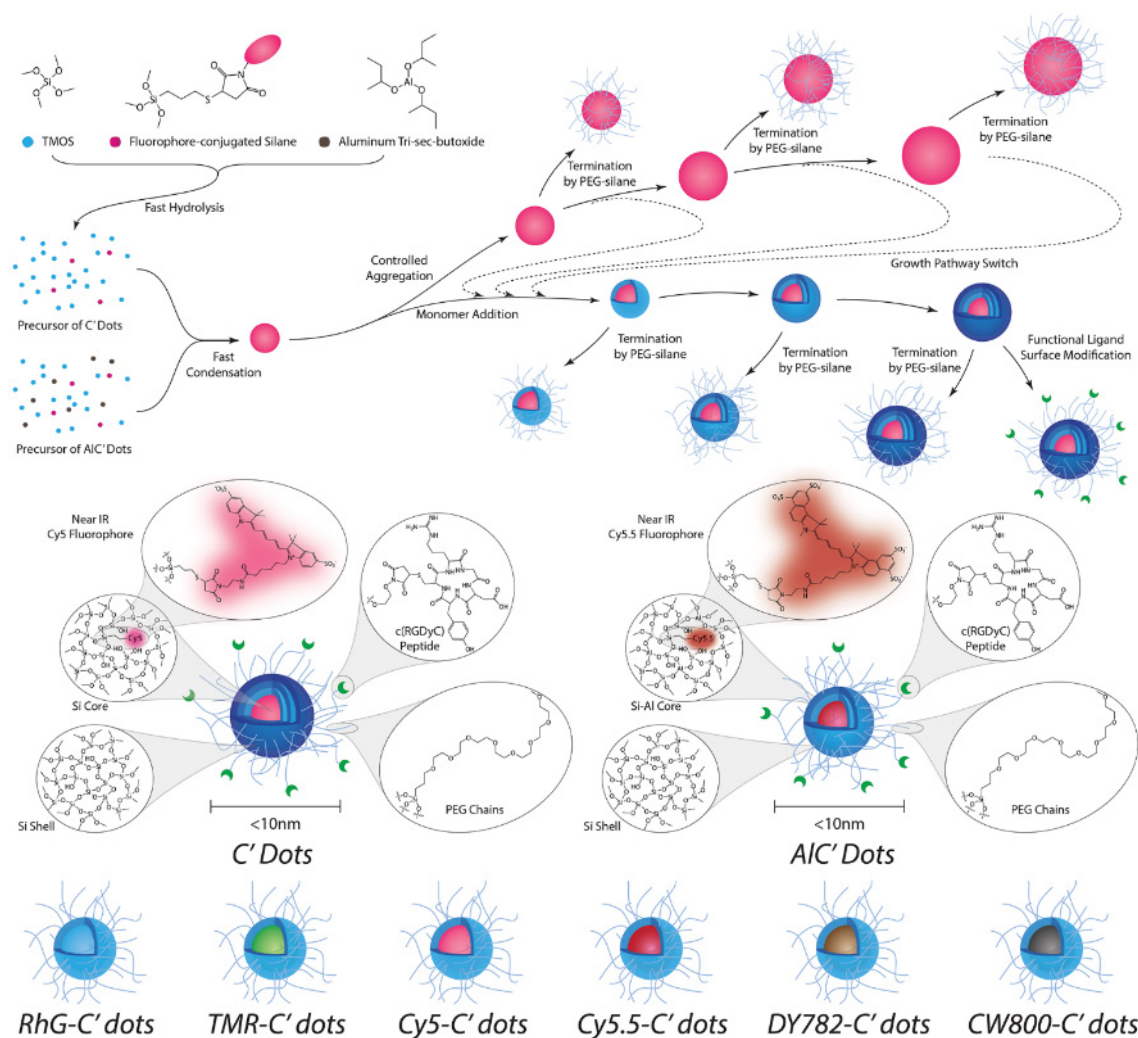


Figure 2.1. Illustration of synthesis system. Illustration of water based fluorescent SNP growth pathways together with the chemical structures of produced particles used in this study (see text for details).

Figure 2.1 presents the aqueous particle synthesis pathways pursued in this study together with the chemical and physical structures of the products. As detailed in the experimental section, <10 nm diameter SNPs are synthesized in pure water, typically at

room temperature, with tetramethyl orthosilicate (TMOS) as silica source and ammonium hydroxide as base catalyst. Upon the formation of particles, PEG-silane with molar mass around 500 g/mole is added into the reaction vessel to terminate particle growth. A subsequent heat treatment at elevated temperature (80°C) is then applied to enhance the condensation degree of PEG-silane on the particle surface.²⁹ The synthesized particles are cleaned through dialysis to remove reaction reagents and then filtered by a 200 nm syringe filter to remove any aggregates or dust before further characterizations. The particle growth period is defined by the time window between the addition of TMOS and the addition of PEG-silane. As particle PEGylation is an integral part of the synthesis, the particles are already surface modified with PEG chains once synthesized and are stable, *e.g.* in high salt containing buffer solutions.^{14,15} Particle size is controlled by varying reaction parameters including concentration of TMOS, concentration of ammonium hydroxide, length of particle growth period, and reaction temperature.

Figure 2.2a-i display transmission electron microscopy (TEM) images at two different magnifications of particles grown under different conditions, revealing the size and size distribution control. For example, Figure 2.2d shows 4.2nm diameter SNPs synthesized using the following parameters: room temperature, 0.043M TMOS, 0.002M ammonium hydroxide, and 24 hours growth period. The diameter of 4.2nm is determined by dynamic light scattering (DLS), while the particle diameter as obtained from TEM image analysis is only around 2-3nm. The particle size measured by DLS is slightly larger than that by TEM because DLS measures hydrodynamic size which includes PEG chains and hydration layers, while TEM only provides information about the diameter of the projected silica core. Shortening the particle growth period from 24 hours to 10 mins, the

synthesized particle diameter decreases from 4.2 nm to 3.7 nm (Fig. 2.2c). Further decrease of the growth period does not result in the decrease of particle size, but to a loss of control of overall size distribution (data not shown). This suggests that the particles go through a rapid growth period during the first 10 minutes due to high precursor concentration, followed by a slow growth mode due to controlled aggregation (see Figs. A1 and A2) of existing silica clusters. To further decrease particle size, the growth period of particles is left at 20 hours, but the concentration of silica source, TMOS, is decreased from 0.046M to 0.011M. As a result, the synthesized particle diameter decreases from 4.2 nm to 2.4 nm (Fig. 2.2a and b). This is because the decrease of TMOS concentration leads to a lower hydrolyzed silica precursor concentration, which in turn leads to slower particle growth. Applying the 4.2 nm particle synthesis parameters, except increasing the concentration of ammonium hydroxide from 0.002M to 0.06M (thereby changing pH from ~8 to about ~10), the average particle diameter increases from 4.2 nm to 5.2 nm (Fig. 2.2e and f). An increase in pH generally causes an increase of hydrolysis rate and decrease of condensation rate. Since the hydrolysis of TMOS in water is always fast,³⁰ most likely the decrease of condensation rate is the dominant effect, leading to the lower particle concentration and bigger particle size. In order to further increase particle size, the reaction temperature of the particle growth period is varied. Applying the 4.2 nm particle synthesis parameters, but increasing reaction temperature from room temperature to 80°C, the average particle diameter further increases from 4.2 nm to 7.3 nm (Fig. 2.2g to i). This could be the result of two effects (see also Fig. A1). First, due to a high surface energy of small particles, at higher temperature silicic acid rapidly condenses into bigger silica clusters with lower concentrations until the silicic acid as precursor is exhausted. Afterwards, since smaller

particles are less stable at higher temperature, particles further slowly aggregate into bigger ones and particle size further increases.

A comparison of size and size distributions as measured by DLS of the nine particle batches with different average diameters is displayed in Fig. 2.2j. The data demonstrates precise particle size control with steps below 1 nm. Considering that a single SiO₂ atomic layer is roughly around 0.4 nm thick, this is equivalent to controlling the particle growth at the level of the deposition of single atomic layers around the particles.^{31,32} Since this control is achieved by varying a combination of four reaction parameters, the synthesis system is endowed with a high degree of chemical versatility. This implies that narrowly size-dispersed ultrasmall SNPs can be synthesized under very different conditions, which should be compatible with other particle modification chemistries (*vide infra*).

Compared to the conventional Stöber method, the main difference of this process is that the reaction solvent is switched from alcohol to water, leading to the better-defined reaction kinetics for ultrasmall SNP growth. In water the hydrolysis rate of tetraalkoxysilanes, and particularly of TMOS, is greatly increased relative to alcohol, and thus even at close-to-neutral pH hydrolysis is still fast enough to generate a homogeneous silicic acid precursor solution.³³ Following the fast hydrolysis, water and near neutral pH further lead to fast condensation generating homogeneously sized SNP seeds at high concentrations. Keeping everything else constant, increasing/decreasing the concentration of TMOS leads to bigger/smaller particles through more/less monomer addition to the seeds. Since after seed formation no further monomer is provided by hydrolysis, the concentration of remaining silicic acid in solution is low and no significant amounts of silicic acid monomers can condense onto the existing seed particles, resulting in the

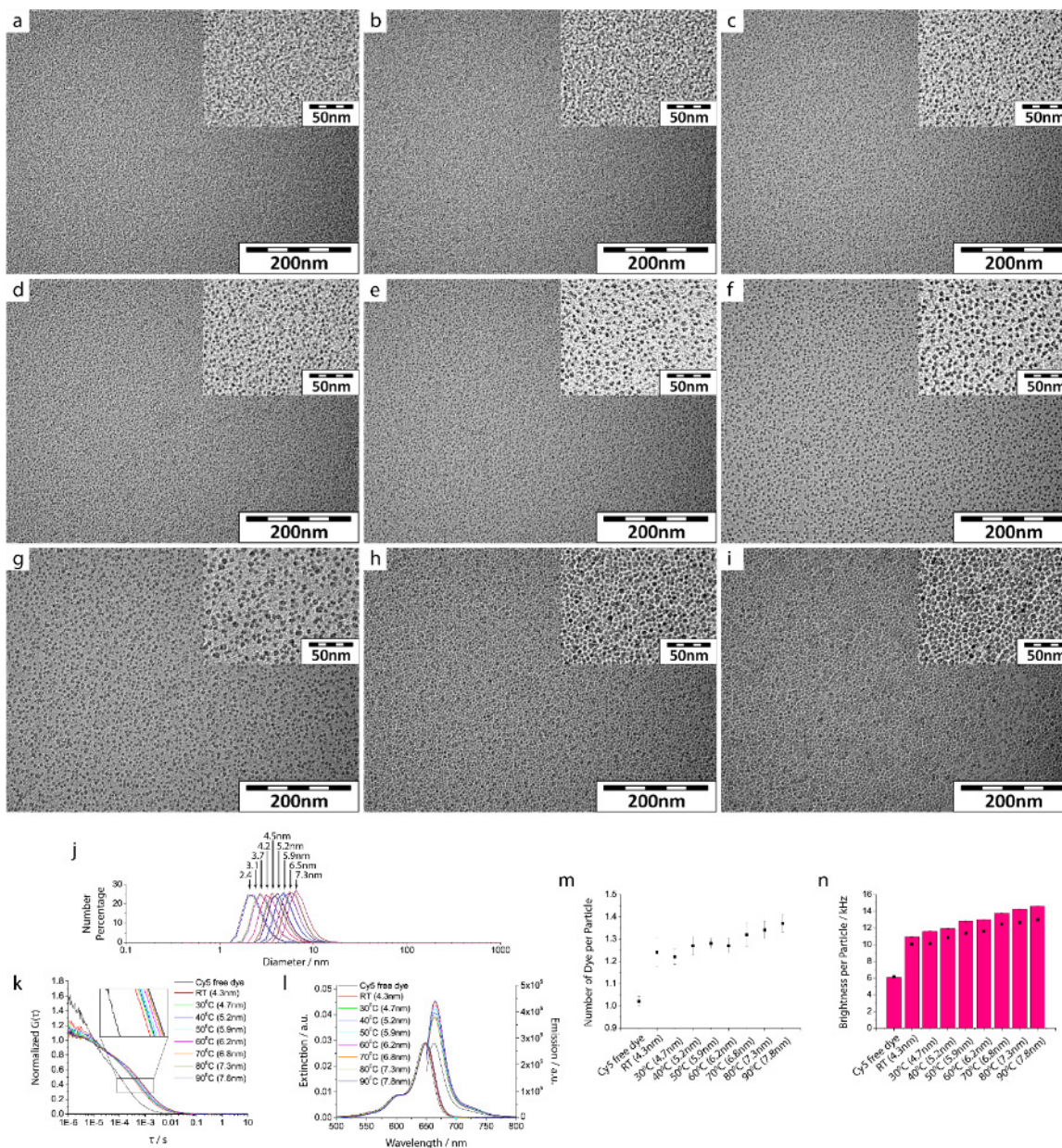


Figure 2.2. Characterizations of blank and fluorescent SNPs. (a-j) Characterization of blank SNPs (*i.e.* without fluorophore encapsulation). (a-i) TEM images at two different magnifications (insets) of blank SNPs with the following average diameters as measured by DLS in aqueous solution: (a) 2.4 nm, (b) 3.1 nm, (c) 3.7 nm, (d) 4.2 nm, (e) 4.5 nm, (f) 5.2 nm, (g) 5.9 nm, (h) 6.5 nm and (i) 7.3 nm. (j) Size distributions of blank SNPs with varying average diameters as measured by DLS in aqueous solution. (k-n) Characterization of Cy5-encapsulated fluorescent SNPs (C' dots) with different average diameters: 4.3 nm, 4.7 nm, 5.2 nm, 5.9 nm, 6.2 nm, 6.8 nm, 7.3 nm and 7.8 nm. The average diameters are measured by FCS. (k) FCS autocorrelation curves; (l) absorbance (matched) and emission spectra; (m) FCS derived number of fluorophores per particle; (n) FCS measured (columns) and calculated (dots) fluorescence brightness per particle of fluorescent SNPs with varying average diameters as compared to free dye in aqueous solution (see text).

production of small particles. As temperature increases, small particles can further aggregate into bigger ones due to decreased surface energy for bigger particles. Finally, terminating particle growth by PEG-silane addition adds another synthesis parameter by which particle size can be precisely controlled and final particle stability is greatly enhanced.

2.4.2 Controlled fluorescent silica nanoparticle growth.

In further experiments fluorescent dyes are covalently encapsulated for the production of fluorescent PEGylated SNPs. To this end, applying the 4.2 nm particle synthesis conditions, additional silane-conjugated Cy5 fluorophore is added into the reaction to co-condense with TMOS into the silica matrix.³⁴ Considering that the Cy5 fluorophore can be quenched by solutions at high base concentration, size control of the Cy5 doped particles is achieved by simply varying temperature, rather than ammonium hydroxide concentration. Synthesized particles are finally purified through gel permeation chromatography (GPC) after the regular cleaning steps to maximize particle purity and fully remove any residual free fluorophores which could otherwise falsify optical particle characterization results (see details in experimental section). The size of fluorescent particles from eight batches for which the reaction temperature was raised from room temperature to 90°C (see experimental section) is characterized by fluorescence correlation spectroscopy (FCS) (Fig. 2.2k). Compared to DLS, FCS shares a similar measurement mechanism, which extracts particle diffusion information from the autocorrelation of signal intensity fluctuations.³⁵ However, instead of scattered light FCS uses fluorescence and thus

is more sensitive to small particles or molecules whose scattering is weak. In Fig. 2.2k the shifts to the right of FCS autocorrelation curves, in particular moving from free dye to dye-encapsulating SNPs, indicate the slower diffusion times of the bigger particles. The average particle diameters are obtained via curve fitting (see Fig. A3 for an example) and vary from 4.3 nm to 7.8 nm in steps below 1 nm, covering a similar size range and exhibiting single atomic layer size control as compared to the blank SNPs measured by DLS in Fig. 2.2j. Images of the fluorescent particles as obtained by TEM are shown in Fig. A4. Absorbance and emission spectra in water of these differently sized dots as compared to the free dye are shown in Fig. 2.2l. Absorbance matching all solutions reveals that silica encapsulated Cy5 dye is brighter than free dye, and that encapsulated Cy5 dye brightness increases with particle size. In previous studies this brightness enhancement has been correlated to an increase in quantum yield due to a change in dielectric constant moving from water to silica, as well as the increased rigidity of the dye in the silica environment.²³ As overall particle size increases, Cy5 fluorophores have a higher probability of being well encapsulated by the silica matrix leading to the observed higher quantum enhancement. The number of fluorophores per particle as well as the brightness per particle can be obtained from FCS derived solution concentration in conjunction with absorbance data.²³ The results are displayed in Fig. 2.2m and n, respectively. As suggested by Fig. 2.2n, each synthesized particle of the different synthesis batches contains around one to two fluorophores, and the number of fluorophores per particle slightly increases as particle size increases. Considering that one Cy5 fluorophore is around 1.2 nm in hydrodynamic diameter and has one negative charge (see molecular structure in Fig.1) repelling it from the negatively charged silica, an average of 1-2 fluorophores per particle is a reasonable

number. As shown in Fig. 2.2m, the brightness per particle as measured by FCS directly (from # of photons hitting the avalanche detector per dye/particle) is at least two times higher than the brightness per single Cy5 fluorophore in water, and increases as particle size increases. The brightness per particle can also be estimated from the product of the brightness per fluorophore and the number of fluorophores per particle (see black dots in Fig. 2.2m). While the overall trends in behavior are the same, it is interesting to note that the brightness per particle as measured directly by FCS consistently overestimates this calculated brightness value for all samples. This is in difference to previous studies of particles synthesized via the Stöber method, in which FCS results underestimated the brightness.²³ At this point we can only speculate that this difference in behavior might be due to improved particle cleaning procedures from free dye via GPC columns used in this study or due to different types of encapsulated fluorophores. Overall the deviations in Fig.2n are small, however, and trends for brightness per particles from FCS and calculations are consistent.

2.4.3 Controlled fluorescent core-shell silica nanoparticle growth.

Additional silica shells are added to particles before PEGylation by further dosing extra silica source into the reaction (Fig. 2.1). Compared to the particle size control via varying temperature, in which particle growth follows the controlled aggregation pathway, particle growth by silica shell additions follows the monomer addition pathway. The key here is that the concentration of hydrolyzed precursor, silicic acid, always stays below the critical concentration for secondary particle nucleation. This can be achieved by optimizing the amount of silica source dosed at any given time and the time gap between doses.

However, simply dosing TMOS always results in even smaller average sizes of the final particles independent of dose and gap width employed (data not shown). This suggests that the additional silica source forms secondary particles rather than condensing onto the surface of existing ones. This is because both hydrolysis and condensation of TMOS in water are fast; upon the addition of a single dose, as mixing via simple stirring may not be fast enough, secondary particle formation is difficult to suppress. In order to circumvent secondary particle nucleation, the silica source used in the shell additions is switched from TMOS to TEOS, because of its slower hydrolysis rate. By optimizing pH and dilution, the hydrolysis of TEOS can be tuned to be just a little bit slower than the time needed for a single dose to thoroughly mix with the entire solution. In this way, once TEOS of each dose spreads out, it hydrolyzes and condenses onto the existing particles fairly fast. As a result, additional silica shells can be efficiently added without secondary particle nucleation, resulting in an increase of average particle size. This is first successfully demonstrated using the pure SNPs (without dye addition), starting from a core size of around 4 nm, and adding three successive shells leading to particle sizes of 5.6 nm (one shell), 6.5 nm (two shells), and 7.8 nm (three shells), see Fig. A5 for TEM and DLS data.

Subsequently, experiments are performed with Cy5 dye containing cores (Fig. 2.3). By adding 1 to 4 silica shells of about 1 nm thickness each to a 5 nm sized Cy5 doped particle core (seed), as revealed by FCS (Fig. 2.3g), Cy5 labeled fluorescent core-shell SNPs are synthesized. The TEM images of these particles, together with the parent core particle, are shown in Fig. 2.3a–e, revealing exquisite size control again at the single atomic layer level. A network pattern of particles can sometime be found in the TEM images, which is the result of capillary forces acting on the particles during water evaporation in

TEM sample preparation.¹⁶ Absorbance matched spectra as well as the corresponding emission spectra of these particles are compared to free dye in Fig. 2.3f. Results suggest a quantum enhancement over free Cy5 dye which increases from ~ 1.3 for the core particle to ~ 1.7 as the number of silica shells increases from 0 to 4. Similar to the case of increasing particle size without extra shells, this brightness increase most likely results from tighter silica encapsulation of Cy5 fluorophore with increasing shell number and a concomitant increase in rigidity through the local silica environment. As the number of shells increases, the FCS derived number of fluorophores per particle does not exhibit any obvious trend (Fig. 2.3h), which is very different compared to the behavior of particles grown to different sizes in Fig. 2.2m. This further corroborates that in the shell addition experiments particles grow through monomer addition rather than controlled aggregation. Although the number of fluorophores per particle remains the same, the enhancement of per dye brightness contributes to an increase of particle brightness as observed by FCS, see Fig. 2.3i.

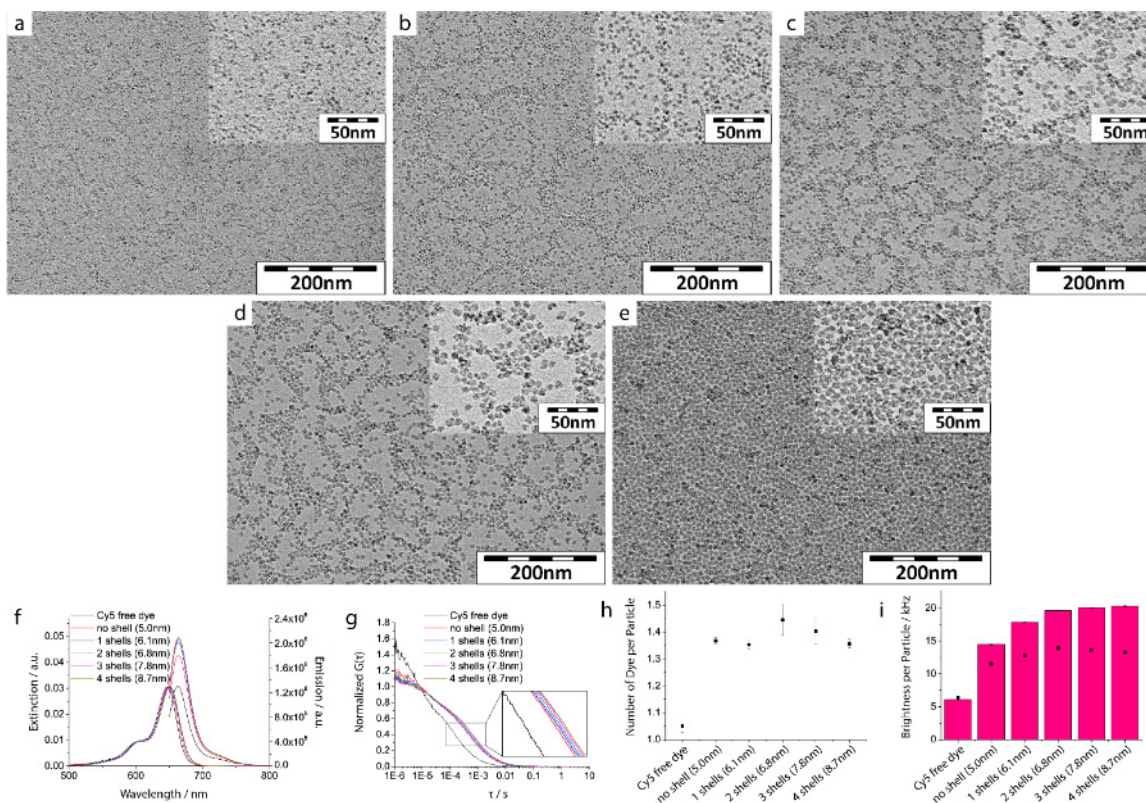


Figure 2.3. Characterizations of core-shell fluorescent SNPs. (a-e) TEM images at two different magnifications (insets) of Cy5-encapsulated fluorescent core-shell SNPs (C' dots) with 0 (core/seed) to 4 shells, and the following average diameters as measured by FCS: 5.0 nm (core/seed), 6.1 nm, 6.8 nm 7.8 nm and 8.7 nm. (f) Absorbance (matched) and emission spectra; (g) FCS autocorrelation curves; (h) FCS derived number of fluorophores per particle; (i) FCS measured (columns) and calculated (black dots) fluorescence brightness per particle of C' dots with 0 (core/seed) to 4 shells as compared to free dye in aqueous solution (see text).

With the water-based synthesis process described here, the size of SNP cores can be tuned via controlled aggregation while extra silica shells can be added via monomer addition (Figure 2.1). In order to show the principle that these two particle growth pathways can be switched in a single synthesis of fluorescent core-shell SNPs, a batch of particles is grown first through controlled aggregation by varying reaction temperature, then through monomer addition by further dosing extra silica source. Small amounts of particles are aliquoted for PEGylation at different synthesis moments and then characterized. Results show a consistent increase of particle size as well as of encapsulated dye quantum enhancement during the synthesis (for details see Supplementary information, Figure A6). Results demonstrate that the architecture of <10 nm fluorescent core-shell SNPs, via core diameter and shell thickness, can be tuned at the sub nanometer single atomic layer level by the particle growth conditions described here.

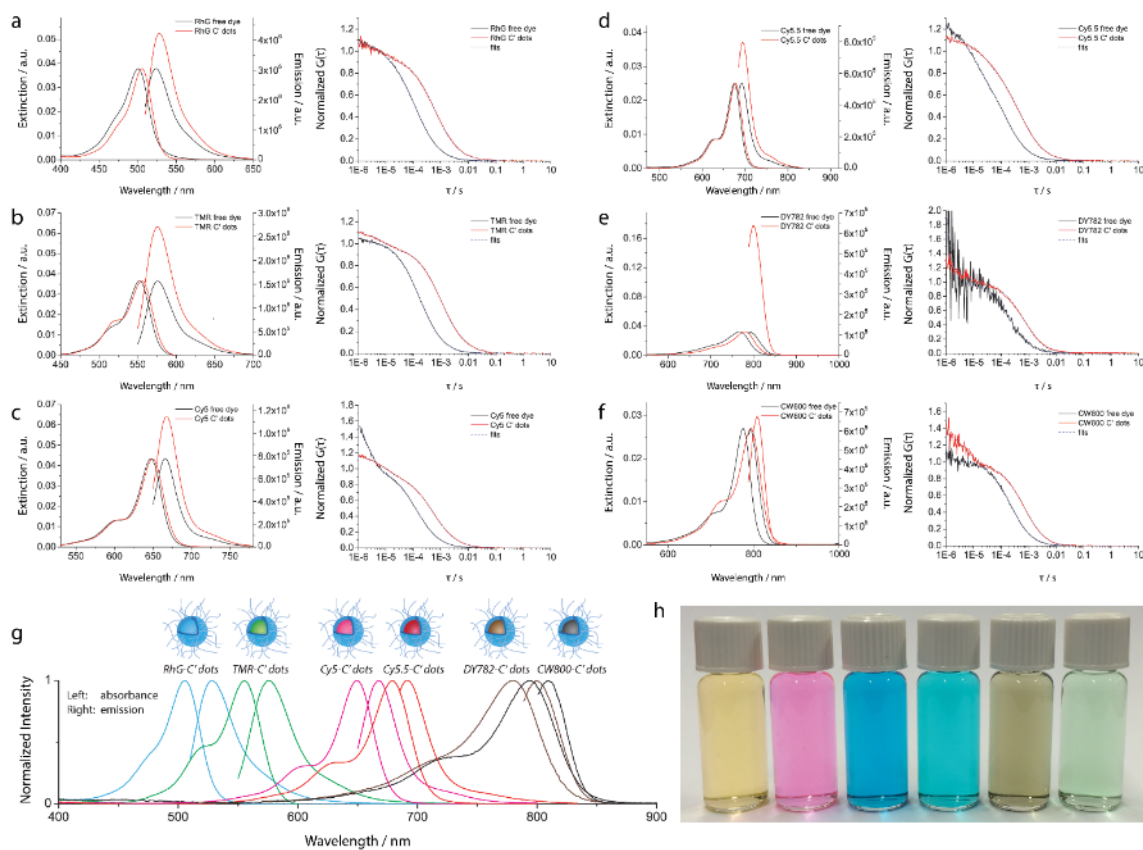


Figure 2.4. Optical characterizations of C' dots encapsulating different fluorophores. (a-f) Absorbance (matched) and emission spectra (left) as well as FCS characterization (right) of C' dots derived from different types of fluorophores. (a) RhG, (b) TMR, (c) Cy5, (d) Cy5.5, (e) DY782 and (f) CW800. (g) Normalized absorbance and emission spectra of C' dots with different dyes/colors. (h) A photo showing the solution appearance of C' dots derived from different color dyes. From left to right: RhG, TMR, Cy5, Cy5.5, DY782 and CW800.

In order to distinguish these new libraries of fluorescent SNPs synthesized in water with precise control over particle size and architecture from the original Cornell dots (C dots) synthesized via a modified Stöber process in alcohol, they will be referred to as Cornell prime dots or simply C' dots.

In addition to Cy5 dye other types of fluorophores, including rhodamine green (RhG), tetramethylrhodamine (TMR), Cy5.5, Dyomics 782 (DY782) and IRDye 800CW (CW800), are encapsulated to produce core-shell C' dots of varying colors. Respective

steady-state spectra and FCS characterization results are displayed in Fig. 2.4a-f summarized in Table 2.1. These C' dots are synthesized following the 4.2 nm sized core protocol plus the addition of a 1 nm thick silica shell. As shown in Table 2.1, final particle sizes vary between 5.2 nm (DY782) and 6.7 nm (Cy5.5), each particle type containing around 1-2 fluorophores. Figure 2.4g and h compare the absorbance/emission spectra and the solution appearance of the different C' dots, respectively. It is interesting to note that the particle synthesis is compatible with different types of fluorophores with fluorescence wavelength all the way from the blue part of the optical spectrum to the NIR. Especially in the 650-800 nm regime, different color NIR C' dots can be synthesized enabling multi-color NIR imaging and NIR multiplexing.

Table 2.1. Optical characterization C' dots with different fluorophores. Comparison of C' dots from different types of fluorophores. Diameter and brightness are measured by FCS while the # of dye molecules per particle is calculated from steady-state absorbance measurements on different C' dots and particle concentrations as measured by FCS.

	Diameter	# of Dye Molecules per Particle	Quantum Enhance ment	Brightness to Free Dye	Abs./Emi. Wavelength
RhG C' dots	6.2nm	1.8	1.4	2.6 times	506/528nm
TMR C' dots	6.5nm	2.0	1.7	2.2 times	556/576nm
Cy5 C' dots	6.1nm	1.4	1.5	2.4 times	649/668nm
Cy5.5 C' dots	6.7nm	1.5	1.5	2.4 times	678/695nm
DY782 C' dots	5.2nm	1.3	5.6	6.2 times	780/799nm
CW800 C' dots	5.5nm	1.2	1.1	1.2 times	792/808nm

2.4.4 Controlled fluorescent silica nanoparticle growth with different inorganic compositions.

Fluorophores with emission spectra moving further out into the NIR typically have larger molar mass and size, therefore requiring more negatively charged sulfate groups on the periphery of their delocalized π -electron systems to generate the desired water solubility, *e.g.* compare molecular structures of Cy5 and Cy5.5 in Figure 2.1. Since silica above its isoelectric point at $\text{pH} > 2.7$ is also negatively charged, it is increasingly challenging to covalently encapsulate such highly negatively charged NIR fluorophores into SNPs due to increasing electrostatic repulsive interactions.²¹ Here we present a solution to this problem by adjusting the aqueous SNP growth solution pH to values ($\text{pH} \sim 1.5$) slightly below the isoelectric point of silica ($\text{pH} \sim 2.7$). Since under these conditions SNPs would have a low (positive) charge density and therefore particle suspensions in aqueous solutions would be unstable, an aluminum alkoxide is added to the reaction mixture together with the silica source (TMOS). At the low pH, aluminum based reaction intermediates are positively charged (while in-framework aluminum replacing silicon in the network carries a negative charge).³⁴ From our experimental results, this stabilizes the growing particles enough to prevent aggregation. As shown below, at the same time the weakly positively charged silica at $\text{pH} \sim 1.5$ provides attractive interactions to negatively charged fluorophores, thereby facilitating their incorporation. Aluminum alkoxides are a good choice for this purpose, as alumina derived from its alkoxides has already been approved for injection as one of the most common immunization adjuvants.³⁷ The resulting ultrasmall NIR fluorescent aluminum containing SNPs may therefore also have potential for clinical translation.

In order to incorporate aluminum into SNPs, the solution pH is adjusted to around 1.5 using HCl. An aluminum-tri-sec-butoxide/isopropanol mixture and TMOS (molar ratio around 1:10) are then added simultaneously followed by addition of PEG-silane after 10 mins. of reaction time to terminate particle growth (see experimental section for details). After adjusting the solution pH back to neutral using ammonium hydroxide, an 80°C heat treatment is applied to enhance covalent particle PEGylation. As evidenced by a combination of TEM and DLS (Fig. A7), around 3 nm and narrowly size-dispersed NPs can be successfully synthesized in this way.

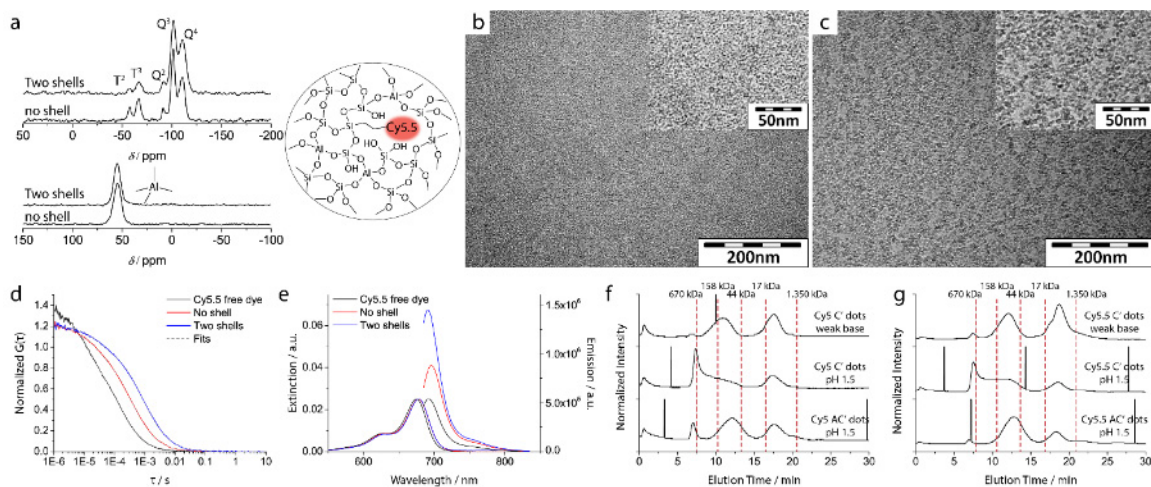


Figure 2.5. Characterizations of aluminosilicate nanoparticles. (a) Solid-state ^{29}Si CP/MAS (top) and ^{27}Al MAS (bottom) NMR spectra of AlC' dots with and without silica shells; the insert on the right shows a model of the molecular structure of the corresponding aluminosilicate network together with covalently encapsulated NIR Cy5.5 dye. (b) TEM image of core ASNPs. (c) TEM image of core-shell ASNPs. (d) FCS autocorrelation curves and (e) absorbance (matched) and emission spectra of Cy5.5 encapsulating core and core-shell ASNPs (AlC' dots) compared to free Cy5.5 dye in aqueous solution. (f, g) GPC elution curves obtained from Cy5 (f) and Cy5.5 (g) encapsulating particle batches synthesized under dramatically different pH conditions as compared to conventional C' dots, see description in text. Vertical hatched lines indicate elution times of molar mass standards (in kilo dalton, kDa) as a guide.

It should be noted that at the strongly acidic conditions used here pure SNPs can hardly be generated. As a result of the proximity of the solution pH to the isoelectric point

of silica at 2.7, the surface charge density of SNPs is not high enough to electrostatically stabilize particles and consequently particle aggregation occurs. In contrast, since the hydrolysis product of aluminum alkoxide at acidic conditions is strongly positively charged, $[\text{Al}(\text{OH}_2)_6]^{3+}$, and in-framework aluminum is negatively charged, we hypothesize that as aluminum co-condenses with silica it may add enough charge to the growing particles so that electrostatic repulsive interactions prevent uncontrolled particle aggregation.³⁶ The diminished negative charge density of growing particles in this synthesis protocol may also help to reduce the repulsion to negatively charged NIR fluorophores thereby facilitating their encapsulation into the NPs. In order to prove this principle, ultrasmall <10 nm Cy5.5 labeled NPs were synthesized by adding dye conjugated silane into the reaction mixture (see experimental section for details). The successful incorporation of aluminum into silica of these particles is checked first by solid-state NMR. The ^{29}Si NMR spectrum in Fig. 2.5a evidences T and Q groups in agreement with previous studies demonstrating a silica-based particle matrix (Q groups) and PEG-silane condensation on the particle surface (T groups).³⁸ The ^{27}Al NMR spectrum only shows one sharp peak at around -56ppm indicating four-fold coordinated in-framework aluminum. An illustration of the molecular structure of the corresponding aluminosilicate network together with covalently encapsulated NIR dye is also shown in Fig. 2.5a.^{24,39} Particle formation was further confirmed by a combination of TEM as well as FCS (Fig. 2.5b and d) and particle size as determined by FCS is 4.2 nm. Unaltered shapes of absorbance and emission spectra suggest survival of the Cy5.5 fluorophore despite the strongly acidic synthesis conditions (Fig. 2.5e).

In order to prove more quantitatively that this synthesis protocol enhances the encapsulation of highly negatively charged fluorophores, the aluminum containing Cy5.5 labeled SNPs, as well as the results of various control reactions, are subjected to GPC characterization immediately after synthesis and before any cleaning step. As shown in Fig. 2.5f and g, the elugrams of conventional Cy5 and Cy5.5 labeled SNPs synthesized using weak base conditions have three main peaks. As indicated in Figure A8, the peak at around 7 min. stems from larger aggregates, which usually will be filtered away via cleaning. The peak at around 18 min. is from unreacted dye molecules, which will be washed away through dialysis. The peak at around 12 min. is the main particle peak. By comparing the peak area of unreacted fluorophores and particles, the percentage of encapsulated fluorophore can be estimated. First of all, the data reveals that the degree of encapsulation greatly depends on fluorophore, and with it on the number of charges per dye. Around 60% silane-conjugated Cy5 dye, which contains one negative charge, is encapsulated into particles at weak base conditions, while this percentage decreases to only ~40% for Cy5.5, which contains three negative charges per molecule. As the reaction pH is decreased to 1.5, no free particle peak is observed for either Cy5 or Cy5.5, whereas the elugrams indicate strong particle aggregation most likely due to loss of particle surface charge. In contrast, as the aluminum alkoxide is submitted to the reaction mixture together with TMOS at low pH, for both dyes a clear particle peak reemerges in the elugrams, while the aggregation peak is strongly suppressed. Interestingly, under the strongly acidic synthesis conditions the encapsulation efficiency as revealed by the areas under the respective peaks for both dyes increases. The effect is stronger for Cy5.5 where the efficiency increases from ~40% to >70%.

Table 2.2. Optical characterization of aluminosilicate C' dots. Comparison of Cy5.5 encapsulating aluminosilicate nanoparticles. Diameter and brightness are measured by FCS while the # of dye molecules per particle is calculated from steady-state absorbance measurements on different C' dots and particle concentrations as measured by FCS.

	Diameter	# of Dye Molecules per Particle	Quantum Enhancement	Brightness to Free Dye
Cy5.5	1.3nm	1.0	-	-
Cy5.5 core	4.2nm	1.4	1.7	2.1 times
Cy5.5 core-shell	7.6nm	1.3	2.6	3.0 times

Two additional silica shells are added to the Cy5.5 encapsulated aluminosilicate core before PEGylation to further enhance the fluorophore quantum efficiency (illustration shown in Fig. 2.1). ^{29}Si and ^{27}Al solid-state NMR spectra of the resulting aluminum containing core-shell nanoparticles (Fig.5a), show consistent characteristics as compared to the particles without shell, corroborating the presence of four-fold coordinated in-framework aluminum. Considering that the T groups in the ^{29}Si spectrum originate from PEG-silane condensing onto the particle surface, the decrease of the T group intensity relative to Q groups in the ^{29}Si spectrum after shell addition is consistent with a decreased surface/volume ratio, which suggests successful silica shell deposition. The average diameter of the core-shell Aluminum containing dots, obtained from TEM (Fig. 2.5c) is around 5 nm (hard particle diameter only), while FCS (Fig. 2.5d) measures 7.6 nm (hard particle plus soft PEG shell plus hydration layer) further suggesting the successful shell addition to the core particle of 4.2 nm (Table 2.2). Interestingly, as measured by steady-

state absorption and FCS concentration analysis, these dots have a quantum enhancement over free dye of 2.6, which is much higher than the value of 1.7 obtained for the core only (Fig. 2.5e, Table 2.2). As shown in Table 2.2, this is confirmed by FCS suggesting that the core-shell particles are around 1.5 times brighter than the core particles. Furthermore, it is important to note that the highest quantum enhancements of plain Cy5.5 C' dots (*i.e.* without addition of aluminum alkoxide) we have synthesized is around 1.7-2.2, even with several nm thick silica shells. We speculate that this very high quantum enhancement over free dye of 2.6 is the result of increased matrix rigidity surrounding the dye since incorporation of aluminum into the silica network is known to enhance its rigidity.²⁴ Considering the quantum yield of Cy5.5 free dye in water is about 0.3,^{40,41,42} the observed enhancement of 2.6 is equivalent to a quantum yield of encapsulated dye of around 0.8, which is quite high and starting to approach the theoretical brightness limit.

In order to distinguish these aluminum containing fluorescent SNPs synthesized in water from C' dots, they will be referred to as AlC' dots. Finally, it is worth emphasizing that as a result of the fast reaction rate of the aluminum alkoxide the final core-shell AlC' dot surface should be indistinguishable from that of conventional C' dots as the aluminum is expected to reside only in the core while the shells are made of plain silica covalently decorated with PEG chains as in the case of the C' dots.

2.4.5 Ligand functionalized fluorescent silica nanoparticles.

Heterobifunctional PEGs are employed to introduce easily accessible ligands onto the PEGylated particle surface of fluorescent SNPs and core-shell SNPs, as well as their aluminum containing analogues. This produces ligand functionalized <10 nm NIR

fluorescent nanoprobe *e.g.* for preclinical and clinical use in diagnostic and therapeutic applications. Ligands interesting for such applications include, but are not limited to, peptides, antibody fragments, various DNA and RNA segments (*e.g.* siRNA), therapeutic molecules including drugs as well as radioisotopes and their respective chelating moieties, and combinations thereof. Here, proof-of-principle is demonstrated using $\alpha_v\beta_3$ integrin-targeting cyclic(arginine-glycine-aspartic acid-D, tyrosine-cysteine) peptides, c(RGDyC), containing a tyrosin (Y) residue to bind a radioisotope, *e.g.* ^{124}I , and a cysteine (C) residue to bind to the maleimido-functionalized heterobifunctional PEGs.^{14,15} As displayed in Figure 2.6a, to that end heterobifunctional PEGs with NHS ester and maleimide groups at their chain ends (NHS-PEG-mal with molar mass around 800 g/mole, see experimental section) are first conjugated with amino silane through reaction of the amine with the NHS ester group. In a second step the resulting silane-PEG-maleimide is further conjugated with c(RGDyC) through thiol-maleimide reaction to produce c(RGDyC) functionalized PEG-silane (c(RGDyC)-PEG-silane). The heterobifunctional PEG is chosen to be a bit longer as compared to the PEG-silane (870 g/mole as compared to 500 g/mole, respectively). This ensures that the surface ligands are sticking out a bit beyond the surface of the PEG-silane coating and are therefore easily accessible (see also models in Figure 2.7). The final c(RGDyC)-PEG-silane is added into the nano-dot synthesis solution together with monofunctional PEG-silane in the PEGylation step. As a result, the surface of the synthesized nano-dots is covalently covered by both the common PEG chains and the longer c(RGDyC) functionalized PEG chains (Fig. 2.1). Figure 2.6b compares the absorbance spectra of free c(RGDyC) peptide, free Cy5 dye, and Cy5 encapsulated C' dot cores (Cy5-C' dots, no silica shell) with / without c(RGDyC) surface functionalization. The

c(RGDyC) peptide has an absorbance peak at 275 nm from the tyrosine residue, while neither the Cy5 free dye nor the Cy5-C' dots show detectable signals in this wavelength range. This absorbance peak can thus be used to verify successful particle surface functionalization. Indeed, the c(RGDyC) functionalized Cy5-C' dots (c(RGDyC)-Cy5-C' dots) show an absorbance peak at around 275 nm in addition to the 650 nm Cy5 absorbance peak. Furthermore, as shown in Figure A9, the FCS measured autocorrelation curve of c(RGDyC)-Cy5-C' dots slightly shifts to the right compared to the dots without c(RGDyC) surface modification, indicating a ~1 nm particle size increase after attaching c(RGDyC) ligands to the particle surface (Table A4). These data suggest the c(RGDyC) peptides have been successfully attached to the particle surface. Combining the absorbance and FCS characterizations, the number of c(RGDyC) ligands per C' dot can be calculated (Supplementary information). As shown in Table A4, from this synthesis batch on average around 16 c(RGDyC) peptides are attached to a single Cy5-C' dot (no silica shell). Further studies will have to elucidate, what average ligand number will provide the best results, *e.g.* wrt. biodistribution and pharmacokinetics. To that end ligand numbers can be varied via the synthesis conditions, *e.g.* by changing the ratio of ligand-bearing and plain PEG-silane added in the particle synthesis step (data not shown).

In order to prove that this surface modification methodology can be applied to other particle platforms in the C' dot family, c(RGDyC) peptides are attached to different types of C' dots under similar reaction conditions. In detail, these include C' dots with additional silica shells, with different types of fluorophore (Cy5.5 vs. Cy5) and with different composition (AlC' dots vs. C' dots). As displayed in Figure 2.6c, all these synthesized particles show the absorbance peak at around 275 nm characteristic for c(RGDyC)

indicating successful c(RGDyC) surface modification in all cases. The number of c(RGDyC) peptides per particle as derived from these optical measurements combined with FCS results slightly varies from 12 to 22 (Table A4).

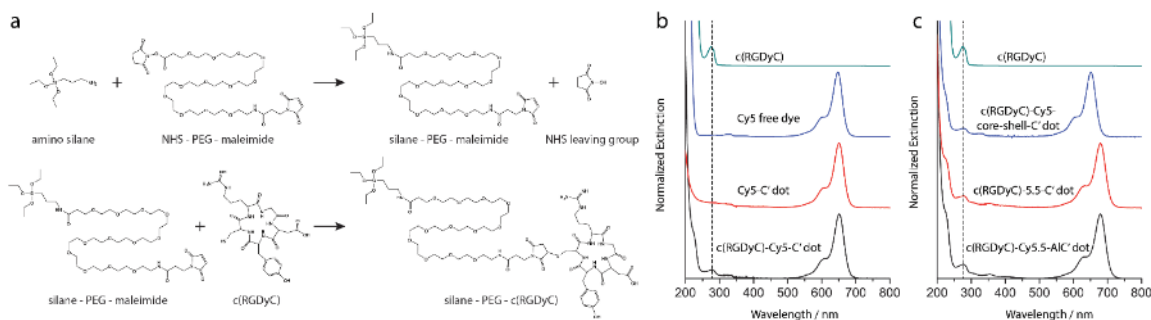


Figure 2.6. SNP surface functionalization with c(RGDyC) peptides. (a) Conjugation chemistry of c(RGDyC) functionalized PEG-silane. (b) Absorbance spectra comparing free c(RGDyC) peptide, free Cy5 dye and Cy5-C' dots (no silica shell) with/without c(RGDyC) surface functionalization suggesting successful c(RGDyC) surface modification. (c) Absorbance spectra comparing free c(RGDyC) peptide and different types of c(RGDyC) surface functionalized C' dots suggesting success of nanoparticle-PEG-surface functionalization with ligands is independent of particle architecture (*i.e.* with or without extra silica shells), types of fluorophores encapsulated, or particle composition (*i.e.* C' dots versus AIC' dots).

Considering that each 6 nm C' dot has roughly around 100 PEG chains on the surface according to thermogravimetric analysis (TGA; see Supplementary information Fig. A10), a number that changes with particle size, it can be estimated that one out of 5-10 PEG chains is functionalized with a c(RGDyC) ligand. Besides absolute ligand number, ligand density is another parameter that is expected to control biological response, and can be tuned via the synthesis parameters discussed in this study. The surface density of monofunctional PEG chains and c(RGDyC)-functionalized PEG chains of the synthesized ~7 nm C' dot are estimated to be roughly 1.7/nm² and 0.2/nm², respectively. For the plain PEG chains this is equivalent to an area per PEG-silane head group of around 0.6 nm². For comparison it is interesting to note that the overall surface density of PEG chains on a high

curvature C' dot surface is very close to the reported ligand densities of shorter functional alkyl-silane monolayers on planar silica⁴³ which is between 1.2/nm² and 2.2/nm², or between 0.83 nm² and 0.45 nm² when expressed as area per head group.

2.4.6 Molecular models of ligand functionalized PEGylated fluorescent core-shell silica nanoparticles.

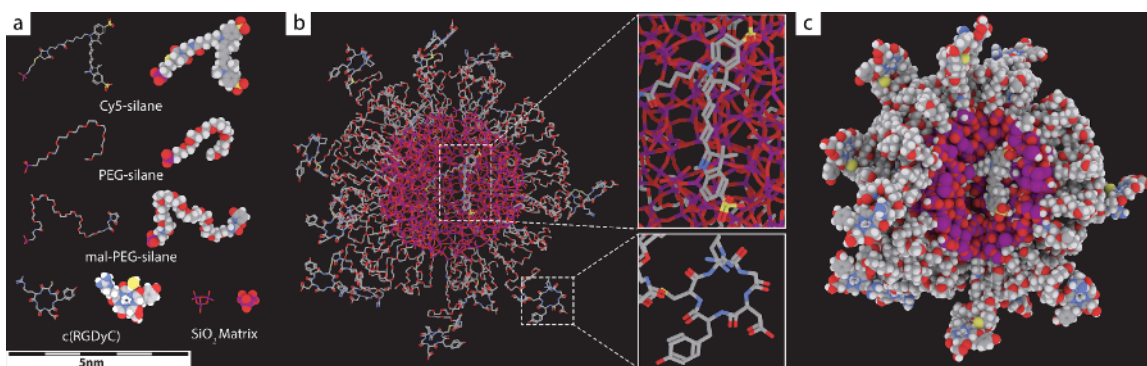


Figure 2.7. Molecular rendering of C' dot. Molecular-graphics rendering of Cy5 fluorophore, PEG-silane, maleimide-functionalized PEG-silane, c(RGDyC) peptide, SiO₂ matrix (a) and a c(RGDyC)-Cy5-C' dot (b and c). The C' dot model consists of a ~3nm silica core which encapsulates one Cy5 fluorophore, a ~1 nm silica shell, a ~1.5 nm PEG layer and 16 easily accessible c(RGDyC) ligands. The molecular models are displayed in different modes for visualization including the molecular framework without hydrogen (b) and the sphere-based molecular model with realistic atomic dimensions (c).

Based on the full analysis results, realistically scaled molecular models of a ligand functionalized Cy5 encapsulating PEGylated core-shell C' dot with c(RGDyC) surface modification (*i.e.* of a c(RGDyC)-Cy5-C' dot) are displayed in Figure 2.7. For size comparison, from top to bottom the left side (Figure 2.7a) shows models of individual components constituting this particle: Cy5 dye, PEG-silane (around 500 g/mole), maleimide-functionalized (*i.e.* heterobifunctional) PEG-silane (around 800 g/mole), c(RGDyC) peptide, as well as silica. The models in Figure 2.7b and 7c represent a cut through a C' dot with a ~3 nm diameter silica core encapsulating one Cy5 fluorophore

(Figure 2.7b, top inset), a ~ 0.5 nm thick silica shell, a ~ 1.5 nm thick PEG layer, and 16 c(RGDyC) ligands (Figure 2.7b, bottom inset) at the end of heterobifunctional PEGs that are a bit longer than the PEG-silanes. According to an amorphous silica density around 1.9-2.2 g/cm³,⁴⁴ this silica nanoparticle consists of about 800 SiO₂ units and about 100 PEG chains on the particle surface. The overall particle size is around 7.5 nm and the overall particle molar mass is about 110 kDa. As shown in Figure 2.7a, the length of a Cy5 fluorophore is between 2 and 3 nm although its hydrodynamic diameter as measured by FCS is only slightly larger than 1 nm (Table A3). It is easy to imagine from Figure 2.7 that a location of the covalently bonded Cy5 fluorophore exactly inside the 3 nm silica core is unlikely given the stochastic nature of the encapsulation process and the electrostatic repulsion between Cy5 and negatively charged deprotonated silica surface hydroxyl groups. In order to be fully covered/encapsulated by silica, rather an additional silica shell is necessary consistent with the fact that extra silica shells result in further quantum yield enhancements (Figure 2.3g and i). It is finally interesting to note that there are only about 10 SiO₂ structural units across the silica core-shell part of the C' dot further emphasizing the near-molecular or macromolecular size of these nanoparticles.

2.5 Conclusions

In this paper we have presented an aqueous synthesis methodology for the generation of narrowly size-dispersed PEGylated SNPs with size control below 1 nm, *i.e.* at the level of single atom layers. Different types of fluorophores including NIR emitting dyes can be encapsulated into the particles to produce fluorescent probes whose brightness can be further enhanced via addition of extra silica shells before PEGylation. This methodology further enables synthesis of <10 nm sized fluorescent SNPs with other compositions. In particular the addition of an aluminum sol gel precursor leads to aluminum containing fluorescent core and core-shell nanoparticles, for which not only the encapsulation efficiency of highly negatively charged NIR fluorophores is enhanced relative to the silica particles, but also the quantum enhancement of individual fluorophores is starting to approach the theoretical brightness limit. Finally, heterobifunctional PEGs can be employed to introduce easily accessible ligands onto the PEGylated particle surface of fluorescent SNPs and core-shell SNPs, as well as their aluminum containing analogues, producing <10 nm NIR fluorescent nanoprobe for preclinical and clinical use in diagnostic and therapeutic applications. In order to distinguish the water-based synthesis derived materials from the earlier alcohol-based modified Stöber process-derived fluorescent core-shell silica nanoparticles referred to as Cornell dots or C dots, these fluorescent SNPs and Al containing SNPs will be referred to as Cornell prime dots or C' dots and AlC' dots. Elucidation of synthesis parameter - NP structure correlations as described here may also help improve fundamental understanding of the mechanisms of early growth states of SNPs.

2.6 Acknowledgments

K. M. gratefully acknowledges NIH for the financial support by Grant 5R01 CA161280-03. The authors acknowledge the Cornell Center for Materials Research (CCMR) and the Nanobiotechnology Center (NBTC) of Cornell University for the use of facilities. The authors gratefully acknowledge M. S. Bradbury of Memorial Sloan Kettering Cancer Center for helpful discussion and kind experimental assistance. The authors also acknowledge C. Ying, D. Zhang, J. Drewes and T. Kao of the Wiesner group at Cornell University for kind assistance. M. H., U, W.-Z. and J. Z gratefully acknowledge the financial support of NSERC and the Canada Research Chairs program.

2.7 References

- (1) Wagner, V.; Dullaart, A.; Bock, A. K.; Zweck, A. The Emerging Nanomedicine Landscape. *Nat Biotechnol.* **2006**, *24*, 1211–1217.
- (2) Peer, D.; Karp, J. M.; Hong, S.; Farokhzad, O. C.; Margalit, R.; Langer, R. Nanocarriers as an Emerging Platform for Cancer Therapy. *Nature Nanotechnol.* **2007**, *2*, 751–760.
- (3) Hrkach J.; Von Hoff D.; Mukkaram Ali M.; Farokhzad O. C.; Langer R.; Zale S. et al. Preclinical Development and Clinical Translation of a PSMA-Targeted Docetaxel Nanoparticle with a Differentiated Pharmacological Profile. *Sci Transl Med.* **2012**, *4(128)*, 128–139.
- (4) Gillies, E. R. ; Fréchet, J. M. Dendrimers and Dendritic Polymers in Drug Delivery. *Drug Discov Today.* **2005**, *10(1)*, 35–43.
- (5) Duncan, R. Polymer Conjugates as Anticancer Nanomedicines. *Nat Rev Cancer.* **2006**, *6(9)*, 688–701.
- (6) Ferrari, M. Cancer Nanotechnology: Opportunities and Challenges. *Nat Rev Cancer.* **2005**, *5(3)*, 161–171.
- (7) Hola, K.; Zhang, Y.; Wang, Y.; Giannelis E.; Zboril R.; Rogach A. L. Carbon Dots- Emerging light Emitters for Bioimaging, Cancer Therapy and Optoelectronics. *Nanotoday* **2014**, *9*, 590–603.
- (8) Choi, J.; Burns, A. A.; Williams, R. M.; Zhou, Z.; Flesken-Nikitin, A.; Zipfel, W. R.; Wiesner, U.; Nikitin, A. Y. Core-shell Silica Nanoparticles as Fluorescent Labels for Nanomedicine. *J. Biomed. Optics* **2007**, *12(6)*, 064007–1–11.

- (9) Sanhai, W. R.; Sakamoto, J. H.; Canady, R.; Ferrari, M. Seven Challenges for Nanomedicine. *Nat Nanotechnol.* **2008**, *3*(5), 242–244.
- (10) Choi, H. S.; Liu, W.; Misra, P.; Tanaka, E.; Zimmer, J. P.; Ipe, B. I.; Bawendi, M. G.; Frangioni, J. V. Renal Clearance of Quantum Dots. *Nature Nanotech.* **2007**, *25*, 1165–1170.
- (11) Burns, A.; Vider, J.; Ow, H.; Herz, E.; Penate-Medina, O.; Baumgart, M.; Larson, S. M.; Wiesner, U.; Bradbury, M. Fluorescent Silica Nanoparticles with Efficient Urinary Excretion for Nanomedicine. *Nano Lett.* **2009**, *9*, 442–448.
- (12) Gao, J.; Chen, K.; Luong, R.; Bouley, D. M.; Mao, H.; Qiao, T.; Gambhir, S. S.; Cheng, Z. A Novel Clinically Translatable Fluorescent Nanoparticle for Targeted Molecular Imaging of Tumors in Living Subjects. *Nano Lett.* **2012**, *12*(1), 281–286.
- (13) Huang, X.; Zhang, F.; Zhu, L.; Choi, K. Y.; Guo N.; Guo J.; Tackett K.; Anilkumar P.; Liu G.; Quan Q.; Choi H. S.; Niu G.; Sun Y. P.; Lee S.; Chen X. Effect of Injection Routes on the Biodistribution, Clearance, and Tumor Uptake of Carbon Dots. *ACS Nano.* **2013**, *7*(7), 5684–5693.
- (14) Benezra, M.; Penate-Medina, O.; Zanzonico, P. B.; Schaer, D.; Ow, H.; Burns, A.; DeStanchina, E.; Longo, V.; Herz, E.; Iyer, S.; Wolchok, J.; Larson, S. M.; Wiesner, U.; Bradbury, M. S. Multimodal Silica Nanoparticles are Effective Cancer-targeted Probes in a Model of Human Melanoma. *J Clin Invest.* **2011**, *121*, 2768–2780.
- (15) Phillips, E.; Penate-Medina, O.; Zanzonico, P. B.; Carvajal, R. D.; Mohan, P.; Ye, Y.; Humm, J.; Gönen, M.; Kalaigian, H.; Schöder, H.; Strauss, H. W.; Larson,

- S. M.; Wiesner, U.; Bradbury, M. S. Clinical Translation of an Ultrasmall Inorganic Optical-PET Imaging Nanoparticle Probe. *Sci Transl Med.* **2014**, *6*, 260ra149.
- (16) Ow, H.; Larson, D.; Srivastava, M.; Baird, B.; Webb, W.; Wiesner, U. Bright and Stable Core–Shell Fluorescent Silica Nanoparticles. *Nano Lett.* **2005**, *5*, 113–117.
- (17) Stöber, W.; Fink, A.; Bohn, E. Controlled Growth of Monodisperse Silica Spheres in the Micron Size Range. *J. Colloid Interface Sci.* **1968**, *26*(1), 62–69.
- (18) Bogush, G. H.; Tracy, M. A.; Zukoski IV, C. F. Preparation of Monodisperse Silica Particles: Control of Size and Mass Fraction. *J. Non-Crystalline Solids* **1988**, *104*(1), 95–106.
- (19) Matsoukas, T.; Gulari, E. Dynamics of Growth of Silica Particles from Ammonia-catalyzed Hydrolysis of Tetra-ethyl-orthosilicate. *J. Colloid Interface Sci.* **1988**, *124*(1), 252–261.
- (20) Yamada H., Urata C., Aoyama Y., Osada S., Yamauchi Y. and Kuroda K. Preparation of Colloidal Mesoporous Silica Nanoparticles with Different Diameters and Their Unique Degradation Behavior in Static Aqueous Systems. *Chem. Mater.* **2012**, *24*(8), 1462–1471.
- (21) Herz, E.; Ow, H.; Bonner, D.; Burns, A.; Wiesner, U. Dye Structure–optical Property Correlations in Near-infrared Fluorescent Core-shell Silica Nanoparticles. *J. Mater. Chem.* **2009**, *19*, 6341–6347.
- (22) Ma, D.; Kell, A. J.; Tan, S.; Jakubek, Z. J.; Simard, B. Photophysical Properties of Dye-Doped Silica Nanoparticles Bearing Different Types of Dye–Silica Interactions. *J. Phys. Chem. C* **2009**, *113*, 15974–15981.

- (23) Larson, D. R.; Ow, H.; Vishwasrao, H. D.; Heikal, A. A.; Wiesner, U.; Webb, W. W. Silica Nanoparticle Architecture Determines Radiative Properties of Encapsulated Fluorophores. *Chem. Mater.* **2008**, *20*, 2677–2684.
- (24) Templin, M.; Wiesner, U.; Spiess, H. W. Multinuclear Solid-state-NMR Studies of Hybrid Organic-inorganic Materials. *Adv. Mater.* **1997**, *9*(10), 814–817.
- (25) Vinogradov, V. V.; Avnir, D. Exceptional Thermal Stability of Therapeutical Enzymes Entrapped in Alumina Sol–gel Matrices. *J. Mater. Chem. B*, **2014**, *2*, 2868–2873.
- (26) Carcouët, C. C.; Van de Put, M. W.; Mezari, B.; Magusin, P. C.; Laven, J.; Bomans, P. H.; Friedrich, H.; Esteves, A. C.; Sommerdijk, N. A.; Van Benthem, R. A.; de With, G. Nucleation and Growth of Monodisperse Silica Nanoparticles. *Nano Letter* **2014**, *14*(3), 1433–1438.
- (27) Keen, D. A.; McGreevy, R. L. Structural Modelling of Glasses using Reverse Monte Carlo simulation. *Nature* **1990**, *344*, 423–425.
- (28) McGreevy R. L.; Pusztai L. Reverse Monte Carlo Simulation: A New Technique for the Determination of Disordered Structures, *Molecular Simulation* **1988**, *1*, 359–367.
- (29) Lin, Y.; Haynes, C. L. Impacts of Mesoporous Silica Nanoparticle Size, Pore Ordering, and Pore Integrity on Hemolytic Activity. *J. Am. Chem. Soc.* **2010**, *132*, 4834–4842.
- (30) Wang, J.; Sugawara-Narutaki, A.; Fukao, M.; Yokoi, T.; Shimojima, A.; Okubo, T. Two-Phase Synthesis of Monodisperse Silica Nanospheres with Amines

- or Ammonia Catalyst and Their Controlled Self-Assembly. *ACS Appl. Mater. Interfaces* **2011**, *3*, 1538–1544.
- (31) Inagaki, S.; Guan, S.; Ohsuna T.; Terasaki, O. An Ordered Mesoporous Organosilica Hybrid Material with a Crystal-like Wall Structure. *Nature* **2002**, *416*, 304-307.
- (32) Murray, C. B.; Norris, D. J.; Bawendi M. G. Synthesis and Characterization of Nearly Monodisperse CdE (E = Sulfur, Selenium, Tellurium) Semiconductor Nanocrystallites. *J. Am. Chem. Soc.* **1993**, *115(19)*, 8706–8715.
- (33) Iler, R. K. The Chemistry of Silica: Solubility, Polymerizaion, Colloid and Surface Properties, and Biochemistry; Wiley: New York, **1979**.
- (34) Burns, A.; Ow, H.; Wiesner, U. Fluorescent Core–shell Silica Nanoparticles: towards “Lab on a Particle” Architectures for Nanobiotechnology. *Chemical Society Reviews* **2006**, *35*, 1028–1042.
- (35) Bacia, K.; Kim, S. A.; Schwille, P. Fluorescence Cross-correlation Spectroscopy in Living Cells. *Nature Method* **2006**, *3(2)*, 83–89.
- (36) Brinker, C. J. Sol-Gel Science, Academic Press Inc.: CA, **1990**.
- (37) Rutenberg, A.; Vinogradov, V. V.; Avnir, D. Synthesis and Enhanced Thermal Stability of Albumins@alumina: towards Injectable sol–gel Materials. *Chem. Commun.* **2013**, *49*, 5636–5638.
- (38) Ma, K.; Werner-Zwanziger, U.; Zwanziger, J.; Wiesner, U. Controlling Growth of Ultrasmall Sub-10 nm Fluorescent Mesoporous Silica Nanoparticles. *Chem. Mater.* **2013**, *25(5)*, 677–691.

- (39) Templin, M.; Friedrich, U.; Wiesner, U.; Spiess, H. W. Precursor-Derived Ceramics; Wiley-VCH: Weinheim, **1999**.
- (40) Nancy, J. L.; Arnold, C. C. Predicted Observable Fluorescent Lifetimes of Several Cyanines. *J. Phys. Chem.*, **1974**, *78(12)*, 1154–1155.
- (41) Xiao, M.; Selvin, P. R. Quantum Yields of Luminescent Lanthanide Chelates and Far-Red Dyes Measured by Resonance Energy Transfer. *J. Am. Chem. Soc.* **2001**, *123(29)*, 7067–7073.
- (42) Ernst, L. A.; Gupta, R. K.; Mujumdar, R. B.; Waggoner, A. S. Cyanine Dye Labeling Reagents for Sulfhydryl Groups. *Cytometry* **1989**, *10(1)*, 3–10.
- (43) Moon, J. H.; Kim, J. H.; Kim, K. J.; Kang, T. H.; Kim, B.; Kim, C. H.; Hahn, J. H.; Park, H. W. Absolute Surface Density of the Amine Group of the Aminosilylated Thin Layers: Ultraviolet–Visible Spectroscopy, Second Harmonic Generation, and Synchrotron-Radiation Photoelectron Spectroscopy Study. *Langmuir* **1997**, *13*, 4305–4310.
- (44) Quercia, G.; Lazaro, A.; Geus, J. W.; Brouwers, H. J. H. Characterization of Morphology and Rexture of Several Amorphous Nano-silica Particles Used in Concrete. *Cement & Concrete Composites* **2013**, *44*, 77–92.

Appendix A: Supplementary information for Chapter 2

Table A1. Synthesis condition of particles with different size

DLS Diameter	Temperatur e	Concentration of TMOS	Concentration of Ammonia hydroxide	Particle Growth Period
2.4nm	RT	0.011M	0.002M	20hrs
3.1nm	RT	0.022M	0.002M	20hrs
3.7nm	RT	0.043M	0.002M	10mins
4.2nm	RT	0.043M	0.002M	20hrs
4.5nm	RT	0.043M	0.02M	20hrs
5.2nm	RT	0.043M	0.06M	20hrs
5.9nm	50	0.043M	0.002M	20hrs
6.5nm	65	0.043M	0.002M	20hrs
7.3nm	80	0.043M	0.002M	20hrs

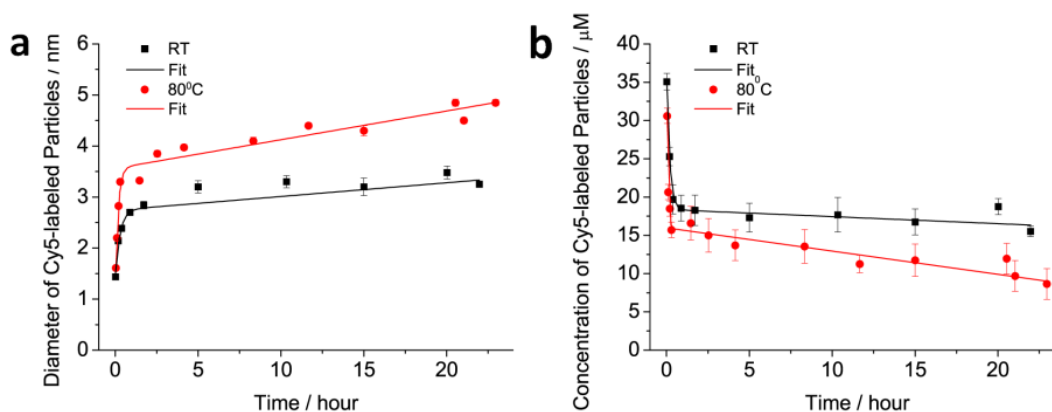


Figure A1. In-situ FCS measurement results. (a) Particle diameter and (b) particle concentration during the reaction and particle growth.

To monitor particle formation during reaction, silane-conjugated Cy5 fluorophore is added together with TMOS to co-condense into silica particles. As a result, via tracing the fluorescence signal from Cy5 fluorophores using FCS, in-situ particle diameter and particle concentration could be monitored. As shown in Fig. A1a and b, upon the addition of silica source(s), TMOS and silane-conjugated Cy5 fluorophores hydrolyze and condense into particles resulting in particle size increases and fluorophore concentration decreases. For both room temperature and 80°C syntheses, particles go through a rapid growth period within the first 10 mins. due to the high concentration of silicic acid present in the reaction mixture. Afterwards, as silicic acid concentration is now depleted due to the initial particle

nucleation and growth burst, particles grow slower through further controlled aggregation. Both the particle diameter and concentration results could be fitted by the following equation:

$$y = y_0 + Ae^{-\frac{t}{t_R}} + Bt$$

The exponential part represents the rapid particle formation kinetics at the beginning of the reaction and the linear part represents the kinetics of the subsequent controlled aggregation step. In the particle diameter equation, y is the average particle diameter at time t , A is the relative amplitude of particle growth from the fast particle formation kinetics with characteristic time t_R , B is the particle growth rate of the later controlled aggregation process and y_0+A is the initial size of silica precursor. Since the FCS traces the Cy5-silane whose hydrodynamic size is about 1.2-1.5nm, the fitted values of y_0+A are consistent with the expectation. (Table A2) In the particle concentration equation, y is the precursor concentration (Cy5-labeled silica cluster) at time t , A is the relative amplitude of particle growth contribution from the fast particle formation kinetics with characteristic time t_R , B is the decreasing rate of particle concentration in the later controlled aggregation process and y_0+A is the initial concentration of Cy5-silane. The fitted parameters are shown in the following table.

Table A2. Synthesis condition of particles with different size

		y_0	A	t_R	B
Diameter	RT	2.74 ± 0.07 nm	-1.30 ± 0.11 nm	0.29 ± 0.05 hr	0.03 ± 0.01 nm/hr
	80°C	3.56 ± 0.11 nm	-2.39 ± 0.16 nm	0.17 ± 0.03 hr	0.06 ± 0.01 nm/hr
Concentration	RT	18.36 ± 1.17 μ M	18.36 ± 1.70 μ M	0.18 ± 0.04 hr	-0.09 ± 0.06 μ M/hr
	80°C	15.97 ± 0.64 μ M	23.76 ± 2.35 μ M	0.06 ± 0.01 hr	-0.30 ± 0.05 μ M/hr

Compared to the room temperature synthesis, particles forming at 80°C have bigger size and lower concentration at around 10 mins. right after the rapid growth period. This could be due to the fact that the particle surface energy is higher at higher temperature.

This is also consistent with the finding that the fitted values of t_R in both diameter and concentration equations are smaller at higher temperature, which indicates the higher rate. After 10 mins., particle size continuously increases and particle concentration slightly decreases at 80°C while at room temperature both changes are smaller. This suggests that at higher temperature particles tend more to aggregate into bigger ones through controlled aggregation due to the increase of surface energy. From the fitted value B, one can estimate the aggregation rate at different temperatures; it is around 0.03 nm/hr at room temperature and 0.06 nm/hr at 80°C.

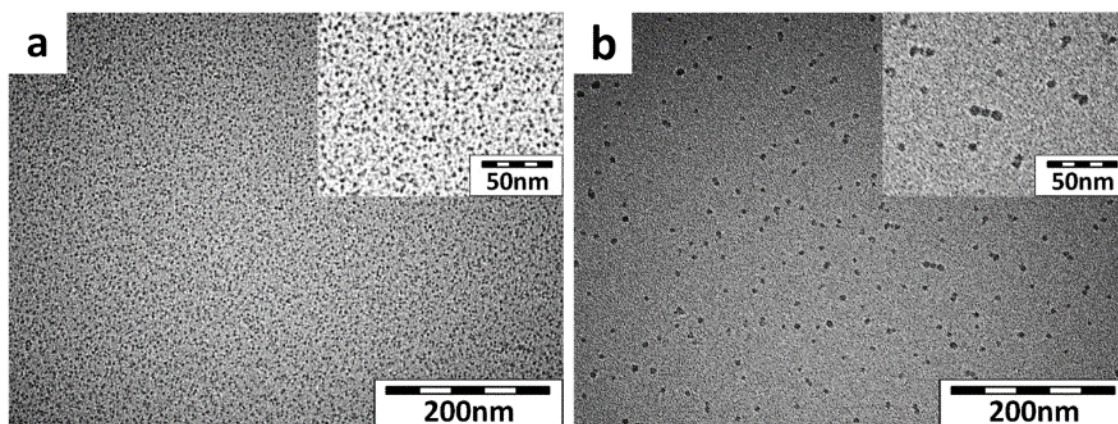


Figure A2. TEM images of SNPs synthesized with/without high temperature treatment. (a) particles synthesized at room temperature and (b) particles first synthesized at room temperature and then subjected to 80°C heat treatment for another three days before growth is terminated by PEG-silane addition.

In order to further demonstrate that particles grow through controlled aggregation at high temperature, a room temperature synthesis reaction is split into two parts 16 hours after the addition of TMOS and dye-silane at which moment the core particles have formed. One of the two particle batches is terminated by PEG-silane addition following the common synthesis procedure and the TEM image of the final product is shown in Fig. A2a.

The other batch is subjected to 80°C heat treatment for another 3 days, followed by reaction termination via addition of PEG-silane. As shown in Fig. A2b, the particles after high temperature treatment have a bigger size than the particles without high temperature treatment (Fig. A2a). Considering that most of the silica source has already condensed onto particles during the first day of reaction, this further particle growth at higher temperature is most likely the result of further growth via aggregation of smaller silica particles. This controlled aggregation could be caused by the fact that at high temperature the surface energy of small particles is so high that they tend to aggregate into bigger ones thereby lowering the overall free energy.

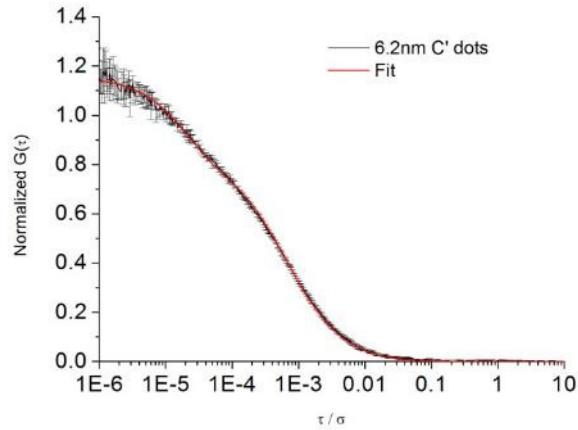


Figure A3. FCS characterization of Cy5 labeled C' dots. 6.2 nm C' dot (dye containing core plus PEG-silane coating) FCS characterization result as an example of a fit of a FCS autocorrelation curve.

FCS autocorrelation curves are fitted by the following equation:

$$G(\tau) = 1 + \frac{1}{N} \cdot \frac{1}{1-A} \cdot \left(1 - A + A \cdot e^{-\frac{\tau}{\tau_R}}\right) \cdot \frac{1}{1 + \frac{\tau}{\tau_D}} * \frac{1}{\sqrt{1 + S^2 \cdot \frac{\tau}{\tau_D}}}$$

where S is the structure factor (ratio between the shorter axis and the longer axis of the elliptical focal spot of FCS setup), N is the average number of particles present in the focal spot, A is the amplitude of triplet state correction, τ_R is the characteristic time of triplet state and τ_D is the diffusion time. The structure factor, S , is obtained from the setup calibration and is fixed in the fit, while the values of N , A , τ_R and τ_D are obtained from the fit. Fig. A3 shows an example of this type of curve fitting. Based on the fitted parameters, average hydrodynamic diameter of particles, fluorescent brightness per particle and concentration of fluorescent particles could be obtained.

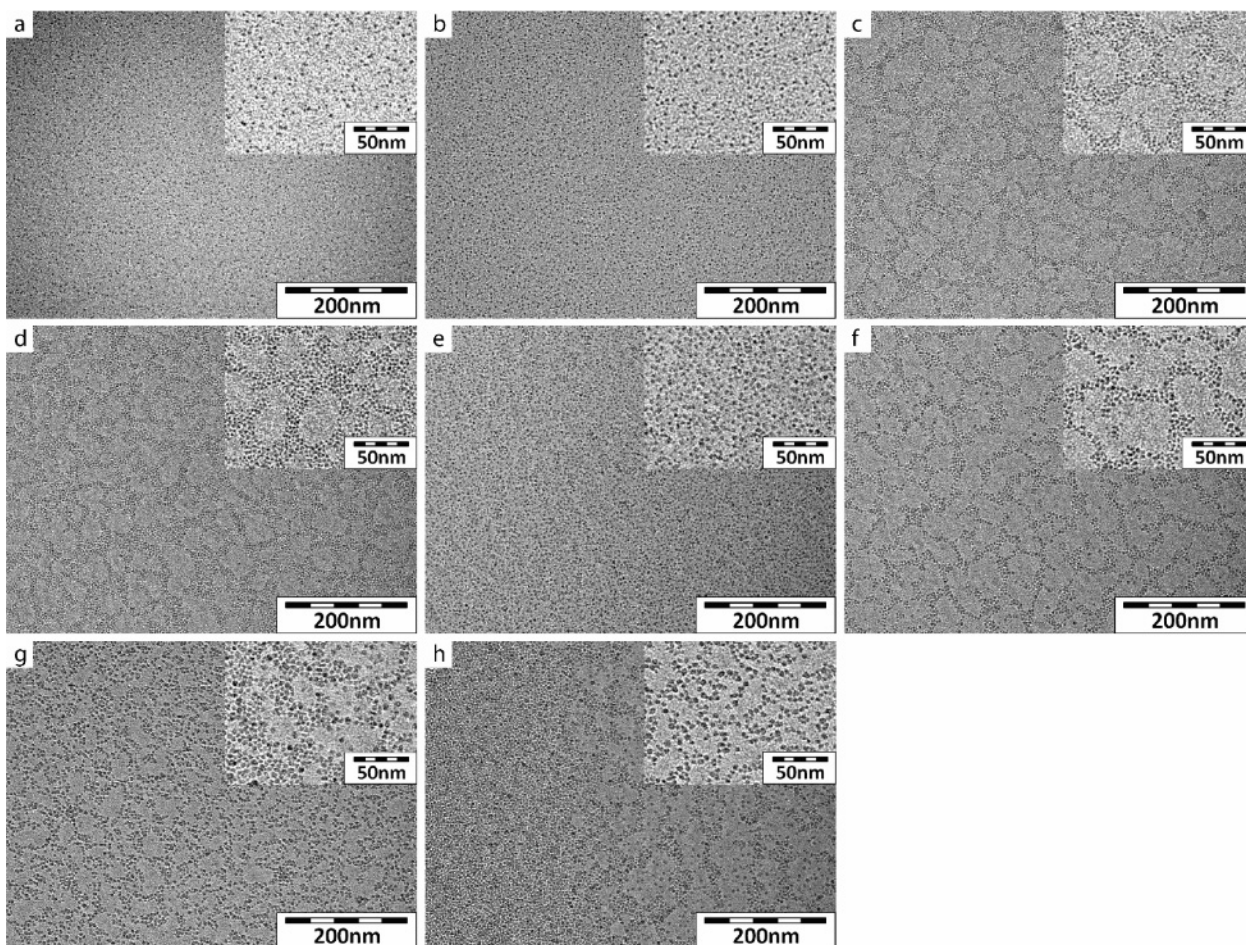


Figure A4. TEM images of of Cy5-encapsulated SNPs. The SNPs are encapsulated with Cy5 and have varied average diameters as measured by FCS. (a) 4.3 nm, (b) 4.7 nm, (c) 5.2 nm, (d) 5.9 nm, (e) 6.2 nm, (f) 6.8 nm, (g) 7.3 nm, (h) 7.8 nm.

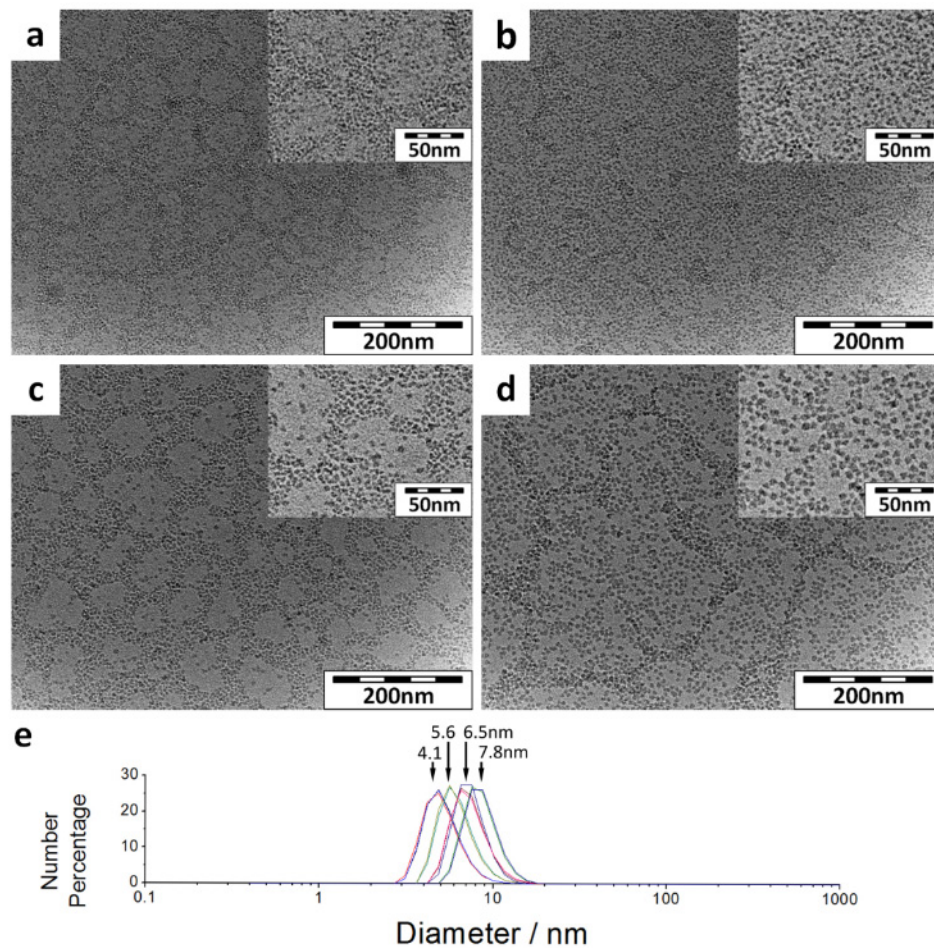


Figure A5. Characterization of blank PEGylated core-shell SNPs. (a-d) TEM images of blank PEGylated core-shell SNPs (without fluorophores) with 0-3 layers of shells. (a) no shell (core/seed) 4.1 nm, (b) 1 shell, 5.6 nm, (c) two shells, 6.5 nm, and (d) three shells, 7.8 nm. The average diameters are measured by DLS. (e) Diameter distribution of SNPs with 0-3 layers of shells as measured by DLS.

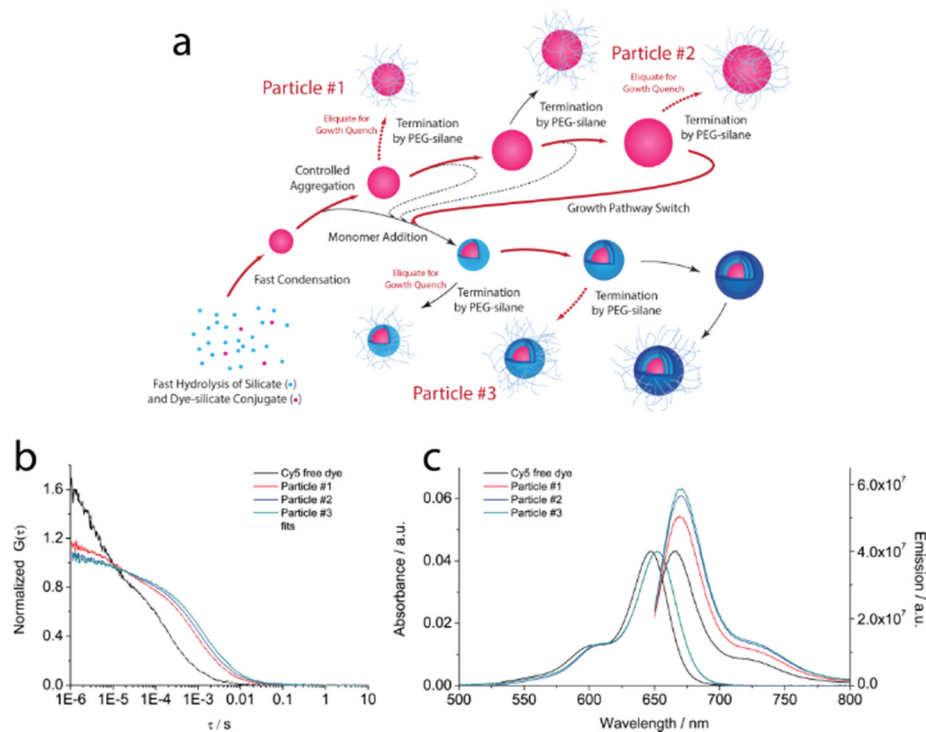


Figure A6. Switching the particle growth mechanism in a single synthesis. As highlighted by the red path in (a), the growth of the forming particles first goes through controlled aggregation followed by monomer addition. Three sets of particles are produced from this synthesis through quenching the particle growth at different reaction time points via addition of PEG-silane. The resulting particles are characterized by (b) FCS and (c) optical absorbance / emission measurements.

In order to prove the principle that these two particle growth pathways, *i.e.* controlled aggregation and monomer addition, can be switched in a single synthesis, a batch of particles is processed first through controlled aggregation by varying reaction temperature, then through monomer addition by further dosing extra silica source. Small amounts of sample solution are aliquoted at different synthesis points in order to quench particle growth via PEGylation. Refer to the red path of Figure A6a as the synthesis pathway. By characterizing the growing particles quenched at different time points, details of the particle growth process could be revealed. Here, the synthesis conditions for ~5 nm particles is first applied (room temperature). 24 hours after the addition of TMOS, 1/3 of

the reaction solution is aliquoted and PEGylated to generate particle #1 (Figure A6a). The remaining 2/3 of the reaction solution is then heated to 80°C and maintained at this temperature for 48 hours followed by cooling down to room temperature. Afterwards, 1/2 of the remaining reaction solution is aliquoted and PEGylated to generate particle #2. The remaining 1/2 of the reaction solution is further subjected to deposition of two extra layers of silica shell. Particles are then PEGylated to generate particle #3. As shown in Table A3, while the diameter of particle #1 is 5.9 nm, the diameter of particle #2 increases to 9 nm after heat treatment. This increase of particle size is due to the controlled aggregation of small particles at high temperature. This aggregation also increases the number of dyes per particle from 1.4 to 2.6. After dosing extra silica source into the reaction solution, a thin silica shell is added onto the existing particle surface through monomer addition and the particle diameter further increases to 11.4 nm. As a result, particle #3 has an estimated core size slightly smaller than 9 nm and a silica shell with thickness around 1 nm. Since it has the same core size as particle #2, the number of dyes per particles remains about the same. However, the quantum enhancement of encapsulated dyes slightly increases from 1.7 to 1.8 due to the fact that the extra silica source further densifies the core matrix and the silica shell further protects the dyes inside the core. As a result, the number of dyes per particle could be increased by expanding the core size while the quantum efficiency could be enhanced by adding a thin layer of blank silica shell. The brightness of a <10 nm particle could be optimized by precisely tuning both the core size and shell thickness through selecting the desired particle growth pathway.

Table A3. Characterizations of particles obtained at different reaction stages. Diameter and brightness are derived from FCS measurements while the # of dye molecules per particle is calculated from steady-state absorbance measurements and FCS concentration results.

	FCS Diameter	# of Dye Molecules per Particle	Relative Quantum Enhancement	Relative brightness compared to free dye
Cy5	1.3nm	1.2	1	1
Particle #1	5.9nm	1.4	1.3	2.2 times
Particle #2	9.0nm	2.6	1.6	3.3 times
Particle #3	11.4nm	2.6	1.7	3.5 times

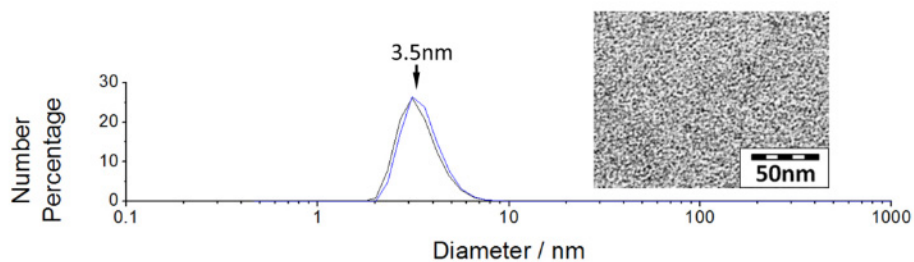


Figure A7. Characterization of aluminosilicate C' dots. DLS size distribution and TEM of ASNPs with average diameter around 3.5 nm.

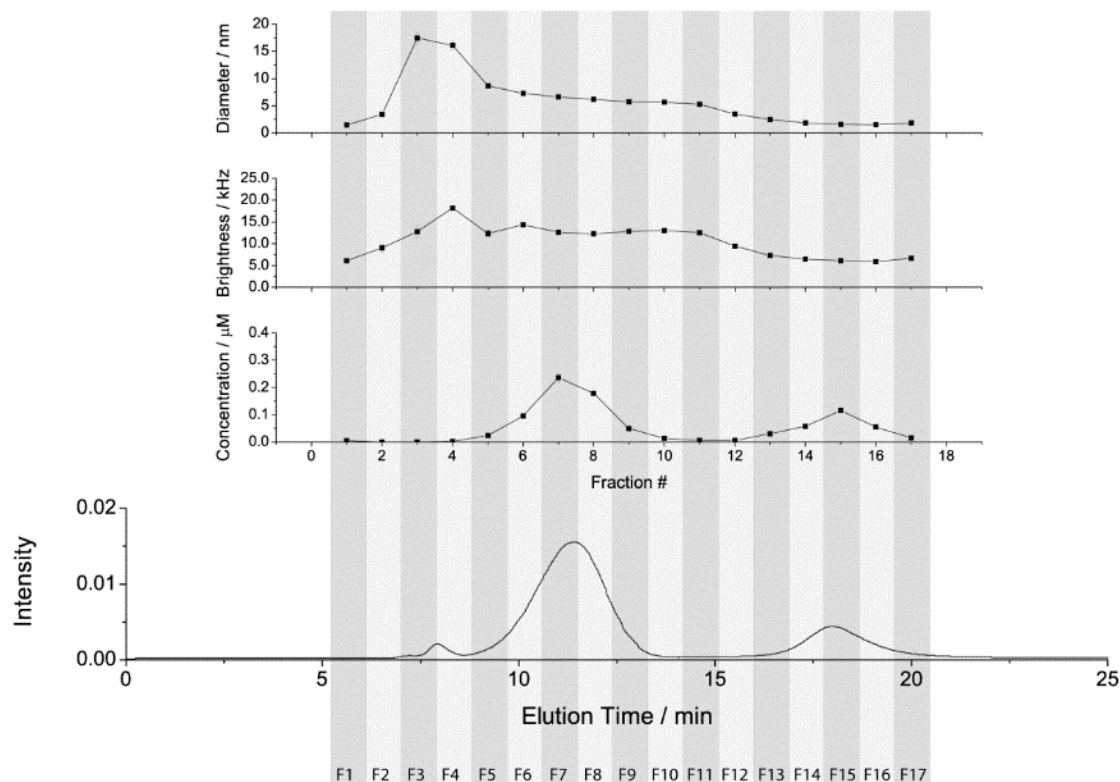


Figure A8. GPC characterization of C' dots right after the synthesis. GPC elugram of as-synthesized Cy5 doped PEGylated SNPs (Cy5-C' dot, no shell, bottom graph) and related FCS characterization results of different fractions (upper three graphs).

In order to assign the peaks in the GPC elugram, a Cy5 doped PEGylated SNP synthesis batch is sorted into different fractions by GPC and each fraction is then subjected to FCS characterization. The average concentration of particles, particle brightness and particle diameter of each fraction are shown in the upper three graphs in Fig. A8. The GPC peak at around 18 min. corresponds to objects in solution with a diameter around 1-2 nm, which in turn corresponds well to the size of free Cy5-silane conjugates or small self-condensed Cy5-silane conjugate clusters. In addition, the brightness per object corresponding to the 18 min. peak is close to the brightness of a single Cy5 fluorophore. We thus conclude that this peak is from free Cy5-silane dye conjugate or Cy5 conjugate clusters which are not encapsulated into particles. The main GPC peak at around 12 min.

corresponds to objects in solution with a diameter of around 6 nm and brightness levels more than two times the brightness of free Cy5 fluorophore. Both parameters correspond well to what is expected for the targeted fluorescent Cy5 encapsulating SNPs. We therefore conclude that the main peak at around 12 min. is from the desired C' dots. The GPC peak at around 6-7 min. corresponds to objects in solution with a fairly big diameter of up to 20 nm. Interestingly, the brightness per object corresponding to this peak is similar to that of a single fluorescent SNP. This peak should therefore not be assigned to objects coming purely from SNP aggregation. Furthermore, although a well-defined small peak can be observed in the GPC equipped with a 275nm detector, this peak corresponds to objects in solution with very low concentration as observed by FCS. This suggests that the larger objects (up to 20 nm) in solution giving rise to this peak with small absorbance at 275nm and low fluorescence may come from impurities of the chemicals used in the synthesis, *e.g.* PEG-silane, but may not have much to do with the particle synthesis reaction.

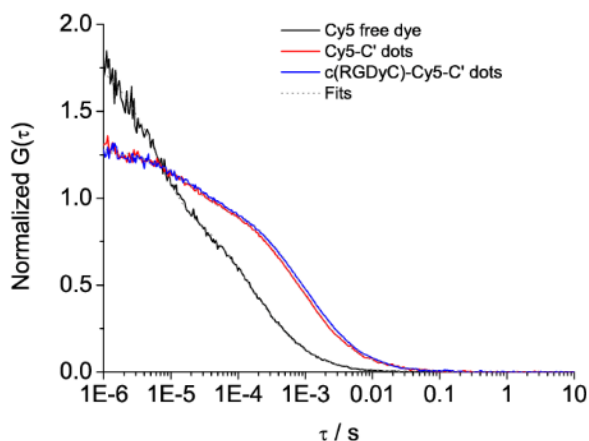


Figure A9. FCS characterizations of c(RGDyC) labeled C' dots. Comparison of FCS measured autocorrelation curves of free Cy5 dye, Cy5-C' dots (core only), and c(RGDyC) functionalized Cy5-C' dots (c(RGDyC)-Cy5-C' dots).

Table A4. Characterization of c(RGDyC) functionalized C' dots.

	FCS Diameter	# of Dye Molecules per Particle	# of c(RGDyC) per Particle
Cy5	1.3nm	-	-
Cy5-C' dots	5.4nm	1.8	-
c(RGDyC)-Cy5-C' dots	6.5nm	1.8	16
c(RGDyC)-core-shell-Cy5-C' dots	7.4nm	1.8	22
c(RGDyC)- Cy5.5-C' dots	6.2nm	1.7	19
c(RGDyC)- Cy5.5-AIC' dots	6.1nm	1.4	12

By combining FCS and optical absorbance measurements, the number of c(RGDyC) ligands per C' dot can be estimated in a similar way as the calculation of the number of dyes per C' dot. For example, the height of the 275nm c(RGDyC) peak in the c(RGDyC)-C' dot optical spectrum (Figure 2.6b in main paper) can be estimated through subtracting from it the absorbance spectrum background obtained from non-c(RGDyC) ligand containing C' dots. Then, by dividing the resulting c(RGDyC) peak height by the extinction coefficient of tyrosine, *e.g.* around $1400 \text{ M}^{-1}\text{cm}^{-1}$, the concentration of total number of c(RGDyC) ligands present in the solution can be calculated. Meanwhile, the concentration of C' dots in solution can be measured by FCS. Finally, by taking the ratio of c(RGDyC) concentration to C' dot particle concentration the number of c(RGDyC) ligands per particle can be estimated. The results suggest that the number of c(RGDyC) ligands on the various C' dots synthesized in this study is between 12 and 22 (see Table A4).

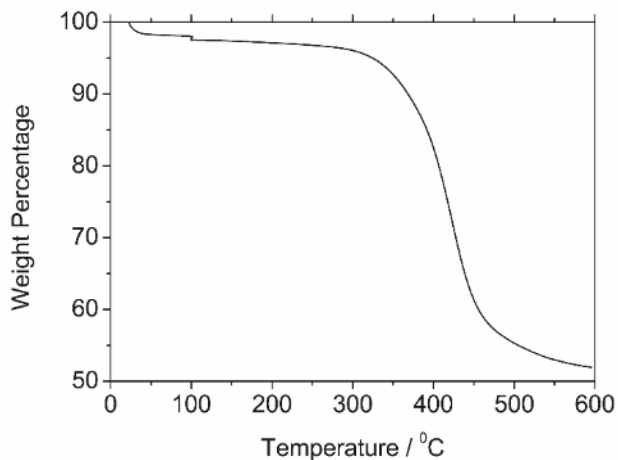


Figure A10. Thermogravimetric analysis of C' dots. TGA curve for a 6 nm (measured by DLS) blank non-fluorescent PEGylated SNP (without fluorophore encapsulation).

A TGA curve for a 6 nm blank non-fluorescent PEGylated SNP (without fluorophore encapsulation) is displayed in Figure A10. The 6 nm average size is the hydrodynamic diameter as measured by DLS. The weight loss up to temperatures of 600°C indicates the presence of organic content in the particle sample. Since this sample synthesis did not include encapsulation steps of a fluorescent dye, the only organic content of the particle stems from the PEG chains on the particle surface. The TGA curve becomes flat at around 600°C suggesting most of the organic content has been burned off leaving inorganic silica as the remaining constituent. From this data it can then be estimated that the weight ratio between silica and PEGs is around 52%:48%. Considering that the 6 nm hydrodynamic diameter PEGylated SNPs have a pure silica core of ~4 nm and a ~1-2 nm PEG layer, the number of PEG chains per particle can be estimated by assuming a silica density of about 1.9-2.2 g/cm³. Results suggest for this simple SNP there are around 80-100 PEG chains on the particle surface. This translates to a PEG density on the particle surface of about 1.7 chains/nm², which is equivalent to an area per PEG-silane head group of around 0.6 nm². The number of PEGs per particle goes up as particle size increases.

Comparing this surface density of PEGs to the number of c(RGDyC) per particle, it can be estimated that on the surface of c(RGDyC)-PEG-C' dots synthesized in this study, there is roughly one c(RGDyC)-labeled PEG chain among every 5-10 unfunctionalized PEG chains (see also main text).

Chapter 3 . Ultra-small Sub-10 nm Near Infrared Fluorescent Mesoporous Silica Nanoparticles

Reprinted with permission from Ma, K.; Sai, H.; Wiesner, U. Ultrasmall Sub-10 Nm Near-Infrared Fluorescent Mesoporous Silica Nanoparticles. *J. Am. Chem. Soc.* **2012**, *134*, 13180–13183. Copyright (2012) American Chemical Society.

3.1 Abstract

Ultra-small sub-10 nm nanoprobe and carriers are of significant interest due to their favorable biodistribution characteristics in *in-vivo* experiments. Here we describe the one-pot synthesis of PEGylated mesoporous silica nanoparticles with a single pore, tunable sizes around 9 nm and narrow size distributions that can be labeled with near infrared dye Cy5.5. Particles are characterized by a combination of transmission electron microscopy, dynamic light scattering, fluorescence correlation spectroscopy, optical spectroscopy, nuclear magnetic resonance spectroscopy and nitrogen sorption/desorption measurements. The possibility to distinguish an “inside” and “outside” may render these particles an interesting subject for further studies in sensing, drug delivery and theranostics applications.

3.2 Introduction

Cancer has become a leading cause of death worldwide, accounting for over 7.5 million deaths in 2008.¹ While one of the most important forms of cancer treatment, chemotherapeutic drugs often also kill healthy cells and cause toxicity to the patient. In the search for improved alternatives nanocarriers have become an emerging platform for cancer therapy enabling drug delivery specifically into tumors.^{2,3} Beginning in the mid-1980s, several types of targeting nanocarriers, based on polymer-protein conjugates and lipids, have successfully reached clinical trials.⁴⁻¹⁰ However, there are still many challenges remaining, including rapid clearance, burst drug release and non-specific uptake.² In order to overcome these challenges, nanocarriers with better properties need to be designed.³ A promising alternative material to polymers is mesoporous silica due to its high-surface area, stability and bio-compatibility. Surface-functionalized mesoporous silica nanoparticles (MSNs) can deliver multiple types of cargo, such as DNA, drug molecules or even quantum dots, into cells and tissues of plants or animals.¹¹⁻²² However, in the current state of development such MSN-based nanocarriers have not yet reached clinical trials. One of the reasons is that silica typically needs a fairly long time to dissolve under physiological conditions, resulting in potential particle accumulation in the body, which may in turn cause long-term toxicity.² Even in cases where MSNs dissolve quite rapidly,²² questions about the dissolution mechanism, bio-distribution and toxicity remain.

One way to overcome these problems is to design nanocarriers with sizes smaller than 10 nm, *i.e.* below what is believed to be the threshold for renal clearance.²³ To this end we recently developed fluorescent core-shell silica nanoparticles referred to as Cornell dots or simply C dots.²⁴⁻²⁶ Synthesized to sizes below 10 nm PEGylated C dots show efficient

renal clearance in animals.²⁷ Carrying cyclic arginine-glycine-aspartic acid (cRGD) peptide ligands as well as radioiodine, an ultrasmall cancer-targeted dual-modality (optical and positron emission tomography, PET) C dot probe for melanoma was indeed recently approved for a first in-human clinical trial.²⁸

In order to endow such ultra-small silica nanoparticles with additional, *e.g.* therapeutic properties for clinical applications it is desirable to develop mesoporous particles with sizes smaller than 10nm. Although recently the size of MSNs has been pushed down to less than 20nm,^{29,30} the synthesis of fluorescent MSNs smaller than 10 nm and with narrow particle size distributions still remains a challenge.

In this paper we present a one-pot synthesis of PEGylated MSNs with sizes precisely tunable around 9nm (Figure 3.1) that have narrow particle size distributions, a single pore and can be labeled with near infrared (NIR) dye Cy5.5. Keys for the successful synthesis of such ultra-small MSNs are (i) fast hydrolysis of the silica (silane) precursors, (ii) slow silica condensation/particle growth, and (iii) particle growth termination via the addition of PEG-silane quenching further silica condensation on the particle surface.

3.3 Experimental section

3.3.1 Materials

All chemicals were used as received. Hexadecyltrimethylammonium bromide (CTAB), dimethyl sulfoxide (DMSO), (3-mercaptopropyl) trimethoxysilane (MPTMS), tetramethyl orthosilicate (TMOS) and 2.0 M ammonium hydroxide in ethanol were purchased from Sigma Aldrich. Methoxy-terminated poly(ethylene glycol) chains (PEG-silane, molecular weight around 500) was purchased from Gelest. Acetic acid was purchased from Mallinckrod. Cy5.5 fluorescent dye was purchased from GE. Absolute anhydrous 99.5% ethanol was purchased from Pharmco-Aaper. De-ionized (D.I.) water was generated using a Millipore Milli-Q system.

3.3.2 Synthesis of sub-10nm ultra-small mesoporous silica nanoparticles.

For the synthesis of 9.3nm mesoporous silica nanoparticles, 0.23mmol of CTAB and 2ml of 0.02M ammonium hydroxide aqueous solution were added into 8ml of D.I. water. Then the solution was stirred at 30°C for 30mins until CTAB fully dissolved. After that, 0.43mmol of TMOS was added into the solution under vigorous stirring and the solution was further stirred at 30°C for 24hs. Following that, 0.21mmol of PEG-silane was added and the solution was stirred at 30°C for another 24hs. In the next step, the temperature was increased from 30°C to 80°C and then stirred at 80°C for another 24hs. Afterwards, the solution was cooled to room temperature and then transferred into a dialysis membrane tube (Pierce, Molecular Weight Cut off 10000). The solution in the dialysis tube was dialyzed in 100ml acid solution (which was a mixture of D.I. water, ethanol and acetic acid

with the volume ratio 1:1:0.007) for 24hs to extract CTAB out of the pores of the particles. This process was repeated three times. The solution was then dialyzed in 2000ml DI-water for another 24hs. This process was again repeated for three times. The particles were finally filtered through a 200nm syringe filter (fisher brand) and then stored. The molar ratio of the reaction was 1 TMOS: 0.53 CTAB : 0.093 ammonium hydroxide : 0.49 PEG-silane : 1292 H₂O. Particles with smaller sizes were synthesized using the same protocol but with lower concentrations of CTAB and TMOS as shown in Table B1. As the concentration of TMOS decreases, the condensation rate of the hydrolyzed silanes decreases. Thus the growth of the particles is slower and the particles become smaller in case all other conditions stay fixed.

3.3.3 Synthesis of Cy5.5 labeled single-pore silica nanoparticles.

Cy5.5 dye with maleimido functionality was conjugated to MPTMS in DMSO. The Cy5.5-silane conjugate was added together with TMOS into the synthesis solution to co-condense into the particles. The molar ratio of Cy5.5-silane conjugate to TMOS is 1: 4855. The remainder of the synthesis protocol was kept the same as for the synthesis of the 9.3nm particles.

3.3.4 Characterization of particle morphology and size.

Transmission electron microscopy (TEM) images were taken using a FEI Tecnai T12 Spirit microscope operated at an acceleration voltage of 120kV. Hydrodynamic particle sizes and size distributions were measured by dynamic light scattering (DLS) using

a Malvern Zetasizer Nano-SZ at 20°C. Each DLS sample was measured three times and results were overlaid, see Figure 3.2a and 4a.

3.3.5 Particle size distribution from TEM image analysis.

In order to obtain size distribution data from TEM images, we measured the diameters of over 100 particles in the same image using a ruler tool provided by the TEM facility software. (Figure B1a depicts this analysis for an image of the 8.2nm particles). The software automatically recorded the diameters of all of the measured particles. Sorting the recorded diameters into bins generated the distribution of the particle size. Considering that the systematic error of the ruler tool can be as high as over 1nm, due to the limited resolution of the TEM, the increment of the bins was set to 2nm in order to optimize the analysis. Furthermore, in order to lower the standard error of each data point, this process was repeated three times for each sample (Figure B1, Figure B2a). The distribution results were then averaged and the standard errors were calculated (Figure B2b). In order to compare the distributions of different samples in one diagram, lines with markers instead of columns were used to display the data (Figure B2b). The average diameters measured by DLS and TEM are compared in Table B2.

3.3.6 TEM characterization of the distribution of the number of pores per particle.

The distribution of the number of pores per particle of each sample was obtained through analyzing over 500 particles on a single TEM image with appropriate magnification. This process was repeated three times for each sample. The distribution results were then averaged and the standard errors were calculated. In order to compare the

distributions of different samples in one diagram, lines with markers instead of columns were used to display the data.

3.3.7 Characterization of the fluorescent properties of Cy5.5 doped mC dots.

Absorption-matched samples were prepared by appropriate dilution of Cy5.5 particles or Cy5.5 free dye with water and measured in quartz cuvettes using a Varian Cary 5000 spectrophotometer (Varian, Palo Alto, CA) (Figure B3a). The extinction coefficient of Cy5.5 ($250,000 \text{ M}^{-1}\text{cm}^{-1}$) was used to calculate the concentration of the dyes in the samples.

Fluorescence measurements of absorption-matched samples were performed on a Photon Technologies International Quantamaster spectrofluorometer (PTI, Birmingham, NJ) in order to estimate the quantum efficiency enhancement per dye of the Cy5.5 dyes in the particles (Figure B3b).

The absorption-matched samples were further measured on a home-built FCS using HeNe 633 nm excitation to characterize fluorescent properties, such as brightness per particle, hydrodynamic diameter and concentration of particles as described in reference 26. The FCS instrument was calibrated for size prior to all measurements. The number of dyes per particle was derived from the ratio between the concentration of dyes measured by absorption spectra and the concentration of particles measured by FCS of the same sample. Results are shown in Table B3.

The slightly elevated number of dyes (#dyes) per diffusing species from FCS measurements of free Cy5.5 dye may be due to a small degree of aggregation of

hydrophobic dye Cy5.5 in water. It should be noted, however, that it is within the error bar of the measurement.

3.3.8 Liquid ^1H NMR analysis.

All liquid ^1H NMR spectra were measured on a Varian Mercury 300 spectrometer. Two samples of the 9.3nm particles were used in liquid ^1H NMR analysis. The first sample was dialyzed into water immediately after synthesis without acid extraction. The second sample was washed following the regular washing steps described in the synthesis protocol (first washed in acid to extract CTAB and later in water). Afterwards, the samples were dried under vacuum and then added into dimethyl sulfoxide- d_6 (DMSO- d_6 , 99.96 % d , Sigma-Aldrich) at an approximate concentration of 5 wt%. The fully-washed sample initially showed some degree of sedimentation; however the sediments slowly redispersed after several hours of storage. Spectra were taken immediately after addition and after 2 days for comparison. Results showed no significant differences except for signal intensity (data not shown). Control samples, *i.e.* CTAB and free PEG-silane, were dissolved in DMSO- d_6 and were measured immediately after dissolution.

The ^1H NMR spectra of the non-acid-extracted sample showed distinct peaks at chemical shifts corresponding to CTAB (0.8 ppm, 1.3 ppm and 3.0 ppm, compare spectra of CTAB and particles in Figures B5a and b), as well as peaks corresponding to PEG chains (3.5 ppm, compare spectra of particles and parent PEG-silane in Figures B5b and d). In comparison, there was no detectable signal from CTAB in the spectra of the fully-washed, CTAB extracted sample (Figure B5c). This demonstrates the successful removal of CTAB via acid extraction.

Successful PEGylation can be inferred from broad signals of protons of PEG chains in the fully-washed sample (Figure B5c), especially the peaks at 0.5 ppm and 1.5 ppm, which correspond to the α - and β -protons next to the silicon center of the PEG-chain. The line width broadening relative to the spectrum of the parent PEG-silane (Figure B5d) indicates limited mobility of these protons, which is attributed to the formation of covalent bonds between PEG chains and the silica particle surface.

3.3.9 Nitrogen sorption/desorption analysis

Nitrogen sorption/desorption measurements were performed on a Micromeritics ASAP 2020 instrument at 77K. Before the measurements, 9.3nm fully-washed particles were first dried under vacuum and then subjected to a plasma etch treatment for different durations of time. Multiple cycles of plasma treatments were performed on a Harrick Plasma Cleaner with 1 min (or in one case 3 mins, see Figure B7) cycle duration, to prevent sample heating.

As demonstrated in Figure B6, without plasma treatment the sample did not show any accessible surface area. This most likely is due to the PEG chains on the particle surface making accurate isotherm measurements difficult, consistent with earlier reports.¹⁻² As the duration of plasma treatment increased, more surface area became accessible.

In order to corroborate the TEM images on pore structure and determine pore size distribution, the duration of plasma treatment was varied from 0 to 60 mins and the adsorption isotherms were used to calculate BJH pore size and pore size distribution, surface area and pore volume (Figure B7). With increasing plasma treatment duration (15, 30, and 60 mins) surface area as well as pore volume increased. At the same time the

average pore diameter increased from 2.8nm (15 mins) to 2.9 nm (30 mins) to 3.0nm (60 min). All of the plasma treated samples gave well defined pore sizes and pore size distributions, consistent with TEM analysis (Figure B7b).

3.4 Results and discussion

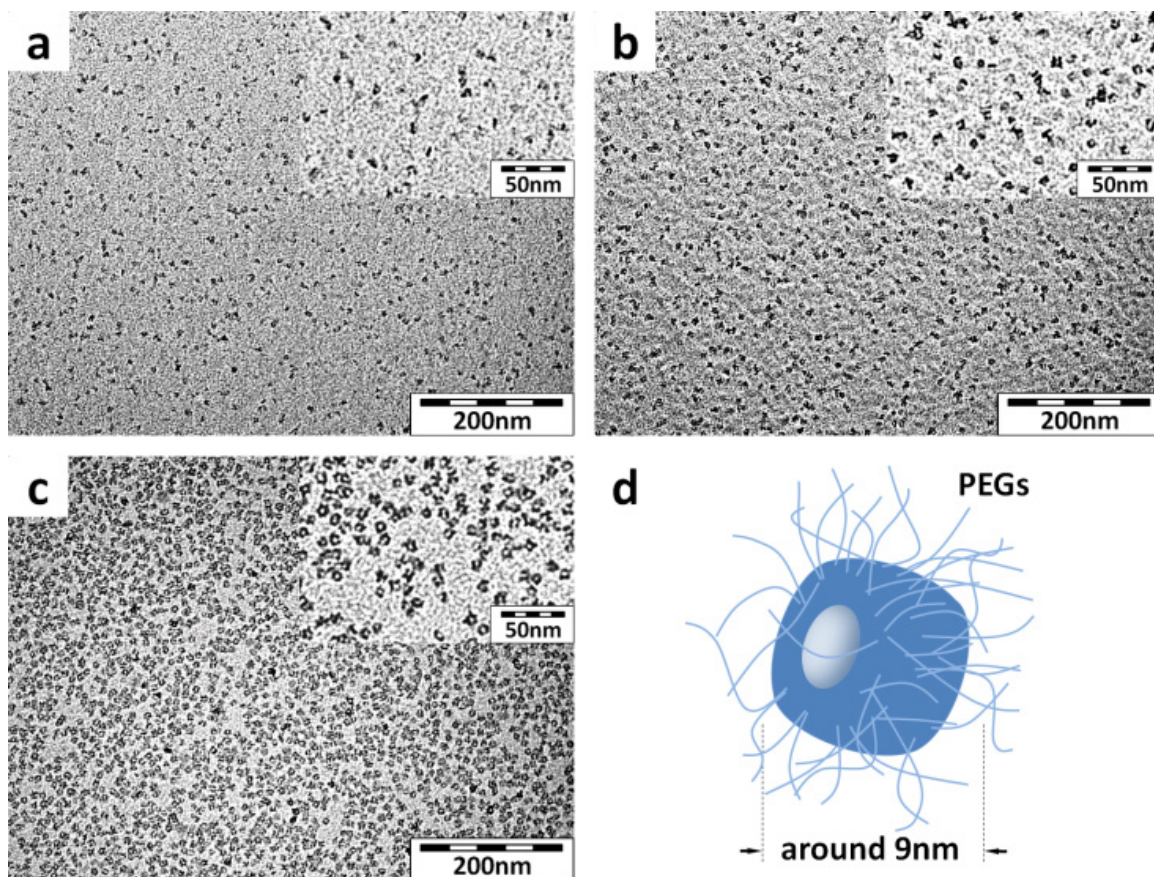


Figure 3.1. TEM images of silica particles with different diameters. (a) 6.6nm, (b) 8.2nm and (c) 9.3nm. Inserts display images of the same samples but at higher magnification. (d) Schematic of a single-pore MSN coated with PEG chains.

As detailed in the Supplementary information section particle synthesis was performed near room temperature (30°C) in aqueous solution in the presence of hexadecyltrimethyl ammonium bromide (CTAB) as structure directing agent, with tetramethyl orthosilicate (TMOS) as silica source and ammonium hydroxide as base

catalyst. PEG-silane was added directly into the synthesis batch to quench particle formation. A post-synthesis heating step and subsequent solution work-up, including acid extraction of CTAB via dialysis, provided the final particles.

While tetraethyl orthosilicate (TEOS) is commonly used in the synthesis of MSNs, here TMOS was chosen as the silica source.³⁰ The hydrolysis rate of TMOS is much faster than that of TEOS and its solubility in water is higher. As a result, instead of forming a second oil-phase and gradually hydrolyzing at the oil droplet-water interface like in the case of TEOS,^{29,31} TMOS directly dissolves in water and hydrolyzes once added into the reaction. An accelerated completion of the hydrolysis process helps initiating/nucleating more MSN growth in the presence of CTAB micelles over a smaller period of time thus leading to smaller particles and better control over particle size distribution. Lowering the condensation rate by moving to near room temperature conditions or lowering the concentration of TMOS and CTAB results in slower particle growth and smaller particles. By carefully optimizing the system, we found conditions where the particles grow from around 2nm to sizes larger than 10nm within a convenient time window. Particle growth is terminated by quenching further condensation on the particle surface through addition of PEG-silane. A final heat-treatment at 80°C at the end of the synthesis improves particle stability. Through the PEGylation step as part of the one-pot synthesis the resulting sub-10nm MSNs are already sterically stabilized, a prerequisite for working in many biological environments.^{32,33}

In order to demonstrate the kind of particle size and size distribution control achievable by this approach Figure 3.1a-c shows transmission electron microscopy (TEM) results on particles from three synthesis batches obtained from varying synthesis conditions

(see Table B1 in Supplementary information) leading to increasing particle size in the direction from a-c. The smaller magnification images illustrate the high degree of homogeneity in particle size while the higher resolution images in the insets reveal details of particle structure. In all cases TEM results suggest that silica has grown around an individual pore formed by CTAB template. An illustration of this type of structure, including the PEG chains on the outside of the particles, is depicted in Figure 3.1d. While in Figure 3.1a single pore particle formation is largely incomplete, Figure 3.1b already displays side-on as well as head-on particles. Particles in Figure 3.1c exhibit the most well-defined structure (for additional particle images see Supplementary information). Figure 3.2a shows results of three independent size measurements for each of the three particle batches by dynamic light scattering (DLS). The data sets are very consistent and provide average hydrodynamic diameters of 6.6nm, 8.2nm and 9.3nm for particles in Figure 3.1a-c, respectively. Alternatively, we determined particle size and size distribution by quantitative TEM image analysis (for details see Supplementary information). TEM average diameters from data in Figure 3.2b are 5.7nm, 7.3nm, and 8.9 nm, *i.e.* slightly smaller than from DLS. Both DLS and TEM results reveal fairly narrow size distributions and absence of any significant aggregation behavior. Smaller average diameters from TEM are expected, as this technique, in contrast to DLS, is insensitive to the PEG layer and water molecules dragged with it. As a result in the following we will use DLS diameters as descriptors of the different particles.

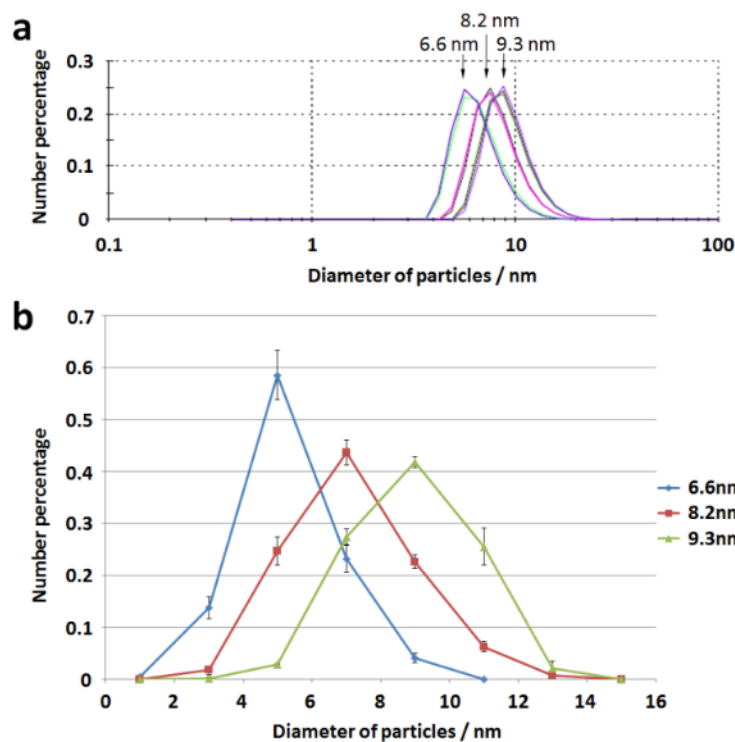


Figure 3.2. Size distribution of mesoporous particles. Size distribution of particles was determined by (a) DLS and (b) TEM image analysis. In DLS each data set was measured three times per batch.

TEM images also allowed analyzing the distribution of the number of pores per particle. As shown in Figure 3.3, for around 90% of the 6.6nm particles single-pore particle formation is incomplete (referred to as “no or half” pore particles in Figure 3.3). As the diameter increases to 8.2nm, the percentage of incomplete single-pore particles significantly drops from around 90% to below 30%. Increasing the diameter to 9.3nm finally results in a fairly narrow distribution of the number of pores per particle in which more than 70% are single-pore particles. This distribution already is quite symmetric. Further increasing particle size most likely would bias the distribution towards an increase in the number of particles with more than one pore. We therefore speculate that the

optimized hydrodynamic particle diameter for achieving single-pore particles in our synthesis should be close to the 9.3nm value of the third synthesis batch.

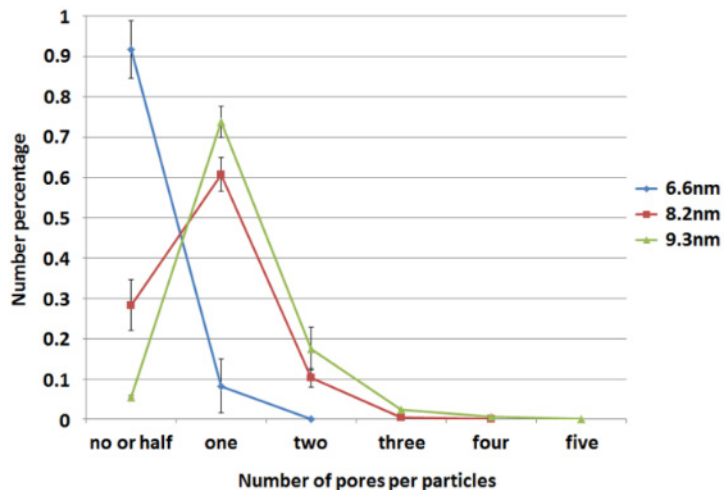


Figure 3.3. Distribution of number of pores per particle. Distribution of number of pores per particle was determined from TEM image analysis; each data point is obtained by averaging three independent analyses.

Particles were further characterized by liquid $^1\text{H-NMR}$ to demonstrate successful CTAB removal by acetic acid extraction and the presence of PEG chains on the particle surface (for details see Supplementary information). In order to independently confirm TEM results on the pore structure we performed nitrogen sorption/desorption measurements on the 9.3 nm particles (see Supplementary information). While such measurements are challenging because of the presence of the PEG chains, working with plasma treated sample batches clearly confirmed the existence of well-defined pores with sizes between 2.8 and 3 nm, depending on the plasma treatment duration.

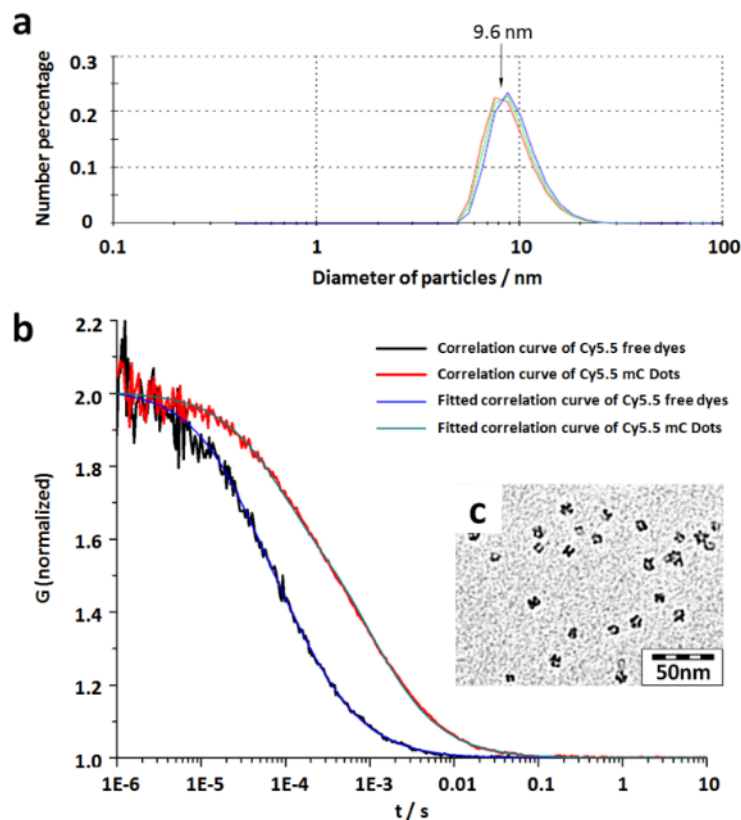


Figure 3.4. Characterization of Cy5.5 labeled mC dots. (a) DLS size measurements. (b) Normalized FCS curves for Cy5.5 free dye (black and blue lines) and Cy5.5 containing mC dots (red and green lines). (c) TEM image of the Cy5.5 mC dots.

In order to visualize such <10 nm sized single-pore silica nanoparticles, in particular in biological environments, labeling with near infrared (NIR) dyes is highly desirable.^{28,34} To this end we slightly modified the synthesis protocol for the 9.3nm particles by simultaneously adding silane conjugated Cy5.5 and TMOS into the reaction mixture (for details see Supplementary information). We will refer to these dye-labeled mesoporous silica nanoparticles as mC dots. Cy5.5 has absorption and emission maxima around 675nm and 700nm, respectively, thus limiting interference from background fluorescence in biological tissue.³⁴ Adding Cy5.5-silane conjugate to the reaction left the particle architecture largely unchanged. The DLS derived average hydrodynamic diameter of this

sample increased to 9.6nm as compared to 9.3 nm for the unlabeled particle (Figure 3.4a). Furthermore, most of the particles still showed single-pore architecture (Figure 3.4c). In order to verify that these particles carry a fluorescent label we used fluorescent correlation spectroscopy (FCS) for further particle characterization (Figure 3.4b). This technique is similar to DLS but uses the fluorescence of the diffusing moiety rather than the scattered light to generate auto-correlation data. Figure 3.4b compares FCS results from free Cy5.5 dye and Cy5.5 labeled single-pore silica nanoparticles. As expected for the slower diffusing particle its curve is shifted to longer times. From the correlation time hydrodynamic diffusion coefficients can be derived.²⁶ They are 1.5 nm and 10.2 nm for free dye and particle, respectively. FCS may thus slightly bias the true particle distribution to larger sizes as not every particle may carry a dye. It should be noted, however, that the differences are rather small (10.2nm from FCS vs. 9.6nm from DLS). As explained in detail in a previous publication,²⁶ from the amplitude $G(0)$ of the FCS autocorrelation one can derive the dye/particle concentration in solution while the optical detector count rate per diffusing species provides a direct measure of its brightness. Furthermore, in combination with static optical and fluorescence spectroscopy, FCS helps to provide information about number of dyes per particle, per dye enhancement over free dye in aqueous solution, as well as particle brightness (for details see Supplementary information). From analysis of spectrophotometer and spectrofluorometer data in combination with FCS concentration information on the free dye and particles, there are around 2.6 Cy5.5 dyes in one particle and the quantum enhancement of the Cy5.5 dye in the particles versus in aqueous solution is around 1.3 (Figure B3). Thus a Cy5.5 doped mC dot is around 3.4 times brighter than a free Cy5.5 dye. This is consistent with direct brightness comparisons from FCS optical

detector count rates (Table B3). It is further consistent with results of equivalent measurements on Cy5 containing ~7 nm C dots.²⁸ Considering that just conjugation to a silane alone can already have a positive effect on the brightness of Cy dyes,³⁴ this analysis remains inconclusive on whether in the present case the Cy5.5 dyes are fully incorporated inside the silica walls or whether they sit at or on the silica surface of the mC dots. Since the final PEG-silane treatment is expected to cover the particle surface with an additional silica surface layer, the latter is unlikely.

It is interesting to note that the single-pore silica nanoparticles described here have an “inside” and an “outside”. As has been shown by others, inside and outside surfaces of such materials can be distinguished when additional conjugation chemistry is desired, *e.g.* to bind targeting or pharmaceutical moieties.³⁵ For example during the PEGylation process the particle pores are occupied by structure directing CTAB molecules. Therefore, in contrast to the outer silica surface, it is expected that the PEG-silane coating has a significantly diminished probability of attaching to the (inside) surface of the pores. After CTAB extraction the unoccupied inside of the pore walls thus can be used for additional silane chemistry to conjugate specific moieties, which could be complementary to what is used on the outside of the PEGchains. Being in a similar size regime it is this ability to distinguish between the inside and the outside, and the larger overall surface area available for conjugation chemistry, which distinguishes these single-pore silica nanoparticles (or mC dots) from conventional C dots. Future work may demonstrate how this feature can be used as an advantage in areas like sensing, drug delivery and theranostics.

3.5 Acknowledgements

K. M. gratefully acknowledges NSF for the financial support by Grant MPS/DMR-1008125. The authors acknowledge the Cornell Center for Materials Research (CCMR) and the Nanobiotechnology Center (NBTC) of Cornell University for the use of facilities. The authors also gratefully acknowledge S. K. Iyer, J. Drewes, Y. Sun and Z. Li of Cornell University and Dr. T. Suteewong of Memorial Sloan-Kettering Cancer for helpful discussions and kind experiment assistance.

3.6 References

- (1) Globocan 2008, *IARC*, **2010**
- (2) Peer, D.; Karp, J. M.; Hong, S.; Farokhzad, O. C.; Margalit, R.; Langer, R. Nanocarriers as an Emerging Platform for Cancer Therapy. *Nat. Nanotech.* **2007**, *2*, 751–760.
- (3) Schroeder, A.; Heller, D. A.; Winslow, M. M.; Dahlman, J. E.; Pratt, G. W.; Langer, R.; Jacks, T.; Anderson, D. G. Treating Metastatic Cancer with Nanotechnology. *Nat. Rev. Cancer* **2012**, *12*, 39–50.
- (4) Couvreur, P.; Kante, B.; Grislain, L.; Roland, M.; Speiser, P. Toxicity of Polyalkylcyanoacrylate Nanoparticles II: Doxorubicin-Loaded Nanoparticles *J. Pharm. Sci.* **1982**, *71*, 790–792.
- (5) Batrakova, E. V.; Dorodnych, T. Y.; Klinskii, E. Y.; Kliushnenkova, E. N.; Shemchukova, O. B.; Goncharova, O. N.; Arjakov, S. A.; Alakhov, V. Y.; Kabanov, A. V. Anthracycline Antibiotics Non-Covalently Incorporated into the Block Copolymer Micelles: In Vivo Evaluation of Anti-Cancer Activity. *J. Cancer* **1996**, *74*, 1545–1552.
- (6) Tolcher, A. W.; Sugarman, S.; Gelmon, K. A.; Cohen, R.; Saleh, M.; Isaacs, C.; Young, L.; Healey, D.; Onetto N.; Slichenmyer, W. Randomized Phase II Study of BR96-Doxorubicin Conjugate in Patients With Metastatic Breast Cancer. *J. Clin. Oncology* **1999**, *17*, 478–484.
- (7) Nakanishi, T.; Fukushima, S.; Okamoto, K.; Suzuki, M.; Matsumura, Y.; Yokoyama, M.; Okano, T.; Sakurai, Y.; Kataoka, K. Development of the Polymer Micelle Carrier System for Doxorubicin. *J. Control. Release* **2001**, *74*, 295–302.

- (8) Torchilin, V. P. Nat. Recent Advances with Liposomes as Pharmaceutical Carriers. *Rev. Drug Discov.* **2005**, *4*, 145–160.
- (9) Duncan, R. Polymer Conjugates as Anticancer Nanomedicines. *Nat. Rev. Cancer* **2006**, *6*, 688–701.
- (10) Torchilin, V. P. Micellar Nanocarriers: Pharmaceutical Perspectives. *Pharm. Res.* **2007**, *24*, 1–16.
- (11) Luo, D.; Saltzman, W. M. Enhancement of Transfection by Physical Concentration of DNA at the Cell Surface. *Nat. Biotechnol.* **2000**, *18*, 893–895.
- (12) Radu, D. R.; Lai, C. Y.; Jęftinija, K.; Rowe, E. W.; Jęftinija, S.; Lin, V. S. Y. A Polyamidoamine Dendrimer-Capped Mesoporous Silica Nanosphere-Based Gene Transfection Reagent. *J. Am. Chem. Soc.* **2004**, *126*, 13216–13217.
- (13) Vivero-Escoto, J. L.; Slowing, I. i.; Trewyn, B. G. and Lin, V. S. Y. Mesoporous Silica Nanoparticles for Intracellular Controlled Drug Delivery. *Small* **2010**, *6*, 1952–1967.
- (14) Rosenholm, J. M.; Peuhu, E.; Eriksson, J. E.; Sahlgren C.; Linden, M. Targeted Intracellular Delivery of Hydrophobic Agents Using Mesoporous Hybrid Silica Nanoparticles as Carrier Systems. *Nano Lett.* **2009**, *9*, 3308–3331.
- (15) Du, L.; Liao, S.; Khatib, H. A.; Stoddart, J. F.; Zink, J. I. Controlled-Access Hollow Mechanized Silica Nanocontainers. *J. Am. Chem. Soc.* **2009**, *131*, 15136–15142.
- (16) Bharali, D. J.; Klejbor, I.; Stachowiak, E. K.; Dutta, P.; Roy, I.; Kaur, N.; Bergey, E. J.; Prasad, P. N.; Stachowiak, M. K. Organically Modified Silica Nanoparticles: A Nonviral Vector for In Vivo Gene Delivery and Expression in The Brain. *Proc. Natl Acad. Sci. USA* **2005**, *102*, 11539–11544.

- (17) Hu, S.; Liu, T.; Huang, H.; Liu, D.; Chen, S. Magnetic-Sensitive Silica Nanospheres for Controlled Drug Release. *Langmuir*, **2008**, *24*, 239–244.
- (18) Roy, I.; Ohulchansky, T. Y.; Bharali, D. J.; Pudavar, H. E.; Mistretta, R. A.; Kaur, N.; Prasad, P. N. Optical Tracking of Organically Modified Silica Nanoparticles as DNA Carriers: A Nonviral, Nanomedicine Approach for Gene Delivery. *Proc. Natl Acad. Sci. USA* **2005**, *102*, 279–284.
- (19) Lee, J. E.; Lee, N.; Kin, T.; Kim, J. and Hyeon, T. Multifunctional Mesoporous Silica Nanocomposite Nanoparticles for Theranostic Applications. *Acc. Chem. Res.* **2011**, *44*, 893–902.
- (20) Torney, F.; Trewyn, B. G.; Lin, V. S. L.; Wang, K. Mesoporous Silica Nanoparticles Deliver DNA and Chemicals into Plants. *Nat. Nanotech.* **2007**, *2*, 295–300.
- (21) Piao, Y.; Burns, A.; Kim, J.; Wiesner, U. and Hyeon, T. Designed Fabrication of Silica-Based Nanostructured Particle Systems for Nanomedicine Applications. *Adv. Funct. Mater.* **2008**, *18*, 3745–3758.
- (22) Ashley, C. E.; Carnes, E. C.; Phillips, G. K.; Padilla, D.; Durfee, P. N.; Brown, P. A.; Hanna, T. N.; Liu, J.; Phillips, B.; Carter, M. B.; Carroll, N. J.; Jiang, X.; Dunphy, D. R.; Willman, C. L.; Petsev, D. N.; Evans, D. G.; Parikh, A. N.; Chackerian, B.; Wharton, W.; Peabody, D. S.; Brinker, C. F. The Targeted Delivery of Multicomponent Cargos to Cancer Cells by Nanoporous Particle-Supported Lipid Bilayers. *Nat. Mater.* **2011**, *10*, 389–397.
- (23) Choi, H. S.; Liu, W.; Misra, P.; Tanaka, E.; Zimmer, J. P.; Ipe, B. I.; Bawendi, M. G.; Frangioni, J. V. Renal Clearance of Quantum Dots. *Nat. Nanotech.* **2007**, *25*, 1165–1170.

- (24) Ow, H.; Larson, D.; Srivastava, M.; Baird, B.; Webb, W.; Wiesner, U. Bright and Stable Core–Shell Fluorescent Silica Nanoparticles. *Nano Lett.* **2005**, *5*, 113–117.
- (25) Burns, A.; Ow, H.; Wiesner, U. Fluorescent Core-Shell Silica Nanoparticles: Towards "Lab on a Particle" Architectures for Nanobiotechnology. *Chem. Soc. Rev.* **2006**, *35*, 1028–1042.
- (26) Larson, D. R.; Ow, H.; Vishwasrao, H. D.; Heikal, A. A.; Wiesner, U.; Webb, W. W. Silica Nanoparticle Architecture Determines Radiative Properties of Encapsulated Fluorophores. *Chem. Mater.* **2008**, *20*, 2677–2684.
- (27) Burns, A.; Vider, J.; Ow, H.; Herz, E.; Penate-Medina, O.; Baumgart, M.; Larson, S. M.; Wiesner, U.; Bradbury, M. Fluorescent Silica Nanoparticles with Efficient Urinary Excretion for Nanomedicine. *Nano Lett.* **2009**, *9*, 442–448.
- (28) P. B.; Schaer, D.; Ow, H.; Burns, A.; DeStanchina, E.; Longo, V.; Herz, E.; Iyer, S.; Wolchok, J.; Larson, S. M.; Wiesner, U. and Bradbury M. Multimodal Silica Nanoparticles are Effective Cancer-Targeted Probes in a Model of Human Melanoma. *J Clin Invest.* **2011**, *121*, 2768–2780.
- (29) Lu, F.; Wu, S.; Hung, Y.; Mou C. Size Effect on Cell Uptake in Well-Suspended, Uniform Mesoporous Silica Nanoparticles. *Small* **2009**, *5*, 1408–1413.
- (30) Urata, C.; Aoyama, Y.; Tonegawa, A.; Yamauchi, Y.; Kuroda, K. Dialysis Process for The Removal of Surfactants to Form Colloidal Mesoporous Silica Nanoparticles. *Chem. Commun.* **2009**, 5094–5096.
- (31) Wang, J.; Sugawara-Narutaki, A.; Fukao, M.; Yokoi, T.; Shimojima, A.; Okubo, T. Two-Phase Synthesis of Monodisperse Silica Nanospheres with Amines or Ammonia

Catalyst and Their Controlled Self-Assembly. *ACS Appl. Mater. Interfaces* **2011**, *3*, 1538–1544.

- (32) Lin, Y.; Abadeer, N.; Haynes C. L. Stability of Small Mesoporous Silica Nanoparticles in Biological Media. *Chem. Commun.* **2011**, *47*, 532–534.
- (33) Lin, Y.; Haynes, C. L. Impacts of Mesoporous Silica Nanoparticle Size, Pore Ordering, and Pore Integrity on Hemolytic Activity. *J. Am. Chem. Soc.* **2010**, *132*, 4834–4842.
- (34) Herz, E.; Ow, H.; Bonner, D.; Burns, A.; Wiesner, U. Dye Structure–Optical Property Correlations in Near-Infrared Fluorescent Core-Shell Silica Nanoparticles. *J. Mater. Chem.* **2009**, *19*, 6341–6347.
- (35) Slowing, I. I.; Vivero-Escoto, J. L.; Wu, C. W.; Lin, V. S. Y. Mesoporous Silica Nanoparticles as Controlled Release Drug Delivery and Gene Transfection Carriers. *Adv. Drug Delivery Rev.* **2008**, *60*, 1278–1288.

Appendix B: Supplementary information for Chapter 3

Table B1. Synthesis condition of particles with different size

	Concentration of CTAB	concentration of TMOS
6.6nm	0.006M	0.011M
8.2nm	0.012M	0.022M
9.3nm	0.023M	0.043M

Table B2. Comparison of the diameters measured by DLS and TEM

Sample	DLS diameters	TEM diameters
6.6nm	6.6nm	5.7nm
8.2nm	8.2nm	7.3nm
9.3nm	9.3nm	8.9nm

Table B3. FCS characterizations of mC dots. Both, average value and standard deviation, are displayed.

	Hydrodynamic diameter	#dyes/particle	Brightness/particle
Cy5.5 free dyes	1.5nm \pm 0.2	1.07 \pm 0.11	1452 kHz \pm 21kHz
Cy5.5 mC dots	10.2nm \pm 0.4	2.60 \pm 0.02	5322 kHz \pm 29kHz

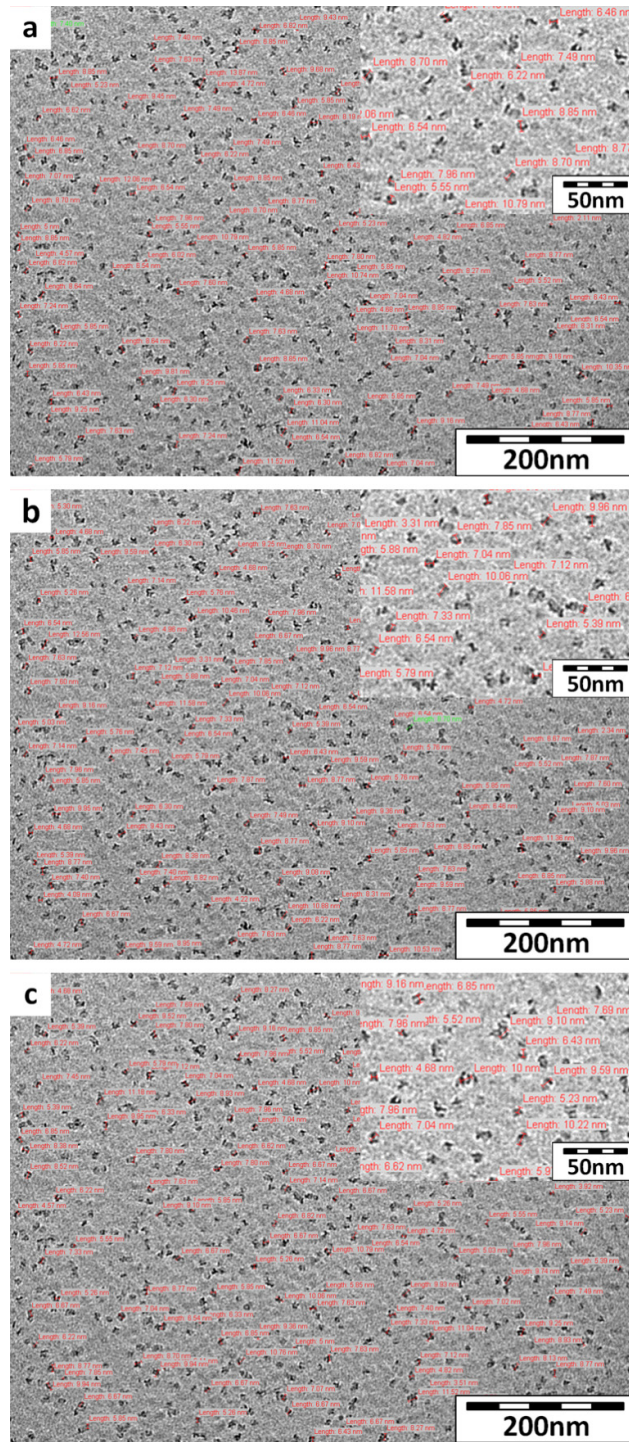


Figure B1. Size analysis of particles using TEM images. TEM images of 8.2nm sample used to analyze the size distribution of particles. (a), (b), (c) depict three separate size determinations using the same TEM image. Inserts display images of the same images but at higher magnification.

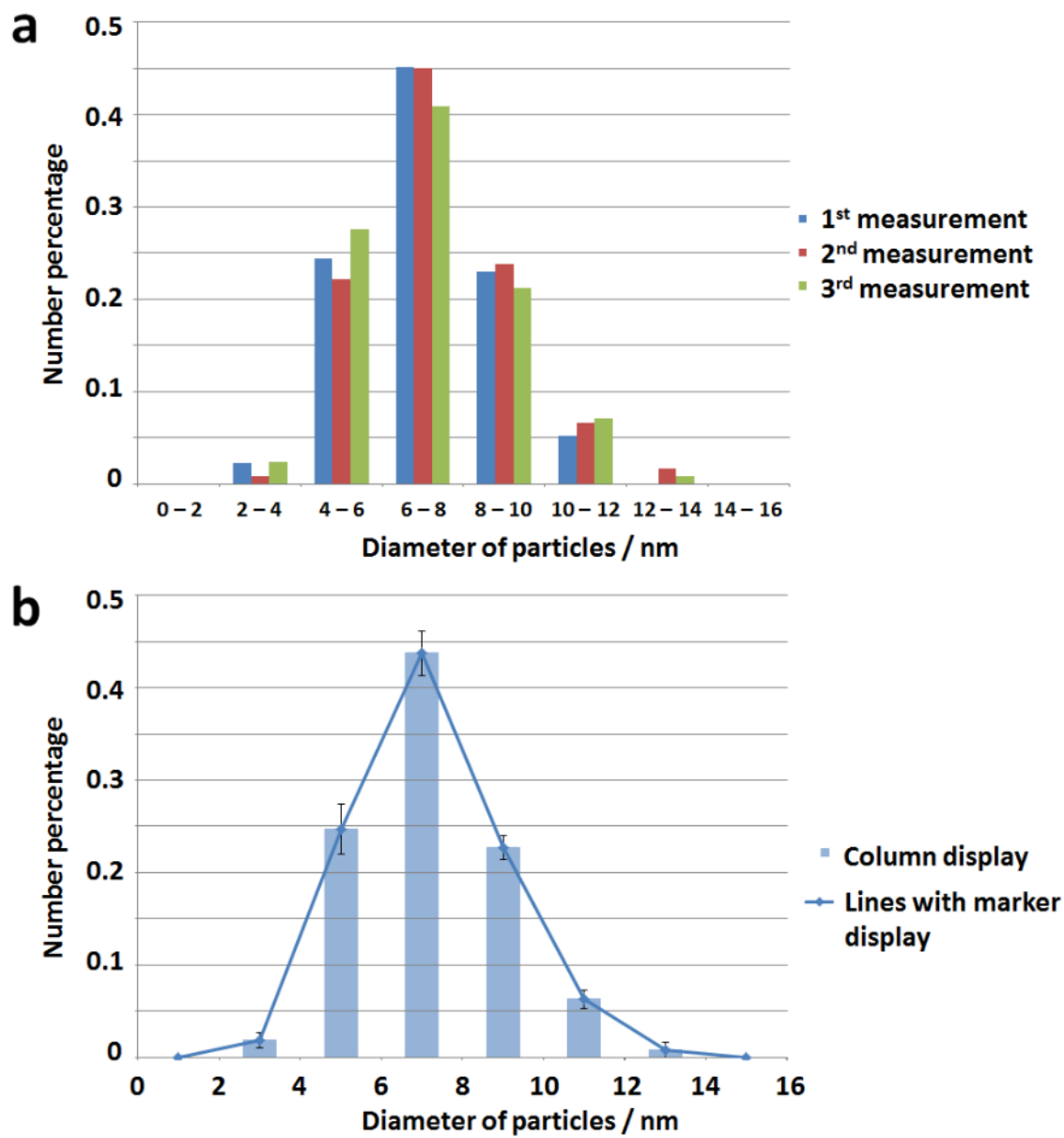


Figure B2. Diameter distribution of 8.2nm sample measured by TEM. (a) Results of three individual measurements using the same TEM image. (b) Final averaged distribution with standard errors displayed for comparison by both columns and lines with markers.

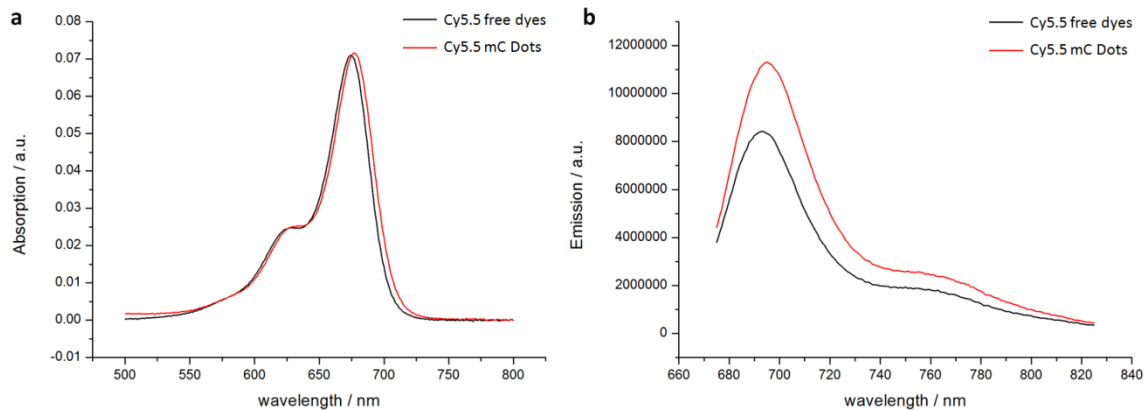


Figure B3. Optical characterization of mC dots. Absorption (a) and emission (b) spectra of Cy5.5 free dye (black line) and Cy5.5 labeled mC dots (red line).

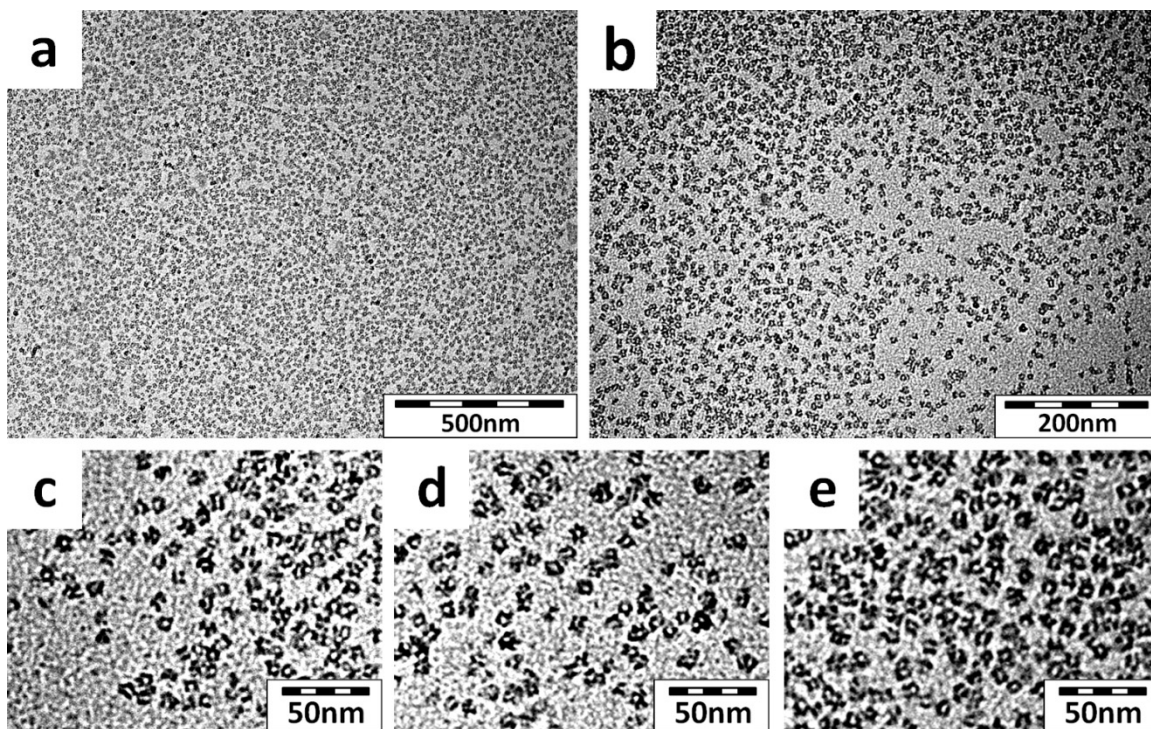


Figure B4. TEM images of 9.3nm particles at different magnification.

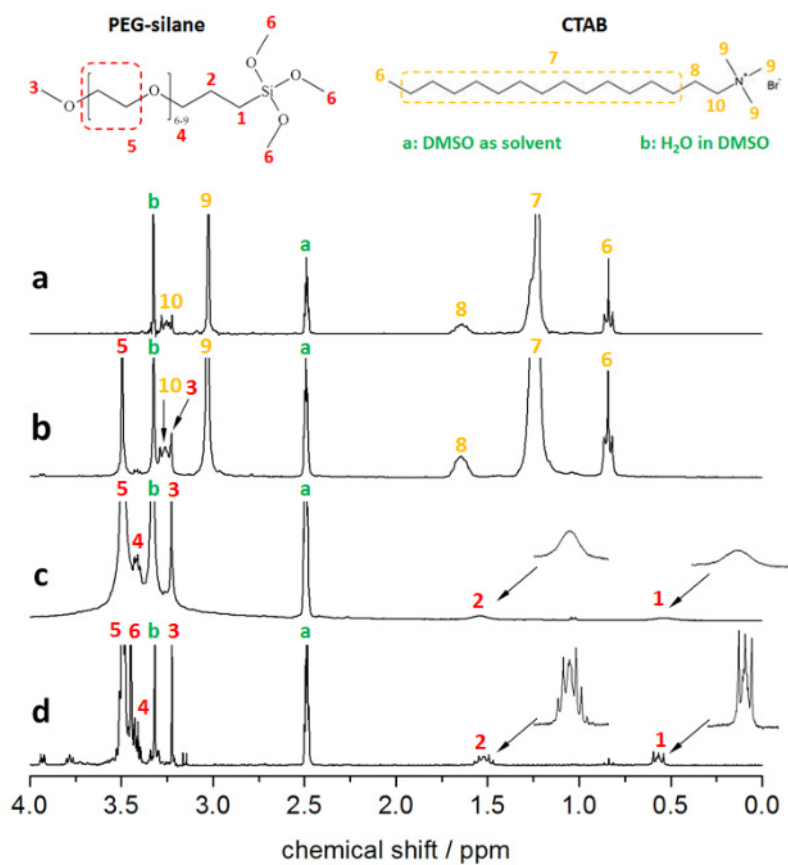


Figure B5. Liquid ^1H NMR spectra. Liquid ^1H NMR spectra of (a) CTAB, (b) 9.3nm particles washed with water without acid extraction, (c) 9.3nm particles first washed with acid to extract CTAB and then washed with water, (d) free parent PEG-silane.

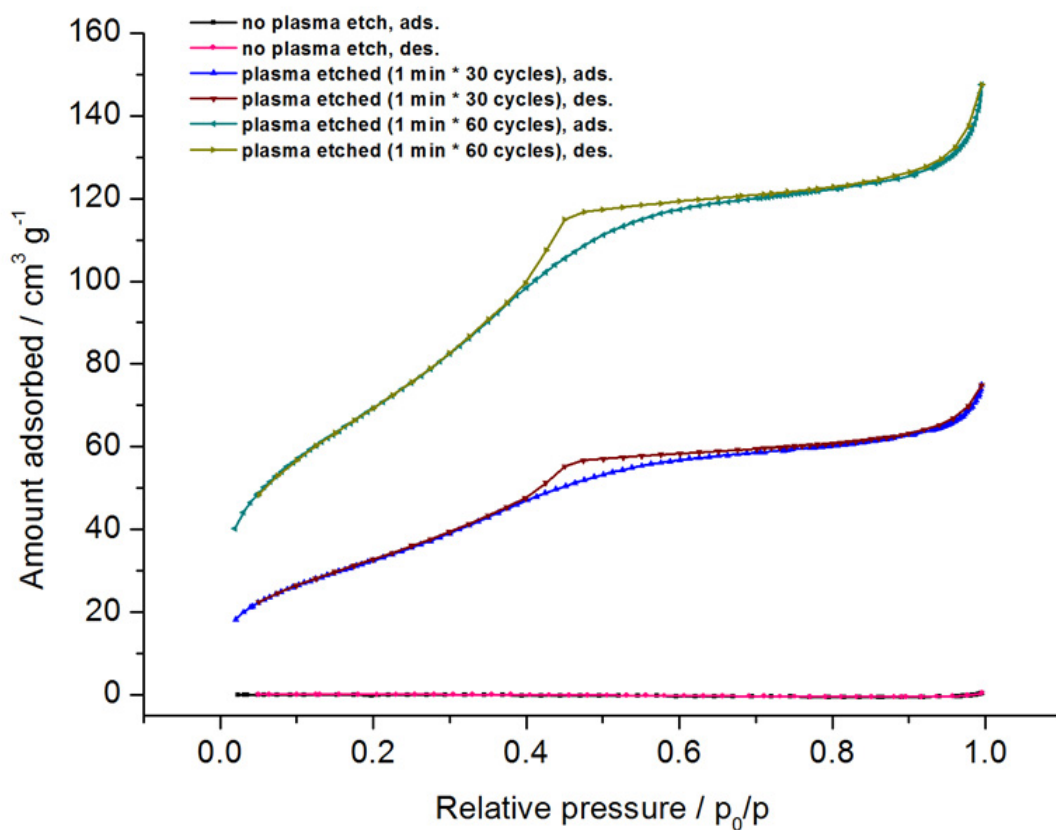


Figure B6. N₂ sorption isotherms of 9.3nm single-pore particles. N₂ sorption isotherms of 9.3nm particles with different durations of plasma treatment.

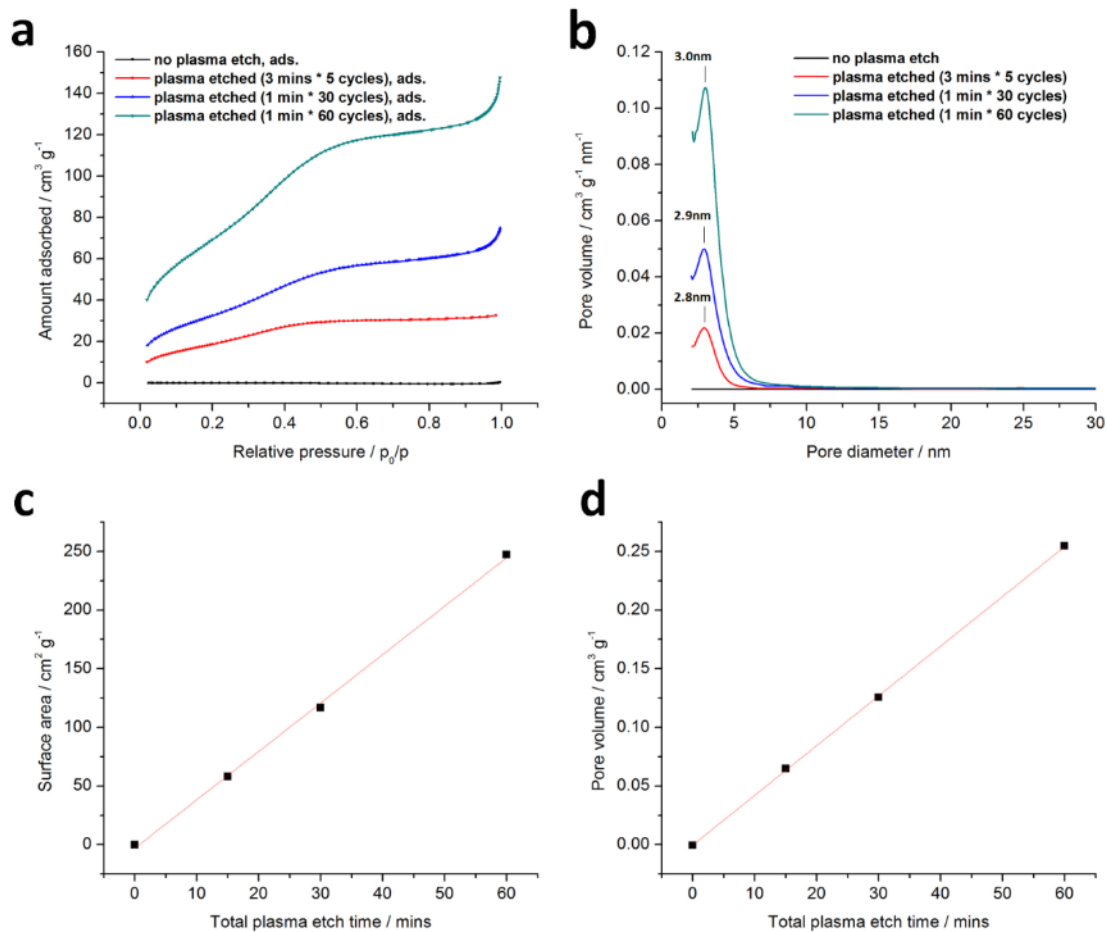


Figure B7. Comparison of pore size distribution, surface area and pore volume of 9.3nm single-pore particles. The results were obtained from nitrogen adsorption data after different durations of plasma treatment (0, 15, 30, and 60 mins). (a) N₂ adsorption isotherms. (b) Pore size distributions obtained from N₂ adsorption isotherms employing the BJH method. Dependence of surface area (c) and pore volume (d) on duration of plasma treatment.

Chapter 4 . Controlling Growth of Ultra-Small Sub-10nm Fluorescent Mesoporous Silica Nanoparticles

Reprinted with permission from Ma, K.; Werner-Zwanziger, U.; Zwanziger, J.; Wiesner, U. Controlling Growth Of Ultrasmall Sub-10 Nm Fluorescent Mesoporous Silica Nanoparticles. *Chem. Mater.* **2013**, *25*, 677–691. Copyright (2013) American Chemical Society.

4.1 Abstract

Mesoporous silica nanoparticles (MSNs) have recently attracted a lot of interest for future nanotheranostic applications due to their large surface-area and high biocompatibility. However, studies to date of MSNs are confined to >10nm particle sizes which may result in unfavorable biodistribution characteristics in *in-vivo* experiments and hence limit their clinical applications. Here we provide a full account of a synthesis approach to ultra-small sub-10nm mesoporous silica nanoparticles with narrow size distributions and homogeneous porous particle morphology. Key features enabling this structure control are (i) fast hydrolysis, (ii) slow condensation, and (iii) capping of particle growth by addition of a PEG-silane at different time-points of the synthesis. Variation of synthesis conditions including monomer/catalyst concentrations, temperature, and time-point of PEG-silane addition leads to synthesis condition – particle structure correlations as mapped out by a combination of results from data analysis of dynamic light scattering (DLS) and transmission electron microscopy (TEM) measurements. Results establish precise control over average particle diameter from 6 to 15nm with increments below 1nm. Solid state nuclear magnetic resonance (NMR) measurements, zeta-potential measurements and thermogravimetric analysis (TGA) were conducted to reveal details of

the particle surface structure. Long-term particle stability tests in deionized (DI) water and PBS 1X buffer solution were performed using DLS demonstrating that the PEGylated particles are stable in physiological environments for months. Fluorescent single pore silica nanoparticles (mC dots) encapsulating blue (DEAC) and green (TMR) dyes were synthesized and characterized by a combination of DLS, TEM, static optical spectroscopy and fluorescence correlation spectroscopy (FCS) establishing probes for multi-color fluorescence imaging applications. The ultra-precise particle size control demonstrated here in particular for sizes around and below 10 nm may render these particles an interesting subject for further fundamental studies of porous silica particle formation mechanisms as well as for sensing, drug delivery and theranostic applications.

4.2 Introduction

Many years of intensive research efforts into the cause and biology of cancer have revealed a high level of complexity.¹ As a result cancer remains one of the most devastating diseases, with the risk of getting cancer before the age of 75 being larger than 18 present.² Providing efficient diagnostic tools and effective therapy of cancer have thus become a major goal of biomedical research worldwide. Until today, one of the paradigms of cancer treatment is chemotherapy. Compared to the complexity of the biology and evolution of the disease, even in a single patient, therapeutic drugs are often rather crude. New treatment paradigms are clearly desirable. In recent years targeted therapies have celebrated astonishing successes and have opened new directions.¹ Furthermore, thanks to advances in protein engineering and nanotechnology, novel traceable and targeted nanocarriers may have the potential to serve as future drug delivery systems and advance cancer theranostics.^{3,4}

Although several types of polymer based therapeutic nanocarriers have been approved for clinical use,⁵⁻¹¹ the search for improved systems and alternative materials is ongoing. Silica nanoparticles, and in particular mesoporous silica nanoparticles (MSNs), are considered such an alternative materials platform and have attracted considerable interest in biomedical research in recent years.¹²⁻²⁶ Encouraged by initial efforts in preparing bright and stable fluorescent core-shell silica nanoparticles referred to as Cornell dots or simply C dots,²⁷⁻²⁹ we began to explore the silica nanoparticle size regime below 10 nm.^{30,31} In this sub-10nm regime nanocarriers are below what is believed to be the threshold for renal clearance, *i.e.* rapid passage through the kidneys into the bladder of an

organism, thus providing an efficient path for achieving favorable biodistributions.³² Furthermore, carrying melanoma cancer targeting ligands (cyclic arginine-glycine-aspartic acid, cRGD) and radioisotopes like ^{124}I enabling positron emission tomography (PET), the ultra-small (<10 nm) dual-modal (optical and PET) C dot probes were approved for a first in-human clinical trial (“target or get out” strategy).³¹

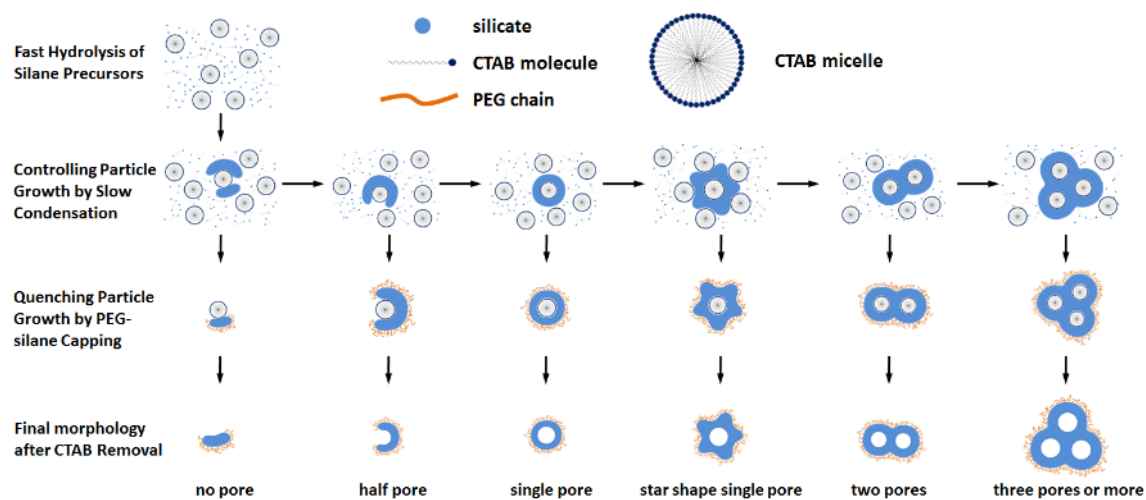


Figure 4.1. Schematics for the synthesis system. Illustration of the synthesis procedure of ultra-small mesoporous silica nanoparticles with different particle size and morphology.

Continuing the search for improved materials for biomedical research, we recently explored pathways to endow ultra-small (<10 nm) fluorescent silica nanoparticles with mesoporosity³³ thus pushing the previous size limit of MSNs from ~20nm^{34,35} down to a size regime where favorable biodistributions are expected.³⁰ The resulting mesoporous C dots (mC dots) provide increased surface area over conventional C dots and may therefore enable, *e.g.* higher therapeutic payloads for clinical applications. In the present paper, we will provide a full account of these results. By studying a broad range of synthesis parameters we will elucidate the conditions leading to controlled particle size and size-distribution. This control will be documented through the synthesis of a series of MSNs with sizes ranging from 6 to 15 nm with increments below 1nm. Characterization results including TGA, ¹³C and ²⁹Si solid state NMR as well as zeta-potential measurements will be reported to reveal details of particle surface structure. Long-term particle stability test in both DI water and PBS 1X buffer solution will be described to document particle stability via successful PEGylation. We will finally generalize the original approach to near-infrared (NIR) mC dots³³ to other colors, *i.e.* to blue and green dots.

The preparation of colloidal particles with narrow size distributions has been quantitatively analyzed since the 1940's and 1950's. According to LaMer's model,³⁶ in a first stage of colloidal synthesis the solute (monomer) concentration is brought up above its solubility limit into the supersaturation regime. In a second stage particle nucleation occurs which in turn diminishes the solute concentration below the threshold concentration for nucleation. In a third stage particle growth continues until the solute concentration drops to its solubility limit. In phase II the most ideal situation for uniform particle size formation is the combination of a strong dependence of the nucleation rate on supersaturation (rapid

nucleation and depletion of solute concentration) and a low growth rate.³⁷ If in stage III the particle growth is diffusion controlled (as opposed to surface reaction controlled), then as first shown by Reiss,³⁸ the initial size distribution as obtained in phase II will further narrow, an effect that is referred to as focusing of the size distribution.³⁹ In the 1980's and 1990's these considerations enabled understanding of growth of sub-10 nm sized semiconductor quantum dots (Q dots) with narrow size distributions leading to, *e.g.* size dependent optical properties.^{39,40} Originally, supersaturation and subsequent nucleation were triggered by rapid injection of metal-organic precursors into vigorously stirred solutions of coordinating solvents.⁴¹ Mechanistic aspects of the formation of uniform nanocrystals via various approaches have recently been reviewed *e.g.* by Hyeon *et al.*⁴²

It is conceptually interesting to compare narrowly size distributed colloidal particle synthesis with the living polymerization of narrowly molar mass distributed macromolecules. Despite differences in the details, many of the general features of these two processes are quite similar. Let's take a look, *e.g.* at living anionic polymerization, a technique which grew enormously in importance through the work of Szwarc in the mid 1950's.^{43,44} In common with other types of chain growth polymerizations there are three steps in living anionic polymerization: initiation, propagation and termination.⁴⁵⁻⁴⁷ Initiation is the start of polymerization during which each initiator species, *e.g.* an organometallic compound or an electron transfer complex, generates carbanion active centre(s). It is commonly assumed that the initiator reacts completely before any of the active centres begin to propagate/grow by adding on further monomer, *i.e.* that the rate constant, k_i , for initiation is much greater than the rate constant, k_p , for propagation. This scenario resembles closely the rapid nucleation and depletion of solute concentration and

the low growth rate that leads to the most ideal situation for uniform colloidal particle size control. Indeed, anionic polymerization in the absence of termination and with $k_i \gg k_p$ always leads to polymers with narrow molar mass distributions, which is why it is widely used to generate polymer standards. Furthermore, under ideal conditions of anionic polymerization, after complete consumption of monomer the propagating polymer chains retain their active carbanionic centres, which repel each other as a result of the negative charge on each chain end. Thus more (of the same or different) monomer can be added to continue polymerization. This can be repeated several times and polymers grow as long as monomer is available, hence the term *living* polymerization. Finally, the living chain ends can be deactivated/”killed”⁴³ and the polymerization/growth terminated by addition of *e.g.* proton donors (usually alcohols). This adds another layer of control to the chain growth as functional end groups can be introduced by using specific termination agents.

In both cases, colloidal particle formation and living anionic polymerization, narrow size distributions can be achieved through a combination of fast nucleation/initiation and slow growth/propagation conditions. Additionally, in both cases capping agents can be used to terminate growth and functionalize surfaces/chain ends. In the following we will discuss how these concepts can be used to generate ultrasmall <10 nm sized MSNs.

As shown in Figure 4.1, there are three key steps which may help the synthesis of ultra-small mesoporous silica nanoparticles with narrow particle size distributions. The first one is fast hydrolysis. To that end tetramethyl orthosilicate (TMOS) was selected as silica source in our experiments since TMOS has the fastest hydrolysis rate among tetraalkoxysilanes and is highly soluble in water.^{48,49} The second one is a relatively slow

condensation rate. Different types of base catalysts, L-lysine and ammonium hydroxide were tested as catalyst in the synthesis. Furthermore, pH, concentration of TMOS and reaction temperature were varied to further control the condensation rate. The third one is the use of an efficient capping agent to terminate particle growth. Here a PEG-silane was used as the termination agent. As the results demonstrate, by employing these key elements, ultra-small sub-10nm single-pore silica nanoparticles with narrow size distributions and high stability became accessible. Using TMOS as silica source, carefully tailoring the condensation rate and quenching particles' growth at appropriate times via addition of PEG-silane allowed precise control of the average diameter of mesoporous silica nanoparticles from around 6nm to larger than 15nm with increments less than 1nm. It is observed that the porous morphology of MSNs evolves as the average particle diameter increases. This structural evolution ultimately may help to better understand the interaction between hexadecyltrimethylammonium bromide (CTAB) micelles and silica precursors, particularly at the very early stages of particle formation.

4.3 Experimental section

4.3.1 Materials.

All chemicals were used as received. Hexadecyltrimethylammonium bromide (CTAB), dimethyl sulfoxide (DMSO), (3-aminopropyl) triethoxysilane (APTES), (3-mercaptopropyl) trimethoxysilane (MPTMS), tetramethyl orthosilicate (TMOS), L-lysine and 2.0 M ammonium hydroxide in ethanol were purchased from Sigma Aldrich. 2-[methoxy(polyethyleneoxy)propyl] trimethoxysilane (PEG-silane, molar mass around 500g/mole) were purchased from Gelest. Acetic acid was purchased from Mallinckrod. DEAC florescent dye with NHS ester functionality, as well as TMR florescent dye with maleimido functionality, was purchased from AnaSpec. Absolute anhydrous 99.5% ethanol was purchased from Pharmco-Aaper. DI water was generated using a Millipore Milli-Q system.

4.3.2 Synthesis of ultrasmall mesoporous silica nanoparticles using L-lysine as catalyst.

For the synthesis of 6.6nm mesoporous silica nanoparticles, 0.23mmol of CTAB and 0.62mmol of L-lysine were added into 10ml of DI water. Then the solution was stirred at 30°C for 30mins until CTAB fully dissolved. After that, 0.43mmol of TMOS was added into the solution under vigorous stirring and the solution was further stirred at 30°C for one hour. Following that, 0.21mmol of PEG-silane was added and the solution was stirred at 30°C for another 24 hrs. In the next step, the temperature was increased from 30°C to 80°C and stirring continued at 80°C for another 24hs. Afterwards, the solution was cooled to room temperature and then transferred into a dialysis membrane tube (Pierce, molecular

weight cut off 10000). The solution in the dialysis tube was dialyzed in 100ml acid solution (a mixture of DI water, ethanol and acetic acid with the volume ratio 1:1:0.007) for 24hs to extract CTAB out of the pores of the particles. This process was repeated three times. The solution was then dialyzed in 2000ml DI-water for another 24hs. This process was again repeated for three times. The particles were finally filtered through a 200nm syringe filter (fisher brand) and then stored at room temperature for further investigations. The molar ratio of the reactants was 1 TMOS: 0.53 CTAB: 2.7 L-lysine: 0.49 PEG-silane: 1292 H₂O. For the synthesis of particles with different average diameters, the initial synthesis temperature was varied from 30°C to 80°C and the time gap of the addition of PEG-silane after the addition of TMOS was varied from less than 1minute to 1 hour, while other synthesis condition remained the same. Details of synthesis conditions are shown in Figure 4.4.

4.3.3 Synthesis of ultrasmall mesoporous silica nanoparticles using ammonium hydroxide as catalyst.

The synthesis procedure using ammonium hydroxide as catalyst was almost the same as the procedure using L-lysine as catalyst. The only difference was that instead of L-lysine a specific amount of ammonium hydroxide was added into the precursor solution as base catalyst. In order to control average particle diameters, initial synthesis temperature, concentration of TMOS and CTAB, concentration of ammonium hydroxide and time point of the addition of PEG-silane were varied independently. In more detail, the initial synthesis temperature was varied from 30°C to 80°C. The concentration of ammonium hydroxide was varied from 0.001M to 0.008M. The concentration of TMOS was varied from 0.011M to 0.046M, while the molar ratio of TMOS to CTAB was fixed at 1:0.49. The

time point of the addition of PEG-silane after the addition of TMOS was varied from less than 1 minute to 24 hours. Details of synthesis conditions are shown in Figure 4.6.

4.3.4 Synthesis of ultra-small single-pore florescent silica nanoparticles (mC dots) with different colors.

TMR and DEAC were used as the florescent dyes to synthesize ultra-small single-pore florescent silica nanoparticles. TMR dye with maleimido functionality was conjugated to MPTMS in DMSO while DEAC dye with NHS ester functionality was conjugated to APTES in DMSO. The synthesis procedure of 9.3nm sized particles using ammonium hydroxide as catalyst was used to prepare fluorescent mC dots. The respective silane-conjugated florescent dye with specific absorption and emission spectrum was added together with TMOS into the synthesis solution to co-condense into the final particle. The molar ratio of dye-silane conjugate to TMOS was 1: 4855.

4.3.5 Characterization of particle morphology.

TEM images were taken using a FEI Tecnai T12 Spirit microscope operated at an acceleration voltage of 120kV. Hydrodynamic particle sizes and size distributions were measured by DLS using a Malvern Zetasizer Nano-SZ operated at 20°C. Each DLS sample was measured three times in DI water and results superimposed in the respective figures in this paper. Number percentage curves are used to present the measurement results. The average diameter of each sample was calculated by averaging the mean diameters of number percentage curves from three measurements.

4.3.6 Analysis of particle size distribution.

In order to obtain size distribution data from TEM images, we measured the diameters of over 100 particles in the same image using a ruler tool provided by the TEM facility software. The software automatically recorded the diameters of all of the measured particles. Sorting the recorded diameters into bins generated the distribution of the particle size. Considering that the systematic error of the ruler tool can be as high as over 1nm, the increment of the bins was set to 2nm in order to optimize the analysis. Furthermore, in order to lower the standard error of each data point, this process was repeated three times for each sample. The distribution results were then averaged and the standard errors were calculated. In order to compare the distributions of different samples in one diagram, lines with markers instead of columns were used to display the data.

4.3.7 Analysis of number of pores per particle distribution.

The distribution of the number of pores per particle of each sample was obtained through analyzing over 500 particles on a single TEM image with appropriate magnification. This process was repeated three times for each sample. The distribution results were then averaged and the standard errors were calculated. In order to compare the distributions of different samples in one diagram, lines with markers instead of columns were used to display the data.

4.3.8 ^{13}C and ^{29}Si solid state NMR characterization.

Samples were first dried in a rotary evaporator before subjected to solid state NMR characterization. All NMR experiments were carried out on a Bruker Avance NMR

spectrometer with a 9.4T magnet (100.65MHz ^{13}C Larmor frequency, 79.51MHz ^{29}Si Larmor frequency) using a probe head for rotors of 4mm diameter.

For the ^{13}C cross-polarization (CP)/ magic angle spinning (MAS) NMR experiments the samples were spun at the magic angle at 8.00 kHz rotation frequency. The ^{13}C CP/MAS NMR spectra were accumulated with 3.0 s repetition times due to the probe duty cycle. The other parameters for the ^{13}C CP/MAS experiments with TPPM proton decoupling were optimized on glycine, whose carbonyl resonance also served as external, secondary chemical shift standard at 176.06ppm. For the final ^{13}C CP/MAS NMR spectrum 1120 scans were accumulated using 200 μs CP contact times.

For the ^{29}Si CP/MAS NMR experiment the samples were spun at 7.00kHz rotation frequency at the magic angle. The CP parameters were optimized on Kaolin, which also served as secondary chemical shift standard to peaks at -91.5 and -90.0 ppm against TMS. For the final spectra, up to 3200 scans were accumulated using CP with ramped proton powers during the 5 ms CP contact times and detection with TPPM proton decoupling. The ^{29}Si CP/MAS NMR scans were accumulated with repetition time of 3 s due to the probe duty cycle.

4.3.9 Characterization of fluorescent properties of dye encapsulating mC dots.

Absorption-matched samples were prepared by appropriate dilution of dye doped particles and free dye with water and measured in quartz cuvettes using a Varian Cary 5000 spectrophotometer (Varian, Palo Alto, CA). The extinction coefficients of DEAC (42000 M⁻¹cm⁻¹), and TMR (98000 M⁻¹cm⁻¹) were used to calculate the concentration of the dyes in the samples.

Fluorescence measurements of absorption-matched samples were performed on a Photon Technologies International Quantamaster spectrofluorometer (PTI, Birmingham, NJ) to estimate the quantum efficiency enhancement per dye of the dyes encapsulated in the particles versus the free dye in aqueous solution.

The absorption-matched samples were further measured on a home-built FCS using solid state 445 nm (for DEAC particles) and HeNe 535 nm (for TMR particles) excitation to characterize sample properties, such as brightness per particle, hydrodynamic diameter and concentration of particles as described in reference.²⁹ The FCS instrument was calibrated prior to all measurements. The number of dyes per particle was derived from the ratio between the concentration of dyes measured by absorption spectra and the concentration of particles measured by FCS of the same sample.

4.3.10 Characterization of PEG contamination, zeta-potential and long-term stability.

Samples were first dried in a rotary evaporator before subjected to thermogravimetric analysis. Thermogravimetric analysis was conducted using a TA instruments Q500 thermogravimetric analyzer. During the measurement, temperature was increased from room temperature 100°C with ramp 10.00°C/min and then remained at 100°C for two hours to fully evaporate water. Afterwards, temperature was further increased to 600°C with ramp 10.00°C/min. PEG contamination was then calculated according to the thermogravimetric analysis results. Zeta-potential of particles was measured in phosphate buffered saline (PBS) 1X solution (pH 7.5) with estimated concentration 3mg/ml using a Malvern Zetasizer Nano-SZ operated at 20°C. Each measurement was repeated for five times and the results were averaged. In order to study

the long-term stability of particles, samples were stored in both DI water and PBS 1X buffer solution at room temperature for months; during which the hydrodynamic size of particles were monitored using a Malvern Zetasizer Nano-SZ operated at 20°C. Each data point was measured five times and the results were averaged.

4.4 Results and discussion

4.4.1 Controlling particle growth through optimizing hydrolysis and condensation.

As discussed in the introduction, it is desirable to have fast hydrolysis in order to synthesize ultra-small silica nanoparticles with narrow size distributions. Fast hydrolysis here means that the time period needed for silane hydrolysis should be much shorter than the time period needed for silica condensation. In the best of all cases, the hydrolysis process can be completed before the majority of hydrolyzed silicic acid derivatives condense. This can be facilitated through using a rapidly hydrolyzing silica source and slowing down the silica condensation rate appropriately, and thereby adjusting particle growth to a convenient time window. This enabled the observation of growth process of MSNs from sub-nanometers to tens of nanometers.

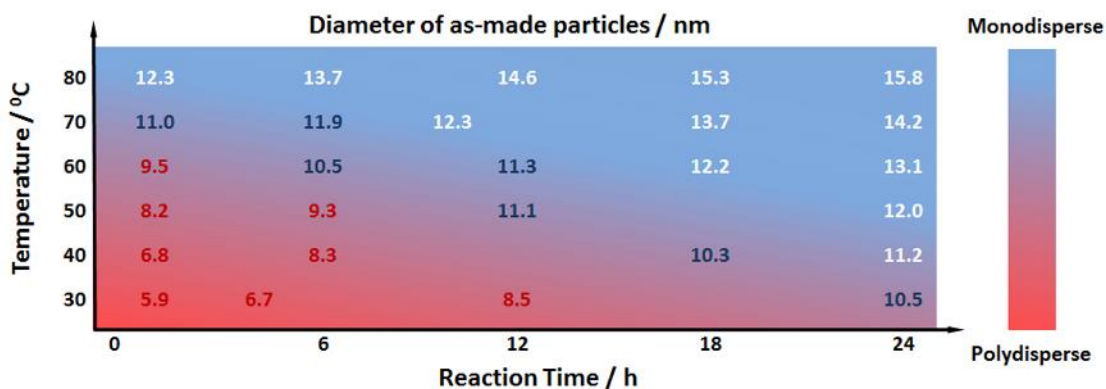


Figure 4.2. Relationship between particle size and stability. A map showing the average diameters of as-made particles synthesized under different reaction conditions as measured by DLS. Each sample was measured three times and the results were then averaged. The graded background color depicts the relationship between the size of as-made particles and their dispersity after being washed.

Here, TMOS was used as silica source since it has the fastest hydrolysis rate among tetraalkoxysilanes.^{48,49} Both hydrolysis rate and condensation rate of silica greatly depend on pH. However, the hydrolysis product of silica, silicic acid, also lowers solution pH, and thus further slows down hydrolysis but accelerates condensation. In order to study the effects of hydrolysis rate and condensation rate on particle size, instead it would be desirable to fix pH during the synthesis. For this reason L-lysine was initially selected as buffer catalyst, which can maintain the pH slightly above 9 when at appropriate concentrations. Since the pKa's of α -(CH₂)₄NH₃⁺, α -NH₃⁺ and α -COOH in L-lysine are estimated to be 10.28, 8.90 and 2.18, respectively,⁵⁰ about 92% of α -(CH₂)₄NH₂ and 33% of α -NH₂ are protonated under the synthesis condition (pH around 9.2). Through the electrostatic interactions between these positively charged protonated amine groups on L-lysine and negatively charged deprotonated hydroxyl groups on the silica surface, L-lysine molecules tend to attach on the surface of silica particles and deactivate the hydroxyl groups. Consequently, this attachment hinders condensation occurring on silica surfaces and thus further slows the growth of silica nanoparticles.⁵¹

Based on these considerations, we synthesized MSNs using TMOS as silica source and L-lysine as catalyst. The initial pH of the reaction was 9.2 and was maintained around 9 through the whole reaction. The synthesis temperature was varied from 30°C to 80°C and the reaction time was varied from 1 hour to 24 hours to control the growth of the particles. The average diameters of the as-made particles under different synthesis conditions were measured by DLS. Results are shown in Figure 4.2. Each data point in Figure 4.2 came from a different synthesis batch. We repeated each synthesis batch one or two times during this study and the results were very close with deviations in size of less than 1nm. Shown

by Figure 4.2, for a particular temperature particles grew bigger as reaction time increased. For example, at 80°C particles grew from around 12nm (after 1 hour) to 16nm in 24 hours. The same trend was observed for all temperatures between 30°C and 80°C. In addition, overall the particle size decreased as synthesis temperature decreased. Please note that by shortening reaction time and lowering synthesis temperature, the average diameter of as-made particles can be pushed down to less than 6nm. These results suggest that by using TMOS as silica source and L-lysine as buffer catalyst, which can further lower the condensation rate through surface association, particle growth can be slowed down to a convenient time window allowing size control in a range from about 5 to 15nm.

However, we found that the stability against aggregation of the synthesized particles greatly depended on size. In order to systematically compare the stability of synthesized particles, we used polydispersity index (PDI) which was measured by DLS as the reference. PDI here is a dimensionless parameter to describe the width of particle size distribution and it is defined as the following,

$$\text{PDI} = \frac{\sigma^2}{Z_D^2}$$

where σ is the standard deviation of particle size distribution and Z_D is the intensity weighted mean hydrodynamic size of particles. The higher PDI indicates the presence of more aggregates in addition to oligomers. According to the PDIs of the same samples but after being washed, different colors were assigned to the data in Figure 4.2. White numbers indicate that the PDIs of the washed samples were lower than 0.25, which is an acceptable value. Red numbers indicate that the final PDIs were higher than 0.7, which suggests particles greatly aggregate after being washed. Blue numbers signify PDIs between 0.7 and

0.25. Based on these data Figure 4.2 shows a graded background color depicting the relationship between the average diameter of as-made particles and their size dispersity after the washing steps. According to Figure 4.2, particles with smaller average diameters always showed higher PDIs once washed. Particularly for the <10nm particles, the PDIs were higher than 0.7 in most cases and no distinct size distribution could be read out in DLS. This suggests that these particles greatly aggregated during the washing steps. Only the particles with average diameters larger than 12nm maintained narrow size distributions in the washing steps. The lower stability and higher size dispersity of the smaller particles could be due to their higher surface energy. Another reason may be the presence of residual free silicic acid in solution when the reaction was stopped, which may lead to uncontrolled condensation during the washing steps and thus cause aggregation. In summary, although the average diameters of as-made particles can be varied from about 5nm to 16nm in this system, additional steps have to be taken to improve particle stability.

4.4.2 Quenching particle growth through addition of PEG-silane.

A PEGylation step is typically conducted before *in-vivo* experiments not only for stabilizing particles, but also for lowering particle surface charge and obtaining better biodistribution characteristics.^{30,31,51-55} Inspired by the comparison of colloidal particle growth with living (anionic) polymerization for the generation of narrowly distributed objects and the use of termination/capping agents in living polymerizations, we contemplated that a PEGylation step could actually be used during the one-pot synthesis to terminate particle growth thereby providing an additional control parameter for particle size. Integrating the PEGylation step into the one-pot synthesis would simultaneously

prevent particle aggregation by sterical stabilization and enable particles to work in high salt containing physiological environments without additional surface modification steps.

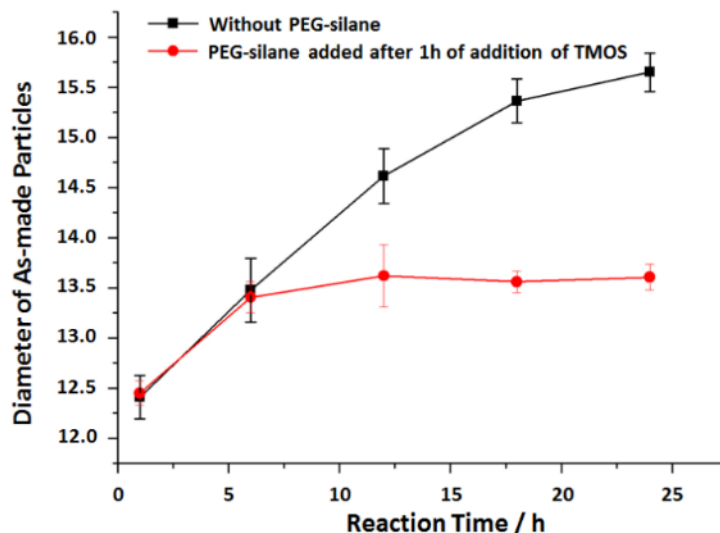


Figure 4.3. Particle growth terminated by PEG addition. Particle diameters as measured by DLS during particle growth in the absence (squares) and presence (circles) of PEG-silane. Each data point was obtained by averaging three independent measurements.

In order to prove the principle of using PEG-silane as a particle capping agent which to terminate particle growth, we compared the growth process of two syntheses, one with PEG-silane and one without PEG-silane. We measured the average particle diameter with DLS, sacrificing a very small amount of the reaction solution at different reaction times (1, 6, 12 18 and 24 hours). For the synthesis with PEG-silane we first measured the average particle diameter after 1 hour reaction to make sure the particle size is comparable with that of the synthesis without PEG-silane (Figure 4.3). At the same time of the measurement, PEG-silane was added into the synthesis mixture. From Figure 4.3, without PEG-silane the MSNs grew from around 12nm (at 1 hour) to around 15nm after one day. In contrast, if PEG-silane was added one hour after the addition of TMOS, the average diameter of the resulting particles grew a bit further to around 13.5nm and then stayed roughly constant

throughout the remainder of the synthesis process. This result suggests that addition of PEG-silane during the reaction indeed can efficiently quench particle growth. Actually, in more detailed studies (data not shown), we observed that the average diameter of particles always increased by several angstroms to several nanometers once PEG-silane was added, depending on the amount of added PEG-silane. This increment occurred within seconds. Data further suggest that PEG-silane molecules first only physically attach to the particles through, *e.g.* Van der Waals interactions or electrostatic interactions, instead of covalently bonding to the particle surface. It is this relatively fast attachment that enables PEG-silane to efficiently quench particle growth. More experiments are clearly needed, however, to further elucidate the exact mechanism of the interaction between PEG-silane and the silica nanoparticles. In order to fully condense the PEG-silane to the silica nanoparticles, a subsequent heat treatment for 24 hrs at 80°C was applied as the final step of the synthesis. No significant size change was observed as a result of this heat treatment, which further indicates the growth of the particles is effectively quenched by PEG-silane.

Quenching particle growth via PEGylation adds a powerful tool to control particle size. Based on results reported in Figure 4.2, in subsequent experiments PEG-silane was added as a capping agent into batches under different synthesis conditions. In more detail, the particle synthesis temperature was varied from 30°C to 80°C to control the growth rate. The time gap between the additions of TMOS and PEG-silane was varied from less than 1 minute to 50 minutes to quench particle growth at different time points. Figure 4.4a maps out the relationship between final average particle diameter as measured by DLS and synthesis conditions. While the x-axis of Figure 4.2 is overall reaction time, the x-axis of Figure 4.4a is a relative time axis between the addition of TMOS and PEG-silane. In all

cases reported in this Figure 4.4a, 24 hours after addition of PEG-silane a 80°C heat treatment for another 24 hours was applied to covalently fix the PEG-silane onto the particle surface. All of the batches showed distinct DLS size curves (Figure 4.4b) with average diameters from 5.6-13.6 nm separated by 1-1.5 nm, as well as relatively low PDIs, indicating no noticeable aggregation after washing. These results further demonstrate the high efficiency of termination via PEG-silane.

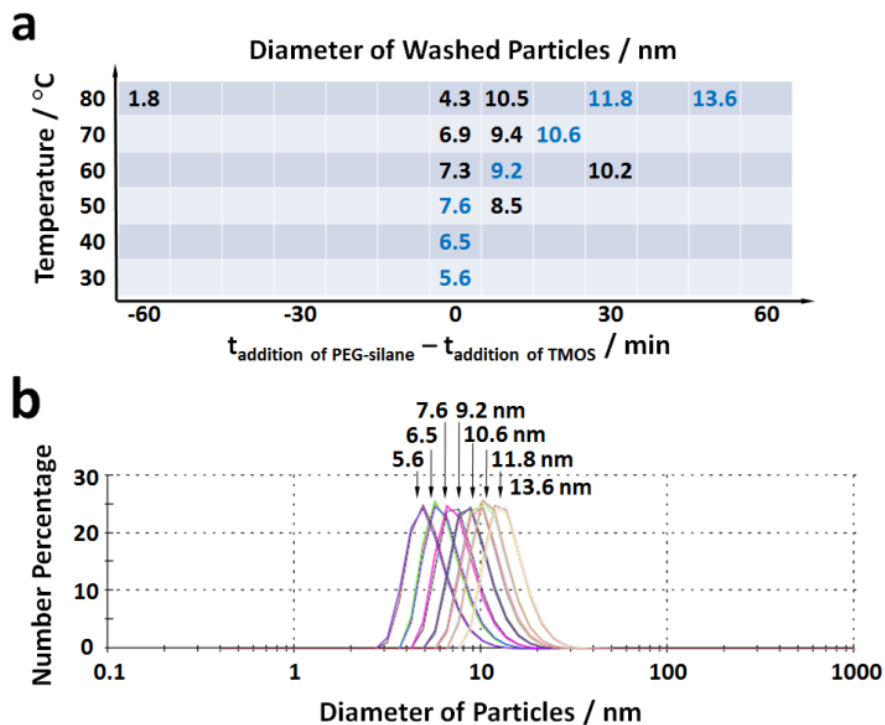


Figure 4.4. Control of particle size of mesoporous silica nanoparticles. (a) A map showing the average diameters of washed particles synthesized under different reaction conditions as measured by DLS. Each sample was measured three times and the results were averaged. (b) DLS measurement results on selected samples as indicated by blue numbers in (a).

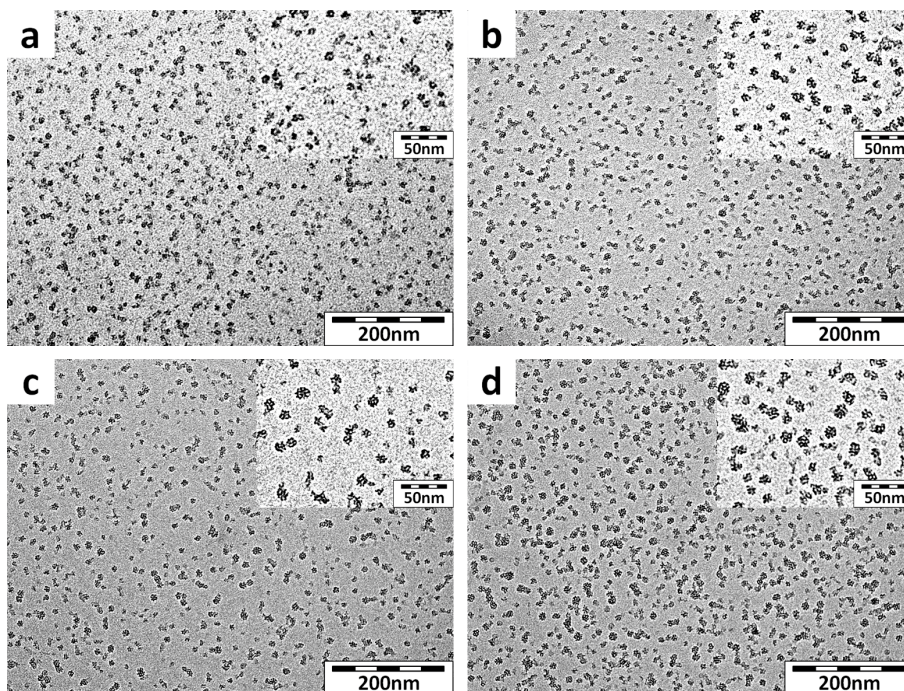


Figure 4.5. TEM images of mesoporous silica particles with different average diameters. (a) 5.6nm, (b) 7.6nm, (c) 10.6nm and (d) 13.6nm. Inserts display images of the same samples but at higher magnification.

From Figure 4.4a, at 80°C, if PEG-silane was added right on top of the addition of TMOS (x axis equals to 0), the final average particle diameter was below 5nm. When PEG-silane was added 50 minutes after the addition of TMOS, the final average particle diameter increased to above 13nm. The same trend was observed as the synthesis temperature decreased. This finding is consistent with that a longer growth period, as PEG-silane is added at later time points, leads to larger particles. Interestingly, from Figure 4.4a by fixing the PEG-silane addition right on top of the TMOS addition, the final average particle diameter first increased but then decreased as temperature increased from 30°C to 80°C. This is very different to the behavior displayed in Figure 4.2 where the as-made particle size continued to increase with temperature, most likely due to an increase of the condensation rate. The difference may be ascribed to the largely different mobility of PEG-

silane at different temperatures. As PEG-silane is a relatively big molecule compared to free silicic acid, its mobility is expected to be more temperature dependent and might greatly increase at the higher synthesis temperatures. Consequently, while at lower temperatures the increasing condensation rate of the silicic acid first leads to larger particles with increasing temperature, at even higher temperatures the PEG-silane mobility increases to a point where the capping reaction becomes the dominant step thus reducing particle size. This effect may also be exacerbated by the tendency of PEG chains to dehydrate at higher temperature thus leading to a tighter coverage of the silica surface and as a result more effectively slowing further particle growth.⁵⁶ From Figure 4.4a, when TMOS and PEG-silane are added on top of each other, the temperature threshold where the reactivity of PEG-silane and silicic acid reverses is between 50°C and 60°C.

Figure 4.5a-d shows TEM images of selected particles with increasing hydrodynamic diameters, of 5.6nm, 7.6nm, 10.6nm and 13.6nm, respectively (as measured by DLS, see Figure 4.4b). The smaller magnification images illustrate the degree of particle size uniformity while the higher resolution images (Figure 4.5, insets) reveal details of particle structure. In Figure 4.5a some of the particles show single-pore structure with diameters close to 10nm while other silica structures do not contain pores and are only 2-3 nm in size. As the average diameter increases to 13.6nm (Figure 4.5b to 4d), larger particles with more pores begin to show up while the percentage of smaller particles decreases. As a result, the average particle diameter increases consistent with the DLS measurements (Figure 4.4b). Both DLS measurements and TEM images indicate reasonably high particle uniformity without any detectable aggregation. However, a finite size distribution within the different particle batches is clearly visible in TEM. This finite particle size distribution

might be due to the use of L-lysine as catalyst. As L-lysine molecules can attach to the surface of the growing silica particles, both the isotropic silica growth and the structure directing effect of CTAB might be disturbed resulting in particle structure inhomogeneities. Another disadvantage of using L-lysine as catalyst is that this attachment effect may also prevent particles from being effectively PEGylated as the particle surface may already be occupied by the catalyst. This in turn could be a problem in *e.g. in-vivo* experiments if not enough PEG chains are attached to stabilize the particles. For these reasons, we turned from L-lysine to other catalysts in our quest to generate ultra-small (<10 nm) MSNs with precise control over size distribution and morphology.

4.4.3 Synthesis using ammonium hydroxide as catalyst.

Several types of base catalysts have been successfully used in the synthesis of MSNs, such as triethanolamine (TEA),^{35,57} tetramethylammonium hydroxide⁵⁸ and ammonium hydroxide⁵⁹. In our study, we selected ammonium hydroxide as catalyst replacing L-lysine for multiple reasons. First, ammonium hydroxide is a common chemical and one of the most used base catalysts in silica synthesis. Second, ammonium hydroxide is a relatively small molecule, which does not tend to attach to the silica surface thereby affecting particle morphology. Finally, in our previous work we did not see any negative effects of ammonium hydroxide *e.g.* on efficient PEGylation.^{30,31}

Results on average particle diameters, as measured by DLS, from synthesis batches obtained under different experimental conditions are mapped out in Figure 4.6. The map is constructed as a set of sub-maps each having the same style as the one displayed in Figure 4.4a. The x axis of each sub-map indicates the time gap between the additions of TMOS

and PEG-silane, while the y axis of each sub-map indicates the initial synthesis temperature. Different sub-maps along the overall x and y directions were obtained for different concentrations of ammonium hydroxide and TMOS, respectively. In this way Figure 4.6 displays what is actually a four dimensional map, as there are a total of four synthesis parameters that were varied: (1) concentration of ammonium hydroxide, (2) concentration of TMOS, (3) addition of PEG-silane relative to TMOS, and (4) initial temperature. Parameters (1), (2) and (4) were used for controlling particle growth rate while parameter (3) was used for controlling the growth period.

First, let's take a look at the sub-map with the concentration of ammonium hydroxide of 0.002M and the concentration of TMOS of 0.0457M (2nd sub-map from top left in Figure 4.6), where the PEG-silane is added on top of TMOS (*i.e.* x axis value = 0): Here the average diameter of the final washed particles increases with increasing synthesis temperature from room temperature to 80°C. It is interesting to note that this monotonic trend is similar to the L-lysine system in absence of PEG-silane capping (Figure 4.2), but very different compared to behavior of the L-lysine system with PEG-silane capping, where the average diameter of washed particles first increased and then decreased with increased temperatures. This difference may be due to a difference of condensation rates in the L-lysine catalyzed system versus the ammonium hydroxide system. For ammonium hydroxide we always observed an immediate drop of solution pH from near 10 to close to neutral upon the injection of TMOS into the reaction, probably due to the instantaneous hydrolysis of TMOS producing silicic acid. This observation is consistent with the expected behavior from calculation results. Since the pK_b of ammonium hydroxide is estimated to be 4.75,⁵⁰ the pH of 0.002M ammonium hydroxide aqueous solution is 10.26. Since the

pK_{a1} and pK_{a2} of orthosilicic acid are estimated to be 9.84 and 13.2, respectively, the pH of the solution drops from 10.26 to 8.42 after all of the 0.0457M TMOS hydrolyzes. For one thing, this almost immediate drop of pH further indicates the ultra-fast hydrolysis of TMOS, which is a prerequisite in the proposed mechanism (Figure 4.1) to obtain narrow particle size distributions. Furthermore, since the silica condensation rate is maximized at the pH around 8.4,³⁴ this reaction condition may actually result in the maximum condensation rate. As the results, a relative high pH triggers the fast hydrolysis of TMOS upon which silicic acid is produced by hydrolysis of TMOS. In turn the produced silicic acid further lowers the pH thus optimizing the particle growth rate. In comparison, the synthesis pH of the L-lysine system always stays around 9 throughout the reaction which reduces both, the initial hydrolysis and the condensation rates of TMOS relative to the ammonium hydroxide catalyzed system. Furthermore, as already discussed the attachment of L-lysine molecules on the silica particle surface can further slowdown the growth of particles. For these reasons, the growth rate of particles is much faster in the ammonium hydroxide catalyzed system than in the L-lysine system. While the non-monotonic dependence of final particle size on synthesis temperature in the L-lysine system (Figure 4.4a, x axis equals to 0) indicated a competition between silicic acid condensation and PEG-silane quenching, in the ammonium hydroxide system this competition does not manifest itself in the particle size since the condensation rate of silicic acid is always fast enough to outcompete PEGylation leading to monotonically increasing particle size with temperature. This trend is observed in almost all of the sub-maps in Figure 4.6. The same sub-map ([ammonium hydroxide] = 0.002M, [TMOS] = 0.0457M) also shows that the average diameter of washed particles always increases when PGE-silane addition is

delayed, irrespective of temperature. In analogy to the L-lysine system, this is simply because a longer growth period results in bigger particles. This trend is also observed in all of the sub-maps in Figure 4.6.

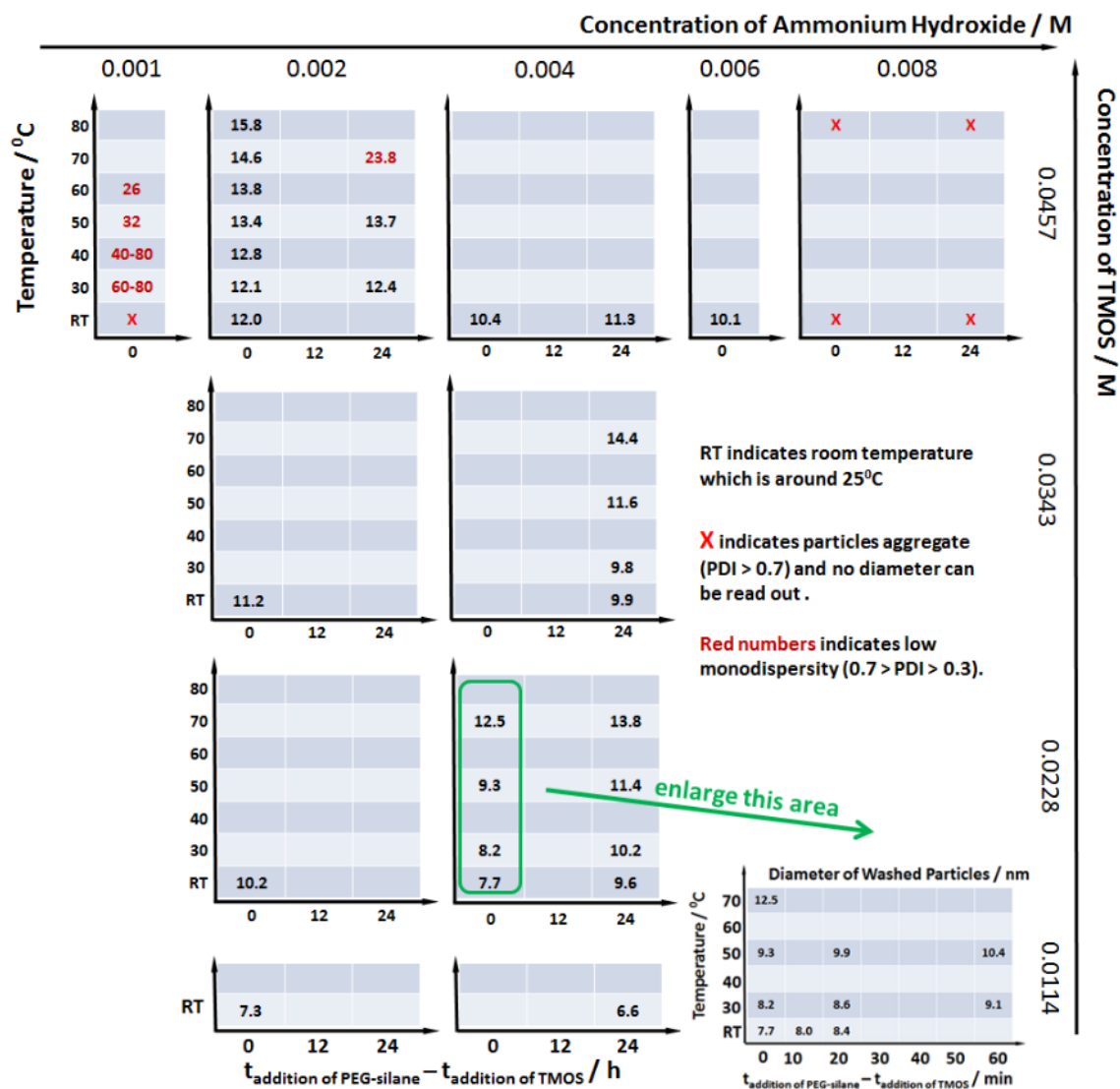


Figure 4.6. Map of synthesis parameters. A map showing the average diameters, as measured by DLS, of washed particles synthesized under different reaction conditions with ammonium hydroxide as catalyst. Each sample was measured three times and results were then averaged.

When we used concentrations of ammonium hydroxide higher than 0.008M, or lower than 0.001M, particle size control was lost. As indicated by the red crosses in Figure

4.6, when the concentration of ammonium hydroxide was 0.008M or higher, silica always formed aggregates and precipitated either during the reaction or during the washing steps. Similarly, when the concentration of ammonium hydroxide was 0.001M or lower, silica formed aggregates at room temperature and no distinct particle diameter could be read out in DLS measurements. As the initial synthesis temperature increased from room temperature to 80°C, average particle diameter gradually decreased from unreadable (aggregation) to around 26nm. It is interesting to note that this monotonic decrease of particle size at higher temperatures is totally opposite to what is observed in other sub-maps with ammonium hydroxide concentrations equal to or higher than 0.002M. This is because the hydrolysis rate of TMOS decreases at lower ammonium hydroxide concentration. When the concentration of ammonium hydroxide decreases below a threshold, the hydrolysis process is not fast enough to complete before particle formation. Consequently, instead of condensation, hydrolysis dominates the growth kinetics of particles by continuously providing silicic acid, which further condenses onto the particles. As a result, higher temperature predominantly increases the hydrolysis rate and results in higher particle concentration but smaller particle size. Actually, this is very similar to the synthesis of silica particles using TEOS as silica source where smaller particles are obtained at higher temperature.⁶⁰ In both, the TEOS system and the near-neutral-pH TMOS system, hydrolysis has a lower kinetic rate than condensation and thus dominates the growth of the particles. This is very different compared to our proposed mechanism for optimal control of particle growth (Figure 4.1) where condensation rather than hydrolysis is the dominating process. Only when hydrolysis is fast enough and condensation becomes the dominant growth process, is it possible to focus on the very early stages of particle

formation and the synthesis of ultra-small mesoporous silica nanoparticles with narrow size distribution becomes possible. According to Figure 4.6, the threshold of ammonium hydroxide concentration to trigger this mechanism in our system is between 0.001M and 0.002M. By comparing the sub-maps in Figure 4.6 for different ammonium hydroxide concentrations from 0.002M to 0.006M, but with the same TMOS concentration of 0.0456M, we can see that particle size decreases as the concentration of ammonium hydroxide increases. Considering that the calculated condensation pH of the synthesis with an ammonium hydroxide concentration of 0.002M is around 8.42, which is slightly higher than 8.4, the pH of maximum condensation rate, higher ammonium hydroxide concentrations will result in higher pH and slower condensation rates, and consequently result in smaller particle sizes.

Within the appropriate region of ammonium hydroxide concentration (0.002M to 0.006M), we further varied the TMOS concentration to control particle growth. TMOS/CTAB ratio was always fixed when the concentration of TMOS was varied. As shown in the sub-maps with the same ammonium hydroxide concentration of 0.002M, but different TMOS concentration, at room temperature the average diameter of washed particles decreased from 12.0nm to 7.3nm when the TMOS concentration decreased from 0.0457M to 0.0114M. The same decreasing trend was observed in batches with ammonium hydroxide concentration of 0.004M. This suggests that as the concentration of TMOS decreases, the condensation rate of TMOS decreases resulting in slower particle growth.

In order to demonstrate the exquisite size control possible with our approach, we enlarged the area in the green circle in Figure 4.6. As shown by the inserted sub-map in Figure 4.6, by fixing the ammonium hydroxide concentration at 0.004M and the TMOS concentration

at 0.0228M, the average particle diameter can be precisely tuned from less than 8nm to larger than 12 nm with increments of about 0.5nm through simply varying synthesis temperature and when PEG-silane is added relative to TMOS in order to quench particle growth.

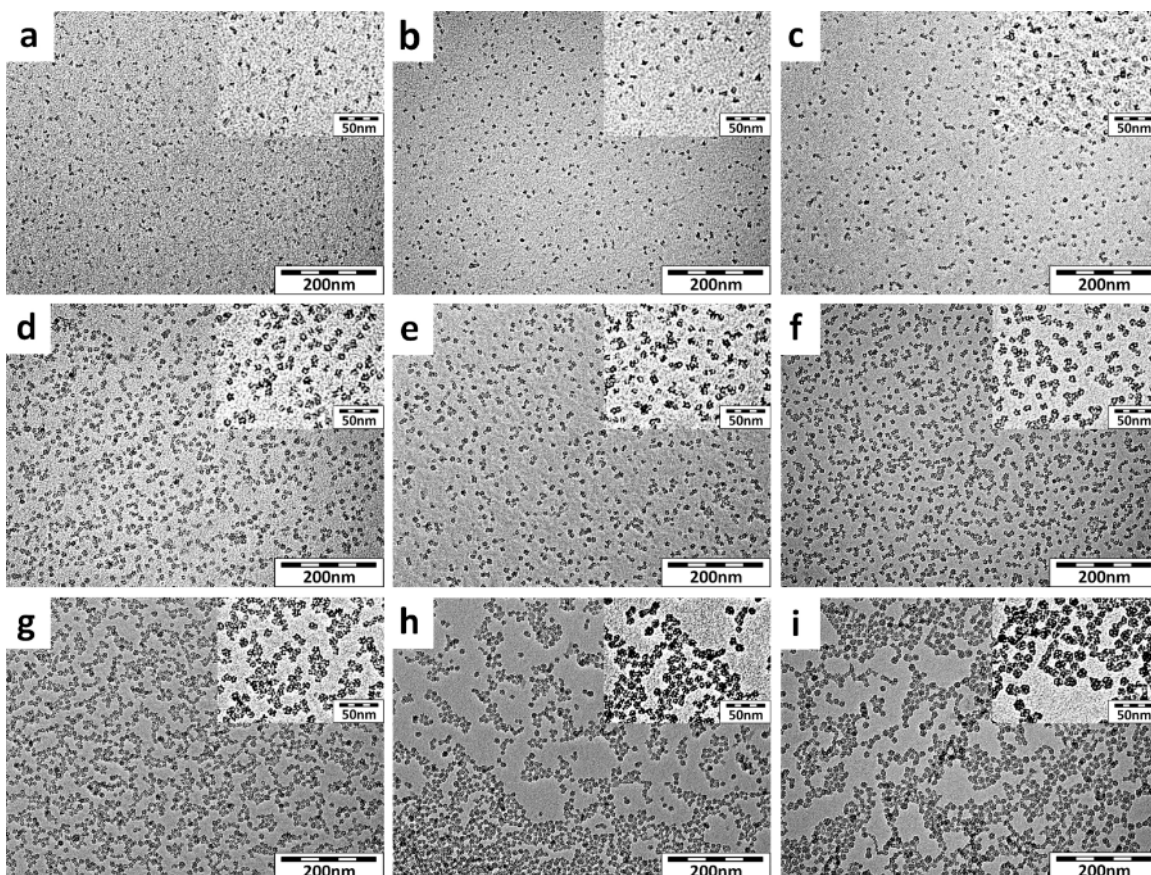


Figure 4.7. TEM images of silica particles with different average diameters. (a) 6.6nm, (b) 7.3nm, (c) 8.2nm, (d) 9.3nm, (e) 10.2nm, (f) 11.3nm, (g) 12.1nm, (h) 13.5nm, and (i) 15.9nm. Inserts display images of the same samples but at higher magnification.

It is important to point out that the exact particle size obtained is sensitive to environmental conditions since precise size control requires very fine control over hydrolysis, condensation and also reaction of PEG-silane. Considering we did not precisely control the environmental conditions, for example by working in humidity-controlled chambers, we found that details of the map shown in Figure 4.6 depended on weather

conditions. For example, we saw that the average particle diameter synthesized under the same reaction conditions became slightly smaller when the season in Ithaca, NY, moved from spring to summer. More generally, considering the particular weather environment of Ithaca, *e.g.* temperature, humidity and pressure, we obtained slightly different average particle diameters when the same experiment was conducted in different locations and during different seasons. However, since there are four synthesis parameters in total, which can be used to control particle size (temperature, concentration of ammonium hydroxide, concentration of TMOS and when PEG-silane is added), under different environmental conditions we were always able to archive the targeted particle diameter by slightly re-optimizing these parameters .

4.4.4 Morphology characterization of ultra-small mesoporous silica nanoparticles.

Nine samples with increasing average diameters out of the map shown in Figure 4.6 were selected for morphology characterization. Figure 4.7 shows the TEM images of the selected samples with diameters ranging from 6.6nm to 15.9nm. The smaller magnification images illustrate the high degree of homogeneity in particle size while the higher resolution images in the insets reveal details of particle structure. Compared to the mesoporous silica nanoparticles synthesized with L-lysine as catalyst (Figure 4.5), the particles synthesized with ammonium hydroxide have a more homogeneous morphology and narrower size distribution. Figure 4.8a summarizes DLS measurement results for these selected samples. Data for the 11.3nm sample is not included in Figure 4.8a because the x axis (particle diameter) is on a log-scale. The DLS curve of the 11.3nm sample thus almost completely overlaps with the curve of the 10.2nm sample. Both, the TEM images as well

as the DLS measurement results suggest that particles of different batches are highly uniform in size without detectable aggregation.

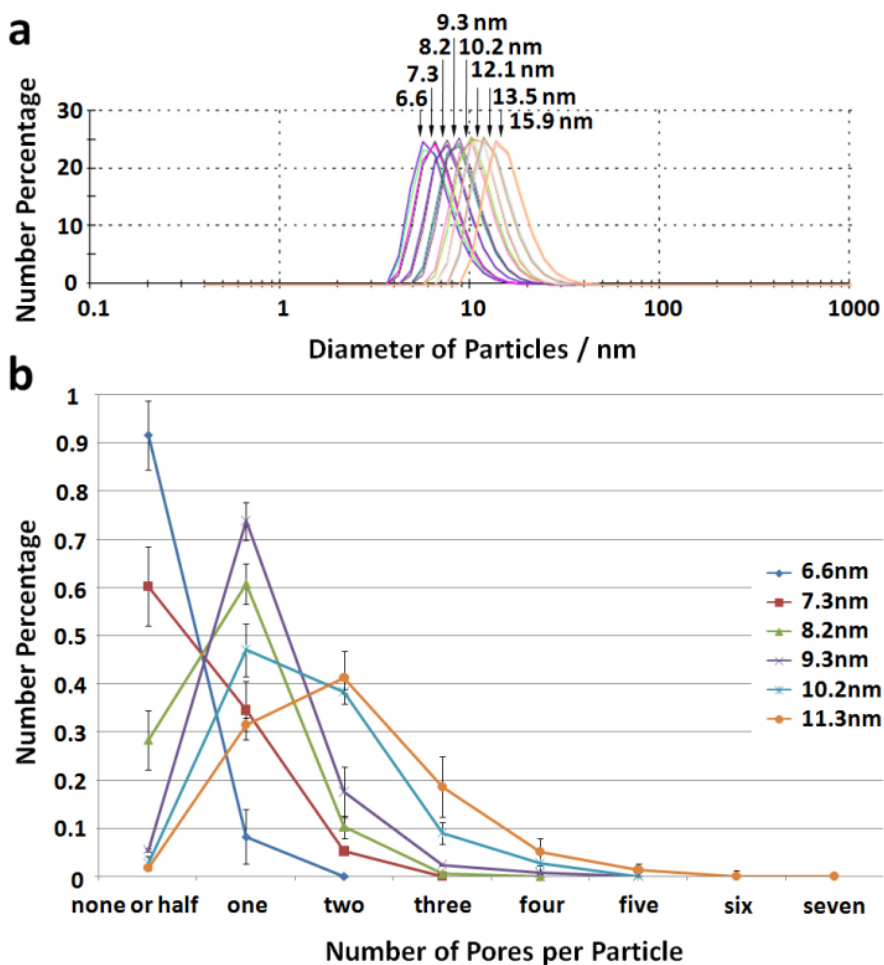


Figure 4.8. Analysis of particle size and morphology distributions. (a) DLS measurement results of selected particles with different average diameters synthesized with ammonium hydroxide as catalyst. (b) Distributions of number of pores per particle determined from TEM image analysis.

The narrow size distribution of particles from different batches enables taking a look at the morphological evolution as a function of particle size. In order to quantitatively assess this evolution, the TEM images of samples in Figure 4.7 were used to analyze the distribution of the number of pores per particle for each of the batches (see experimental section for details). Results of this analysis are shown in Figure 4.8b. As the average

diameter of the particles increases, the distribution of the number of pores per particle shifts to larger numbers and, more interestingly, becomes wider. Among the batches studied, the 9.3nm sample has the most homogeneous pore morphology; more than 70 percent of the particles are single-pore particles. Non-pore or half-pore particles, *i.e.* pieces that stem from unfinished micelle encapsulation by the growing silica (see Figure 4.1) can hardly be found.

In order to relate particle morphology to particle size, we further quantitatively analyzed the distribution of particle diameter on the basis of the TEM data (see experimental section for details). As demonstrated by the data in Figure 4.9, all samples showed relatively narrow size distributions. However, as the average diameter increases, in analogy to the analysis in Figure 4.8b of the number of pore distributions, the distributions of particle diameter shift to the right side and become wider. Obviously, these two distributions are related. In order to further elucidate this relation we inserted a series of TEM images of individual particles into the top of Figure 4.9. This series nicely details the morphological evolution of individual particles with increasing diameter as depicted by the x-axis. As particles grow from around 3nm to close to 20nm, the number of pores per particle gradually increases from none to more than four. Through snapshots of particles from various batches this series of images graphically illustrates the growth process of an individual mesoporous silica nanoparticle with time, compare also with Figure 4.1. It is interesting to note that the TEM image of the silica particle with diameter around 10-11nm actually exhibits a single-pore star-shaped morphology (Figure 4.9). Actually, we could find lots of particles with this star-shape morphology in the related low magnification TEM images (Figure 4.7 e and f), suggesting that there are always several CTAB micelles surrounding one particle during its formation. Another interesting point is that almost all

of the single-pore particles have accessible pores, instead of the formation of hollow shells (Figure 4.7 d to f). This might suggest that the association of CTAB micelles in the silica particle formation process is more dynamic rather than static. More experimental work is clearly needed, however, to draw further conclusions on the exact role of CTAB micelles and free CTAB molecules, in particular in the very early stages of the formation of the porous silica nanoparticles studied here.

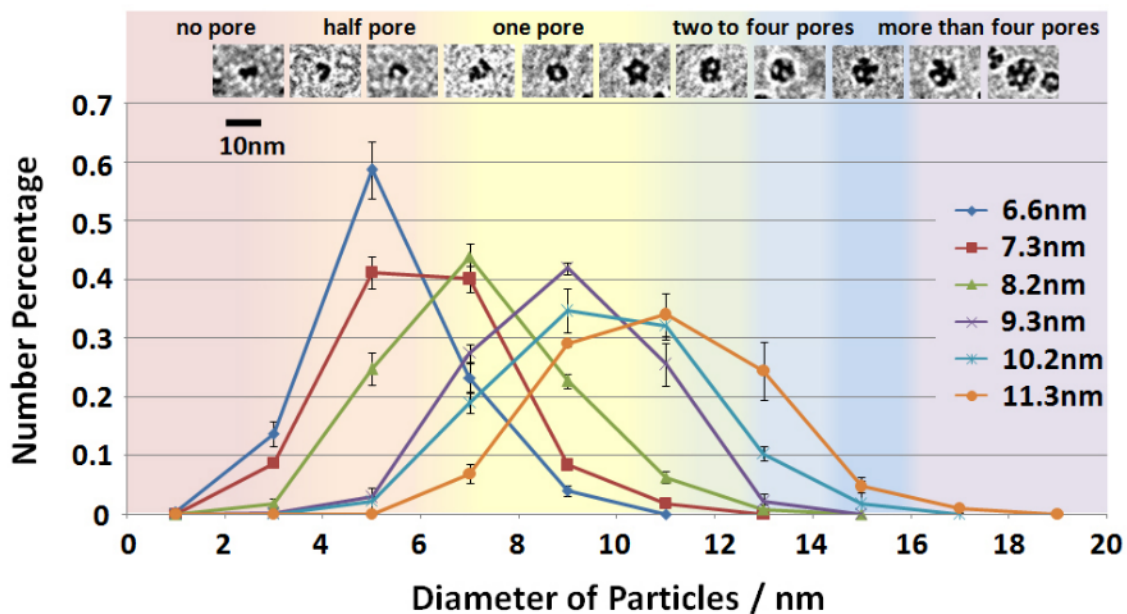


Figure 4.9. Morphology evolution dependent on particle size. Particle size distributions as determined by TEM image analysis. Inserted TEM images (top) correlate particle morphology with size. Colors identify size ranges leading to the same particle morphology.

In order to further facilitate the direct comparison between the distributions of particle diameter with the distributions of the number of pores per particle, in Figure 4.9 we assigned different colors to particle diameter ranges leading to the same number of pores per particle. For example, the pink area represents non-pore or half-pore particles while the yellow area represents single-pore particles. Colors change gradually as there is no distinct cut-off size between different morphologies. In Figure 4.9, the yellow area is

the biggest area beginning from around 6nm and ending at around 11nm. All particles with diameters within this area are single-pore particles. In comparison, the areas of two-pore to four-pore particles are smaller. This is reasonable in light of geometrical considerations. In order to maintain a relatively low overall surface energy, MSNs always tend to have sphere-like shape. For this reason, growing a new pore on a bigger particle with more pores will cause less increment of particle size.

From the color code in Figure 4.9, it is straightforward to tell the morphology distribution of samples with different average diameters, consistent with the independent measurements shown in Figure 4.8b. For example, the diameter distribution of the 6.6nm sample occupies both the pink and yellow areas, which suggests there are non-pore particles, half-pore particles and also single-pore particles present in this sample. According to Figure 4.9, the percentage of the non-pore and half-pore particles in this sample is roughly around 80%, which is close to the independent measurement result around 90% shown in Figure 4.8b. The slight discrepancy is due to the fact that there is no distinct cut-off diameter between particles with different pore morphologies. Since Figure 4.9 provides a semi-quantitative idea about the morphological homogeneity of a given size distribution, it is a very helpful diagram in guiding the synthesis of ultra-small mesoporous silica nanoparticles, *e.g.* for nanotheranostic applications. According to Figure 4.9, among the particles with well-developed pores, the single-pore particles cover the widest diameter range from around 6nm to around 11nm (yellow area in Figure 4.9). First, this size range matches well with the targeted size window for rapid renal excretion and favorable biodistribution characteristics of nanoparticles.^{30-32,61} Second, considering the fact that the diameter distribution of synthesized samples is always several nanometers wide, this 6-

11nm size range is able to include almost the entire size distribution of an individual particle synthesis batch. It thus allows achieving an optimum in homogeneity in pore morphology within a single synthesis. For these reasons, the size region from 6nm to 11nm, as indicated as the yellow area in Figure 4.9, is typical the golden region for synthesis of single-pore silica nanoparticles to serve as the desirable nanocarriers with fast renal clearance.

One of the presented samples whose diameter distribution fits into this range is the 9.3nm sample (Figure 4.9). As shown in the corresponding TEM images (Figure 4.7d), the synthesized particles are uniformly sized and homogeneous in morphology, *i.e.* almost all of the particles have a single well-defined pore. This is further elucidated for this batch by the number of pores per particle distribution analysis shown in Figure 4.8b.

4.4.5 Local structure and long-term stability of ultra-small single pore silica nanoparticles.

In our previous study we already characterized mC dots via liquid ^1H NMR to demonstrate successful CTAB removal as well as the presence of PEG chains on the particle surface.³³ CTAB removal was further corroborated in our first study by nitrogen sorption/desorption measurements.³³ In order to reveal local structure, here the 9.3nm single pore particles were subjected to ^{13}C and ^{29}Si solid state NMR characterizations. As shown in Figure 4.10a, the ^{13}C solid state NMR spectrum shows peaks at around 9 ppm, 23 ppm, 59 ppm, 71 ppm and 73 ppm which correspond to signals from the PEG-silane (see inserted figure). The absence of a peak from the methoxy groups (Figure 4.10a, labeled 5), expected at around 50ppm, indicates complete hydrolysis and suggests condensation of PEG-silane onto the particle surface. Furthermore, the absence of signals in the ^{13}C solid

state NMR spectrum of peaks from CTAB expected at 34, 32 and 29ppm, respectively, is consistent with our earlier liquid NMR results (*vide supra*) confirming its complete removal. The ^{29}Si solid state NMR spectrum in Figure 4.10b shows five peaks. The peaks at around -111 ppm, -102 ppm and -92 ppm correspond to Q^4 ($\text{Si}(\text{OSi})_4$), Q^3 ($\text{Si}(\text{OSi})_3(\text{OH})$), and Q^2 ($\text{Si}(\text{OSi})_2(\text{OH})_2$) groups. The peaks at around -67 ppm and -58 ppm correspond to T^3 ($\text{R-Si}(\text{OSi})_3$) and T^2 ($\text{R-Si}(\text{OSi})_2(\text{OH})$) groups. The presence of T groups in addition to Q groups further indicates the condensation of PEG-silane on the particle surface. Considering the particles were dialyzed using a dialysis membrane with 10k molecular weight cut off before NMR characterization, self-condensed PEG-silane should have been washed away from this sample. For this reason, the T groups actually represent the PEG-silane which condenses onto the particles and confirm the formation of a PEG layer on the silica nanoparticles.

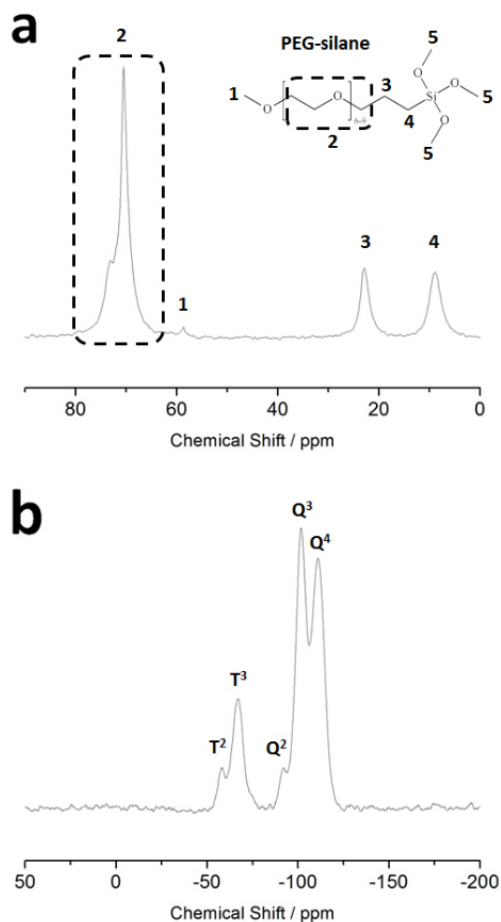


Figure 4.10. Solid state NMR spectra of 9.3nm mesoporous silica particles. (a) ^{13}C solid state NMR spectrum. (b) ^{29}Si solid state NMR spectrum.

In order to quantitatively characterize the density of PEG chains on the particle surface, 9.3nm single pore particles were subjected to TGA. From Figure 4.11a, around 58wt% of inorganic material (silica) remained as temperatures increased from room temperature to 600°C, while around 40wt% of organic components (mostly PEG) were burned away. The number of chains per particle and the surface density of PEG chains can then be estimated by simplifying the morphology of the 9.3nm (hydrodynamic diameter) single pore particles as tubes with 8nm outer diameter, 3nm inner diameter and 8nm length. The density of dense silica nanoparticle is between 1.4 to 2.1 g/cm³.⁴⁹ Using the lowest

density of silica 1.4 g/cm^3 in calculation, there are at least 400 PEG chains per particle and the PEG chains surface density is about 1.6 PEGs/nm^2 . Considering the surface density of native silanol groups on bare silica is $4.9/\text{nm}^2$, this number suggests that the surface of the single pore particles is almost fully covered by PEG chains. This is consistent with the zeta-potential of these particles measured in PBS 1X (pH 7.5) as -3.4mV *i.e.* very close to zero, despite a very short PEG chain length. For a 10ml reaction, around 15-18mg powder of the 9.3nm dialyzed particles were collected after drying using a rotary evaporator, of which 58wt% or 10mg was silica. Considering 0.22mmol of TMOS were added into the 10ml reaction in theory generating about 14mg of silica at 100% yield, the estimated yield of the reaction is about 71%. Losses in yield could *e.g.* be the result of premature termination of the reaction by addition of PEG-silane.

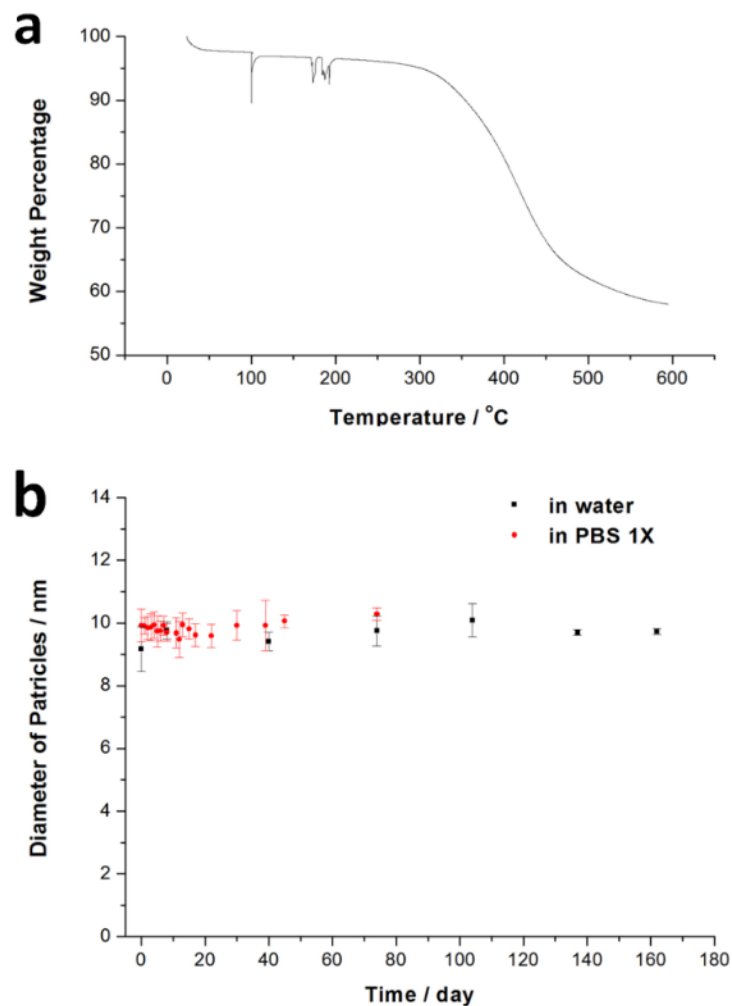


Figure 4.11. Thermogravimetric analysis and long-term stability of PEGylated single-pore silica nanoparticles. (a) Thermogravimetric analysis of dried 9.3nm single pore silica nanoparticles. (b) Long-term stability test of 9.3nm single pore silica nanoparticles in both PBS 1X and DI water measured by DLS.

Via PEGylation the particles are sterically stabilized after synthesis for *in-vivo* applications. In order to test the long-term stability of these ultra-small mesoporous particles in physiologically relevant media, the 9.3nm single pore particles were transferred into PBS 1X (pH 7.5) and the hydrodynamic particle size was monitored over several months via DLS. From Figure 4.11b, in PBS 1X the average hydrodynamic particle diameter increased to 9.7nm and remained close to this value for more than two months (at

which point we stopped measurements as bacteria had grown in the vial). Furthermore, in DI water the particles retained their initial size for almost half a year, see Figure 4.11b. These data demonstrate that particles neither degrade nor aggregate on these time scales corroborating the stable PEGylation protocol developed here.

4.4.6 Ultra-small fluorescent single-pore silica nanoparticles with multiple colors.

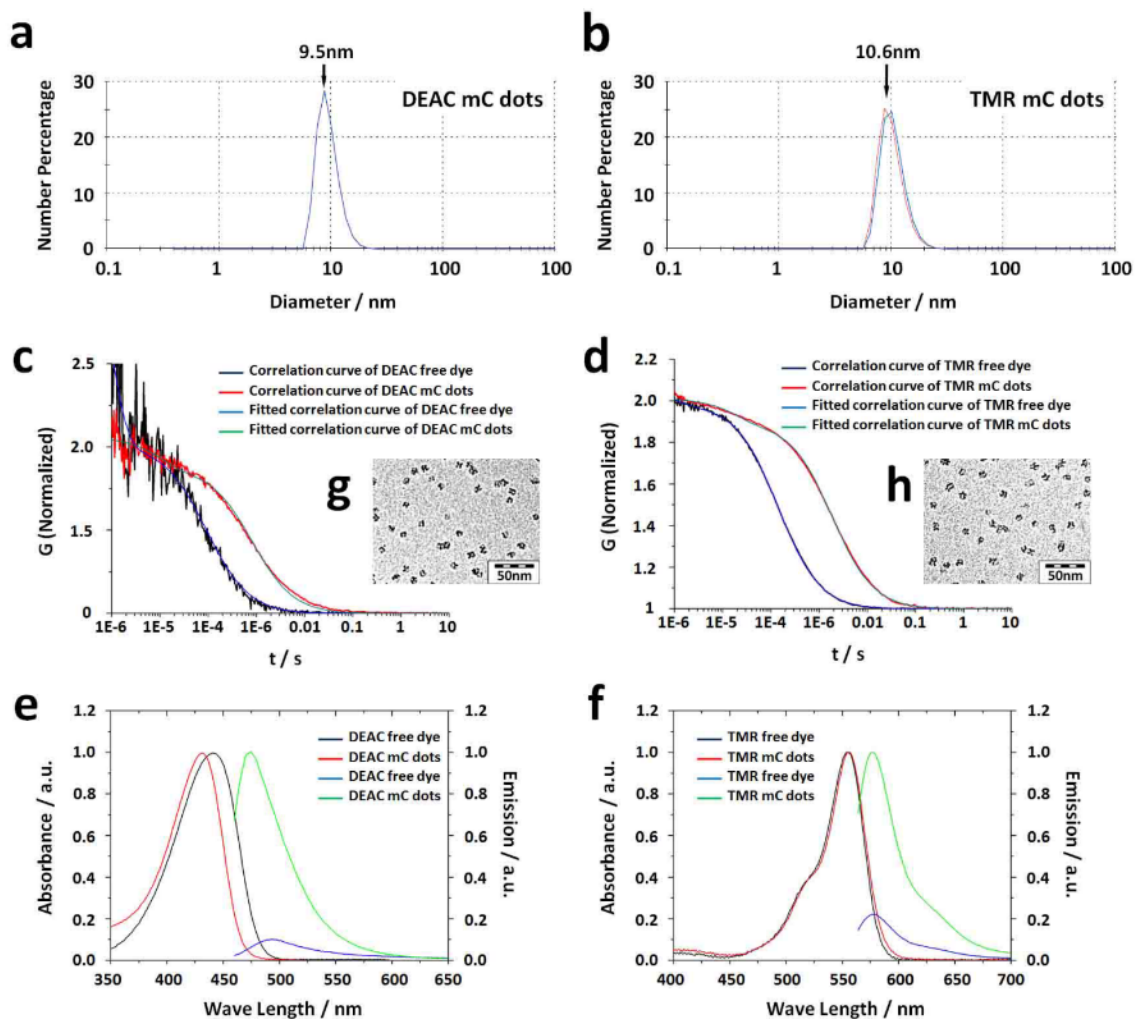


Figure 4.12. Characterization of mC dots with different colors. Graphs (a), (c), (e) and (g) display characterization results for DEAC labeled mC dots. Graphs (b), (d), (f) and (h) show characterization results for TMR labeled mC dots. Graphs (a) and (b) show DLS measurement results of dye labeled mC dots. Graphs (c) and (d) show the comparison of FCS correlation curves between free dye molecules and dye-labeled mC dots. Graphs (e) and (f) display spectrophotometer and spectrofluorometer measurement results of free dye

molecules and dye-labeled mC dots. Displays (g) and (h) show TEM images of dye labeled mC dots.

As discussed above, the particles synthesized in this system with average diameter around 9.3nm have the most homogeneous single-pore morphology and also potentially the most favorite biodistribution characteristics. In order to further visualize such sub-10nm single-pore silica nanoparticles in *in-vitro* and *in-vivo* experiments, labeling with fluorescent dyes is highly desirable. To this end we slightly modified the synthesis protocol for the 9.3nm particles by simultaneously adding silane conjugated dyes and TMOS into the reaction mixture. In our previous report, we have showed that in this way near infrared (NIR) fluorescent dye Cy5.5 could be successfully encapsulated into the single pore silica nanoparticles leading to ultra-small (<10nm) NIR fluorescent mesoporous silica nanoparticles or, in short, mC dots.³³ Here, we generalized this approach to other colors for multi-color imaging applications. In addition to Cy5.5, two types of dyes with different absorption and emission characteristics, DEAC (blue) and TMR (green), were used for the synthesis of mC dots. Shown by Figure 4.12a and b, the average hydrodynamic diameters of the DEAC and TMR dye-labeled mC dots were 9.5nm and 10.6nm respectively. Figure 4.11g and h show TEM images of the respective mC dots. From these images most of the particles maintained the single-pore morphology. Both, DLS measurements and TEM images, suggest that adding silane-conjugated dyes does not significantly change morphological characteristics of the single-pore silica nanoparticles as compared to the non-fluorescent species. From photospectrometer and fluorometer measurements, Figure 4.12e and f, the absorption/emission maxima of DEAC and TMR free dye are around 440/495nm and 554/579nm, respectively, while those of the encapsulated dyes are at 431/475nm and 556/576nm, respectively. From previous studies it is known that

encapsulation into silica can enhance the fluorescence intensity due to an increase in quantum efficiency of the dyes.^{27,29} Through absorption matching of free dye and particle solutions and comparing the emission maxima (Figure 4.12e and f), we determined the relative quantum enhancements of DEAC and TMR in our silica particles versus free dye in aqueous solution as 12.3 and 3.5, respectively. In other words, encapsulated in the mC dots a DEAC/TMR dye is 12.3/3.5 times brighter than as a free dye in aqueous solution. In order to further quantify size and brightness characteristics of the mC dots we used fluorescent correlation spectroscopy (FCS) for particle characterization. Figure 4.11c and d show comparisons of FCS correlation curves between free dyes and dye-labeled mC dots for DEAC and TMR, respectively. In both cases the FCS correlation curves of the particles are shifted to longer time due to that the larger particles need the longer time to diffuse through the same focal observation volume. FCS derived particle diameters for DEAC free dye/DEAC based mC dot and TMR free dye/TMR based mC dot are 1.4/9.7nm and 1.6/13.2nm, respectively. This is in reasonable agreement with the DLS results, *vide-supra*, verifying that the silica particles detected in DLS are successfully labeled with dye. Furthermore, FCS measurements also provide the concentration of the diffusing species. By combining this information with results of static optical measurements shown in Figure 4.11e and f, one can derive the average number of dyes per particle,²⁹ which was 1.2 and 2.1 for DEAC and TMR labeled mC dots, respectively. According to previous studies on structure-photophysical property correlations of C dots,^{29,62-64} the high quantum enhancements observed here for TMR, and in particular DEAC labeled mC dots, suggest that the dyes are incorporated inside the silica walls of the mC dots.

4.5 Conclusions

In this paper we have shown that proper choice of silica precursors (TMOS, dye-conjugated silanes), solvent (water) catalyst (L-lysine, ammonium hydroxide) and reaction conditions (monomer and catalyst concentrations, temperature, time-point of addition of PEG-silane capping agent) leads to exquisite control over size and size distribution of ultra-small (<10 nm) CTAB directed MSNs. Key elements of achieving this control are (i) fast hydrolysis (by means of TMOS as monomer), (ii) slow condensation (by means of moderate temperatures and low monomer/catalyst concentrations) and (iii) quenching of particle growth by addition of PEG-silane as a capping agent. The latter simultaneously achieves steric stabilization of particles for work in high-salt containing physiological environments. Results establish access to uniform, sub-10 nm, single pore fluorescent silica nanoparticles (mC dots) of various colors including NIR probes, with potential application as a theranostic nanomaterials platform with rapid renal excretion.

By controlling the particle growth rate and quenching the growth at appropriate time-points, average particle diameters can be precisely tailored from around 6nm to larger than 15nm with increments below 1nm. Furthermore, through analyzing particle diameter distributions and number of pores per particle distributions, we found that the synthesis batch with average particle diameter around 9.3nm had the most homogeneous single-pore morphology. This is fortunate as the associated size distribution matches the established size window for favorable renal excretion and biodistribution characteristics of PEG-ylated nanoparticles.^{30-32,61} Our approach enables the isolation and characterization of species at the very early stages of mesoporous silica nanoparticle formation. In future studies it may

thus provide a model system to investigate the mechanism of, *e.g.* the interaction between CTAB micelles and growing silica species at these early stages.

Finally, these results point towards exciting opportunities for further tailoring the ultra-small mesoporous particle materials platform. For example, in this paper we only reported results on C16 CTAB surfactant as structure directing agent. Varying the alkyl chain length of the surfactant, *e.g.* between C12 and C20, might further enable tailoring of pore size as well as overall particle size. Another dimension for tailoring the materials platform is a variation in composition. Rather than working with pure silica as reported here, other oxides, mixtures of oxides, or calcium phosphate based materials can be envisioned. This includes, *e.g.* aluminosilicates, as shown in related previous work of one of the co-authors,⁶⁵ or calcium phosphate silica composites.⁶⁶

4.6 Acknowledgements

K. M. gratefully acknowledges NSF for the financial support by Grant MPS/DMR-1008125. The authors acknowledge Cornell Center for Materials Research (CCMR) and Nanobiotechnology Center (NBTC) of Cornell University for the use of facilities. The authors also gratefully acknowledge H. Sai, S. K. Iyer, J. Drewes, Y. Sun and Z. Li of Cornell University and Dr. T. Suteewong of Memorial Sloan-Kettering Cancer for helpful discussions and kind experiment assistance.

4.7 References

- (1) B. Dunn, Cancer: Solving an Age-Old Problem. *Nature* **2012**, *483*, S2–S6.
- (2) Globocan 2008, *IARC*, **2010**
- (3) Peer, D.; Karp, J. M.; Hong, S.; Farokhzad, O. C.; Margalit, R.; Langer, R. Nanocarriers as an Emerging Platform for Cancer Therapy. *Nat. Nanotech.* **2007**, *2*, 751–760.
- (4) Schroeder, A.; Heller, D. A.; Winslow, M. M.; Dahlman, J. E.; Pratt, G. W.; Langer, R.; Jacks, T.; Anderson, D. G. Treating Metastatic Cancer with Nanotechnology. *Nat. Rev. Cancer* **2012**, *12*, 39–50.
- (5) Couvreur, P.; Kante, B.; Grislain, L.; Roland, M.; Speiser, P. Toxicity of Polyalkylcyanoacrylate Nanoparticles II: Doxorubicin-Loaded Nanoparticles. *J. Pharm. Sci.* **1982**, *71*, 790–792.
- (6) Batrakova, E. V.; Dorodnych, T. Y.; Klinskii, E. Y.; Kliushnenkova, E. N.; Shemchukova, O. B.; Goncharova, O. N.; Arjakov, S. A.; Alakhov, V. Y.; Kabanov, A. V. Anthracycline Antibiotics Non-Covalently Incorporated into the Block Copolymer Micelles: In Vivo Evaluation of Anti-Cancer Activity. *J. Cancer* **1996**, *74*, 1545–1552.
- (7) Tolcher, A. W.; Sugarman, S.; Gelmon, K. A.; Cohen, R.; Saleh, M.; Isaacs, C.; Young, L.; Healey, D.; Onetto N.; Slichenmyer, W. Randomized Phase II Study of BR96-Doxorubicin Conjugate in Patients With Metastatic Breast Cancer. *J. Clin. Oncology* **1999**, *17*, 478–484.

- (8) Nakanishi, T.; Fukushima, S.; Okamoto, K.; Suzuki, M.; Matsumura, Y.; Yokoyama, M.; Okano, T.; Sakurai, Y.; Kataoka, K. Development of The Polymer Micelle Carrier System for Doxorubicin. *J. Control. Release* **2001**, *74*, 295–302.
- (9) Torchilin, V. P. Recent Advances with Liposomes as Pharmaceutical Carriers. *Nat. Rev. Drug Discov.* **2005**, *4*, 145–160.
- (10) Duncan, R. Polymer Conjugates as Anticancer Nanomedicines. *Nat. Rev. Cancer* **2006**, *6*, 688–701.
- (11) Torchilin, V. P. Micellar Nanocarriers: Pharmaceutical Perspectives. *Pharm. Res.* **2007**, *24*, 1–16.
- (12) Luo, D.; Saltzman, W. M. Enhancement of Transfection by Physical Concentration of DNA at The Cell Surface. *Nature Biotechnol.* **2000**, *18*, 893–895.
- (13) Radu, D. R.; Lai, C. Y.; Jeftinija, K.; Rowe, E. W.; Jeftinija, S.; Lin, V. S. Y. A Polyamidoamine Dendrimer-Capped Mesoporous Silica Nanosphere-Based Gene Transfection Reagent. *J. Am. Chem. Soc.* **2004**, *126*, 13216–13217.
- (14) Vivero-Escoto, J. L.; Slowing, I. i.; Trewyn, B. G. and Lin, V. S. Y. Mesoporous Silica Nanoparticles for Intracellular Controlled Drug Delivery. *Small* **2010**, *6*, 1952–1967.
- (15) Rosenholm, J. M.; Peuhu, E.; Eriksson, J. E.; Sahlgren C.; Linden, M. Targeted Intracellular Delivery of Hydrophobic Agents using Mesoporous Hybrid Silica Nanoparticles as Carrier Systems. *Nano Lett.* **2009**, *9*, 3308–3331.
- (16) Du, L.; Liao, S.; Khatib, H. A.; Stoddart, J. F.; Zink, J. I. Controlled-Access Hollow Mechanized Silica Nanocontainers. *J. Am. Chem. Soc.* **2009**, *131*, 15136–15142.

- (17) Bharali, D. J.; Klejbor, I.; Stachowiak, E. K.; Dutta, P.; Roy, I.; Kaur, N.; Bergey, E. J.; Prasad, P. N.; Stachowiak, M. K. Organically Modified Silica Nanoparticles: A Nonviral Vector for In Vivo Gene Delivery and Expression in The Brain. *Proc. Natl Acad. Sci. USA* **2005**, *102*, 11539–11544.
- (18) Hu, S.; Liu, T.; Huang, H.; Liu, D.; Chen, S. Magnetic-Sensitive Silica Nanospheres for Controlled Drug Release. *Langmuir*, **2008**, *24*, 239–244.
- (19) Roy, I.; Ohulchansky, T. Y.; Bharali, D. J.; Pudavar, H. E.; Mistretta, R. A.; Kaur, N.; Prasad, P. N. Optical Tracking of Organically Modified Silica Nanoparticles as DNA Carriers: A Nonviral, Nanomedicine Approach for Gene Delivery. *Proc. Natl Acad. Sci. USA* **2005**, *102*, 279–284.
- (20) Lee, J. E.; Lee, N.; Kin, T.; Kim, J. and Hyeon, T. Multifunctional Mesoporous Silica Nanocomposite Nanoparticles for Theranostic Applications. *Acc. Chem. Res.* **2011**, *44*, 893–902.
- (21) Torney, F.; Trewyn, B. G.; Lin, V. S. L.; Wang, K. Mesoporous Silica Nanoparticles Deliver DNA and Chemicals into Plants. *Nat. Nanotech.* **2007**, *2*, 295–300.
- (22) Piao, Y.; Burns, A.; Kim, J.; Wiesner, U. and Hyeon, T. Designed Fabrication of Silica-Based Nanostructured Particle Systems for Nanomedicine Applications. *Adv. Funct. Mater.* **2008**, *18*, 3745–3758.
- (23) Ashley, C. E.; Carnes, E. C.; Phillips, G. K.; Padilla, D.; Durfee, P. N.; Brown, P. A.; Hanna, T. N.; Liu, J.; Phillips, B.; Carter, M. B.; Carroll, N. J.; Jiang, X.; Dunphy, D. R.; Willman, C. L.; Petsev, D. N.; Evans, D. G.; Parikh, A. N.; Chackerian, B.; Wharton, W.; Peabody, D. S.; Brinker, C. F. The Targeted Delivery of

- Multicomponent Cargos to Cancer Cells by Nanoporous Particle-Supported Lipid Bilayers. *Nat. Mater.* **2011**, *10*, 389–397.
- (24) Lin, Y.; Abadeer, N.; Haynes C. L. Stability of Small Mesoporous Silica Nanoparticles in Biological Media. *Chem. Commun.* **2011**, *47*, 532–534.
- (25) He, Q.; Shi, J.; Zhu, M.; Chen, Y.; Chen, F. The Three-Stage In Vitro Degradation Behavior of Mesoporous Silica in Simulated Body Fluid. *Micropor. Mesopor. Mater.* **2010**, *131*, 314–320.
- (26) Yamada, H.; Urata, C.; Aoyama, Y.; Osada, S.; Yamauchi, Y.; Kuroda, K. Preparation of Colloidal Mesoporous Silica Nanoparticles with Different Diameters and Their Unique Degradation Behavior in Static Aqueous Systems. *Chem. Mater.* **2012**, *24*, 1462–1471.
- (27) Ow, H.; Larson, D.; Srivastava, M.; Baird, B.; Webb, W.; Wiesner, U. Bright and Stable Core–Shell Fluorescent Silica Nanoparticles. *Nano Lett.* **2005**, *5*, 113–117.
- (28) Burns, A.; Ow, H.; Wiesner, U. Fluorescent Core-Shell Silica nNanoparticles: Towards "Lab on a Particle" Architectures for Nanobiotechnology. *Chem. Soc. Rev.* **2006**, *35*, 1028–1042.
- (29) Larson, D. R.; Ow, H.; Vishwasrao, H. D.; Heikal, A. A.; Wiesner, U.; Webb, W. W. Silica Nanoparticle Architecture Determines Radiative Properties of Encapsulated Fluorophores. *Chem. Mater.* **2008**, *20*, 2677–2684.
- (30) Burns, A.; Vider, J.; Ow, H.; Herz, E.; Penate-Medina, O.; Baumgart, M.; Larson, S. M.; Wiesner, U.; Bradbury, M. Fluorescent Silica Nanoparticles with Efficient Urinary Excretion for Nanomedicine. *Nano Lett.* **2009**, *9*, 442–448.

- (31) P. B.; Schaer, D.; Ow, H.; Burns, A.; DeStanchina, E.; Longo, V.; Herz, E.; Iyer, S.; Wolchok, J.; Larson, S. M.; Wiesner, U. and Bradbury M. Multimodal Silica Nanoparticles are Effective Cancer-Targeted Probes in a Model of Human Melanoma. *J. Clin. Invest.* **2011**, *121*, 2768–2780.
- (32) Choi, H. S.; Liu, W.; Misra, P.; Tanaka, E.; Zimmer, J. P.; Ipe, B. I.; Bawendi, M. G.; Frangioni, J. V. Renal Clearance of Quantum Dots. *Nat. Nanotech.* **2007**, *25*, 1165–1170.
- (33) Ma, K.; Sai, H.; Wiesner, U. Ultrasmall Sub-10 nm Near-Infrared Fluorescent Mesoporous Silica Nanoparticles. *J. Am. Chem. Soc.* **2012**, *134*, 13180–13183.
- (34) Lu, F.; Wu, S.; Hung, Y.; Mou, C. Size Effect on Cell Uptake in Well-Suspended, Uniform Mesoporous Silica Nanoparticles. *Small* **2009**, *5*, 1408–1413.
- (35) Urata, C.; Aoyama, Y.; Tonegawa, A.; Yamauchi, Y.; Kuroda, K. Dialysis Process for The Removal of Surfactants to Form Colloidal Mesoporous Silica Nanoparticles. *Chem. Commun.* **2009**, 5094–5096.
- (36) LaMer, V. K.; Dinegar R. H. Theory, Production and Mechanism of Formation of Monodispersed Hydrosols. *J. Am. Chem. Soc.* **1950**, *72*, 4847–4854.
- (37) Sugimoto, T. Preparation of Monodispersed Colloidal Particles. *Adv. Colloid Interface Sci.* **1987**, *28*, 65–108.
- (38) Reiss, H. The Growth of Uniform Colloidal Dispersions. *J. Chem. Phys.* **1951**, *19*, 482–487.
- (39) Murray, C. B.; Kagan, C. R.; Bawendi, M. G. Synthesis and Characterization of Monodisperse Nanocrystals and Close-Packed Nanocrystal Assemblies. *Annu. Rev. Mater. Sci.* **2000**, *30*, 545–610.

- (40) Bawendi, M. G.; Steigerwald, M. L.; Brus, L. E. The Quantum Mechanics of Larger Semiconductor Clusters ("Quantum Dots"). *Annu. Rev. Phys. Chem.* **1990**, *41*, 477–496
- (41) Murray, C. B.; Norris, D. J.; Bawendi, M. G. Synthesis and Characterization of Nearly Monodisperse CdE (E = S, Se, Te) Semiconductor Nanocrystallites. *J. Am. Chem. Soc.* **1993**, *115*, 8706–8715.
- (42) Kwon, S. G.; Hyeon, T. Formation Mechanisms of Uniform Nanocrystals via Hot-Injection and Heat-Up Methods. *Small* **2011**, *7*, 2685–2702.
- (43) Szwarc, M. Living Polymers. *Nature* **1956**, *178*, 1168–1169.
- (44) Smid, J. Historical Perspectives on Living Anionic Polymerization. *J. Polym. Sci. Part A.* **2002**, *40*, 2101–2107.
- (45) Hsieh, H.; Quirk, R. *Anionic Polymerization: Principles and practical applications*; Marcel Dekker, Inc.: New York, 1996.
- (46) Quirk, R. *Encyclopedia of Polymer Science and Technology*; John Wiley and Sons: New York, 2003.
- (47) Blackeley, D.; Twaits, R. *Addition Polymers: Formation and Characterization*; Plenum Press: New York, 1968
- (48) Wang, J.; Sugawara-Narutaki, A.; Fukao, M.; Yokoi, T.; Shimojima, A.; Okubo, T. Two-Phase Synthesis of Monodisperse Silica Nanospheres with Amines or Ammonia Catalyst and Their Controlled Self-Assembly. *ACS Appl. Mater. Interfaces* **2011**, *3*, 1538–1544.
- (49) Brinker, C. J. *Sol-Gel Science*, Academic Press Inc.: CA, 1990.

- (50) McKee, T.; McKee, J. R. *Biochemistry*; McGraw-Hill Companies Inc.: New York, 2003.
- (51) Yokoi, T.; Sakamoto, Y.; Terasaki, O.; Kubota, Y.; Okubo, T.; Tatsumi, T. Periodic Arrangement of Silica Nanospheres Assisted by Amino Acids. *J. Am. Chem. Soc.* **1996**, *118*, 13664–13665.
- (52) Lin, Y.; Haynes, C. L. Impacts of Mesoporous Silica Nanoparticle Size, Pore Ordering, and Pore Integrity on Hemolytic Activity. *J. Am. Chem. Soc.* **2010**, *132*, 4834–4842.
- (53) Schipper, M. L.; et al. Particle Size, Surface Coating, and PEGylation Influence the Biodistribution of Quantum Dots in Living Mice. *Small* **2009**, *5(1)*, 126–134.
- (54) Hauck, T. S.; Anderson, R. E.; Fischer, H. C.; Newbigging, S.; Chan, W. C. W. In Vivo Quantum-Dot Toxicity Assessment. *Small* **2010**, *6(1)*, 138–144.
- (55) Lin Y.; Abadder, N.; Hurley, K. R.; Haynes, C. L. Ultrastable, Redispersible, Small, and Highly Organomodified Mesoporous Silica Nanotherapeutics. *J. Am. Chem. Soc.* **2011**, *133*, 20444–20457.
- (56) Jeong, B.; Bae, Y. H.; Kim, S. W. Thermoreversible Gelation of PEG–PLGA–PEG Triblock Copolymer Aqueous Solutions. *Macromolecules*, **1999**, *32*, 7064–7069.
- (57) Möller, K.; Kobler, J.; Bein, T. Colloidal Suspensions of Nanometer-Sized Mesoporous Silica. *Adv. Funct. Mater.* **2007**, *17*, 605–612.
- (58) Beck, J. S.; Vartuli, J. C.; Roth, W. J.; Leonowicz, M. E.; Kresge, C. T.; Schmitt, K. D.; Chu, C. T.; Olson, D. H.; Sheppard, E. W.; McCullen, S. B.; Higgins, J. B.; Schlenker, J. L. *J. Am. Chem. Soc.* **1992**, *114*, 10834–10843.

- (59) Stöber, W.; Fink, A. A New Family of Mesoporous Molecular Sieves Prepared with Liquid Crystal Templates. *J. Colloid Interface Sci.* **1968**, *26*, 62–69.
- (60) Tan, C. G.; Bowen, B. D.; Epstein, N. *J. Colloid Interface Sci.* **1987**, *188*, 290–293.
- (61) Gao, J.; Luong, R.; Bouley, D. M.; Mao, H.; Qiao, T.; Gambhir, S. S.; Cheng, Z. A Novel Clinically Translatable Fluorescent Nanoparticle for Targeted Molecular Imaging of Tumors in Living Subjects. *Nano Lett.* **2012**, *12*, 281–286
- (62) Herz, E.; Ow, H.; Bonner, D.; Burns, A.; Wiesner, U. Dye Structure–Optical Property Correlations in Near-Infrared Fluorescent Core-Shell Silica Nanoparticles. *J. Mater. Chem.* **2009**, *19*, 6341–6347.
- (63) Herz, E.; Marchincin, T.; Connelly, L.; Bonner, D.; Burns, A.; Switalski, S.; Wiesner, U. Relative Quantum Yield Measurements of Coumarin Encapsulated in Core-Shell Silica Nanoparticles. *J. Fluoresc.* **2010**, *20*, 67–72.
- (64) Cohen, B.; Martin, C.; Iyer, S. K.; Wiesner, U.; Douhal, A. Single Dye Molecule Behavior in Fluorescent Core–Shell Silica Nanoparticles. *Chem. Mater.* **2012**, *24*, 361–372.
- (65) Templin, M.; Franck, A.; Du Chesne, A.; Leist, H.; Zhang, Y.; Ulrich, R.; Schädler, V.; Wiesner, U. Organically Modified Aluminosilicate Mesostructures from Block Copolymer Phases. *Science* **1997**, *278*, 1795–1798.
- (66) Altinoglu, E. I.; Russin, T. J.; Kaiser, J. M.; Barth, B. M.; Eklund, P. C.; Kester, M.; Adair, J. H. Near-Infrared Emitting Fluorophore-Doped Calcium Phosphate Nanoparticles for In Vivo Imaging of Human Breast Cancer. *ACS Nano* **2008**, *2*, 2075–2084.

Chapter 5 . Elucidating the Mechanism of Silica Nanoparticle PEGylation Processes using Fluorescence Correlation Spectroscopies

5.1 Abstract

Surface modification with polyethylene glycol (PEG; PEGylation) is a widely used technique to improve nanoparticle (NP) stability, biocompatibility and biodistribution profiles. In particular, PEGylation of silica surfaces and coatings plays a pivotal role across various classes of NPs. Despite the use of numerous protocols there is limited fundamental understanding of the mechanisms of these processes for NPs. Here, after reaction optimization for particle stability, we employ fluorescence correlation and cross-correlation spectroscopy (FCS, FCCS) on ultrasmall (< 10 nm) fluorescent silica nanoparticles (SNPs) as a test bed. We show unexpected fast reaction kinetics in successful PEGylation observed even at nano molar concentrations and attributed to instant non-covalent adsorption of PEG molecules to the SNP surface preceding covalent attachment. Further studies of various reaction conditions enable the elucidation of process design criteria for NP PEGylation and surface modification with functional ligands, which may be applicable to a broad range of NPs thereby accelerating progress in fields ranging from bio-sensing to nanomedicine.

5.2 Introduction

The global market for nanomedicine is expected to grow with an annual rate of 12.3% and reach a value of >170 billion in 2019.¹ As one of the most promising nanomedicine candidates, multifunctional organic-inorganic hybrid NPs have attracted significant research attention world-wide for both imaging/diagnostics and therapeutics.²⁻⁵ However, in order to successfully translate hybrid NPs from the laboratory to the clinic, PEGylation is an essential step to endow NPs with long-term stability as well as favorable biodistribution and pharmacokinetics (PK) profiles.⁶⁻⁸ In the last decade, silica coating techniques have been established to stabilize inorganic NPs in aqueous media without disturbing their physical properties.⁹ Therefore the PEGylation of silica surfaces and coatings plays a pivotal role for nanomedicine applications across various classes of nanomaterials, including dense¹⁰ and mesoporous silica nanoparticles (SNPs),^{11,12} quantum dots,¹³ gold NPs,^{14,15} magnetic NPs,¹⁶ graphene,¹⁷ and carbon nanotubes.¹⁸

Compared to the well-studied PEGylation of pharmaceuticals,¹⁹ *e.g.* proteins and peptides, the PEGylation of NPs enabling desirable biodistribution and PK often remains challenging due to the complexity of the interfacial reactions between NP surfaces and ligand molecules.^{20,21} Despite the use of numerous protocols to PEGylate specific NPs,²² little is known mechanistically about how this process proceeds, which in turn hampers the production of clinically translatable nanomaterials. To that end, here we take advantage of highly-tunable silica sol-gel chemistry and use ultras-small (<10 nm diameter) fluorescent SNPs, referred to as Cornell prime dots (C' dots), as a test bed to study the PEGylation mechanism of silica surfaces.^{10,23,24} Compared to larger NPs, ultras-small SNPs are more sensitive to surface reactions due to the enhanced particle surface to volume ratio.²⁵

Furthermore, using ultrasmall SNPs it is possible to work with relatively short PEG ligands (molar mass <1000 g/mole) for which the effects of different polymer conformations on the particle surface are less significant thereby reducing the complexity of the kinetics of attachment.²⁶ Finally, work on ultrasmall SNPs is particularly relevant as such <10 nm diameter particles have recently been successfully translated into the clinic²⁷ and multiple human clinical trials are currently ongoing.

Conventional techniques to characterize the result of NP PEGylation reactions include dynamic light scattering (DLS),²⁸ thermogravimetric analysis (TGA),²⁹ nuclear magnetic resonance (NMR) spectroscopy³⁰ and Raman analysis.³¹ These techniques provide detailed information on PEG loading and conformation on particle surfaces, however, little mechanistic insight is gained about how a successful PEGylation process proceeds. Fluorescence correlation spectroscopy, FCS, exploits fluorescence fluctuations induced by diffusing species in a confocal setup to analyze their mobility and concentrations.^{32,33} Its dual-color variant, fluorescence cross correlation spectroscopy, FCCS, simultaneously monitors the diffusion of two species with distinct fluorescence, and thus further provides information on their binding and co-localization (Fig. 5.1).³⁴ FCS and FCCS have been widely applied in the field of biology to study *e.g.* enzymatic reactions and protein interactions.^{35,36} Their application in material science remains limited,^{37,38} however, and is often confined to polymers.^{39,40} Especially, the use of FCCS to analyze the processes of nanomaterial fabrication has rarely been reported. Here, after varying PEGylation reaction conditions to optimize for particle stability, we labeled SNPs and PEGs with Cy5 and ATTO488 fluorophores, respectively, and introduced FCS and FCCS to interrogate details of the PEGylation pathway (Fig. 5.1). We found fast reaction kinetics

during successful PEGylation unexpected for conventional silanol hydrolysis and condensation and preventing NP aggregation in the transition from electrostatic to steric stabilization. Effects were attributed to an instant non-covalent association of PEGs and SNP surfaces, observed even at nano molar concentrations and accelerating covalent attachment (Fig. 5.1). Further studies on various reaction conditions enabled the elucidation of reaction design criteria for successful PEGylation, as well as NP surface modification with functional ligands. Results highlighted that NP surface modification reactions may involve multiple processes driven by different interactions, whose understanding is critical for optimal outcomes.

5.3 Experimental Section

5.3.1 Materials.

All chemicals were used as received without further purification. Dimethyl sulfoxide (DMSO), ethanol, (3-aminopropyl)triethoxysilane (amine-silane), (3-mercaptopropyl) trimethoxysilane (thiol-silane), tetramethyl orthosilicate (TMOS), ammonium hydroxide and polyethylene glycol (PEG 400, molecular weight 400 g/mole) were purchased from Sigma Aldrich. 2-[Methoxy(polyethyleneoxy)propyl] trimethoxysilane (PEG-silane, molar mass around 500 g/mole) was purchased from Gelest. Maleimido functionalized Cy5 fluorophore was purchased from GE healthcare. Amine functionalized ATTO488 fluorophore was purchased from ATTO-Tech. NHS ester functionalized PEGs, as well as heterobifunctional PEGs functionalized with both NHS ester and maleimido, were purchased from Quanta BioDesign. c(RGDyC) peptide was purchased from Peptide International. DI water was generated using a Millipore Milli-Q system.

5.3.2 Conjugation of Cy5-silane.

Maleimido functionalized Cy5 was mixed with thiol-silane in DMSO at molar ratio 1: 25 and concentrations of about 1mM. The mixtures were left under nitrogen overnight to label Cy5 fluorophore with silane through thiol-ene reaction.

5.3.3 Conjugation of ATTO488-PEG.

NHS ester functionalized PEGs were mixed with amine functionalized ATTO488 fluorophore in DMSO at molar ratio 1: 1.1 and concentrations of about 10mM. The mixtures were left under nitrogen overnight to label PEGs with ATTO488 fluorophores through amide bond formation.

5.3.4 Conjugation of c(RGDyC)-PEG-silane.

Heterobifunctional PEGs functionalized with NHS ester and maleimido groups (NHS-PEG-mal) were first mixed with amino-silane in DMSO at molar ratio 1: 1.1 and concentrations of about 10mM. The mixtures were left under nitrogen for two days to label NHS-PEG-mal with silane through amide bond formation. Afterwards, c(RGDyC) peptide was added into the mixture at c(RGDyC): PEG molar ratio 0.9: 1. The mixtures were left under nitrogen for another day to further label mal-PEG-silane with c(RGDyC) through thiol-ene reaction.

5.3.5 Synthesis of ultrasmall silica nanoparticles.

For the synthesis of 4-5 nm silica nanoparticles, 0.02 mmol ammonium hydroxide was added into 10 mL DI water as base catalyst. 0.43 mmol of TMOS was added into the solution under vigorous stirring. The stirring continued for 24 hours at room temperature. If applicable, silane conjugated Cy5 fluorophore, which was obtained through mixing maleimido functionalized Cy5 and MTPMS in DMSO at molar ratio 1:25, was added together with TMOS for fluorescent SNP synthesis. Afterwards, specific amounts (see main text) of PEG-silane were added and the solution was kept stirring for another 24 hours. If

applicable, c(RGDyC) functionalized PEG-silane was added right before the addition of PEG-silane for the synthesis of cancer-targeting PEGylated SNPs. Following that, the temperature was increased to 80°C and the stirring was stopped. The reaction was left at 80°C for 24 hours. The solution was finally cooled to room temperature and transferred into a dialysis membrane tube (Pierce, molecular weight cutoff, MWCO 10,000) for dialysis. The dialysis tube was then immersed into 2000 ml DI water and the water was changed twice per day for three days to clean the PEGylated SNPs. The particles were finally filtered through a 200 nm syringe filter (Fisher) and stored at room temperature for further characterization. The molar ratio of the reactants was 1 TOMS: 0.5 PEG-silane: 1292 H₂O. For the synthesis of particles with varying PEG surface density, the PEG-silane concentration used in the reaction was varied from 0 to 23.0mM.

5.3.6 Zeta potential measurements.

Zeta potential of the synthesized PEGylated SNPs was measured with a Malvern Zetasizer Nano-SZ operated at 20 °C. Samples were first concentrated using spinfilters (GE Healthcare, 30k MWCO) by up to 10 times for the desired signal to noise ratio. Details of the zeta potential measurement optimization can be found in Appendix C. Each sample was measured five times and the results were averaged.

5.3.7 DLS size measurements.

Hydrodynamic particle sizes and size distributions were measured by DLS using a Malvern Zetasizer Nano-SZ system operated at 20 °C. Each DLS sample was measured five times and the results were averaged.

5.3.8 TEM measurements.

TEM images were taken on a FEI Tecnai T12 Spirit microscope operated at an acceleration voltage of 120 kV. The TEM samples were prepared by dropping one droplet of the PEGylated SNP solution onto a TEM grid (EMS, carbon film on copper grids) and evaporation of solvent

5.3.9 TGA measurements.

TGA was conducted using a TA Instruments Q500 thermogravimetric analyzer. Before subjected to TGA, the synthesized PEGylated SNPs were first dried out from the aqueous solution using a FreeZone freeze dryer. During TGA measurements, the temperature was first increased to 100 °C with a ramp rate of 10 °C /min, and kept isothermal at 100 °C for 20 minutes to remove remaining water. The temperature was then increased up to 600 °C with a ramp rate of 10 °C /min and kept isothermal at 600 °C for 60 mins before the sample was cooled down to room temperature.

5.3.10 FCS and FCCS measurements.

FCS and FCCS measurements on the various Cy5-C' dot and ATTO488-PEG samples were conducted using a home-built FCS/FCCS set-up. A 635nm solid-state laser was used as the excitation source for the red channel and a 488nm solid-state laser was used as the excitation source for the blue channel. Small amounts of the reaction solution were aliquoted about every 1-2 mins during the synthesis for FCS measurements to monitor changes of SNP size. See Appendix C for detailed data analysis procedures.

5.3.11 Conductivity measurements.

Conductivity measurements were carried out using an Orion Star A215 pH/conductivity Benchtop multiparameter meter. About 24 hours after TMOS addition, the conductivity probe was inserted into the reaction solution for recording the solution conductivity. After that, 1.5ml PEG-silane or PEG 400 was added. To monitor the PEGylation reaction, the solution conductivity was recorded up until the high temperature treatment step.

5.3.12 Estimation of PEG-silane and c(RGDyC)-PEG-silane reaction conversion percentage.

The conversion percentage of PEG-silane with or without c(RGDyC) functionalization was estimated by taking the ratio of PEG-silane present in the final purified SNPs to the amount of PEG-silane added into the synthesis. The amount of PEG-silane (without cancer-targeting peptide functionalization) present in the final purified SNPs was estimated from TGA (provides mass) and FCS measurements (provides particle concentration). The amount of c(RGDyC)-PEG-silane present in the final purified SNPs was estimated by absorbance measurements as described elsewhere.¹⁰

5.4 Results and discussion

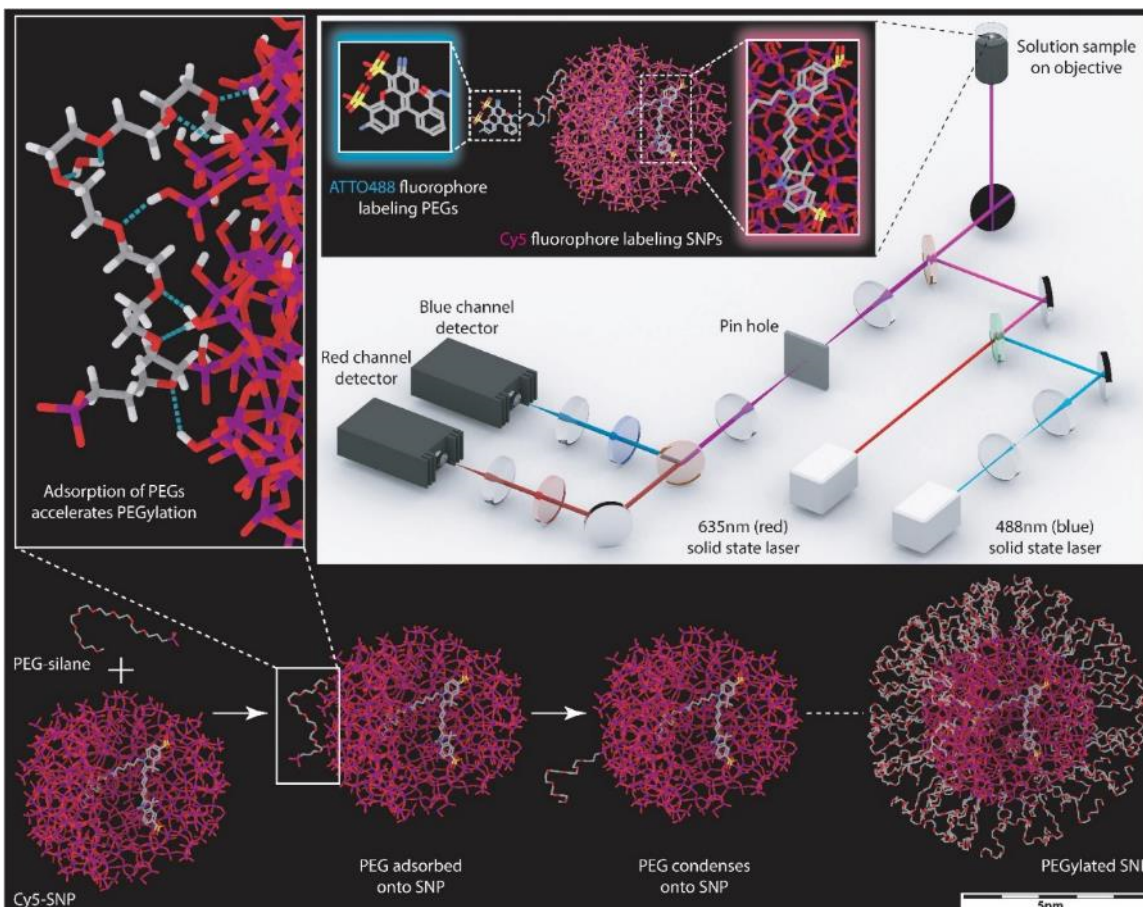


Figure 5.1. Illustration of SNP PEGylation mechanism as characterized by FCS and FCCS. The SNP PEGylation process (bottom) was monitored by FCS and FCCS (top right). In order to endow SNPs and PEGs with distinct fluorescence, they were labeled with Cy5 and ATTO488 fluorophores, respectively. Upon the addition of PEG-silane into SNP solution, a fast non-covalent association of PEGs and silica preceded the condensation of PEG-silane on SNP surface. The specific affinity between PEGs and silica accelerated the reaction kinetics thereby playing a key role in successful PEGylation. In the molecular renderings silicon, oxygen, carbon, hydrogen (only shown in inset on upper left, together with hydrogen bonds in light blue), nitrogen and sulfur atoms are color coded by purple, red, gray, white, blue and yellow, repetitively.

A series of SNPs with varying surface PEG density were first synthesized according to a previously reported method in which PEGylation is an integral part of the synthesis strategy to obtain narrowly size distributed particles.¹⁰ When the concentration of PEG-silane was increased from zero to 23mM, the number of PEG chains per particle and surface

PEG density gradually increased to about 70 PEGs/particle and 1.7 PEGs/nm², respectively (Table C1). The Flory radius of PEGs used in this study was about 1.7nm, which was larger than the 0.8nm PEG to PEG distance obtained from this surface PEG density (Appendix C). This is consistent with full PEG coverage on the SNP surface with brush-like PEG structure (Fig. 5.1).⁴¹ Dynamic light scattering (DLS) and transmission electron microscopy (TEM) studies suggested that both the bare SNPs as well as the PEGylated SNPs with 1.7 PEGs/nm² exhibited narrow particle size distributions and homogeneous particle morphology (Fig. C1). In contrast, SNPs with intermediate surface PEG densities showed reduced monodispersity due to insufficient surface PEG coverage (Appendix C and Fig. C1 and C2).

The SNPs were further transferred into PBS buffer solution for long-term stability tests. During the test period, small amounts of sample solution were aliquoted for hydrodynamic size measurements. The bare SNPs gradually aggregated in buffer solution over a period of 20-30 days (Fig. 5.2a) due to the screening effect of surface charge by buffer salts.⁴² Interestingly, at the surface PEG density of 0.2 PEGs/nm², the SNPs aggregated immediately after being transferred into buffer solution. As surface PEG density further increased to 1.0 PEGs/nm², aggregation was greatly suppressed, but a gradual increase of particle size was still observed suggesting a slow aggregation process (Fig. C3). In contrast, SNPs with higher surface PEG density remained stable throughout the test period (Fig. 5.2a and Fig. C3). From the results a surface PEG density threshold for preventing SNP aggregation was estimated to be about 1.2 PEGs/nm². From the combination of DLS, TEM and zeta potential measurements, however, 1.7 PEGs/nm² was

identified as the ideal value to assure well PEGylated SNPs with uniform morphology, as well as narrowly-distributed size distribution and zeta-potential (Figs. C1 and C2).¹⁰

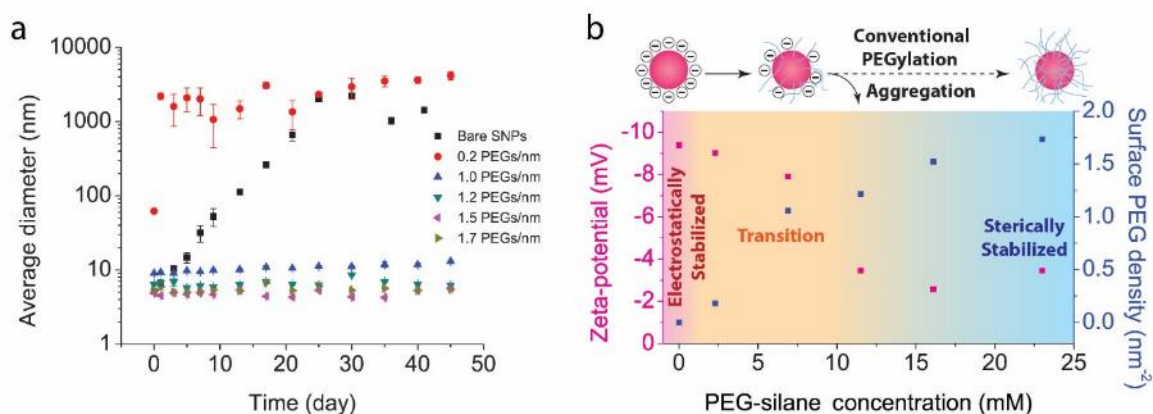


Figure 5.2. Long-term stability test and SNP stability transition. (a) Stability test of SNPs with varying surface PEG density in PBS buffer solution (see similar plot with linear scale in Supplementary Figure C3). (b) Comparison of average zeta-potential and surface PEG density of SNPs in water (no buffer) synthesized at varying PEG-silane concentration. A gradual background color change indicates SNP stability. While the bare SNPs are electrostatically stabilized via negative surface charges (red regime), the fully PEGylated SNPs are sterically stabilized (blue regime). SNPs with surface PEG density in-between are unstable because electrostatic stabilization is greatly diminished while steric stabilization is not yet sufficient (yellow regime in b).

These results indicated a SNP stability transition depending on surface PEG density (Fig. 5.2b). At neutral pH in water (no buffer) the surface of bare SNPs is covered by deprotonated silanol groups and the resulting negative surface charge prevents particle aggregation through electrostatic repulsion (red regime in Fig. 5.2b). On the other end of the scale the SNP surface is covalently modified with a dense layer of PEGs. Although the native surface charge is quenched, SNPs are now sterically stabilized by a neutral PEG corona (blue regime in Fig. 5.2b). In-between these two cases, when the surface PEG density gradually increases from zero to 1.2 PEGs/nm², the SNPs go through a transition from electrostatic to steric stabilization, as indicated *e.g.* by a decrease in negative zeta-potential (yellow regime in Fig. 5.2b). In this transition regime, SNPs lose long-range

electrostatic stabilization due to a decrease in deprotonated and charged surface silanol groups, while the surface PEG density is not yet high enough to provide short-range steric stabilization. The result is particle aggregation, leading to particle precipitation or at least a broadening of the particle size distribution. It is interesting to note that the SNPs most heavily aggregated for the very low surface PEG density of ~ 0.2 PEGs/nm² (Fig. 5.2a and Fig. C1). This suggests electrostatic repulsion between SNPs also plays a key role in determining particle size during SNP formation, in addition to the effects of the kinetics of silane hydrolysis and condensation. Even a small decrease in SNP surface charge density may disturb the system's charge balance and lead to particle aggregation.

Because of this stability transition, a fast PEGylation kinetics is highly desirable for the preparation of narrowly size dispersed PEGylated SNPs. Otherwise, SNPs may aggregate before enough PEGs condense onto the surface. In order to understand the PEGylation kinetics in more detail, we synthesized SNPs in water with Cy5 fluorophores covalently encapsulated into the core, referred to as Cy5-C' dots, and used FCS to monitor the growth-terminating PEGylation reaction (Fig. 5.3a and Fig. C4).¹⁰ In comparison to DLS, FCS uses fluorescence for signal processing thereby excluding any scattering noise from unreacted reagents, *e.g.* self-condensed PEG-silane. It is therefore highly sensitive to size changes of fluorescent SNPs during reactions. Additionally, it provides multiple parameters from a single measurement, including hydrodynamic size, concentration and single-particle brightness,^{37,43} and thus is ideally suited to reveal details of the association between particles and PEG ligands.

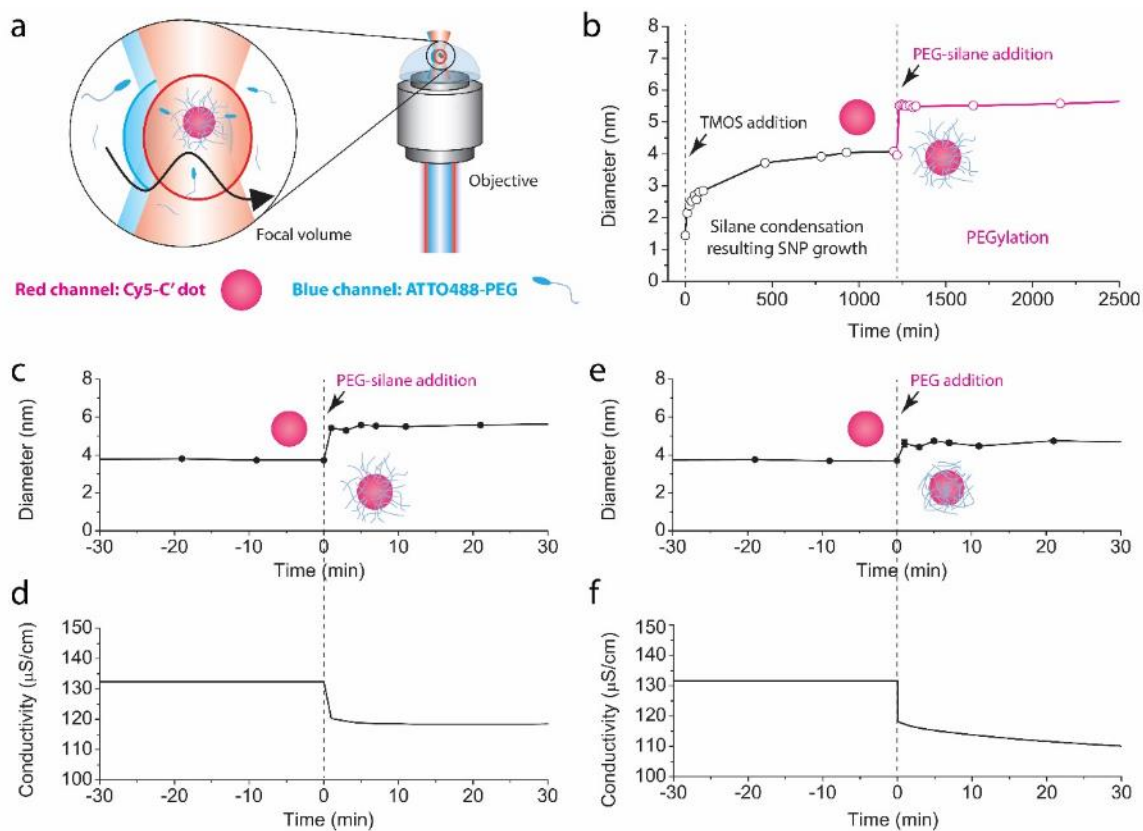


Figure 5.3. PEGylation process as monitored by FCS and conductivity measurements. (a) Illustration of the focal volume of FCS/FCCS setup. As fluorescence-labeled species diffuse through the focal volume, signal fluctuations are detected and information on sample mobility and co-localization is extracted from the correlations of these signal fluctuations. (b) Change of SNP size during formation (black curve) and PEGylation (red curve) steps. (c and d) Evolution of particle size (c) and solution conductivity (d) as PEG-silane is added. (e and f) Evolution of particle size (e) and solution conductivity (f) as non-functionalized PEG is added.

Figure 5.3b shows the change of particle size throughout the synthesis reaction over a period of about two days, including initial growth (black) and termination via PEGylation (red) steps. Bare Cy5-C' dots with diameter around 4nm formed during a period of about a day after injection of silica source, TMOS, and dye-silane conjugate, consistent with DLS and TEM characterization results (Fig. C1). When PEG-silane was added to reach a concentration of 23mM resulting in a final surface PEG density of 1.7 PEGs/nm², the average hydrodynamic size quickly jumped from 4 nm to 5.5 nm (Fig. 5.3b and Fig. C5),

and then stayed fairly constant at around 5.5-6nm for the remainder of the reaction time. The quick size increase was within the time resolution of the experiments (~1-2 minutes, Fig. 5.3c). During the same time fluorescence brightness per particle as well as particle concentration from FCS remained constant (Figs. C6a and b), indicating that this immediate size increase following PEG-silane addition was not caused by particle aggregation, which in turn would lead to an increase in single particle brightness and a decrease in particle concentration. Comparing the size evolution of the SNP growth process via silane hydrolysis and condensation (black part) with that of the PEG-silane addition (red part) in Figure 5.3b, it is safe to conclude that the fast size increase is not the result of the condensation reaction between PEG-silane molecules and SNP surface silanol groups (Fig. C7).⁴² Instead, results point to an instant non-covalent association between PEG-silane molecules and SNPs. This interpretation is corroborated by in-situ solution conductivity measurements showing a drop right after PEG-silane addition on a similar time scale suggesting the screening of SNP surface charges via PEG-silane association (Fig. 5.3d).⁴⁴

In order to further investigate the origin of this fast association, the same experiments were performed using PEGs without silane functionalization. Right after PEG addition, a similar particle size increase of around 1 nm and drop in conductivity were observed (Figs. 5.3e, f and Fig. C5), while particle brightness and concentration stayed unchanged (Figs. C6c and d). Additional experiments further suggested that the FCS derived size increase was not the result of a viscosity increase caused by PEG addition (Fig. C5c).⁴⁵

We subsequently labeled PEGs with fluorophore ATTO488, referred to as ATTO488-PEG (Fig. C8), and used FCCS to further analyze the non-covalent interaction between PEGs and silica. The red channel of the FCCS setup monitored the diffusion of Cy5-C' dots, while the blue channel monitored the diffusion of ATTO488-PEGs (Fig. 5.1). When PEGs are associated with SNPs, their diffusion through the focal volume is synchronized, introducing correlated signal fluctuations in both channels and thus a positive cross-correlation readout (Fig. 5.3a), providing further co-localization information on PEGs and SNPs.³⁴

The FCCS measurements require sample concentrations in the nano molar range,³⁵ which is much lower than the concentrations of SNPs (around 20 μ M) and PEG-silanes (around 23mM) in the PEGylation protocol.¹⁰ Such low reaction concentrations may change the association behavior between PEGs and SNPs. In order to circumvent this problem, we first diluted the original Cy5-C' dot solution to about 30 nM concentration, to which a small amount of ATTO488-PEGs was added to reach about 150nM concentration. Afterwards, extra non-functionalized PEGs were added to raise the overall PEG concentration to 23mM (Fig. 5.4a top panel). The final solution was immediately subjected to FCCS measurements. The results showed a clear cross-correlation readout (Fig. 5.4b, light green line). The hydrodynamic size obtained from the cross-correlation was larger than 5nm, indicating a highly specific detection of ATTO488-PEGs adsorbed onto Cy5-C' dots (Table C2). Detailed analysis further suggested that under these conditions about one out of fifty ATTO488-PEG molecules was adsorbed to the SNPs. This indicated the existence of a large amount of extra unattached PEGs during PEGylation, consistent with DLS results (Appendix C and Fig. C9).

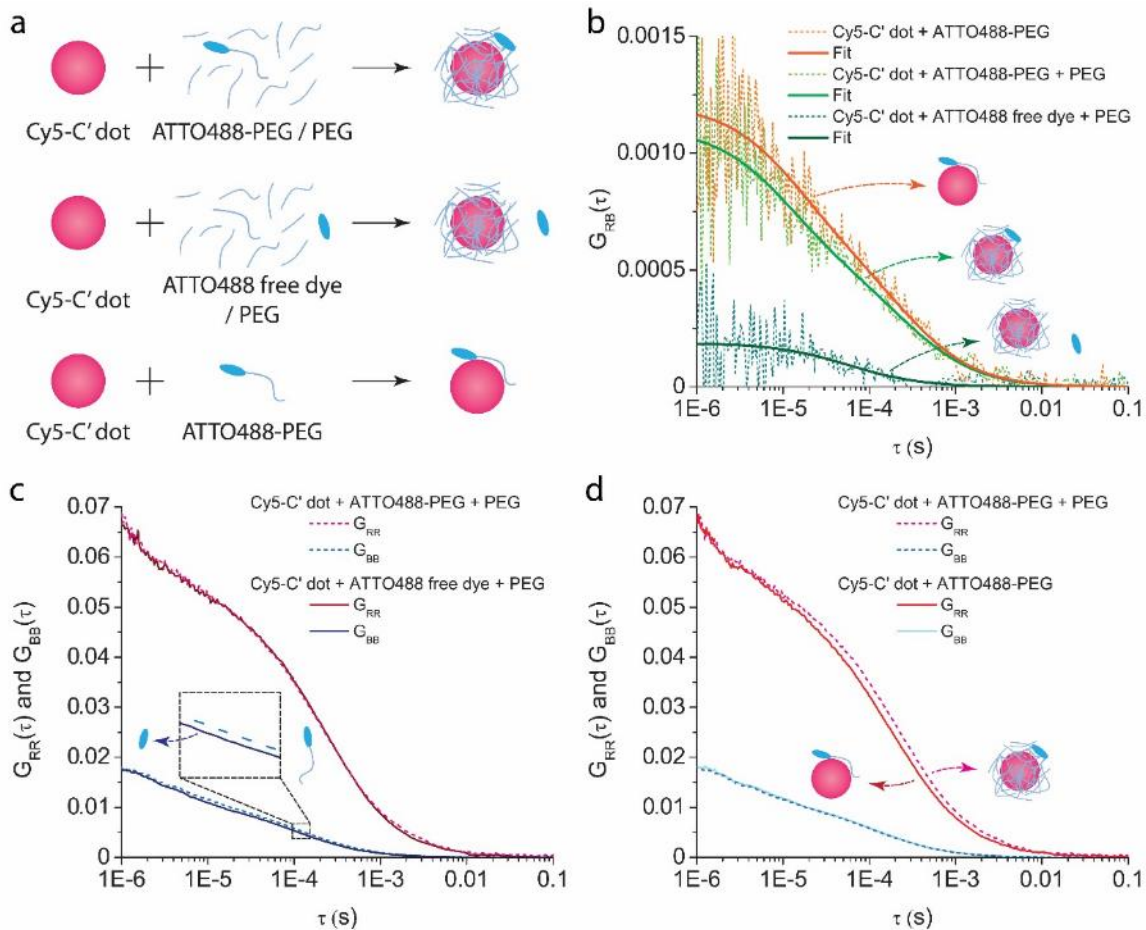


Figure 5.4. Association of PEGs and SNPs as characterized by FCS and FCCS. (a) Experimental designs. ATTO488-PEG/PEG (top), ATTO488 free dye/PEG (middle) and ATTO488-PEG only (bottom) were added to diluted Cy5-C' dot solutions, respectively, and the resulting mixtures were subjected to FCS and FCCS measurements immediately after PEG addition. (b) Comparison of FCCS cross-correlation curves from all three experiments in a. (c) Comparison of FCS red and blue channel auto-correlation curves of Cy5-C' dot solutions to which ATTO488-PEG/PEG (top panel in a) and ATTO488 free dye/PEG (middle panel in a) were added, respectively. (d) Comparison of FCS red and blue channel auto-correlation curves of ATTO488-PEG added to Cy5-C' dot solutions with (top panel in a) and without (bottom panel in a) extra non-functionalized PEGs.

To further ensure the observed association of ATTO488-PEGs and SNPs was not due to PEG functionalization with dye, the same experiments were performed with ATTO488 free dye instead of ATTO488-PEGs (Fig. 5.4a middle panel). The corresponding red channel auto-correlation curve overlapped with the one from the experiment using ATTO488-PEGs, both of which resulted from the PEG-adsorbing SNPs (Fig. 5.4c top red

curves). In contrast, the blue channel auto-correlation slightly shifted to the left, confirming the faster diffusion of ATTO488 free dye as compared to ATTO488-PEG (Fig. 5.4c bottom blue curves). Finally, for this case a substantially weaker cross-correlation signal was detected (Fig. 5.4b, dark green line), whose resulting hydrodynamic size was much smaller than what was expected from the SNP size (Table C2). This suggested that this weak cross-correlation was most likely due to leaking of fluorescence from ATTO488 fluorophore to the red channel, rather than the specific co-localization of ATTO488 free dye and SNPs. The lack of cross-correlation signal is consistent with ATTO488 fluorophore carrying a net negative charge leading to electrostatic repulsive interactions with the negatively charged SNPs.²⁴ Although this inter-channel cross-talk added noise to the cross-correlation analysis, the obvious enhancement of cross-correlation caused by PEG conjugation of ATTO488 fluorophore provided evidence of PEGs being adsorbed on SNP surfaces (Fig. 5.4b).

The same experiments were also performed without the addition of extra non-functionalized PEGs, where both SNPs and PEGs had nano molar concentrations (Fig. 5.4a bottom panel). After ATTO488-PEG addition, no increase of average SNP size was detected via the red channel auto-correlation, suggesting a substantial decrease of the amount of PEGs adsorbed onto the SNP surface due to their low concentration (Fig. 5.4d). Despite the small amount of PEG adsorption, a strong cross-correlation signal was again detected (Fig. 5.4b, orange line). This demonstrates that the association between PEGs and SNPs happens even at extremely low concentration, here close to nano molar regime. This association is due to the specific affinity between PEGs and silica, most likely caused by

hydrogen bonding between the silanol groups on the SNP surface and both the ether oxygens and hydroxyl end groups of non-functionalized PEGs (Fig. 5.1).⁴⁶⁻⁴⁸

The fast adsorption of PEGs to SNP surface quickly shortens the average distance between the silanol groups of PEG-silanes and the silanol groups on the SNP surface, thereby significantly accelerating PEG-silane condensation (Fig. 5.1). This conclusion was supported by additional FCS experiments, showing that adsorbed PEGs without silane functionalization were released from the SNP surface upon dilution. In contrast, no release of PEG-silanes was observed, even when the SNP solution was greatly diluted immediately after PEG-silane addition (Fig. C10).

Fundamental knowledge of reaction pathways allows educated design of process conditions. In order to elucidate favorable experimental conditions for PEGylation assisted by the non-covalent silica-PEG association described here, reaction solvent composition and solution pH were varied before the addition of non-functionalized PEGs to SNP solutions. Silica PEGylation reactions are typically conducted in water, alcohol, or their mixtures. Interestingly, when the alcohol (here ethanol) fraction of the solvent mixture increased to >20%, no substantial size increase was detected anymore after PEG addition (Fig. 5.5a). These results suggest that alcohol amounts >20% are sufficient to effectively suppress rapid PEG adsorption. In contrast, PEG adsorption was relatively insensitive to solution pH, with the association only being suppressed at relatively high values above pH 11. These data suggest that silica PEGylation reactions should be conducted at low alcohol content and under basic pH values typical for promoting silica condensation.

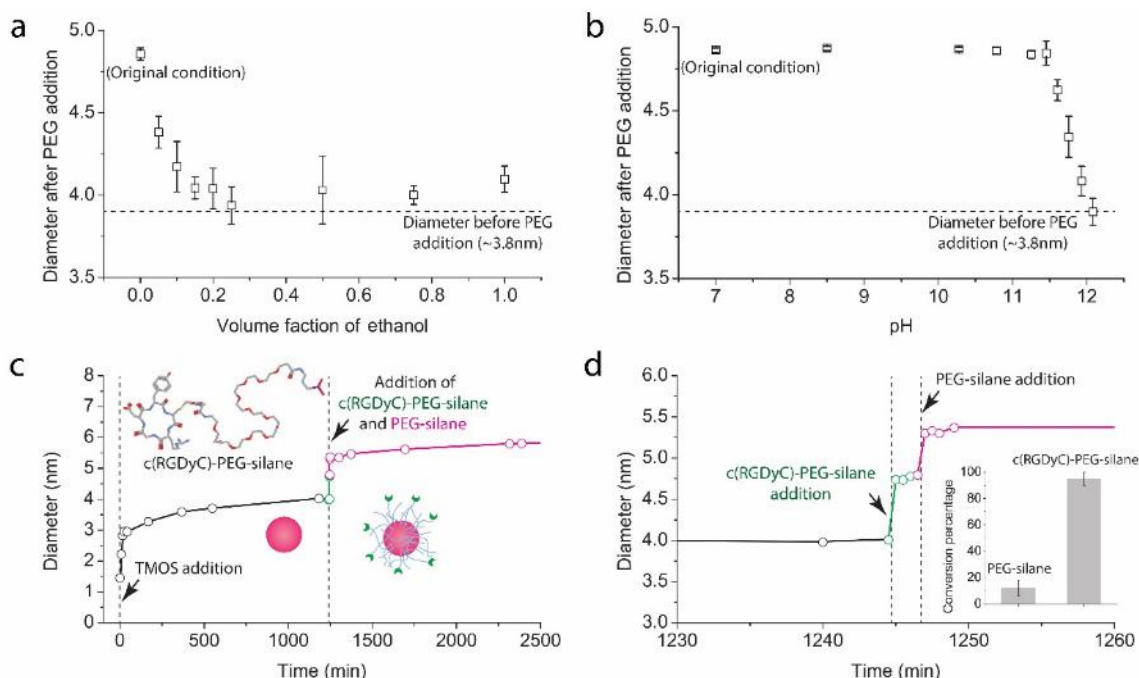


Figure 5.5. Association of ligands and SNPs under different conditions. (a and b) Non-covalent association between SNPs and PEGs (without silane functionalization) in aqueous solution with varying (a) volume fraction of ethanol and (b) pH. The solution pH in b was adjusted by varying the concentration of ammonium hydroxide. The dashed lines indicate SNP size before PEG addition. (c) Change of SNP size throughout a reaction in which c(RGDyC)-PEG-silane (insert) was added (green part) right before PEG-silane addition (red part) in order to surface modify the SNPs with cancer-targeting ligands. (d) Zoomed-in view of c to the reaction period around ligand addition (color code as in c). Comparison of the conversion percentage of PEG-silane versus c(RGDyC)-PEG-silane (insert in d) suggests that the stronger affinity between c(RGDyC) peptides and SNPs facilitated the surface modification reaction.

Our results indicate that a fast non-covalent association of PEGs and silica accelerates the formation of covalent bonds between PEG-silane and SNP surfaces, and therefore plays a key role in successful PEGylation (Fig. 5.1). For nanomedicine applications of hybrid NPs this immediately raises the question whether similar pathways are active when reactions involve PEGs functionalized with specific targeting groups, *e.g.* peptides or antibodies. In order to address this question, SNPs were surface modified with PEGs conjugated to cancer-targeting peptides, c(RGDyC) (see insert in Fig. 5.5c for molecular structure model). Cyclic RGD is known to bind to cell surface proteins

(integrins), overexpressed *e.g.* in melanoma, and therefore is a relevant model peptide to investigate these effects with.²⁷ To that end peptide functionalized and non-functionalized PEG-silanes were subsequently added to the same SNP solution. Upon the addition of c(RGDyC)-PEG-silane a similar instant increase of particle size as for pure PEGs was observed suggesting the immediate surface attachment of cancer-targeting groups to the SNP surface (Fig. 5.5c). Non-functionalized PEG-silane added to cover the remaining SNP surface led to a second stepwise particle size increase suggesting successful PEGylation (see zoomed-in version of Fig. 5.5c in d). It is important to note that further analysis indicated that the conversion percentage of c(RGDyC)-PEG-silane was much higher than that of PEG-silane and began approaching 100% (insert in Fig. 5.5d). This demonstrated an increased affinity to the silica surface of the peptide functionalized over the pure PEG-silane consistent with experience that peptides adsorb on silica surfaces.^{49,50} The enhanced affinity facilitates surface modification reactions of SNPs with PEG bound peptides and may therefore substantially reduce manufacturing costs of multifunctional pharmaceutical NPs by providing high reaction yields.

5.5 Conclusions

The mechanistic details of NP PEGylation processes elucidated in this paper suggest that non-covalent association between ligand molecules, *e.g.* PEGs and PEG-peptide conjugates, and NP surfaces can be used to facilitate NP surface modification reactions through accelerating covalent attachment. This two-step reaction process, *i.e.* first adsorption and then covalent attachment, shares similarities with many biology processes. For example, in protein translation tRNA-associated amino acids are brought together first through specific hydrogen bond-induced interactions between ribosome and mRNA before covalent bond formation via dehydration. We expect these findings to build a foundation providing rational process design criteria not only for successful PEGylation, but also for NP surface modification with functional ligands, important in fields ranging from bio-sensing and bio-imaging to nanomedicine. Finally, the affinity between PEGs and silica may add to the existing family of non-covalent interactions for the fabrication of novel self-assembled nanomaterials.

5.6 Acknowledgements

The authors gratefully acknowledge National Institutes of Health for the financial support under Award Number 5R01 CA161280-03. Research reported in this publication was further supported by the National Cancer Institute of the National Institutes of Health under Award Number U54CA199081. This work made use of the Cornell Center for Materials Research shared facilities supported through the NSF MRSEC program (DMR-1120296), and the Nanobiotechnology Center shared research facilities at Cornell.

5.7 References

- (1) Nanomedicine Market (Neurology, Cardiovascular, Anti-Inflammatory, Anti-Infective, and Oncology Applications) - Global Industry Analysis, Size, Share, Growth, Trends and Forecast, 2013 - 2019. *Transparency Market Research*. 2014.
- (2) Chauhan, V. P.; Jain, R. K. Strategies for Advancing Cancer Nanomedicine. *Nat. Mater.* **2013**, *12*, 958–962.
- (3) Torchilin, V. P. Multifunctional, Stimuli-Sensitive Nanoparticulate Systems for Drug Delivery. *Nat. Rev. Drug Discov.* **2014**, *13*, 813–827.
- (4) Veisoh, O.; Tang, B. C.; Whitehead, K. A.; Anderson, D. G.; Langer, R. Managing Diabetes with Nanomedicine: Challenges and Opportunities. *Nat. Rev. Drug Discov.* **2014**, *14*, 45–57.
- (5) Kotagiri, N.; Sudlow, G. P.; Akers, W. J.; Achilefu, S. Breaking the Depth Dependency of Phototherapy with Cerenkov Radiation and Low-Radiance-Responsive Nanophotosensitizers. *Nature Nanotech.* **2015**, *10*, 370–379.
- (6) Cho, K.; Wang, X.; Nie, S.; Chen, Z.; Shin, D. M. Therapeutic Nanoparticles for Drug Delivery in Cancer. *Clin. Cancer Res.* **2008**, *10*, 1310–1316.
- (7) Harris, J. M.; Chess, R. B. Effect of Pegylation on Pharmaceuticals. *Nat. Rev. Drug Discov.* **2003**, *2*, 214–221.
- (8) Petros, R. A.; Desimone, J. M. Strategies in the Design of Nanoparticles for Therapeutic Applications. *Nat. Rev. Drug Discov.* **2010**, *9*, 615–627.
- (9) Guerrero-Martínez, A.; Pérez-Juste, J.; Liz-Marzán, L. M. Silica-Coated Nanomaterials: Recent Progress on Silica Coating of Nanoparticles and Related Nanomaterials. *Adv. Mater.* **2010**, *22*, 1182-1195.

- (10) Ma, K.; Mendoza, C.; Hanson, M.; Werner-Zwanziger, U.; Zwanziger, J.; Wiesner, U. Control of Ultrasmall Sub-10 nm Ligand-Functionalized Fluorescent Core–Shell Silica Nanoparticle Growth in Water. *Chem. Mater.* **2015**, *27*, 4119–4133.
- (11) Lin, Y.-S.; Abadeer, N.; Hurley, K. R.; Haynes, C. L. Ultrastable, Redispersible, Small, and Highly Organomodified Mesoporous Silica Nanotherapeutics. *J. Am. Chem. Soc.* **2011**, *133*, 20444–20457.
- (12) Ma, K.; Sai, H.; Wiesner, U. Ultrasmall Sub-10 nm Near-Infrared Fluorescent Mesoporous Silica Nanoparticles. *J. Am. Chem. Soc.* **2012**, *134*, 13180–13183.
- (13) Koole, R.; Schooneveld, M. M. V.; Hilhorst, J.; Castermans, K.; Cormode, D. P.; Strijkers, G. J.; Donegá Celso De Mello; Vanmaekelbergh, D.; Griffioen, A. W.; Nicolay, K.; Fayad, Z. A.; Meijerink, A.; Mulder, W. J. M. Paramagnetic Lipid-Coated Silica Nanoparticles with a Fluorescent Quantum Dot Core: A New Contrast Agent Platform for Multimodality Imaging. *Bioconjugate Chem.* **2008**, *19*, 2471–2479.
- (14) Schooneveld, M. M. V.; Cormode, D. P.; Koole, R.; Wijngaarden, J. T. V.; Calcagno, C.; Skajaa, T.; Hilhorst, J.; Hart, D. C. 't; Fayad, Z. A.; Mulder, W. J. M.; Meijerink, A. A Fluorescent, Paramagnetic and PEGylated Gold/Silica Nanoparticle for MRI, CT and Fluorescence Imaging. *Contrast Media Mol. Imaging* **2010**, *5*, 231–236.

- (15) Sun, Y.; Sai, H.; Stein, F. V.; Riccio, M.; Wiesner, U. Water-Based Synthesis of Ultrasmall PEGylated Gold–Silica Core–Shell Nanoparticles with Long-Term Stability. *Chem. Mater.* **2014**, *26*, 5201–5207.
- (16) Yoon, T.-J.; Yu, K. N.; Kim, E.; Kim, J. S.; Kim, B. G.; Yun, S.-H.; Sohn, B.-H.; Cho, M.-H.; Lee, J.-K.; Park, S. B. Specific Targeting, Cell Sorting, and Bioimaging with Smart Magnetic Silica Core-Shell Nanomaterials. *Small* **2006**, *2*, 209–215.
- (17) Wang, Y.; Wang, K.; Zhao, J.; Liu, X.; Bu, J.; Yan, X.; Huang, R. Multifunctional Mesoporous Silica-Coated Graphene Nanosheet Used for Chemo-Photothermal Synergistic Targeted Therapy of Glioma. *J. Am. Chem. Soc.* **2013**, *135*, 4799–4804.
- (18) Liu, J.; Wang, C.; Wang, X.; Wang, X.; Cheng, L.; Li, Y.; Liu, Z. Mesoporous Silica Coated Single-Walled Carbon Nanotubes as a Multifunctional Light-Responsive Platform for Cancer Combination Therapy. *Adv. Funct. Mater.* **2015**, *25*, 384–392.
- (19) Roberts, M.; Bentley, M.; Harris, J. Chemistry for Peptide and Protein PEGylation. *Adv. Drug Deliv. Rev.* **2002**, *54*, 116–127.
- (20) Xia, X.-R.; Monteiro-Riviere, N. A.; Riviere, J. E. An Index for Characterization of Nanomaterials in Biological Systems. *Nature Nanotech.* **2010**, *5*, 671–675.
- (21) Kreyling, W. G. *et al.* In Vivo Integrity of Polymer-Coated Gold Nanoparticles. *Nature Nanotech.* **2015**, *10*, 619–623.

- (22) Jokerst, J. V.; Lobovkina, T.; Zare, R. N.; Gambhir, S. S. Nanoparticle PEGylation for Imaging and Therapy. *Nanomedicine* **2011**, *6*, 715–728.
- (23) Ow, H.; Larson, D. R.; Srivastava, M.; Baird, B. A.; Webb, W. W.; Wiesner, U. Bright and Stable Core–Shell Fluorescent Silica Nanoparticles. *Nano Lett.* **2005**, *5*, 113–117.
- (24) Herz, E.; Ow, H.; Bonner, D.; Burns, A.; Wiesner, U. Dye Structure–Optical Property Correlations in Near-Infrared Fluorescent Core-Shell Silica Nanoparticles. *J. Mater. Chem.* **2009**, *19*, 6341–6341.
- (25) Kim, B. H.; Hackett, M. J.; Park, J.; Hyeon, T. Synthesis, Characterization, and Application of Ultrasmall Nanoparticles. *Chem. Mater.* **2014**, *26*, 59–71.
- (26) Gennes, P. G. D. Polymer Solutions near an Interface. Adsorption and Depletion Layers. *Macromolecules* **1981**, *14*, 1637–1644.
- (27) Phillips, E.; Penate-Medina, O.; Zanzonico, P. B.; Carvajal, R. D.; Mohan, P.; Ye, Y.; Humm, J.; Gonen, M.; Kalaigian, H.; Schoder, H.; Strauss, H. W.; Larson, S. M.; Wiesner, U.; Bradbury, M. S. Clinical Translation of an Ultrasmall Inorganic Optical-PET Imaging Nanoparticle Probe. *Sci. Transl. Med* **2014**, *6*, 260ra149.
- (28) Brown, W. *Dynamic Light Scattering: the Method and Some Applications*; Oxford University Press: Oxford, England, 1993.
- (29) Butterworth, M.; Illum, L.; Davis, S. Preparation of Ultrafine Silica- and PEG-Coated Magnetite Particles. *Colloids Surfaces A: Physicochem. Engin. Asp.* **2001**, *179*, 93–102.

- (30) Garcia-Fuentes, M.; Torres, D.; Martín-Pastor, M.; Alonso, M. J. Application of NMR Spectroscopy to the Characterization of PEG-Stabilized Lipid Nanoparticles. *Langmuir* **2004**, *20*, 8839–8845.
- (31) Levin, C. S.; Bishnoi, S. W.; Grady, N. K.; Halas, N. J. Determining The Conformation of Thiolated Poly(Ethylene Glycol) on Au Nanoshells by Surface-Enhanced Raman Scattering Spectroscopic Assay. *Anal. Chem.* **2006**, *78*, 3277–3281.
- (32) Schwille, P. Fluorescence Correlation Spectroscopy and Its Potential for Intracellular Applications. *Cell Biochem. Biophys.* **2001**, *34*, 383–408.
- (33) Elson, E. L. Fluorescence Correlation Spectroscopy: Past, Present, Future. *Biophys. J.* **2011**, *101*, 2855–2870.
- (34) Schwille, P.; Meyer-Almes, F.; Rigler, R. Dual-Color Fluorescence Cross-Correlation Spectroscopy for Multicomponent Diffusional Analysis in Solution. *Biophys. J.* **1997**, *72*, 1878–1886.
- (35) Bacia, K.; Kim, S. A.; Schwille, P. Fluorescence Cross-Correlation Spectroscopy in Living Cells. *Nature Meth.* **2006**, *3*, 83–89.
- (36) Lippincott-Schwartz, J.; Snapp, E.; Kenworthy, A. Studying Protein Dynamics in Living Cells. *Nat. Rev. Mol. Cell Biol* **2001**, *2*, 444–456.
- (37) Larson, D. R.; Ow, H.; Vishwasrao, H. D.; Heikal, A. A.; Wiesner, U.; Webb, W. W. Silica Nanoparticle Architecture Determines Radiative Properties of Encapsulated Fluorophores. *Chem. Mater.* **2008**, *20*, 2677–2684.

- (38) Röcker, C.; Pötzl, M.; Zhang, F.; Parak, W. J.; Nienhaus, G. U. A Quantitative Fluorescence Study of Protein Monolayer Formation on Colloidal Nanoparticles. *Nature Nanotech.* **2009**, *4*, 577–580.
- (39) Jaskiewicz, K.; Larsen, A.; Lieberwirth, I.; Koynov, K.; Meier, W.; Fytas, G.; Kroeger, A.; Landfester, K. Probing Bioinspired Transport of Nanoparticles into Polymersomes. *Angew. Chem.* **2012**, *51*, 4691–4695.
- (40) Schaeffel, D.; Staff, R. H.; Butt, H.-J.; Landfester, K.; Crespy, D.; Koynov, K. Fluorescence Correlation Spectroscopy Directly Monitors Coalescence During Nanoparticle Preparation. *Nano Lett.* **2012**, *12*, 6012–6017.
- (41) Gennes, P. G. D. Conformations of Polymers Attached to an Interface. *Macromolecules* **1980**, *13*, 1069–1075.
- (42) Brinker, C. J.; Scherer, G. W. *Sol-Gel Science the Physics and Chemistry of Sol-Gel Processing*; Academic Press: Boston, 1990.
- (43) Lakowicz, J. R. *Principles of Fluorescence Spectroscopy*; Plenum Press: New York, 1983.
- (44) Nyffenegger, R.; Quellet, C.; Ricka, J. Synthesis of Fluorescent, Monodisperse, Colloidal Silica Particles. *J. Colloid Interface Sci.* **1993**, *159*, 150–157.
- (45) Kirinčič, S.; Klofutar, C. Viscosity of Aqueous Solutions of Poly(Ethylene Glycol)s at 298.15 K. *Fluid Phase Equilib.* **1999**, *155*, 311–325.
- (46) Preari, M.; Spinde, K.; Lazic, J.; Brunner, E.; Demadis, K. D. Bioinspired Insights into Silicic Acid Stabilization Mechanisms: The Dominant Role of

- Polyethylene Glycol-Induced Hydrogen Bonding. *J. Am. Chem. Soc.* **2014**, *136*, 4236–4244.
- (47) Pochylski, M.; Aliotta, F.; Blaszcak, Z.; Gapiński, J. Structuring Effects and Hydration Phenomena in Poly(Ethylene Glycol)/Water Mixtures Investigated by Brillouin Scattering. *J. Phys. Chem. B* **2006**, *10*, 20533–20539.
- (48) Derkaoui, N.; Said, S.; Grohens, Y.; Olier, R.; Privat, M. Polyethylene Glycol Adsorption On Silica: From Bulk Phase Behavior to Surface Phase Diagram. *Langmuir* **2007**, *23*, 6631–6637.
- (49) Puddu, V.; Perry, C. C. Peptide Adsorption on Silica Nanoparticles: Evidence of Hydrophobic Interactions. *ACS Nano* **2012**, *6*, 6356–6363.
- (50) Patwardhan, S. V.; Emami, F. S.; Berry, R. J.; Jones, S. E.; Naik, R. R.; Deschaume, O.; Heinz, H.; Perry, C. C. Chemistry of Aqueous Silica Nanoparticle Surfaces and the Mechanism of Selective Peptide Adsorption. *J. Am. Chem. Soc.* **2012**, *134*, 6244–6256.

Appendix C: Supplementary Information for Chapter 5

Estimation of number of PEG chains per SNP and surface PEG density

The number of PEG chains per SNP and surface PEG density were estimated according to the following equations:

$$\text{Number of PEG chains per SNP} = \left(\frac{4}{3}\pi r^3\right) \cdot \rho \cdot \frac{F_{PEG}}{1-F_{PEG}} / M_{PEG} / N_A \quad (1)$$

$$\text{Surface PEG density} = \text{Number of PEG chains per SNP} / (4\pi r^2) \quad (2)$$

where r is the radius of bare SNPs, which is estimated to be 1.8nm according to TEM, DLS and FCS characterization results (Supplementary Fig. C1). ρ is the density of amorphous silica, for which the value of 1.9g/cm³ was used. F_{PEG} is the weight percentage of organic PEGs on the SNP surface as obtained from TGA (Supplementary Fig. C1a). M_{PEG} is the molar mass of PEGs attached on SNP surface. Since the PEG-silane used in the PEGylation contained 6-9 EO units, M_{PEG} is estimated to be 360 g/mole. N_A is the Avogadro constant. The calculated number of PEG chains per particle and surface PEG density of SNPs synthesized at different PEG-silane concentrations are summarized in the following table. Although the errors introduced via TGA measurements, the density estimation of SNP silica matrix, and SNP size could add about 10-20% error to these values, these calculations provide a valuable estimation of the PEG loading and confirmation of successful PEGylation.

PEG conformation on SNP surface can be described in terms of the Flory radius (F) according to the following equation¹:

$$F = \alpha n^{\frac{3}{5}} \quad (3)$$

where n is the number of monomers per PEG chain and α is the length of one EO monomer. There are two main conformations that PEG chains can acquire depending on SNP surface PEG density. If the surface PEG density is low, PEG chains will acquire mushroom-like conformations. This usually happens if the PEG to PEG distance on SNP surface (D) is larger than the Flory radius ($D > F$). In contrast, if the PEG to PEG distance is close to or smaller than the Flory radius ($D \leq F$), PEG chains will acquire brush-like conformations. Brush-like conformations are more favorable than mushroom-like conformations in endowing nanoparticles with high bio-compatibility and desirable biodistribution profiles.

Table C1. Estimation of number of PEG chains per SNP and surface PEG density

PEG-silane concentration	Weight percentage of PEGs	Number of PEG chains per SNP	Surface PEG density (PEG/nm ²)	PEG to PEG distance, D (nm)
No PEG	-	-	-	-
2.3 mM	9 wt%	8	0.2	2.4
6.9 mM	36 wt%	44	1.0	1.1
11.5 mM	39 wt%	49	1.2	1.0
16.1 mM	44 wt%	61	1.5	0.9
23.0 mM	48 wt%	72	1.7	0.8

For the PEG-silane used in the PEGylation protocol, α is estimated to be about 0.35nm^{1,2} and n ranges from 6 to 9. Therefore, the Flory radius was estimated to be around 1.7nm. According to Supplementary Table C1, SNPs synthesized at PEG-silane concentrations of 6.9mM and above had $D < F$, and therefore a brush-like conformation of

PEGs was expected. In contrast, SNPs synthesized at the PEG-silane concentration of 2.3mM had $D > F$, and therefore a mushroom-like conformation was expected. This agreed well with the results of long-term stability test, where the SNPs with surface PEG density of 0.2 PEG/nm² (mushroom conformation) strongly aggregated, whereas aggregation was suppressed for SNPs with higher surface PEG density (brush conformation).

Characterizations of SNPs with varying surface PEG density

Supplementary Figure C1a compares TGA results of PEGylated SNPs synthesized at different PEG-silane concentrations. The TGA plots were normalized to the weight percentage at 300⁰C because curves fluctuated at lower temperatures due to water removal. The weight decrease from 300⁰C to 600⁰C corresponded to the loss of organic PEG compounds, according to which the number of PEG chains per SNP and the surface PEG density were estimated as described above. The PEGylated SNPs were further characterized by DLS, zeta-potential and TEM. The SNPs were up concentrated before zeta-potential measurements for the desired signal-to-noise ratio (Supplementary Fig. C2). The bare SNPs without PEGylation had hydrodynamic sizes around 5nm and an average zeta-potential close to -10eV (Supplementary Fig. C1b and c). The TEM image (Supplementary Fig. C1d) demonstrated high particle monodispersity and homogeneity. In comparison, SNPs with the highest surface PEG density (1.7 PEGs/ nm²) also exhibited a narrow particle size distribution and homogeneous particle morphology (Supplementary Fig. C1b and i). However, the average zeta-potential increased to about -2eV (Supplementary Fig. C1c), suggesting covalent attachment of PEGs on the SNP surface. When the surface PEG density decreased from 1.7 to 1.2 PEGs/nm², the zeta-potential distribution slightly broadened (Supplementary Fig. C1c). At even lower surface PEG

densities, the SNPs aggregated as indicated by both DLS and TEM (Supplementary Fig. C1b, e and f), and the average zeta-potential shifted to negative values due to the lower surface coverage with PEGs (Supplementary Fig. C1c).

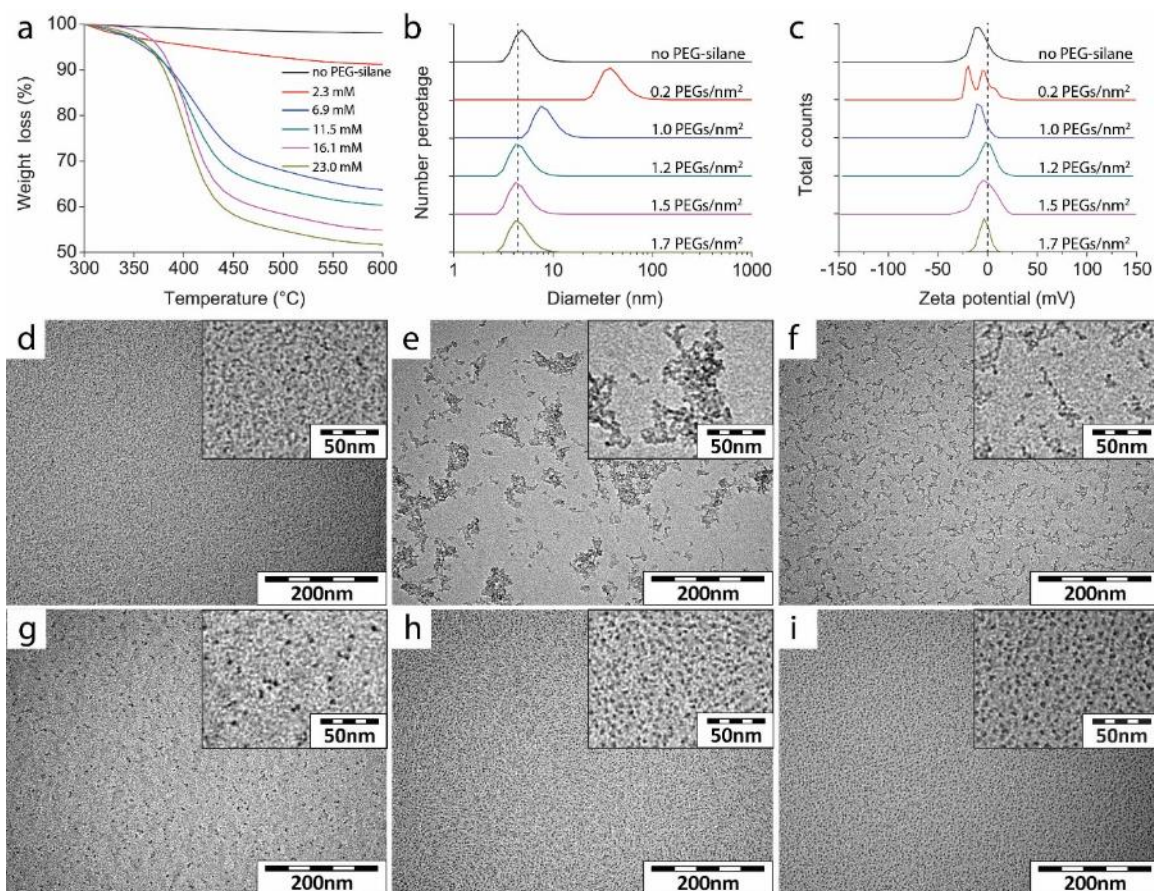


Figure C1. Characterization of SNPs with varying surface PEG density. (a to c) TGA (a), hydrodynamic size distribution from DLS (b) and zeta-potential distribution (c) of SNP synthesized at different PEG-silane concentrations: 0, 2.3, 6.9, 11.5, 16.1 and 23.0 mM. The surface PEG density was estimated according to the size of bare SNPs and the weight percentage of PEG chains as described in the text (Supplementary Table C1). (d to i) TEM images at two different magnifications (see insets) of SNPs with varying surface PEG density: 0, 0.2, 1.0, 1.2, 1.5 and 1.7 PEGs/nm².

Optimization of Zeta Potential measurements

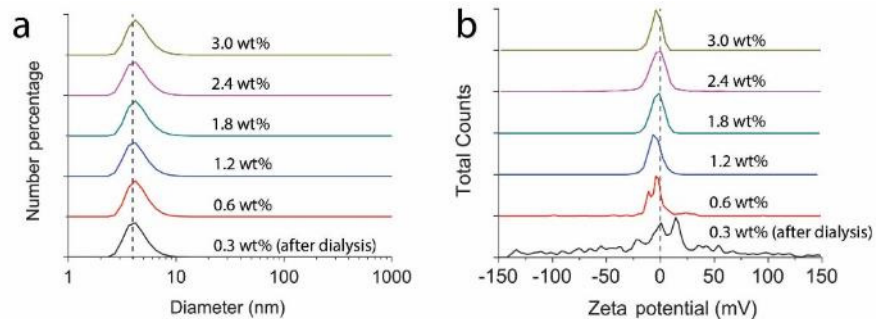


Figure C2. Optimization of zeta-potential measurements. Distributions of particle size from DLS (a) and zeta-potential (b) of PEGylated SNPs at different concentrations. Results were obtained from SNPs with surface PEG density of 1.7 PEGs/nm².

Zeta-potential measurements of ultrasmall PEGylated SNPs are challenging due to the weak scattering signal of small SNPs. In order to obtain reliable results, PEGylated SNPs were up-concentrated prior to zeta-potential measurements. DLS derived particle size distributions confirmed that the up-concentration of PEGylated SNPs did not cause any particle aggregation (Supplementary Fig. C2a). But the signal to noise ratio of zeta potential measurements was significantly enhanced at the higher particle concentrations (Supplementary Fig. C2b). For this reason, all samples were first up-concentrated by ten times (from 0.3% after dialysis to 3%) before zeta-potential measurements were conducted.

Long-term stability tests

In order to reveal details of particle size changes in PBS buffer, Figure 5.2a in the main manuscript is re-plotted here on a linear scale (Supplementary Figure C3). Zooming in to the smallest sizes (Supplementary Figure C3, right side) shows that SNPs with surface PEG density of 1.0 PEG/nm² gradually increased in size after transfer into PBS buffer solution suggesting slow aggregation due to insufficient surface PEG coverage. In contrast, SNPs with higher surface PEG density remained stable throughout the test period of about 45 days.

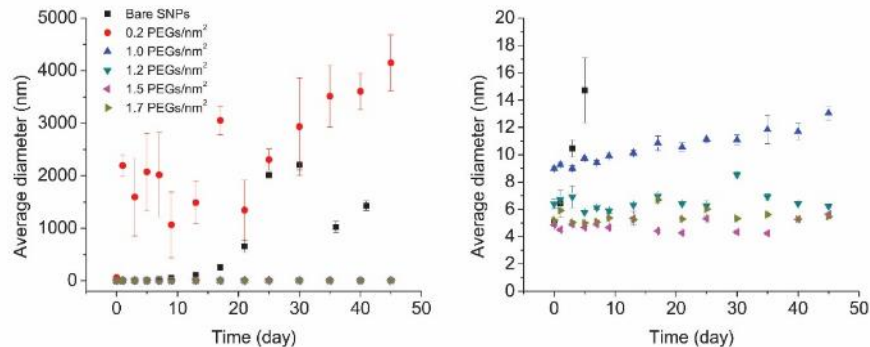


Figure C3. Linear plot of results of long-term SNP stability tests. While the plot on the left shows the entire data set from SNPs with all six different surface PEG densities, zooming-in to small sizes only on the right reveals details in size changes of SNPs with relatively high surface PEG density, *i.e.* ≥ 1.0 PEG/nm².

FCS/FCCS setup

The home-built FCS/FCCS setup consisted of a 635nm excited red channel and a 488nm excited blue channel, which monitored the diffusion of Cy5-C' dots and ATTO 488-PEGs, respectively. Specific dichroic mirrors and filters were used to split the excitations and emission fluorescence. The detector of the blue channel collected fluorescence with wavelength between 530 and 590nm (ATTO488 fluorophore), while the detector of the red channel collected fluorescence with wavelength longer than 650nm (Cy5 fluorophore). A correlator-card was used to correlate fluorescence fluctuations from the two channels to generate auto- and cross-correlation curves as shown in the manuscript and below.

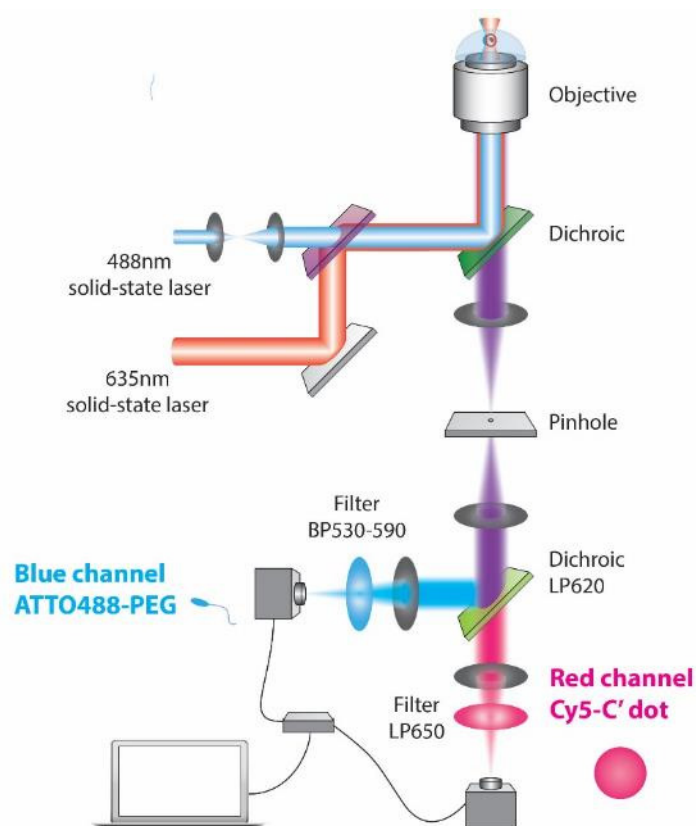


Figure C4. FCS and FCCS experimental setups. Detailed design of home-built FCS/FCCS setup.

SNP size change upon the addition of PEG-silane and PEGs

As described in the main manuscript, the average SNP size quickly jumped up after PEG-silane addition. Supplementary Figure C5a shows a comparison of the normalized FCS auto-correlation curves of Cy5-C' dots before and right after PEG-silane addition. The average hydrodynamic particle size, particle concentration and single-particle fluorescence brightness were obtained from fitting the auto-correlation curves according to procedures detailed in previous publications^{3,4}. The obvious right shift of the auto-correlation curve after PEG-silane addition suggested a slower diffusion constant and thus a bigger particle size. A similar right shift of the auto-correlation curve was also observed when PEG-silane was replaced by non-functionalized PEG (Supplementary Fig. C5b). In contrast, the auto-

correlation curves remained almost unchanged when Cy5-C' dots were replaced by AF647 free dye (Supplementary Fig. C5c). This cross experiment corroborated that the shift in correlation curves to the right was indeed due to a true particle size increase after addition of PEG-silane or PEG and was not caused by an increase in solution viscosity upon PEG chain addition. The latter in turn would have also lead to a right shift of the correlation curve of AF647 free dye, which was not observed.

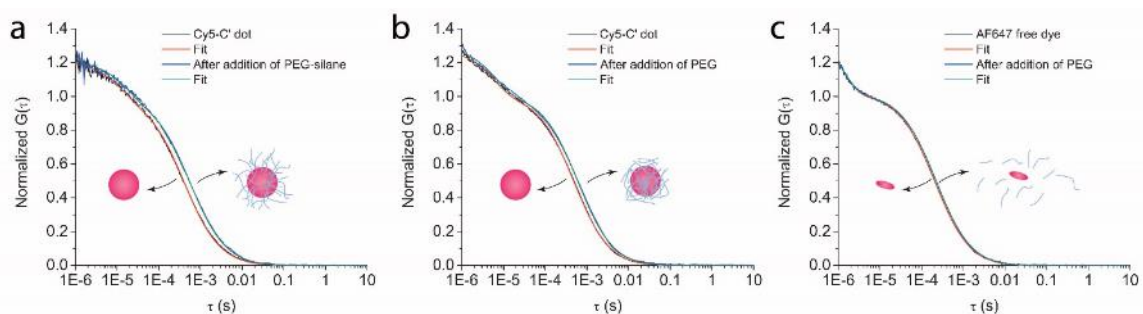


Figure C5. Particle size changes before and after PEG additions. Comparison of auto-correlations of Cy5-C' dots (a and b) and AF647 standard free dye (c) before and after the addition of PEG-silane (a) or non-functionalized PEGs (b and c) together with their fits.

Changes of SNP concentration and brightness during PEGylation

The changes of SNP properties during PEGylation was monitored by FCS. In addition to the change of particle size (Fig. 5.3c and e in main manuscript), the FCS derived evolution in particle concentration and single-particle fluorescence brightness are plotted in Supplementary Figure C6. The fact that particle concentration and brightness remained unchanged before and after the addition of PEG-silane and PEG further corroborated that the instant increase of SNP size was due to a fast association between SNP and PEG chains, but not to SNP aggregation.

Comparison of kinetics of silane condensation and SNP PEGylation

The SNP size evolution was monitored via FCS throughout the SNP synthesis reaction, until the high temperature treatment step (Fig. 5.3b). We did not take the high

temperature treatment into consideration here because first, it partially quenched Cy5 fluorophores leading to additional complexity in the FCS analysis and second, we found it may not be essential to achieve successful PEGylation. Supplementary Figure C7 directly compares the kinetics of SNP formation and PEGylation steps by renormalizing TMOS monomer and PEG-silane additions to $t=0$, respectively (see Fig. 5.3b in main manuscript displaying the “true” unaltered time dependence). While the SNP formation kinetics, resulting from silane hydrolysis, particle nucleation, and silane condensation, was relatively slow (black line in Fig. 5.3b and Supplementary Fig. C7), the attachment of PEG-silane to SNPs was completed almost instantly within the time resolution of 1 to 2 minutes of the experiment (red line in Fig. 5.3b and Supplementary Fig. C7). This fast PEGylation kinetics is inconsistent with the expected time scale of PEG silane hydrolysis and condensation onto the particle surface as the condensation rate of PEG-silane is much slower as compared to that of silicic acid due to the conjugation of the silane to the PEG chain. This suggested that the fast PEGylation kinetics was not likely due to silane condensation, but instead was caused by a non-covalent association between PEGs and silica surface.

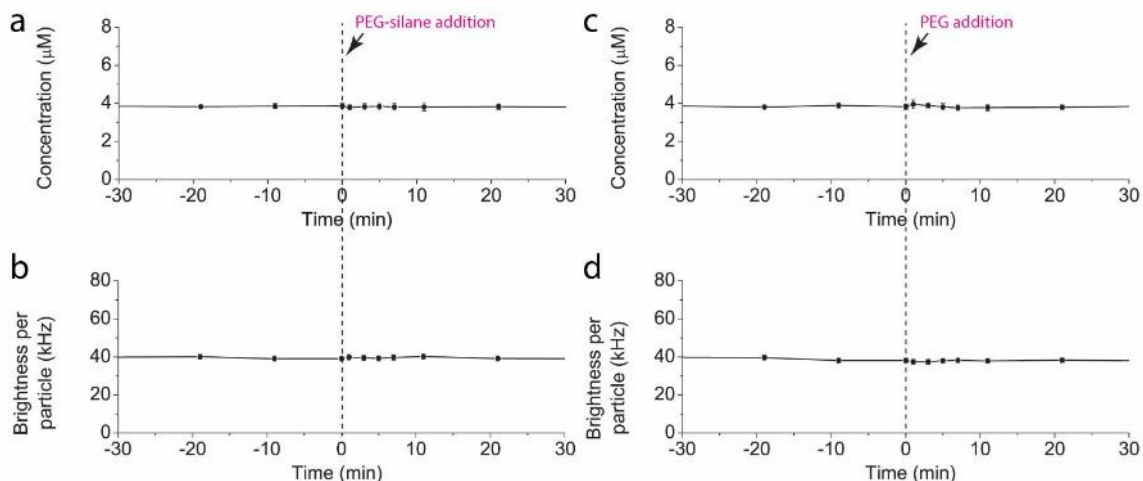


Figure C6. PEGylation reactions as monitored by FCS. Evolution of the FCS derived SNP properties concentration (a and c) and fluorescence brightness per particle (b and d) during PEGylation reactions with PEG silanes (left side) and non-functionalized PEGs (right side). Results were obtained from FCS measurements on Cy5-C' dots.

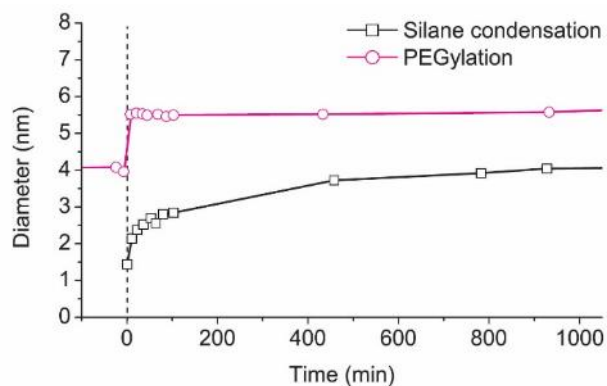


Figure C7. Comparison of kinetics of SNP formation and PEGylation steps. The plot directly compares the kinetics of silane condensation (black curve) and the kinetics of PEGylation (red curve) by renormalizing TMOS monomer and PEG-silane additions to $t=0$, respectively.

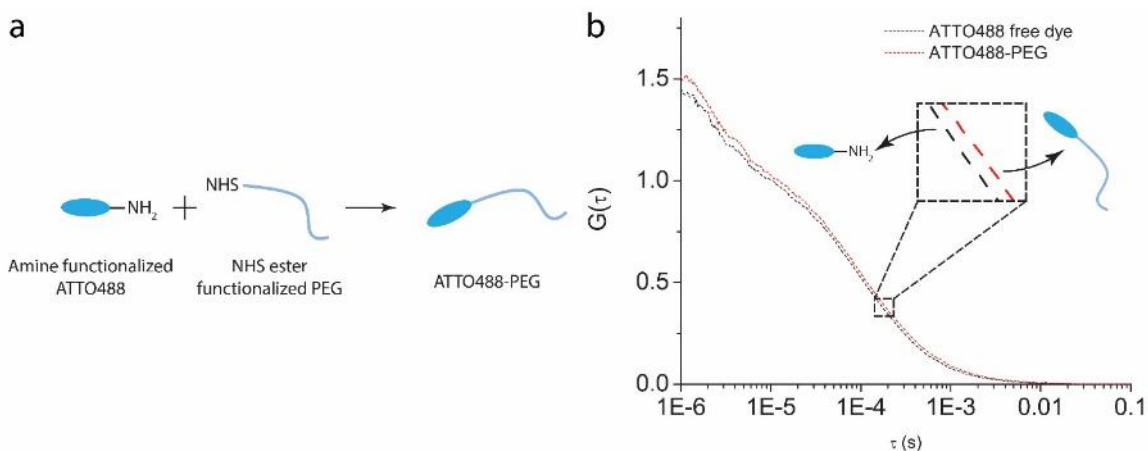


Figure C8. Labeling PEGs with ATTO488 fluorophores. (a) Illustration of the conjugation reaction of amine-functionalized ATTO488 fluorophores and NHS ester-functionalized PEGs. (b) Comparison of the auto-correlations of ATTO488 free dye and ATTO488-labeled PEGs.

Conjugation of ATTO488 to PEGs

In order to endow PEGs with fluorescence for FCS and FCCS measurements, amine-functionalized ATTO488 was conjugated to NHS ester-functionalized PEGs via amide bond formation (Supplementary Fig. C8a). The fluorophore conjugated PEG, ATTO488-PEG, was then subjected to FCS measurements. The auto-correlation curve of ATTO488-PEG slightly shifted to the right as compared to that of ATTO488 free dye (Supplementary Fig. C8b) suggesting slower diffusion from the larger hydrodynamic size. According to the fit of the auto-correlation curves, ATTO488-PEG had an average hydrodynamic size of about 1.9 nm, while ATTO488 free dye was about 1.7 nm in size. Results corroborated successful conjugation of ATTO488 to PEG.

Analysis FCCS results

The general expression for auto- and cross-correlation functions is given as the following^{5,6}.

$$G_{ij}(\tau) = \frac{\langle \delta F_i(t) \cdot \delta F_j(t+\tau) \rangle}{\langle F_i(t) \rangle \cdot \langle F_j(t) \rangle} \quad (4)$$

where $\langle F_i(t) \rangle$ and $\langle F_j(t) \rangle$ are the time-averaged fluorescence signals of two distinct fluorescent species i and j . $\delta F_i(t)$ and $\delta F_j(t + \tau)$ are their fluorescence fluctuations at time t and $t+\tau$. The expression in (4) provides the single-color auto-correlation when $i=j$, while it provides the dual-color cross-correlation when $i \neq j$. For a dual-color FCS/FCCS setup, which measures the diffusion of two species with distinct blue (ATTO-PEG) and red fluorescence (Cy5-C' dot), the correlations can be expressed in the following way:

Red channel (Cy5-C' dot):

$$G_{RR}(\tau) = \frac{\langle N_R \rangle \cdot Diff_R(\tau) + \langle N_{RB} \rangle \cdot Diff_{RB}(\tau)}{(\langle N_R \rangle + \langle N_{RB} \rangle)^2} \quad (5)$$

Blue channel (ATTO488-PEG):

$$G_{BB}(\tau) = \frac{\langle N_B \rangle \cdot Diff_B(\tau) + \langle N_{RB} \rangle \cdot Diff_{RB}(\tau)}{(\langle N_B \rangle + \langle N_{RB} \rangle)^2} \quad (6)$$

Cross over (ATTO488-PEG adsorbed Cy5-C' dot):

$$G_{RB}(\tau) = \frac{\langle N_{RB} \rangle \cdot Diff_{RB}(\tau)}{(\langle N_R \rangle + \langle N_{RB} \rangle) \cdot (\langle N_B \rangle + \langle N_{RB} \rangle)} \quad (7)$$

where A_i is the average number of species i ($i = R, B$ or RB) present in the focal volume, and $Diff_i(\tau)$ is the temporal correlation decay caused by diffusion. Since blinking of Cy5 and ATTO488 fluorophores can also be recognized via auto-correlations, a triplet state correction is added to the expression of $Diff_i(\tau)$ for $i = R$ and B . $Diff_i(\tau)$ can therefore be expressed in the following way:

Cy5-C' dot:

$$Diff_R(\tau) = \frac{1}{1-A_R} \cdot \left(1 - A_R + A_R \cdot e^{-\frac{\tau}{\tau_{trip.R}}} \right) \cdot \frac{1}{1+\frac{\tau}{\tau_{D.R}}} \cdot \frac{1}{\sqrt{1+S^2 \cdot \frac{\tau}{\tau_{D.R}}}} \quad (8)$$

ATTO488-PEG:

$$Diff_B(\tau) = \frac{1}{1-A_B} \cdot \left(1 - A_B + A_B \cdot e^{-\frac{\tau}{\tau_{trip.B}}} \right) \cdot \frac{1}{1+\frac{\tau}{\tau_{D.B}}} \cdot \frac{1}{\sqrt{1+S^2 \cdot \frac{\tau}{\tau_{D.B}}}} \quad (9)$$

ATTO488-PEG adsorbed Cy5-C' dot:

$$Diff_{RB}(\tau) = \frac{1}{1+\frac{\tau}{\tau_{D.RB}}} \cdot \frac{1}{\sqrt{1+S^2 \cdot \frac{\tau}{\tau_{D.RB}}}} \quad (10)$$

where A_i is the average percentage of triplet state fluorophores and $\tau_{trip.i}$ is the triplet relaxation time ($i= R \text{ or } B$). $\tau_{D,i}$ is the diffusion time ($i= R, B \text{ or } RB$). S is the structure factor of the FCS/FCCS setup (ratio of the short axis to the long axis of the elliptical focal spot) which is obtained from calibration of the setup with a known standard fluorophore.

In our experiments, $\langle N_{RB} \rangle \ll \langle N_R \rangle, \langle N_B \rangle$ due to the weak affinity between PEGs and silica (Fig. 5.5b and d). The expressions of $G_i(\tau)$ can therefore be simplified as follows:

Red channel (Cy5-C' dot):

$$G_{RR}(\tau) \cong \frac{Diff_R(\tau)}{\langle N_R \rangle} = \frac{1}{\langle N_R \rangle} \cdot \left(1 - A_R + A_R \cdot e^{-\frac{\tau}{\tau_{trip.R}}} \right) \cdot \frac{1}{1+\frac{\tau}{\tau_{D.R}}} \cdot \frac{1}{\sqrt{1+S^2 \cdot \frac{\tau}{\tau_{D.R}}}} \quad (11)$$

Blue channel (ATTO488-PEG):

$$G_{BB}(\tau) \cong \frac{Diff_B(\tau)}{\langle N_B \rangle} = \frac{1}{\langle N_B \rangle} \cdot \left(1 - A_B + A_B \cdot e^{-\frac{\tau}{\tau_{trip.B}}} \right) \cdot \frac{1}{1+\frac{\tau}{\tau_{D.B}}} \cdot \frac{1}{\sqrt{1+S^2 \cdot \frac{\tau}{\tau_{D.B}}}} \quad (12)$$

Cross over (ATTO488-PEG adsorbed Cy5-C' dot):

$$G_{RB}(\tau) \cong \frac{\langle N_{RB} \rangle \cdot Diff_{RB}(\tau)}{\langle N_R \rangle \cdot \langle N_B \rangle} = \frac{\langle N_{RB} \rangle}{\langle N_R \rangle \cdot \langle N_B \rangle} \cdot \frac{1}{1+\frac{\tau}{\tau_{D.RB}}} \cdot \frac{1}{\sqrt{1+S^2 \cdot \frac{\tau}{\tau_{D.RB}}}} \quad (13)$$

In order to further include artificial cross-talk signal between the two channels, the cross-correlation curves were also fitted with two-component correlation function, where $Diff_i(\tau)$ is expressed as follow:

$$Diff_i(\tau) = F_1 \cdot \frac{1}{1 + \frac{\tau}{\tau_{D.i.1}}} \cdot \frac{1}{\sqrt{1 + S^2 \cdot \frac{\tau}{\tau_{D.i.1}}}} + (1 - F_1) \cdot \frac{1}{1 + \frac{\tau}{\tau_{D.i.2}}} \cdot \frac{1}{\sqrt{1 + S^2 \cdot \frac{\tau}{\tau_{D.i.2}}}} \quad (14)$$

F_1 and $(1-F_1)$ are the percentages of the two diffusion species, respectively. If a second diffusing species was successfully identified, the results were taken. Otherwise, the cross-correlation curve were fitted using equation (13).

The diffusion time $\tau_{D,i}$, and number of average particles in the focal volume, $\langle N_{Ri} \rangle$, can be obtained from fitting the correlation curves as described above. The concentration of species i can then be calculated by:

$$\langle C_i \rangle = \frac{\langle N_i \rangle}{V_{eff}} \quad (15)$$

where the focal volume V_{eff} is obtained from calibration of the setup. The hydrodynamic diameter of measured particles can then be calculated by:

$$d_{hydrodynamic} = \frac{kT}{6\pi\eta D} \quad (16)$$

where k is the Boltzmann constant, T is the sample temperature (room temperature) in Kelvin and η is the viscosity of the sample solution at temperature T .

The analysis results of the FCS and FCCS measurements are summarized in Supplementary Table C2. By dividing the concentration of ATTO-PEG adsorbing Cy5-C' dot obtained from the cross-correlation by the concentration of ATTO488-PEG obtained from the blue channel auto-correlation, it was estimated that about one out of 100 ATTO488-PEGs were adsorbed by the Cy5-C' dot. Since in a typical experiment on

average only about 50% of all SNPs are labeled by Cy5³, it was then estimated that under these conditions there was about one out of 50 PEGs adsorbed by the SNPs. Although this association percentage of PEGs is expected to significantly increase when SNP concentration is increased in the non-diluted PEGylation process, it indicated the existence of a large amount of extra PEG molecules which did not attach to SNPs during PEGylation.

Table C2. Summary of FCCS measurement results

Sample	Channel	Signal fractions	Apparent concentration	Hydrodynamic diameter
 Cy5-C' dots + ATTO488-PEG / PEG	Red	100%	33.1 ± 0.1 nM	4.3 ± 0.2 nm
	Blue	100%	149.6 ± 0.3 nM	2.0 ± 0.1 nm
	Cross	45 ± 8% 55 ± 7%	1.4 ± 0.3 nM Caused by the cross-talk between the two channels	5.7 ± 0.2 nm
 Cy5-C' dots + ATTO488 / PEG	Red	100%	32.7 ± 0.2 nM	4.2 ± 0.2 nm
	Blue	100%	155.2 ± 0.2 nM	1.8 ± 0.2 nm
	Cross	100%	0.5 ± 0.1 nM	1.2 ± 0.5 nm
 Cy5-C' dots + ATTO488-PEG	Red	100%	33.3 ± 0.2 nM	3.4 ± 0.1 nm
	Blue	100%	146.3 ± 0.2 nM	2.1 ± 0.2 nm
	Cross	52 ± 9% 48 ± 12%	1.8 ± 0.3 nM Caused by the cross-talk between the two channels	5.6 ± 2.0 nm

This conclusion was further supported by the DLS particle size measurements (Supplementary Fig. C9). Right after SNP synthesis, a strong scattering signal from diffusing species with average hydrodynamic diameter about 1 nm was detected, which was attributed to free PEG-silane molecules or self-condensed PEG-silane clusters with considerable concentration. In contrast, after dialysis the average hydrodynamic size increased to about 5nm consistent with TEM and FCS, indicating the successful removal of extra unattached PEGs by dialysis and the high monodispersity of the remaining PEGylated SNPs.

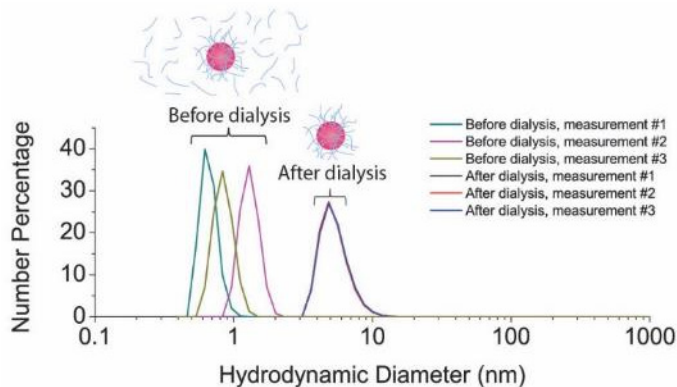


Figure C9. Unattached PEG-silane recognized by DLS. Comparison of PEGylated SNPs solution before and after dialysis indicating the considerable amount of unattached PEG-silane left from PEGylation. Each measurement was repeated three times.

By comparing the amount of PEGs left in the cleaned PEGylated SNPs, which could be obtained from TGA, and the known amount of PEGs added into the reaction, it was estimated that only 10% to 30% of added PEGs ended up on the SNPs (Fig, 5d insert). This is consistent with FCCS and DLS observations, in which large amounts of extra unattached PEG-silane were detected. However, the fast association kinetics of PEGs and silica, as well as their specific affinity, is independent from this low conversion percentage of PEG-silanes. As long as enough PEG-silane is added, the successful PEGylation of SNPs can be completed in a very short period of time.

Adsorption of PEGs accelerates their condensation onto SNP surfaces

Additional experiments were performed to study at which step during PEGylation the covalent bonds form between PEG-silane and SNPs. To that end, the SNP solution was significantly diluted immediately after PEG addition. If no covalent bond forms, the adsorbed PEGs will be released from SNPs upon dilution due to the low PEG concentration, resulting in the decrease of average SNP size. Otherwise, the PEGs cannot

be released from SNPs upon dilution due to the covalent attachment, and the average SNP size will remain unchanged.

As shown in Supplementary Figure C10, immediately after addition of PEG-silane or unfunctionalized PEGs, the auto-correlation curve of Cy5-C' dots shifted to the right, indicating the increase of average SNP size caused by PEG adsorption. Afterwards, the reaction solution was immediately diluted 10^5 times, followed by FCS size measurements. The dilution was performed within 30 seconds after PEG addition. If non-functionalized PEG was added, the Cy5-C' dot auto-correlation curve shifted back to the left upon dilution, suggesting the decrease of average SNP size caused by the release of PEGs (Supplementary Fig. C10b). In contrast, if PEG-silane was added, the Cy5-C' dot auto-correlation curve remained almost unchanged after dilution, suggesting no change in SNP size (Supplementary Fig. C10a). These results demonstrated that no PEG-silane was released from SNPs, even though the reaction concentration was decreased 10^5 times. Results indicated that covalent bonds between PEG-silane and SNPs had already formed upon PEG-silane addition, whose kinetics was surprisingly fast. These results, together with the data described in the main manuscript, provided evidence that the non-covalent association between PEGs and silica greatly accelerated the formation of covalent bonds between PEG-silane and SNPs, and therefore contributed to the successful PEGylation.

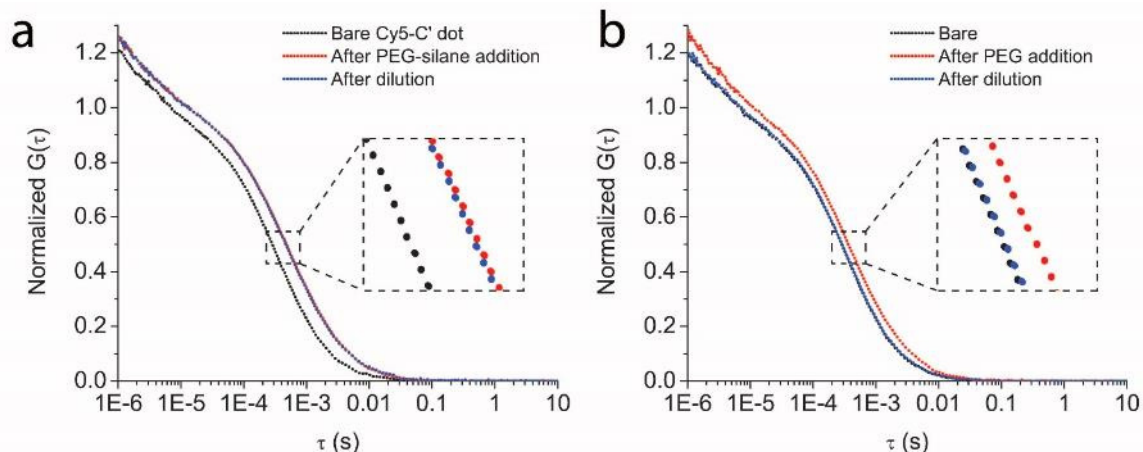


Figure C10. Release of adsorbed PEGs from SNPs. (a) Comparison of auto-correlation of Cy5-C' dots before/after PEG-silane addition and after dilution. (b) Comparison of auto-correlation of Cy5-C' dots before/after non-functionalized PEG addition and after dilution.

Reference for Appendix C.

- (1) Gennes, P. G. D. Conformations of polymers attached to an interface. *Macromolecules* **13**, 1069–1075 (1980).
- (2) Jokerst, J. V., Lobovkina, T., Zare, R. N. & Gambhir, S. S. Nanoparticle PEGylation for imaging and therapy. *Nanomedicine* **6**, 715–728 (2011).
- (3) Ma, K. *et al.* Control of ultras-small sub-10 nm ligand-functionalized fluorescent core-shell silica nanoparticle growth in water. *Chem. Mater.* 4119–4133 (2015).
- (4) Ow, H. *et al.* Bright and stable core-shell fluorescent silica nanoparticles. *Nano Lett.* **5**, 113–117 (2005).
- (5) Bacia, K., Kim, S. A. & Schwille, P. Fluorescence cross-correlation spectroscopy in living cells. *Nat. Meth.* **3**, 83–89 (2006).
- (6) Kettling, U., Koltermann, A., Schwille, P. & Eigen, M. Real-time enzyme kinetics monitored by dual-color fluorescence cross-correlation spectroscopy. *Proceedings of the National Academy of Sciences* **95**, 1416–1420 (1998).

Chapter 6 . Formation Pathways of Mesoporous Silica Nanoparticles with Dodecagonal Tiling

6.1 Introduction

Quasicrystals exhibit highly ordered local structure but lack long range translational periodicity, and permit symmetry operations that are forbidden in classical crystallography, *e.g.* five-, eight-, ten- and twelve-fold rotations.^{1,2} They have been observed in a wide variety of materials, including metal alloys,^{1, 3} thin films,⁴ liquid crystals,⁵ polymers,⁶ colloids⁷ and mesoporous networks,⁸ demonstrating that quasicrystals can be considered a universal form of ordering.⁹ Despite increasing attention to the identification of novel quasicrystalline materials, little has been shown experimentally regarding their early growth pathways. Multiple formation mechanisms have been proposed via theoretical models.¹⁰⁻¹⁶ For example, recent computer simulations demonstrate that design criteria such as shape polydispersity and anisotropic particle surface modifications^{17,18} may promote quasicrystalline order in self-assembled systems. However, direct experimental observation of early formation stages and processes of quasicrystals remains a challenge. Here we show that by taking advantage of highly tunable silica sol-gel chemistry, the early stages of quasicrystalline mesoporous silica formation can be experimentally preserved as nanoparticles. The size of these mesoporous silica nanoparticles (MSNs) can be tuned from > 100 nm, for which dodecagonal tiling patterns are well developed, down to < 30 nm, where particles consist of only a single triangle or square tiling unit. Simultaneously, the quasicrystallinity of the mesopore structure can be controlled via a single experimental parameter. Based on these observations, a library of MSNs with varying size and quasicrystallinity is synthesized and compared to growth simulations. Our results elucidate

early formation pathways of dodecagonal quasicrystalline mesoporous silica and demonstrate an experimental control parameter that can be used to tune quasicrystallinity, thereby providing fundamental insights into quasicrystal formation mechanisms.

Since its discovery in 1992, mesoporous silica has attracted widespread attention. There have been reports of bulk¹⁹⁻²¹ and nanoscale mesoporous silica²²⁻²⁴ with a variety of pore structures, including hexagonal,¹⁹ cubic,²⁴ and quasicrystalline structures.^{8,26} The formation of mesoporous silica is a result of silica condensation directed by molecular templates, such as surfactants or polymers.^{19,25} This co-assembly process is driven by non-directional interactions between micelles and silica precursors, making mesoporous silica similar to systems of metal alloys, where non-directional bonding plays a key role in achieving the non-periodic bonding geometries required for quasicrystal formation.⁹ Inspired by this analogy, we have synthesized MSNs with dodecagonal tiling and used them to study the early formation mechanisms of quasicrystalline mesoporous silica.

6.2 Experimental section

6.2.1 Materials

Hexadecyltrimethylammonium bromide (CTAB, $\geq 99\%$), ethyl acetate (EtOAc, ACS grade), ammonium hydroxide (NH₄OH, 29%), 1,3,5-trimethylbenzene (TMB, 99%), *N*-(2-aminoethyl)-3-aminopropyltrimethoxysilane (AEAPTMS, 95%), (3-aminopropyl)trimethoxysilane (APTMS, 95%), tetraethyl orthosilicate (TEOS, $\geq 99\%$), tetramethyl orthosilicate (TMOS, $\geq 99\%$), hydrochloric acid (HCl, 36.5-38%), acetic acid (glacial), and ethanol (absolute, anhydrous) were used as received without further purification. Deionized water (Milli-Q, 18.2 M Ω ·cm) was used throughout.

6.2.2 Synthesis of MSNs with varying [TMB] (TEOS/AEAPTMS system)

Round bottom flasks (14/20, 100mL) and egg-shaped stir bars (L x Dia.: 19 x 9.5 mm) were used in all TEOS/AEAPTMS syntheses described in this paper. MSNs were prepared with [TMB] ranging from 12mM to 205mM. EtOAc (0.44mL), NH₄OH (1.35 mL), and then TMB were added to an aqueous solution of CTAB (52.5mL, 2.61 mM) stirring at 650 rpm. After 30 minutes, a mixture of TEOS (0.25mL) and AEAPTMS (0.0375 mL) was added to the reaction and allowed to react for 5 minutes. Then, additional water (18.45 mL) was added and the reaction was left stirring for 24 hours. On completion of the reaction, the particle suspension was neutralized with 2M HCl, before cleaning by repeated centrifugation and redispersion in EtOH. CTAB was removed from the resulting particles by adding 5 vol% of acetic acid to the suspension and stirring for 30 minutes. Following

CTAB removal, the particles were again cleaned by repeated centrifugation and redispersion in EtOH.

In order to study the effect of stirring rate on the structure of these particles, MSNs were synthesized using constant [TMB] (29 mM) and four different stirring rates: 500 rpm, 650 rpm, 800 rpm, and 1000 rpm. All other synthesis parameters were unchanged from the above description.

6.2.3 Synthesis of MSNs with varying [TMB] and pH (TMOS/APTMS system).

Round bottom flasks (14/20, 25 mL) and egg-shaped stir bars (L x Dia.: 19 x 9.5 mm) were used in all TMOS/APTMS syntheses described in this paper. MSNs were prepared with [TMB] ranging from 14mM to 72mM and [NH₄OH] ranging from 15mM to 150mM. High [TMB] resulted in more quasicrystalline particles and high [NH₄OH] resulted in larger particle sizes. NH₄OH and TMB were added to an aqueous solution of CTAB (10 mL, 22.78 mM) stirring at 600 rpm. After 30 minutes, a mixture of TMOS (34 μL) and APTMS (25 μL) was added to the reaction and allowed to react for 24 hours. On completion of the reaction, the particle suspension was cleaned by repeated centrifugation and redispersion in EtOH. CTAB was removed from the resulting particles by adding 5 vol% of acetic acid to the suspension and stirring for 30 minutes. Following CTAB removal, the particles were again cleaned by repeated centrifugation and redispersion in EtOH.

6.2.4 Characterization

Transmission electron microscopy (TEM) images were taken using a FEI Tecnai T12 Spirit microscope operated at an acceleration voltage of 120 kV. Fast Fourier transform (FFT) patterns were analyzed by ImageJ software. Each TEM sample was prepared by evaporating 10 μL of suspension on TEM grid in dry air.

Small-angle x-ray scattering (SAXS) patterns were obtained at the G1 station at the Cornell High Energy Synchrotron Source (CHESS) using a 10 keV beam and a sample-to-detector distance of 40 cm. All samples were powders prepared by vacuum drying MSN suspensions and were imaged soon after drying.

Nitrogen sorption measurements were performed using a Micromeritics ASAP2020 instrument. For each measurement, approximately 10 mg of freshly vacuum-dried powder sample was degassed at room temperature under vacuum overnight prior to the analysis.

6.2.5 Tiling Analysis

The edges of the square-triangle tiling correspond to the six dodecagonal directions in physical (or parallel) space. Each vertex in parallel space can be expressed as

$$\mathbf{r}^{\parallel} = n_1\mathbf{e}_1^{\parallel} + n_2\mathbf{e}_2^{\parallel} + n_3\mathbf{e}_3^{\parallel} + n_4\mathbf{e}_4^{\parallel},$$

where n_i is a unique set of integer coordinates and $\mathbf{e}_i^{\parallel} = \{\cos(\alpha(i-1)), \sin(\alpha(i-1))\}$ with $\alpha = \pi/3$ and $i = 1-4$. The corresponding vector \mathbf{r}^{\perp} in perpendicular space is

$$\mathbf{r}^{\perp} = n_1\mathbf{e}_1^{\perp} + n_2\mathbf{e}_2^{\perp} + n_3\mathbf{e}_3^{\perp} + n_4\mathbf{e}_4^{\perp},$$

where n_i is again a unique set of integer coordinates and the dodecagonal directions in perpendicular space are $\mathbf{e}_i^\perp = \{\cos(7\alpha(i - 1)), \sin(7\alpha(i - 1))\}$ with $\alpha = \pi/3$ and $i = 1-4$. As shown in Figure 6.2c and d, the 2D parallel and perpendicular spaces are identified by means of consistency of $\mathbf{e}_1^{\parallel,\perp}$ and $\mathbf{e}_3^{\parallel,\perp}$.

Following transformation from parallel to perpendicular space, a crystalline pattern, *e.g.* with pure square or triangle packing, remains unchanged. In contrast, a quasicrystalline pattern shrinks upon translation to perpendicular space. The degree of shrinkage reflects the disorder in the triangle-square packing and can be used as a measure of quasicrystallinity. For this reason, the quasicrystallinity of a pattern can be obtained by comparing the radii of gyration of the patterns in parallel and perpendicular spaces. The relationship between the radii of gyration in the two spaces can be described by the linear equation $R_{g\perp} = AR_{g\parallel} + B$, where the slope provides the magnitude of the phason strain, a quantitative measure of quasicrystallinity. The phason strains of an ideal quasicrystal and crystal are 0 and 1, respectively.

Tilings of the synthesized MSNs were obtained from TEM images using a self-written MATLAB program, where 10% tolerance of edge orientation and edge length are allowed and undeveloped pores were not counted. These tilings were further analyzed by using a second self-written program to calculate $R_{g\parallel}$ and $R_{g\perp}$ and to quantify the presence of the four fundamental geometrical conformers present in the structure, *i.e.* 4^4 , 3^34^2 , 3^2434 and 3^6 (see details in main text). Considering that differently sized MSNs synthesized at the same [TMB] but at varying pH are expected to have similar micelle size and size distribution, a linear fit ($R_{g\perp} = AR_{g\parallel} + B$) was applied to MSNs synthesized at the same [TMB]. For MSNs synthesized at the highest [TMB] with the highest quasicrystallinity,

the plot of $R_{g\perp}$ vs. $R_{g\parallel}$ was described well by this linear relationship. This suggests that individual MSNs have the same type of crystalline pattern, and thus the fitted slope represents the phason strain of the structure obtained from this [TMB]. In contrast, as [TMB] decreased, large particles synthesized at intermediate [TMB] exhibited substantial fluctuations in the plot of $R_{g\perp}$ vs. $R_{g\parallel}$, suggesting that the MSN structure obtained from those synthesis conditions was heterogeneous. Therefore, in this case the slope of the linear fit does not reflect the phason strain of these individual particles. However, the fact that the slope of these fits increased with increasing [TMB] (or decreased with decreasing [TMB]) suggests that the average quasicrystallinity of all the MSNs from a single synthesis is highly dependent on [TMB].

6.2.6 Growth Simulations

Growth of quasicrystalline mesoporous silica materials has previously been modeled as a random aggregation of triangle and square tiles⁸. The relationship between these fundamental triangle/square units and CTAB micelle packings is illustrated schematically in Figure 6.1b to e. While these simulations do not directly address the details of the micelle packing process, they can play an important role in developing an understanding of the structural arrangement of triangle/square tiles observed experimentally in quasicrystalline mesoporous silica. We have therefore modeled our experimental system using a similar tiling process.⁸

We employed a random square-triangle tiling process wherein cluster growth, seeded by an individual equilateral triangle or square tile, proceeds by sequential and irreversible edge-to-edge addition of triangle and square tiles with edge length a . The seed

tile and all subsequent tiles were randomly chosen from a weighted distribution defined by an input triangle/square ratio. New tiles were placed at random, according to a probability-weighted list of candidate growth sites defined as edges that lie on the boundary of the growing cluster. Candidate sites were assigned probabilities according to physically inspired interaction potential energies. The tiling process proceeded until the final particle size, determined at the start of each simulation from a weighted normal distribution about an average particle size, was reached. Importantly, we did not make any effort to suppress the stochastic noise that accompanies this process. Comparison with experimental data showed that these results may reflect local fluctuations of the micelle sizes in solution.

In defining interaction potentials for candidate growth sites, we included two separate contributions, one that reflects the incoming shape and the geometry of the site and one that is directly related to the distance, d , of the site from the center of mass of the growing cluster. Interaction potentials were optimized so that an input triangle/square ratio of 2.3 produced clusters with quasicrystalline features and were then held constant for the remainder of these simulations. The form of the attachment probability, P , associated with each candidate site was also considered a fitting parameter and was ultimately determined to be:

$$P = P_s \times (d/d_0)^{-10},$$

where P_s is the attachment probability associated with the surface site geometry, and d , the distance from center parameter is normalized by d_0 , the shortest radial distance from the particle edge to its center of mass. Contributions to P_s are specified as follows:

- (1) The edge-edge contact between a square and a triangle P_{ST} , two triangles P_{TT} , two squares P_{SS} .

- (2) The interaction between an incoming square tile and an incomplete 90° corner, P_R .
- (3) The interaction between an incoming triangle tile and incomplete 60° or 120° corners, P_T .

Using a triangle/square ratio of 2.3, parameter values were $P_{ST} = 0.75$, $P_{TT} = 0.001$, $P_{SS} = 0.001$, $P_R = 0.75$, and $P_T = 0.75$. We found that it was necessary to include P_{TT} and P_{SS} as repulsive parameters to prevent the formation of large hexagonal or cubic domains, which were not observed in our experimental particles. Additionally, P_R and P_T were included as attractive parameters to discourage defect formation. For sites that could be assigned to multiple categories, the highest P_S was used. Thus each growth site was given a single interaction potential, specifically defined as the probability that particular site will be filled. For each tile addition, a revised list of interaction potentials was generated to reflect changes to the list of candidate growth sites and a specific growth site was randomly chosen from this probability-weighted list. Optimized values of P_S were kept constant for the remainder of the simulations where the triangle/square number ratio was varied to reflect the range of [TMB] used in experiments.

In order to address the possibility that only growth sites with very low attachment probabilities exist, an additional threshold parameter is included. This attachment threshold, T , is given by

$$T = 0.000075 \times r,$$

where r is the maximum radial distance from the particle edge to its center of mass. If the growth site chosen from the distribution of attachment probabilities is below T , then the

tile is not placed. Instead, a new tile is chosen from the shape distribution and the choice is repeated. If after 100 attempts, no site with $P > T$ is chosen, then the growth site is temporarily removed from the list of candidate sites and a new tile is again chosen. This process is repeated until a tile can be placed and the growth can proceed.

For each triangle/square ratio, four batches of particles with varying average diameter were generated and combined for analysis. Final particle size was determined at the start of each simulation by random choice from a probability weighted distribution about an average size. The simulation was terminated when the particle reached the predetermined size. In defining the distribution of particle sizes, we utilized a set of four normal distributions with mean (μ) and variance (σ) parameters as follows.

$$\text{Set A: } (\mu, \sigma) = (1.5, 0.5)$$

$$\text{Set B: } (\mu, \sigma) = (3.5, 1.5)$$

$$\text{Set C: } (\mu, \sigma) = (6.0, 2.0)$$

$$\text{Set D: } (\mu, \sigma) = (7.5, 2.5)$$

These distributions were chosen to reflect the sizes of the particles observed in experiments.

6.2.7 Fitting of the relationship between $R_{g\perp}$ and the total number of squares before the first triangle is attached.

The black dots in Figure 6.4b and c, for which no triangle ever entered the simulations, represent the relationship between the total area and the radius of gyration of a 2D square packing. However, it is interesting to note that all the other data points in Figure 6.4c, which came from the simulations whose final structure does contain triangles, lie on the same curve. This indicates that the growth of particles in perpendicular space

follows the same trend whether or not a triangle is involved in the particle growth; and this is independent of the particle's final quasicrystallinity. In order to quantitatively resolve this general relationship, all the data in Figure 6.4c were fitted using the equation $N = N(R_g \perp)$ of 2D tiling of squares. To derive the fitting equation, an approximation was first made that the shape of the overall tiling is a perfect square. This is consistent with experiments in which cubic MSNs always have square facets (Fig. 6.1d).

According to the definition of the radius of gyration R_g , the radius of gyration of a 2D square packing follows the following equation:

$$R_g^2 = \frac{1}{(\sqrt{N} + 1)^2} \sum_{n=0}^{(\sqrt{N}+1)^2} r_n^2$$

where N is the total number of squares and r_n is the distance of point n to the center of mass of the packing.

$$r_n = a \cdot \sqrt{(x_n^2 + y_n^2)}$$

where x_n and y_n are the normalized coordinates of point n in the coordinate system whose origin is the mass center of the overall square tiling. a is the edge length of a single square tile and $a=1$.

R_g can then be expressed as:

$$\left(\frac{R_g}{a}\right)^2 = \frac{1}{6} \left((\sqrt{N} + 1)^2 - 1 \right)$$

Solving for N yields the relationship between R_g and N .

$$N = 6 \left(\frac{R_g}{a} \right)^2 - 2 \sqrt{6 \left(\frac{R_g}{a} \right)^2 + 1} + 2$$

N for large packings, where $6 \left(\frac{R_g}{a} \right)^2 \gg 1$, can be approximated by:

$$N \approx 6 \left(\frac{R_g}{a} \right)^2 - 2\sqrt{6} \left(\frac{R_g}{a} \right) + 2 \approx 6 \left(\frac{R_g}{a} \right)^2 - 4.9 \left(\frac{R_g}{a} \right) + 2$$

Since $a=1$,

$$N \approx 6R_g^2 - 4.9R_g + 2$$

We therefore fit the data in Figure 6.4c using the equation

$$N = AR_g^2 + BR_g + C$$

where the fitted values A, B and C are equal to 6.3, -6.3 and 2.6, respectively. These values agree well with the theoretical expectations as described above.

6.3 Results and discussion.

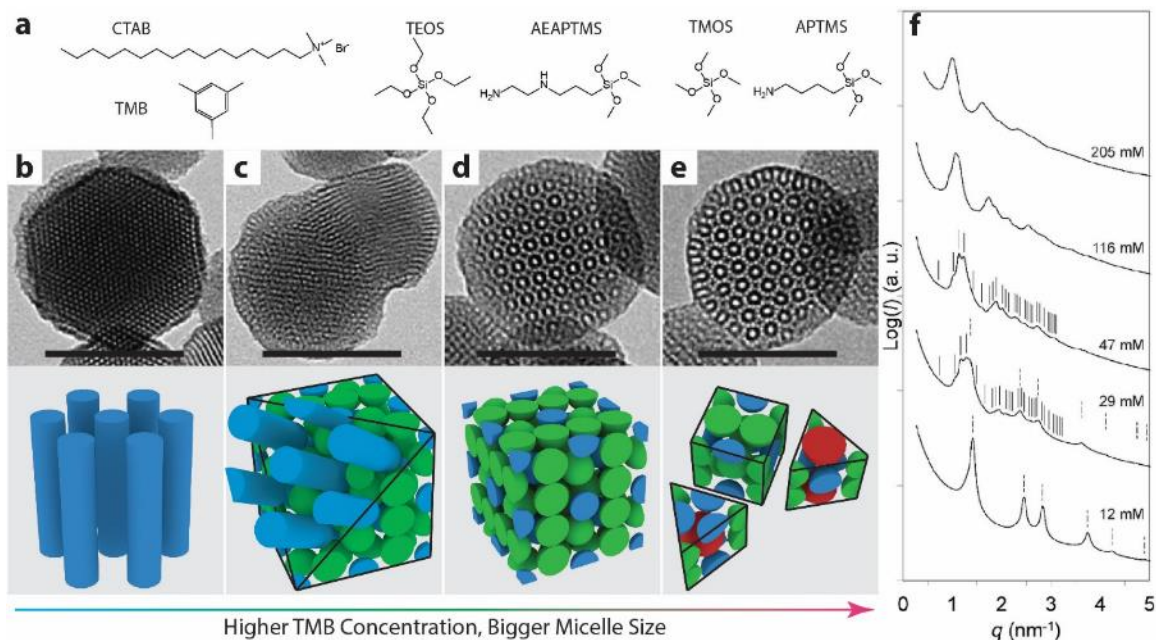


Figure 6.1. Four MSN structures observed as a function of [TMB] and their structural characterization. (a) Chemical structures of key compounds used in TEOS/AEAPTMS and TMOS/APTMS synthesis systems. (b to e) TEM images and corresponding 3D micelle packing models for MSNs prepared from TEOS/AEAPTMS with (b) 12 mM, (c) 29 mM, (d) 47 mM, and (e) 116 mM TMB. Scale bars in all TEM images are 100 nm. (f) SAXS patterns for MSNs synthesized with increasing [TMB]; q denotes the scattering vector, defined as $q = 4\pi \sin\theta/\lambda$, with 2θ being the total scattering angle and λ being the x-ray wavelength (1.23 Å). In the SAXS patterns for the first three samples, expected peak positions for hexagonal $P6mm$ and cubic $Pm\bar{3}n$ lattices are indexed by dashed and solid lines, respectively.

MSNs were synthesized by co-condensing two organosilane precursors in the presence of CTAB surfactant (Fig. 6.1a). A micelle pore expander, TMB, was added to systematically vary CTAB micelle size.^{27, 28} The TEM images in Figure 6.1b to e show MSNs with four distinct morphologies found with increasing TMB concentration, [TMB], moving from hexagonal to multicompartment (Fig. D1-3) to cubic and finally to a structure with dodecagonal symmetry. SAXS measurements averaging over macroscopic sample

volumes corroborate the structural transitions observed in TEM (Fig. 6.1f). At 12 mM [TMB], the SAXS pattern shows reflections consistent with hexagonal symmetry. When [TMB] is increased to 29 mM, a well-resolved set of cubic $Pm\bar{3}n$ reflections from the particle cores is superposed with a prominent set of hexagonal $P6mm$ reflections from the particle arms. This pattern is consistent with previously reported SAXS measurements from multicompartment MSNs.²² At 47 mM TMB, the SAXS pattern shows reflections consistent with a cubic particle with $Pm\bar{3}n$ lattice²⁴. As [TMB] is further increased to 116 mM and finally to 205 mM, the SAXS patterns lose more and more features and lattices cannot unambiguously be assigned. TEM tilt series (Fig. D4) as well as TEM tomography failed to establish the three-dimensional particle structure, the latter as a result of severe beam damage of the organic-silica hybrids during data acquisition.

Pore size analysis of nitrogen sorption measurements (Fig. D5) on the particles after CTAB removal show a marked pore size increase and broadening of the pore size distribution with increasing [TMB]. The [TMB] induced structural transitions are illustrated schematically by the sphere packings²⁹ at the bottom of Figure 6.1b to e, consistent with discussions in ref. 8. Hexagonal MSNs have channel-like pores which are templated by elongated CTAB micelles (blue). In contrast, $Pm\bar{3}n$ cubic MSNs are composed of two types of spherical micelles, one of which is slightly larger (green) than the other (blue) due to increased TMB loading. As [TMB] is further increased, MSNs with dodecagonal symmetry are formed, incorporating even larger micelles (red). Additional experiments showed that the same structural transitions and pore size increases are observed for MSNs synthesized at 29 mM TMB with increasing stirring rates (Fig. D6 and 7). Two organosilane systems, TEOS/AEAPTMS and TMOS/APTMS, examined

independently showed similar transitions as a function of [TMB] (Fig. D8). This result suggests that the observed structural transitions do not depend as much on the specific silica chemistries as they do on the increased micelle size and broadened micelle size distributions associated with increasing [TMB].

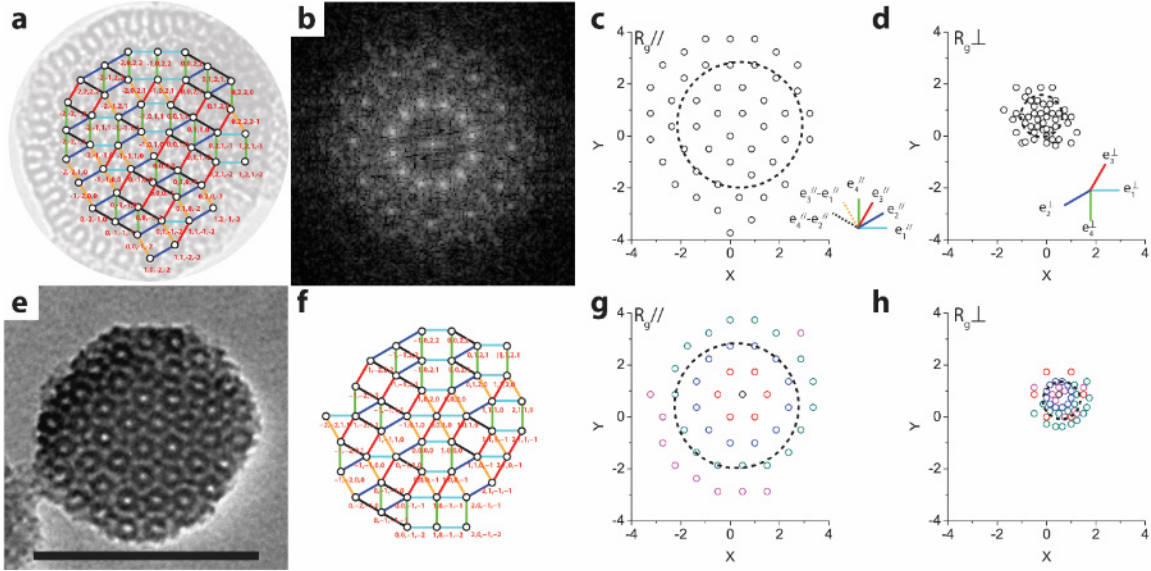


Figure 6.2. Analysis of MSNs with dodecagonal tiling. (a) TEM image of a MSN with dodecagonal symmetry synthesized using TEOS/AEAPTMS superposed with its square-triangle tiling and parallel space coordinates. Edges with different colors correspond to the six dodecagonal directions in parallel space. The corresponding dodecagonal directions in parallel and perpendicular space are shown in c and d, respectively. (b) FFT of the TEM image in (a) exhibiting 12-fold symmetry. (c and d) Parallel and perpendicular space coordinates for the triangle-square tiling shown in (a). Dotted circles with radius equal to $R_{g//}$ and $R_{g\perp}$ are shown on the parallel and perpendicular space plots, respectively. (e and f) TEM image and tiling of an MSN with dodecagonal symmetry synthesized using TMOS/APTMS. (g and h) Parallel and perpendicular space coordinates for the tiling shown in (f). The colors in g and h show how individual points move during the transformation. Images in a and e have the same magnification; scale bar is 100 nm.

Pore patterns of MSNs like the one in Figure 6.1e were tiled using squares and equilateral triangles, which are projections of 3-dimensional packings of differently sized micelles (shown in the bottom panel of Fig. 6.1e). The tile edges correspond to dodecagonal directions and each vertex can be described by $\mathbf{r}^{\parallel} = n_1\mathbf{e}_1^{\parallel} + n_2\mathbf{e}_2^{\parallel} + n_3\mathbf{e}_3^{\parallel} + n_4\mathbf{e}_4^{\parallel}$ (Fig. 6.2a, f). These MSNs exhibit two distinctive features of dodecagonal quasicrystals. Fast Fourier

transforms (FFTs) of TEM images reveal 12-fold symmetry (Fig. 6.2b) and no translational periodicity is observed in tiling patterns extracted from the TEM images (Fig. 6.2a, f). In this study, we focus on the early growth of mesoporous silica materials and will refer to our particles as quasicrystals if a sharp twelve-fold diffraction pattern can be obtained and no periodicity is observed on the scale of the sample.¹⁷

Each vertex in parallel (Fig. 6.2c, g) space corresponds to a unique vertex in perpendicular (Fig. 6.2d, h) space.¹⁴ Figure 6.2g and h show by color how individual points move during this transformation. A comparison of the radii of gyration in parallel and perpendicular space, $R_{g\perp}$ vs. $R_{g\parallel}$, is a measure of the quasicrystallinity of a pattern: the more a pattern shrinks, the more quasicrystalline it is (compare patterns in Fig. 6.2c/g to d/h). TEM images in Figure 6.2a and e and their respective tilings (Fig. 6.2a and f) show that dodecagonal MSNs synthesized using the two different organosilane systems had similar pore structure. Therefore, the somewhat simpler TMOS/APTMS system was chosen for most of the mechanistic studies.

Figure 6.3a illustrates the range of particle structures obtained from over ~50 synthesis batches of particles (see also Fig. D9). Changes in MSN pore structure with increasing [TMB] can be qualitatively assessed by comparing the triangle-square tilings extracted from TEM images (Fig. 6.3A). As [TMB] is increased, the resulting patterns become increasingly quasicrystalline. As pH is lowered, effectively increasing the rate of silane condensation, MSNs with particle sizes down to ~30 nm or a single square/triangle unit were obtained. Figure 6.3b shows a plot of $R_{g\perp}$ versus $R_{g\parallel}$ calculated from the tilings of individual MSNs synthesized with systematic variations in [TMB] and pH. As described above, the transition from cubic to dodecagonal symmetry is primarily the result of the

increasing micelle size and size distributions associated with increasing [TMB]. Therefore, MSNs synthesized at constant [TMB] and variable pH are represented by a single color (Fig. 6.3b). MSNs synthesized at the highest [TMB] are well described by the linear fit $R_{g\perp} = AR_{g//} + B$, where the slope provides the magnitude of the phason strain, a quantitative measure of quasicrystallinity.^{8,14} The lowest phason strain of particles synthesized using TMOS/APTMS (TEOS/AEAPTMS) was 0.14 (0.19) (see TEOS/AEAPTMS data in Fig. D10). These values approach the zero-phason strain of an ideal dodecagonal quasiperiodic tiling,⁸ demonstrating the high quasicrystallinity of the MSNs. Particles synthesized at intermediate [TMB] exhibited substantial fluctuations in the plot of $R_{g\perp}$ versus $R_{g//}$ (Fig. 6.3b). More specifically, individual particles from a single batch of MSNs synthesized in this regime may be cubic, quasicrystalline, or mixed phase. Finally, MSNs synthesized at the lowest [TMB] were dominated by cubic behavior, but a few quasicrystalline MSNs could always be found in a batch. For this reason, although a perfectly cubic crystal has a phason strain of 1, the highest slope observed in this study was slightly smaller than 1.

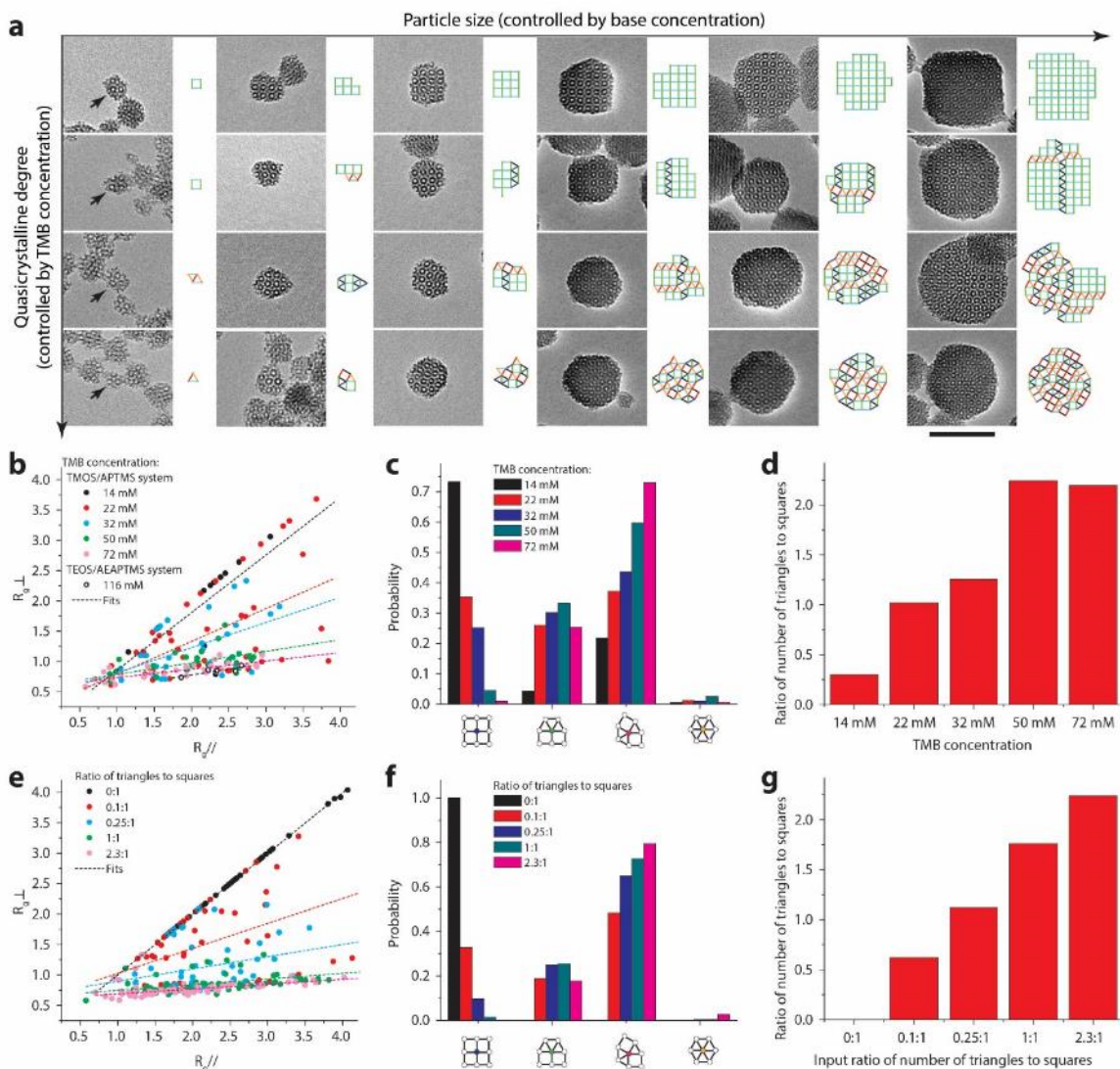


Figure 6.3. Analysis of a set of experimental and simulated MSN structures exhibiting transitions from cubic to dodecagonal symmetry. (a) TEM images and corresponding square-triangle tilings of MSNs (arrows) synthesized with the TMOS/APTMS system. All images have the same magnification; scale bar is 100 nm. (b) Plot of R_{\perp} in perpendicular vs. parallel space, calculated for MSNs synthesized from either the TMOS/APTMS system and five different [TMB] or from the TEOS/AEAPTMS system and one [TMB]. (c) Distribution of pore conformers (square, fan, quasicrystalline, and hexagonal) calculated for MSNs synthesized with the TMOS/APTMS system using five different [TMB]. (d) Ratio of triangle to square tiles calculated for MSNs in (c). (e to g) Plots corresponding to (b to d) for 500 MSNs derived from simulations with 5 different triangle to square ratios.

From the tiling analysis the distribution of four fundamental geometrical conformations was derived for all batches/particles, *i.e.* 4^4 , 3^34^2 , 3^2434 and 3^6 , where 4 and 3 represent square and triangle base units and the exponent indicates the number of adjacent

base units incident on a single vertex (Fig. 6.3c). This analysis suggests that with increasing [TMB], cubic 4^4 conformers decrease, triangle rich 3^2434 conformers increase, and mixed 3^34^2 conformers first increase but then roughly stay constant. All MSN samples analyzed have low abundance of 3^6 conformers. At the same time, the ratio of the overall numbers of triangles to squares increases with [TMB] (Fig. 6.3d). These data suggest that the presence of triangles in the tiling patterns is directly related to [TMB] and determines the resulting quasicrystallinity. Furthermore, the presence of large fluctuations in pore structure, observed for MSNs synthesized at intermediate [TMB] between 22 mM and 50 mM, suggests that fast silica condensation prevents the CTAB micelles from reaching their equilibrium packing configuration. Computer simulations were carried out in order to further address the origin of these fluctuations.

Quasicrystal growth has previously been modeled in 2-dimensions using triangle-square tilings.^{8,10,15} We have developed an irreversible MSN growth model that produces tilings that mimic the observed features of our experimental system (see Supplementary Information for details). Particle growth in these simulations proceeds via irreversible aggregation of square and equilateral triangle tiles. Each tile is randomly chosen from a weighted shape distribution given by an input triangle/square number ratio that represents the micelle size distribution at varying [TMB]. For each triangle/square ratio, several batches of particles with size distributions that approximately match those of experimentally observed particles are generated and combined for analysis. Simulated particles were analyzed according to the methods outlined for the experimental particles. Although this is a simplified model, comparison of Fig. 6.3e through g with Fig. 6.3b through d shows that it was sufficient to reproduce the experimentally observed features.

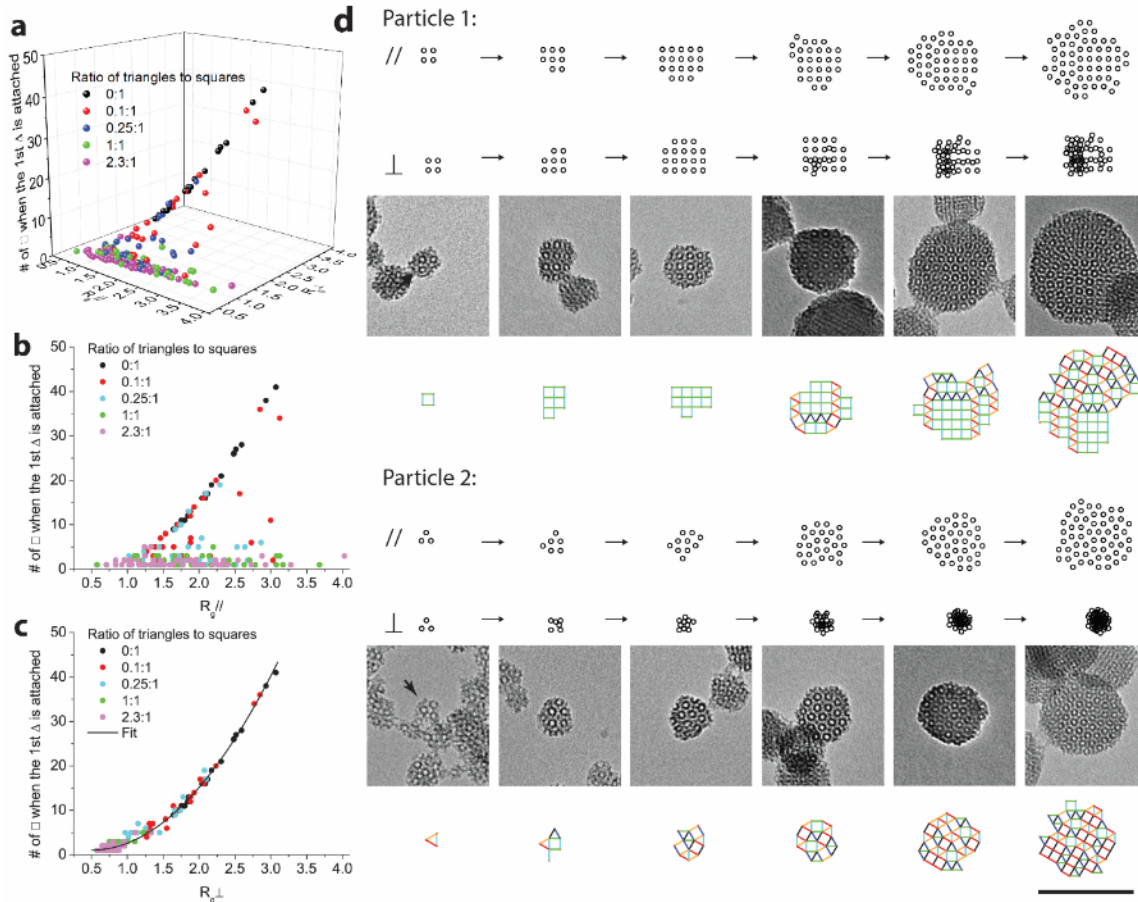


Figure 6.4. Analysis of single particle growth trajectories from simulations and comparison to experimental results. (a) 3D plot showing that phason strain is highly dependent on the time at which the first triangle is added to the growing particle. (b and c) 2D projections of the 3D plot in (a). The data in (c) is fitted using equation $N a^2 = A R_{g\perp}^2 + B R_{g\perp} + C$, where $a=1$ is the edge length of a square tile, N is the number of tiles, and A , B and C are fitting parameters. This is consistent with the theoretical relationship between the area and the radius of gyration, R_g , of a 2D square packing pattern (Supplementary Information). (d) Single particle growth trajectories of two simulated particles with triangle/square ratio equal to 0.1 with vertices plotted in both parallel and perpendicular space. Simulated growth stages are compared to experimental TEM images of MSNs and their tilings. All images have the same magnification; scale bar is 100 nm.

Analysis of simulated single particle growth trajectories (Fig. 6.4a) shows the relationship between quasicrystallinity ($R_{g//}$ vs. $R_{g\perp}$) and the size of the particle or the number of square tiles present (plotted along the z-axis) when the first triangle is added. For perfect cubic particles, the total number of squares at the end of the simulation is counted instead. At the highest triangle/square input ratio of 2.3³⁰, all data points (purple)

are highly concentrated in a low z range in Figure 6.4a, suggesting that the early appearance of a first triangle contributes to the growth of highly quasicrystalline particles. By comparison, the appearance of the first triangle in particles with a triangle/square input ratio of 0.1 (red) is widely distributed in the growth process causing the spread in quasicrystallinity observed in Figure 6.3e. 2D projections of Figure 6.4a, which represent the dependence of $R_{g\parallel}$ and $R_{g\perp}$ on the timing (*i.e.* particle size) of the first triangle addition are shown in Figure 6.4b and c, respectively. In Figure 6.4c, all data points fall onto a master curve, $N = N(R_{g\perp})$, that relates the area of a 2D square tiling pattern ($\propto N$) to its radius of gyration (see Supplementary Information). Side-by-side comparison of Figure 6.4b and c reveals that the first triangle addition seeds the growth of a quasicrystalline phase. While particle growth in real (parallel) space does not depend on the timing of the triangle addition, particle growth in perpendicular space is mostly terminated as soon as the first triangle is added. Single particle growth trajectories (Fig. 6.4d) of two simulated particles with the same triangle/square input ratio (0.1) illustrate this effect. Similarities between tilings from TEM images of particles synthesized at intermediate [TMB] and tilings of simulated particles at various stages of growth support the assumption that the formation of MSNs with dodecagonal tilings can be described using our model (Fig. 6.4d).

6.4 Conclusions

Precise control of a highly tunable silica sol-gel chemistry has enabled experimental observation of the early formation stages of quasicrystalline mesoporous silica. Our results suggest that a sufficient width of micelle size distribution frustrates crystal formation and that incorporation of differently sized building blocks (here micelles) at early times in the growth process promotes quasicrystalline order.

6.5 Acknowledgements

This work was supported by the U.S. Department of Energy, Office of Science, Basic Energy Sciences, under Award No. DESC0010560. This work made use of the Cornell Center for Materials Research Shared Facilities, which are supported through the NSF MRSEC program (DMR- 1120296), and the Nanobiotechnology Center shared research facilities at Cornell. This work is based upon research conducted at the Cornell High Energy Synchrotron Source (CHESS) which is supported by the National Science Foundation and the National Institutes of Health/National Institute of General Medical Sciences under NSF award DMR-1332208.

6.6 References

- (1) Shechtman, D.; Blech, I.; Gratias, D.; Cahn, J. W. Metallic Phase with Long-Range Orientational Order and No Translational Symmetry. *Phys. Rev. Lett.* **1984**, 433–435.
- (2) Levine, D.; Steinhardt, P. J. Quasicrystals: A New Class of Ordered Structures. *Phys. Rev. Lett.* **1984**, 53, 2477–2480.
- (3) Bindi, L.; Steinhardt, P. J.; Yao, N.; Lu, P. J. Natural Quasicrystals. *Science* **2009**, 324, 1306–1309.
- (4) Förster, S.; Meinel, K.; Hammer, R.; Trautmann, M.; Widdra, W. Quasicrystalline Structure Formation in a Classical Crystalline Thin-Film System. *Nature* **2013**, 502, 215–218.
- (5) Zeng, X.; Ungar, G.; Liu, Y.; Percec, V.; Dulcey, A. E.; Hobbs, J. K. Supramolecular Dendritic Liquid Quasicrystals. *Nature* **2004**, 428, 157–160.
- (6) Hayashida, K.; Dotera, T.; Takano, A.; Matsushita, Y. Polymeric Quasicrystal: Mesoscopic Quasicrystalline Tiling in A B C Star Polymers. *Phys. Rev. Lett.* **2007**, 98, 195502–195505.
- (7) Talapin, D. V.; Shevchenko, E. V.; Bodnarchuk, M. I.; Ye, X.; Chen, J.; Murray, C. B. Quasicrystalline Order in Self-Assembled Binary Nanoparticle Superlattices. *Nature* **2009**, 461.
- (8) Xiao, C.; Fujita, N.; Miyasaka, K.; Sakamoto, Y.; Terasaki, O. Dodecagonal Tiling in Mesoporous Silica. *Nature* **2012**, 487, 349–353.
- (9) Tolbert, S. H. Mesoporous Silica: Holey Quasicrystals. *Nat. Mater.* **2012**, 11, 749–751.

- (10) Joseph, D.; Elser, V. A Model of Quasicrystal Growth. *Phys. Rev. Lett.* **1997**, *79*, 1066–1069.
- (11) Achim, C. V.; Schmiedeberg, M.; Löwen, H. Growth Modes of Quasicrystals. *Phys. Rev. Lett.* **2014**, *112*, 255501–255505.
- (12) Levine, D.; Steinhardt, P. J. Quasicrystals. I. Definition and Structure. *Phys. Rev. B* **1986**, *34*, 596–616.
- (13) Oxborrow, M.; Henley, C. L. Random Square-Triangle Tilings: A Model for Twelffold-Symmetric Quasicrystals. *Phys. Rev. B* **1993**, *48*, 6966–6998.
- (14) Leung, P. W.; Henley, C. L.; Chester, G. V. Dodecagonal Order in a Two-Dimensional Lennard-Jones System. *Phys. Rev. B* **1989**, *39*, 446–458.
- (15) Kuo, K. H.; Feng, Y. C.; Chen, H. Growth Model of Dodecagonal Quasicrystal Based on Correlated Tiling of Squares and Equilateral Triangles. *Phys. Rev. Lett.* **1988**, *61*, 1740–1743.
- (16) Engel, M.; Damasceno, P. F.; Phillips, C. L.; Glotzer, S. C. Computational Self-Assembly of a One-Component Icosahedral Quasicrystal. *Nat. Mater.* **2014**, *14*, 109–116.
- (17) Iacovella, C. R.; Keys, A. S.; Glotzer, S. C. Self-Assembly of Soft-Matter Quasicrystals and Their Approximants. *Proc. Natl. Acad. Sci. USA* **2011**, *108*, 20935–20940.
- (18) Linden, M. N. V. D.; Doye, J. P. K.; Louis, A. A. Formation Of Dodecagonal Quasicrystals in Two-Dimensional Systems of Patchy Particles. *J. Chem. Phys.* **2012**, *136*, 054904–054914.

- (19) Kresge, C. T.; Leonowicz, M. E.; Roth, W. J.; Vartuli, J. C.; Beck, J. S. Ordered Mesoporous Molecular Sieves Synthesized by a Liquid-Crystal Template Mechanism. *Nature* **1992**, *359*, 710–712.
- (20) Hoffman, F.; Cornelius, M.; Morell, J.; Fröba, M. Silica-Based Mesoporous Organic-Inorganic Hybrid Materials. *Angew. Chem. Int. Ed.* **2006**, *45*, 3216–3251.
- (21) Sakamoto, Y.; *et al.* Direct Imaging of the Pores and Cages of Three-Dimensional Mesoporous Materials. *Nature* **2000**, *408*, 449–453.
- (22) Suteewong, T.; Sai, H.; Hovden, R.; Muller, D.; Bradbury, M. S.; Gruner, S. M.; Wiesner, U. Multicompartment Mesoporous Silica Nanoparticles With Branched Shapes: An Epitaxial Growth Mechanism. *Science* **2013**, *340*, 337–341.
- (23) Ma, K.; Sai, H.; Wiesner, U. Ultrasmall Sub-10 nm Near-Infrared Fluorescent Mesoporous Silica Nanoparticles. *J. Am. Chem. Soc.* **2012**, *134*, 13180–13183.
- (24) Suteewong, T.; Sai, H.; Cohen, R.; Wang, S.; Bradbury, M.; Baird, B.; Gruner, S. M.; Wiesner, U. Highly Aminated Mesoporous Silica Nanoparticles With Cubic Pore Structure. *J. Am. Chem. Soc.* **2011**, *133*, 172–175.
- (25) Huo, Q.; Margolese, D. I.; Ciesla, U.; Feng, P.; Gier, T. E.; Sieger, P.; Leon, R.; Petroff, P. M.; Schüth, F.; Stucky, G. D. Generalized Synthesis of Periodic Surfactant/Inorganic Composite Materials. *Nature* **1994**, *368*, 317–321.
- (26) Gao, C.; Sakamoto, Y.; Terasaki, O.; Che, S. Formation Of Diverse Mesophases Templated by a Diprotic Anionic Surfactant. *Chem. Eur. J.* **2008**, *14*, 11423–11428.

- (27) Schmidt-Winkel, P.; Lukens, W. W.; Yang, P.; Margolese, D. I.; Lettow, J. S.; Ying, J. Y.; Stucky, G. D. Microemulsion Templating of Siliceous Mesoporous Cellular Foams with Well-Defined Ultralarge Mesopores. *Chem. Mater.* **2000**, *12*, 686–696.
- (28) Blin, J. L.; Su, B. L. Tailoring Pore Size of Ordered Mesoporous Silicas Using One or Two Organic Auxiliaries as Expanders. *Langmuir* *18*, 5303–5308.
- (29) Frank, F. C.; Kasper, J. S. Complex Alloy Structures Regarded as Sphere Packings. II. Analysis and Classification of Representative Structures. *Acta Crystallogr.* **1959**, *12*, 483–499.
- (30) Stampfli, P. A dodecagonal quasiperiodic lattice in two dimensions. *Helv. Phys. Acta* **1986**, *59*, 1260–1263.

Appendix D: Supplementary information for Chapter 6

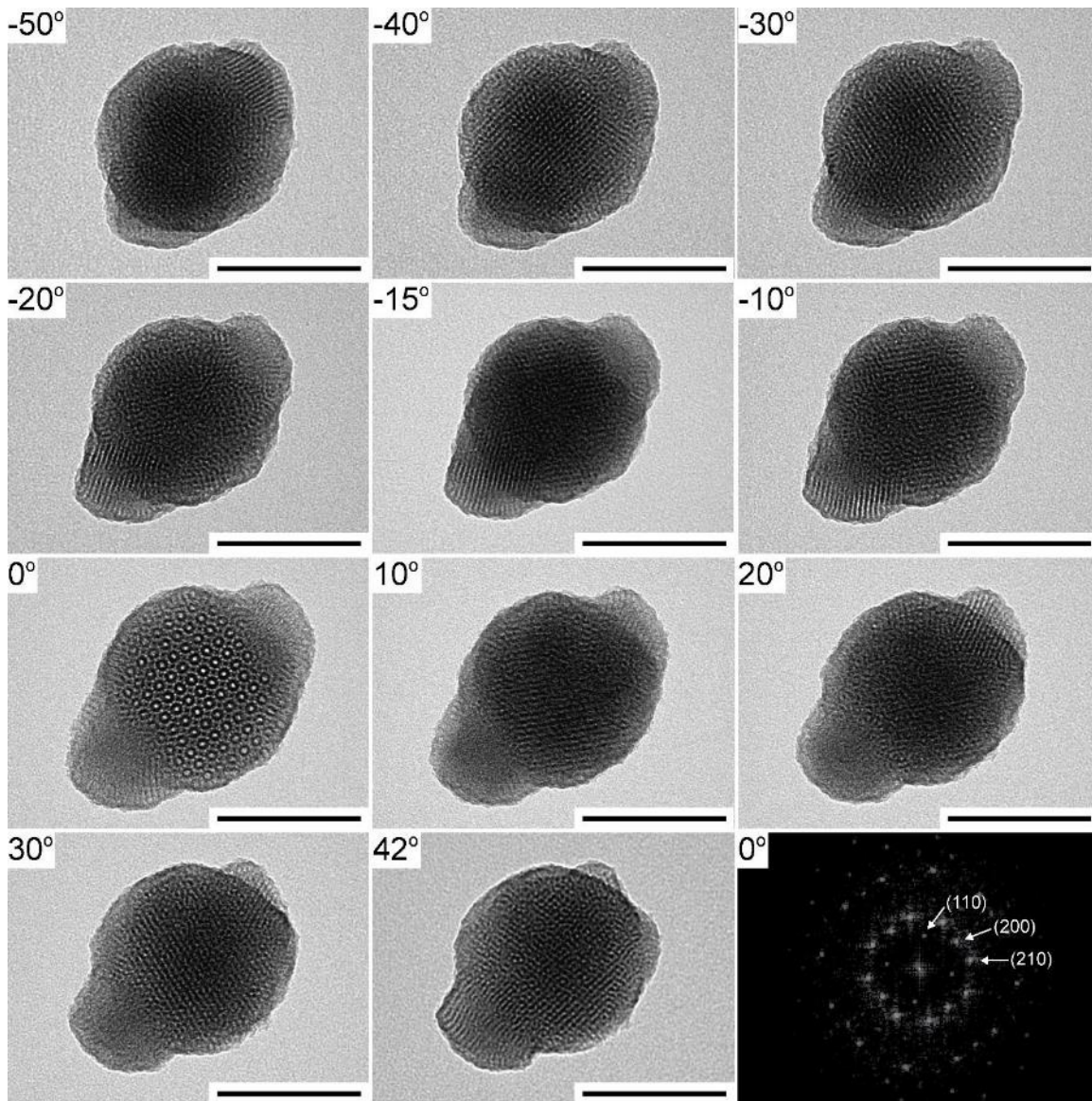


Figure D1. Single-tilt TEM images of a multicompartiment MSN with two branches derived from TEOS/AEAPTMS system. TEM tilt series of an MSN prepared using 29 mM TMB. An FFT of the entire cubic core area of the particle taken at 0° shows the

characteristic four-fold cubic pattern along the (001) zone axis. All scale bars are 100 nm.

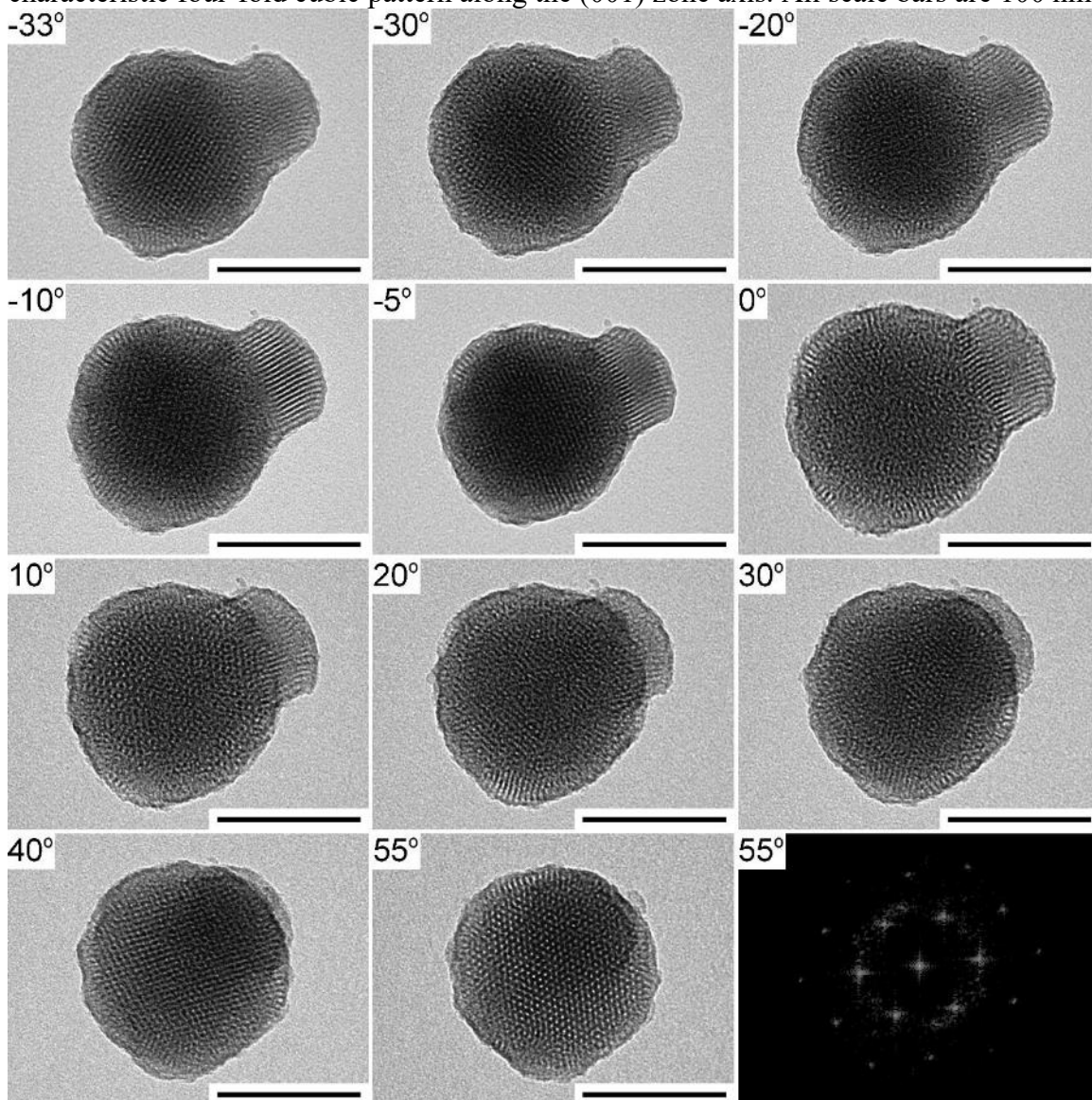


Figure D2. Single-tilt TEM images of another multicompartiment MSN with one branch derived from TEOS/AEAPTMS system. TEM tilt series of an MSN prepared using 29 mM TMB. An FFT of the particle was taken at 55° along the (111) zone axis. All scale bars are 100 nm.

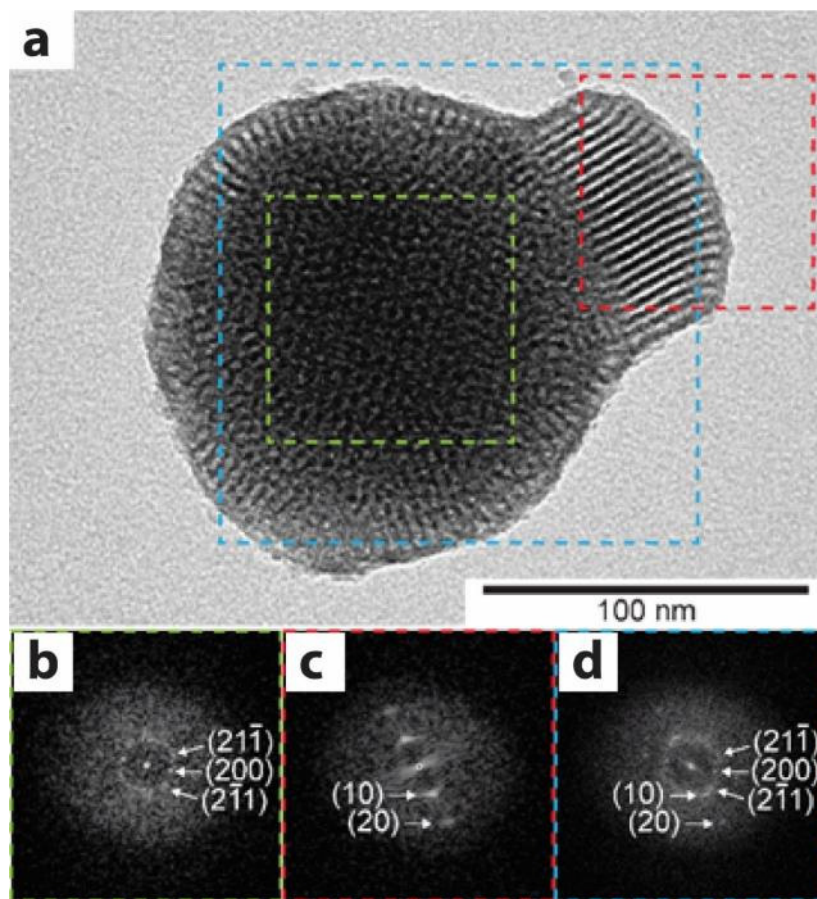


Figure D3. FFT analysis of multicompartiment MSN derived from TEOS/AEAPTMS system. (a) TEM image of a multicompartiment MSN with one branch taken at -10° (from Fig. D2). (b) FFT of the cubic core region in a (green box), showing spots from the cubic $Pm\bar{3}n$ lattice along the (110) zone axis. (c) FFT of the hexagonal branch region in a (red box), showing spots from the hexagonal $P6mm$ lattice. (d) FFT of the region containing both compartments in a (blue box), showing that the cubic (211) and hexagonal (10) spots reside closely with a lattice mismatch of 8.5% (larger for cubic lattice). This lattice mismatch is compensated by low-angle defects at the (111) plane.

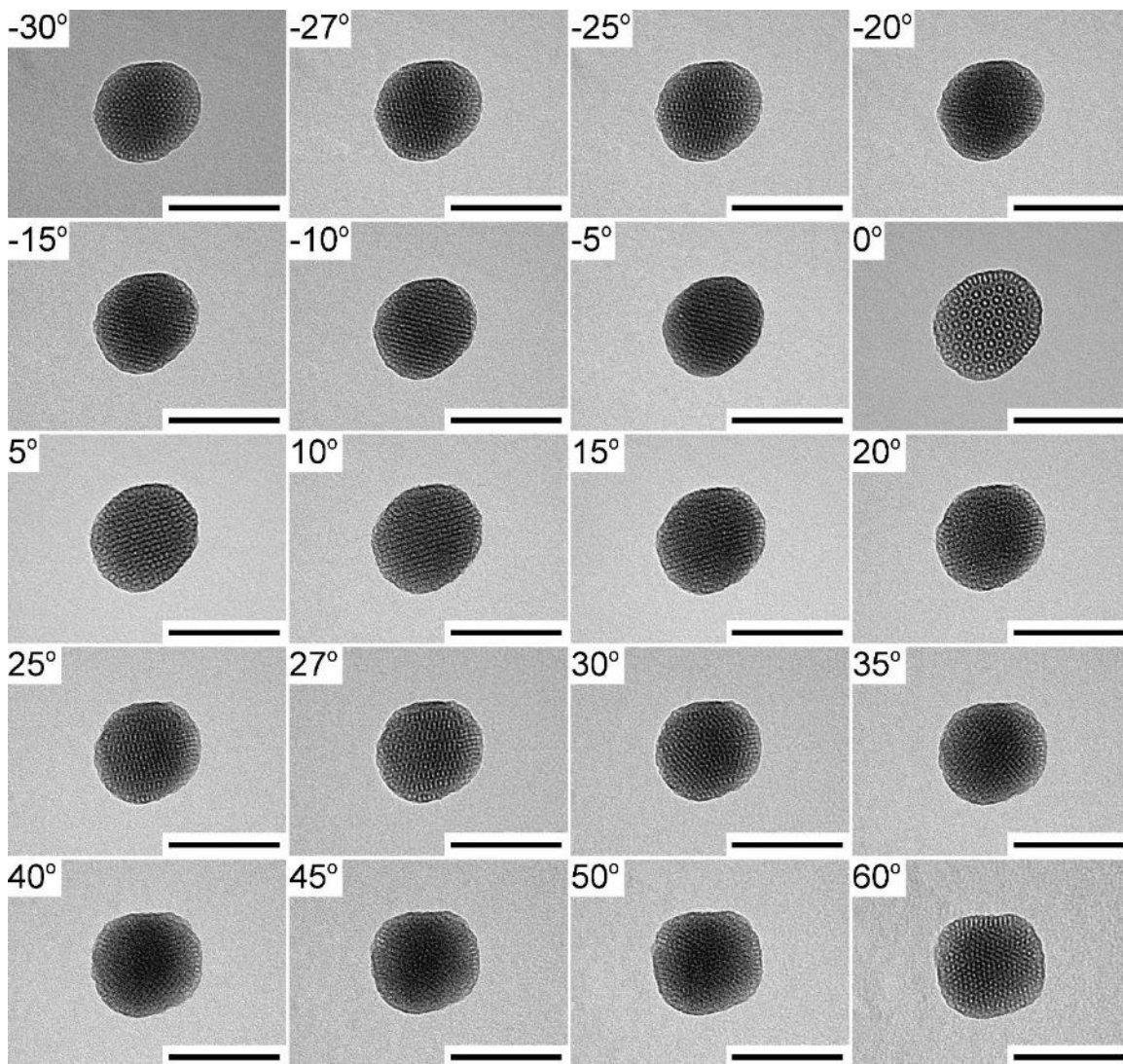


Figure D4. Single-tilt TEM study of a MSN with dodecagonal tiling derived from the TEOS/AEAPTMS system. From these images it is difficult to extract the three-dimensional particle structure. All scale bars are 100 nm.

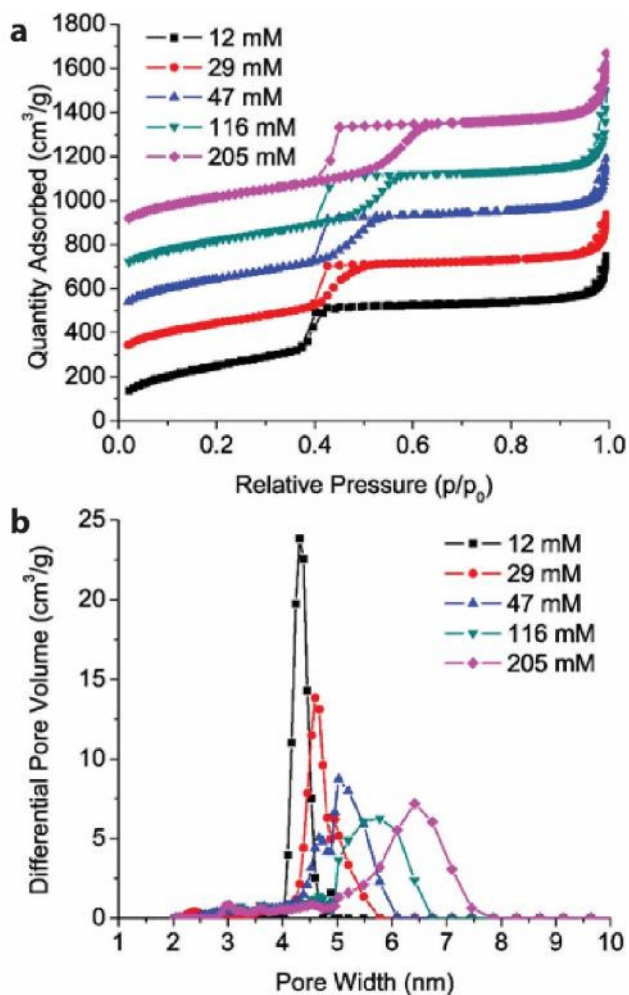


Figure D5. Nitrogen sorption isotherms and corresponding pore size analyses for TEOS/AEAPTMS derived particles synthesized with increasing [TMB]. (a) Nitrogen sorption isotherms of MSNs prepared with varying [TMB]. Starting from the second isotherm, each set is offset along the y -axis by $200 \text{ cm}^3/\text{g}$ compared to the previous one. (b) The corresponding density functional theory (DFT) derived pore size distributions. All samples exhibited type IV isotherms with increasing size of hysteresis loops, attributed to the expansion of mesopores, which was further elucidated by the pore size distributions calculated using a DFT model.

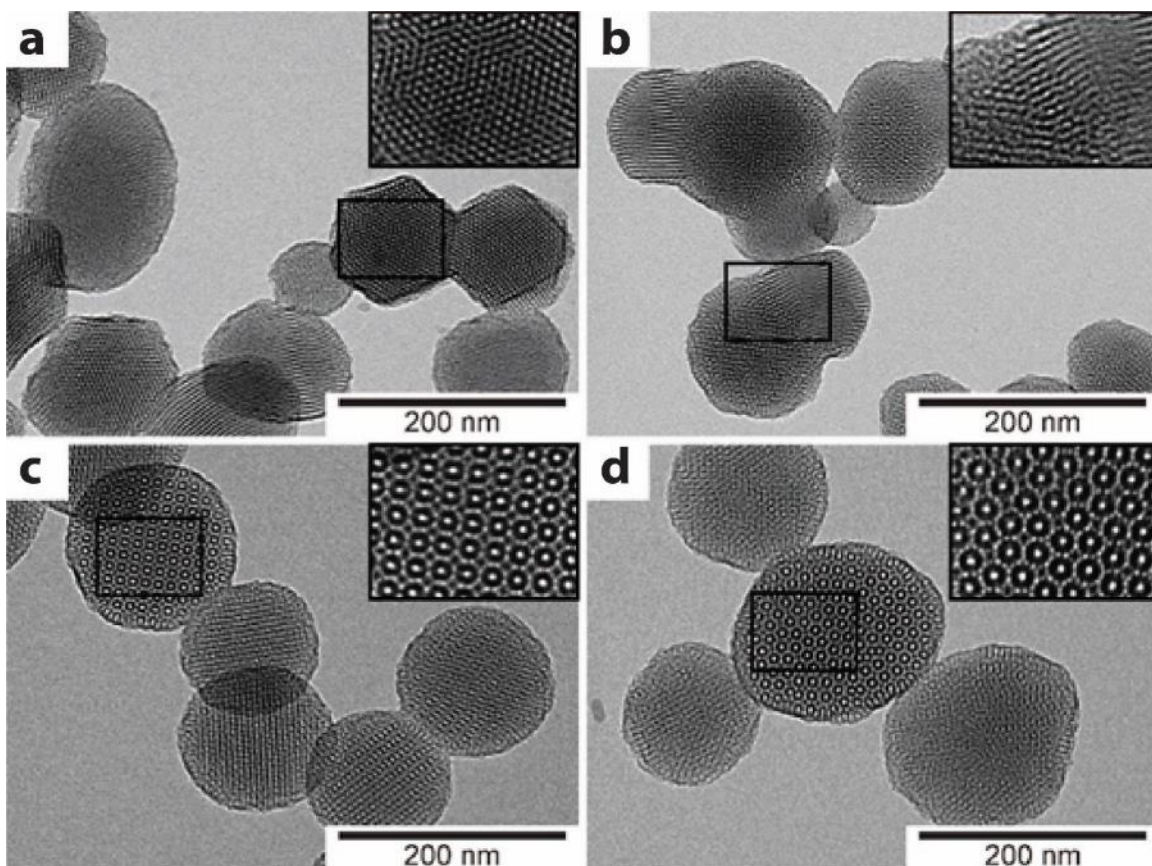


Figure D6. Structure evolution of TEOS/AEAPTMS derived MSNs as a function of stirring rate. TEM images of MSNs prepared from 29 mM TMB at stirring rates of (a) 500 rpm, (b) 650 rpm, (c) 850 rpm, and (d) 1000 rpm. Insets are magnified images on selected areas (rectangles).

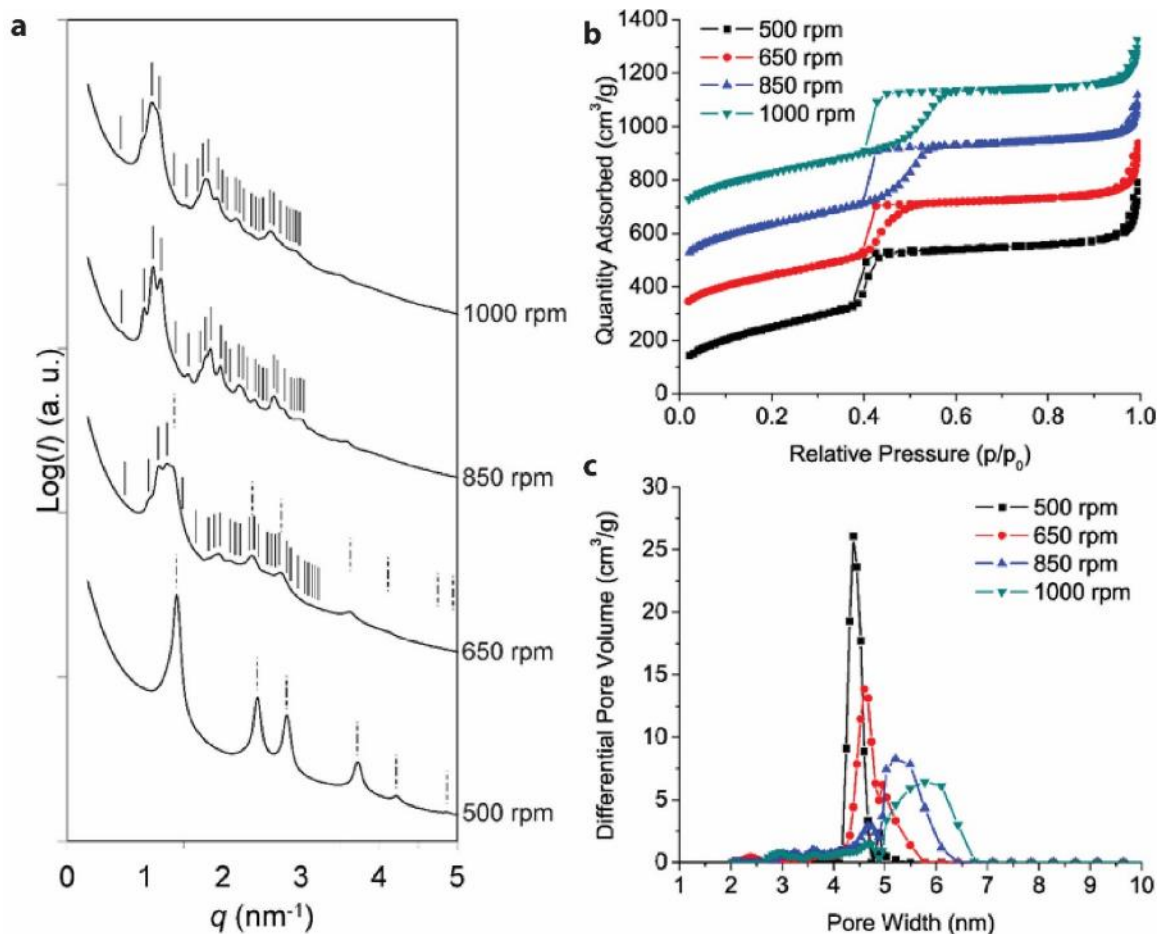


Figure D7. Structure evolution of TEOS/AEAPTMS derived MSNs as a function of stirring rate as revealed by SAXS and nitrogen sorption measurements. (a) SAXS patterns, (b) nitrogen sorption isotherms, and (c) DFT pore size distributions derived from data shown in (b) of MSNs prepared from 29 mM TMB at varying stirring rates. In the SAXS patterns, expected peak positions for cubic $Pm\bar{3}n$ and hexagonal $P6mm$ lattices are indexed by solid and dash lines, respectively. In (b), starting from the second curve, each isotherm is offset along the y-axis by 200 cm^3/g compared to the previous one.

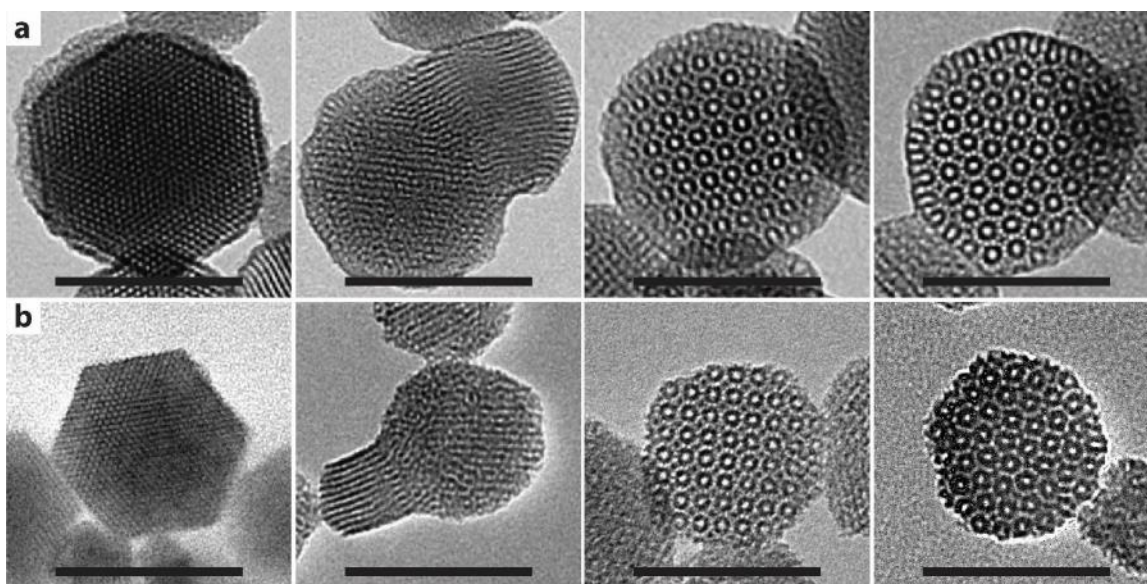


Figure D8. Structural comparison of MSNs synthesized with varying [TMB] using two different silane systems as revealed by TEM. (a) TEOS/AEAPTMS system (same images as in Fig. 6.1 of main text). (b) TMOS/APTMS system. As [TMB] increases (from left to right) from 0 mM to 11 mM to 14 mM and finally to 72 mM, respectively, the structures of MSNs from both systems change from hexagonal, to multicompartment, to cubic, and finally to a structure with dodecagonal symmetry. Scale bars are 100 nm.

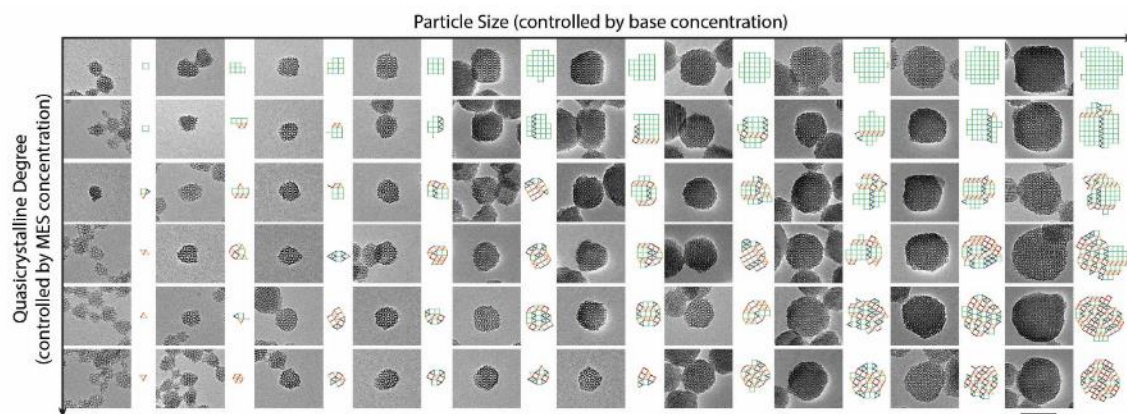


Figure D9. MSNs with varying particle size and quasicrystallinity. Extended data set relative to what is shown in Figure 6.2a of the main text, including TEM images and square-triangle tilings of MSNs synthesized using the TMOS system. Scale bar is 100 nm.

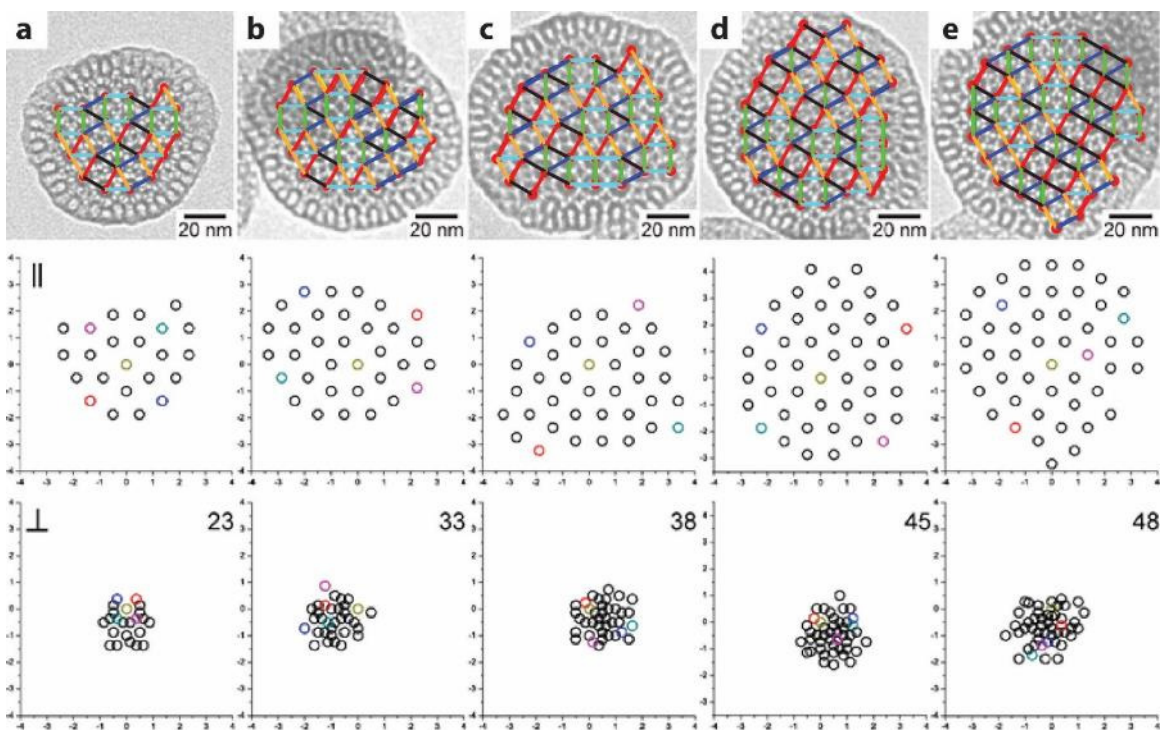


Figure D10. TEM images, square-triangle tilings, and arrangements of vertices in parallel and perpendicular spaces for five MSNs synthesized with the TEOS/AEAPTMS silane system at 116mM TMB with increasing numbers of vertices. (a-e) Top row: square-triangle tilings superposed on high-magnification TEM images of five dodecagonal MSNs with (a) 23, (b) 33, (c) 38, (d) 45, and (e) 48 vertices. The randomly colored points in the middle and bottom panels show how individual points move during the transformation from parallel to perpendicular space.

Chapter 7 . Conclusions

In my thesis I have developed an aqueous synthesis approach to sub-10nm silica nanoparticles with unprecedented control and accuracy over structural and compositional parameters. By introducing surfactant-directed molecular self-assembly into the synthesis system, the particle structure can be further tailored. For example, a ~3nm pore can be integrated into sub-10nm silica nanoparticles for loading/release of molecular cargos. In addition, the nanoparticles can be endowed with fluorescence for imaging applications via the covalent encapsulation of fluorescent dyes into the silica matrix. Finally, fluorescence correlation spectroscopy was introduced as an appropriate and powerful tool for the investigation of nanoparticle size, brightness, and surface modification with biocompatible polyethylene glycol and cancer targeting ligands.

Based on these results, I have developed a nanomaterial platform which contains a series of clinically applicable silica-based nanomaterials with varying structures, compositions and properties, *e.g.* C' dots, AlC' dots and mC dots. In particular, C' dots, which are ultras-small PEGylated fluorescent silica nanoparticles synthesized in water, have already been used in the clinic. Multiple clinical trials on cancer patients using these particles are currently undergoing at Memorial Sloan Kettering Cancer Center (MSKCC) in New York City.

In addition to nanomedicine applications, this synthesis platform provides insights into the fundamental understanding of the early formation mechanisms of self-assembled nanostructures. To that end, the formation process of quasi-crystalline mesoporous silica nanoparticles was investigated highlighting structural details of building blocks and

pathways responsible for the switch between crystalline (cubic symmetry) and quasicrystalline states.

Looking forward, this synthesis platform developed in my PhD providing precise and reliable control over structural and compositional details of ultrasmall silica nanomaterials now opens a gate to an exciting new area of clinical applications of inorganic silica-based nanomedicines. Access to such ultrasmall inorganic-based nanomaterials can potentially lead to the development of new cancer therapies and new investigational methodologies for biology studies. To that end, one of the next steps of this work is to translate other particle products of this platform into the clinic, *e.g.* AIC' dots and mC dots. Since the particle functionality can be specifically designed in this synthesis platform through the precise control of *e.g.* particle size, structure, fluorescence and targeting properties, the clinical use of the whole family of these nanomaterials with diversified functionality in the future may greatly contribute to personalized cancer treatments. Meanwhile, I expect that many exciting new discoveries regarding the fundamental understanding of how such nanoparticles interact with biological environments will be made along this process.

This highly tunable silica synthesis system also provides unprecedented ways to study early silica nanomaterial formation pathways. For example, it can be used as a model approach by quenching the early formation stages of self-assembled nanomaterials, including but not limited to quasi-crystalline mesoporous silica as described in Chapter 6. For instance, via introducing a similar approach to surfactant self-assembly directed organic-silica hybrid nanostructure formation, the early evolution of micelle-silica assemblies may be quenched providing insights into early formation mechanisms.

Furthermore, since this synthesis system is in aqueous solution with pH values ranging from neutral to slightly basic, it is potentially compatible with many biological materials and processes enabling, *e.g.* the self-assembly of silica with DNA and proteins. Therefore, integrating this silica synthesis system with the diversity of biology, the programming language of biomolecules, *e.g.* DNA origami, may be used as a novel tool to direct the structure formation of nanosilica for the fabrication of programmable inorganic-based nanomaterials. If this is achievable, each generated inorganic silica nanoparticle or nanostructure can contain a significant amount of information specifically designed by computer programs. Access to such processes would be revolutionary, leading to the discoveries of new nanomaterials and associated and previously unknown material properties.

In summary, I expect that in the future, using this highly tunable synthesis system, advanced silica-based inorganic nanomedicines will be developed and translated into the clinic providing real benefits to cancer patients, the ultimate goal. Simultaneously, new discoveries are expected, both on the side of fundamental understanding of nanomaterial formation as well as on the clinical side including diagnostic, therapeutic, as well as theranostic nanomaterials.